

Hans-Jörg Huth

Fatigue Design of Hydraulic Turbine Runners

Hans-Jörg Huth

Fatigue Design of Hydraulic Turbine Runners

A thesis submitted in partial fulfilment of the requirements for the
Norwegian academic degree of *Doktor Ingeniør*

Norwegian University of Science and Technology (NTNU)
Department of Engineering Design and Materials
Trondheim, Norway

February 2005

Supervised by:

Prof. TeknD Gunnar Härkegård

Admission committee:

Prof. TeknD Sören Sjöström (first opponent)
Siemens Industrial Turbomachinery AB, and
Linköping Institute of Technology, Sweden

Dr.ing. Steinar Faanes (second opponent)
General Electric Energy (Norway) AS

Prof. dr.ing. Per Jahn Haagensen (chair)
Norwegian University of Science and Technology, Trondheim, Norway

Electronically distributed at:

<http://urn.nb.no/URN:NBN:no-2316>

Online bibliographic description:

<http://www.diva-portal.org/ntnu/theses/abstract.xsql?dbid=434>

Doctoral thesis 2005:19

ISBN 82-471-6900-2 (printed)

ISBN 82-471-6899-5 (electronic)

ISSN 1503-8181

Copyright © 2005 by Hans-Jörg Huth

Printed in Norway by NTNU Trykk

Typeset with L^AT_EX

Also kommt, wie bei der künstlerischen, so bei der naturwissenschaftlichen, auch bei der mathematischen Behandlung alles an auf das Grundwahre, dessen Entwicklung sich nicht so leicht in der Spekulation als in der Praxis zeigt; denn diese ist der Prüfstein des vom Geist Empfangenen, des von dem innern Sinn für wahr Gehaltenen.

Johann Wolfgang von Goethe

Preface

This work was funded by General Electric Energy (Norway) AS in Kjeller (formerly Kværner Energy, Oslo) and the Norwegian Research Council within the STÅLMAT project for a period of three years.

The work was performed at the Department of Engineering Design and Materials Technology of the Norwegian University of Science and Technology (NTNU) in Trondheim. In addition to the project work, the author was employed at the department as a scientific assistant for the accumulated time of one year.

In 2002, the author had a stay of three months at the Department of Civil Engineering, Environment and Architecture of the University of Parma, Italy.

Spending so many years on the quest for new knowledge, insight and conclusions in the course of this present work, a look over the shoulder longer back to the early beginnings of research on fatigue and notch effects appeared to be more than just interesting to the author. One chapter was dedicated to a history review.

This thesis partly includes the following publications:

- G. Härkegård, H.-J. Huth, and S. Faanes. FEA-based fatigue assessment methodology for hydraulic turbine runners. In A. Strang et al., editors, *Proceedings of the 5th International Charles Parsons Turbine Conference*, pages 1105–1118, London, 2000. IOM Communications Ltd.
- H.-J. Huth. Fatigue crack growth from shape-optimised notches in hydraulic turbine runners. In A. F. Blom, editor, *Proceedings of the Eighth International Fatigue Congress*, volume 5, pages 3007–3014, Stockholm, Sweden, 2002.
- A. Carpinteri, R. Brighenti, H.-J. Huth, and S. Vantadori. Fatigue growth of a surface crack in a welded T-joint. *International Journal of Fatigue*, 27(1), 2005.

Abstract

Turbine runners experience start-stop cycles and vibration cycles. Cracks initiated from service or manufacturing defects and propagated by start-stop cycles become critical when the stress intensity range due to vibrational loading exceeds the threshold for fatigue crack growth.

In Francis turbine runners, semi-elliptical surface cracks tend to propagate from the quarter-circular transition of the welded T-joint transition between the blade and the band or crown. Assuming a crack to grow under a constant stress amplitude equal to that at the most highly loaded location at the welded joint between the blade and the band or crown of a Francis turbine runner yields a conservative estimate of the life of the runner. A more accurate prediction of fatigue life is obtained by considering the growth of a crack in the real, inhomogeneous stress field. For an idealised T-joint under pure bending, the stress field has been determined by means of plane strain finite element analysis.

Finite element models of the entire Francis runner are built with respect to the calculation of fluid dynamic properties. Since in these models geometry transitions are modelled as a sharp notch, both a finite and a zero transition radius have been modelled, and the influence of the mesh size on the maximum stress has been investigated.

For relatively small cracks, it is shown that the structural component geometry does not remarkably influence the stress intensity factor values, provided that the stress field in the vicinity of the crack is approximately the same. Therefore, in order to simplify the stress intensity factor retrieval and to generate a solution of extended applicability, a cracked finite-thickness plate is examined instead of the actual T-joint geometry. The stress intensity factors along the front of a semi-elliptical surface crack in such a plate are determined by means of an analysis using finite quarter-point wedge elements for different elementary loading conditions that can be employed to model the actual stress field at the expected crack location in the examined T-joint. By applying the superposition principle and the power series expansion of the actual stress field due to the load applied to the T-joint considered, an approximate stress intensity factor for the cracked T-joint has been obtained.

The growth of semi-elliptic surface cracks in the stress field of the T-joint has been analysed using stress intensity factors of both own and literature solutions and employing a two-parameter model based on the Paris law. The theoretical fatigue crack growth predictions are in acceptable agreement with observations from experimental fatigue testing.

Furthermore, an iterative shape optimisation methodology has been applied to the two locations of stress concentration that show the highest local stress amplitudes and there-with are the most critical areas for fatigue of the Francis turbine runner. It is shown that stress concentration due to bending can be virtually eliminated. Large-scale geometry changes minimise stress concentration but create shapes that are sensitive to manufactur-

ing tolerances. Fracture-mechanical fatigue crack growth methodology calculations and experimental fatigue testing of moderately optimised shapes revealed that the runner's fatigue properties could be increased by factors 1.5–1.8 and 2–2.5, respectively.

Acknowledgements

The writer wishes to express his gratitude to Professor Gunnar Härkegård, under whose guidance this investigation was conducted, for his patient guidance and criticism throughout the investigation, for all the valuable ideas and suggestions, and for our conversations on science and politics, often until late in the evening, and which I enjoyed much.

The author is also indebted to General Electric Energy (Norway) AS in Kjeller as a source of both technical information and generous funding. Further thanks go to the members of the Department who were involved in my work, and to Mr. Odd Nerdahl at SINTEF for his help in the laboratory.

I thank Professors Andrea Carpinteri, Roberto Brighenti, Andrea Spagnoli and Sabrina Vantadori at the University in Parma, Italy, for their hospitality during my stay in Parma, for new ideas and insight, and for the exciting teamwork.

I want to thank my parents who supported and encouraged me throughout my whole education. With delight I remember my mother taking English lessons to be able to practice English with me when i attended grammar school, and my father arousing my interest in engineering in our common bicycle repairs.

To my beloved fiancée Marit Eline: thank you for all your patience and support, for your love and everything that makes it so worthwhile to know you.

Contents

Preface	i
Abstract	iii
Acknowledgements	v
List of Symbols	xvii
1 Introduction	1
1.1 Turbine Design and Classification	1
1.2 Francis Turbines	2
1.3 Background and Motivation	4
1.4 Outline of the Thesis	5
2 History of Fatigue and the Notch Effect	7
2.1 Early Research on Fatigue	7
2.2 Stress Concentration	9
2.3 Stress Concentration Factor and Fatigue	10
2.4 Approaches to Fatigue Design	11
3 Francis Runner	13
3.1 Material	13
3.2 Manufacturing	13
3.3 Loading	14
3.3.1 LCF Loading	15
3.3.2 HCF Loading	16
3.4 Notch Stress Analysis	17
3.4.1 T-joint	17
3.4.2 Trailing Edge	20
4 Fatigue Design Methodology	25
4.1 Stress-Life Approach	25
4.1.1 SN Curves	25
4.1.2 Fatigue Life Approach	27
4.2 Damage Tolerance Criterion	28
4.3 Simplified Fatigue Crack Growth	29

5	Stress Intensity Factors	31
5.1	Basics and History	31
5.1.1	Different Types of Crack Surface Displacement	31
5.1.2	SIF Definition	32
5.2	SIF Retrieval	34
5.2.1	Crack Tip Stress Singularity	34
5.2.2	Quarterpoint Finite Elements	35
5.2.3	Superposition Principle	36
5.3	Solutions for Fatigue Crack Growth Calculation	38
5.3.1	Internal Pore	39
5.3.2	Newman and Raju	39
5.3.3	Pommier, Sakae and Murakami	39
5.3.4	Carpinteri, Brighenti, Huth and Vantadori	40
5.3.5	Further Solutions	43
5.4	Component Geometry Influence	43
6	Shape Optimisation	47
6.1	Introduction	47
6.2	Basic Theory	49
6.2.1	Steps in Shape Optimisation	49
6.2.2	Gradient based Optimisation	50
6.2.3	Surface Generation by B-splines	51
6.3	Optimisation of the T-joint Transition	53
6.3.1	Optimisation Process	53
6.3.2	Results	54
6.4	Optimisation of the Trailing Edge Transition	55
6.4.1	Optimisation Process	58
6.4.2	Results	58
7	Fatigue Testing	61
7.1	T-joint Test	62
7.1.1	Specimen Manufacturing	62
7.1.2	Fatigue Testing	63
7.1.3	Beach Marking	63
7.1.4	Results	65
7.2	Trailing Edge Transition Test	65
7.2.1	Specimen Manufacturing	65
7.2.2	Fatigue Testing	68
7.2.3	Results	70
8	Local Stress Approach	73
8.1	Neuber Notch Stress	73
8.2	Effect of Stress Ratio	74

9	Fatigue Crack Growth Analysis	79
9.1	Introduction	79
9.1.1	Regimes of Fatigue Crack Growth	79
9.1.2	Size of plastic Zone	81
9.1.3	Application of SIF Solutions	81
9.2	Pommier et al. SIF Code Implementation	82
9.2.1	FCG in the Stress Field of the quarter-circular T-joint Transition	84
9.2.2	Shape Optimisation and FCG Methodology	85
9.3	Carpinteri et al. SIF Code Implementation	87
9.3.1	SIFs for T-joints	88
9.3.2	FCG Simulation	92
9.4	Methods Comparison	95
9.4.1	SIF Values	95
9.4.2	FCG Methodology Calculation	100
9.4.3	FCG Calculation and Beach Marks	101
10	Summary	105
10.1	Discussion and Conclusions	105
10.2	Suggestions for further Work	107
	References	109
A	Stress Concentration Factor Formula due to Rainer	123
B	Stress Intensity Factor Solutions	125
B.1	SIF Formulae due to Newman and Raju	125
B.2	SIF Formulae due to Pommier et al.	126
C	Experimental Fatigue Test Data	127
C.1	Fatigue Test SN Data	127
D	Material Stress–Strain Data	129
E	Visual Basic Codes	133
E.1	Newman-Raju FCG Subroutine	133
E.2	Pommier et al. FCG Subroutine	137
E.3	Carpinteri et al. FCG Subroutine	144

List of Figures

1.1	Hydroelectric power station. Scheme and Notation	3
1.2	Francis turbine. Notation	3
2.1	Elliptic hole in plate under tension	9
2.2	Spherical cavity in an infinite body in tension	11
3.1	Francis turbine runner. Notation	14
3.2	Francis turbine runner. Service stress history	15
3.3	Turbine blade subjected to a bending load	16
3.4	Simplified model of T-joint between turbine runner blade and band/crown	18
3.5	T-joint FE model for nominal bending load	19
3.6	Quarter-circular T-joint model FE mesh	19
3.7	Sharp T-joint model FE mesh	19
3.8	Influence of FE mesh density and transition radius on T-joint K_t values	20
3.9	Trailing edge transition FE model for nominal tensile load	21
3.10	Trailing edge radii influence on FE stress concentration analysis	23
3.11	Blade size influence on FE stress concentration analysis of trailing edge	23
4.1	SN curve of 17Cr-4Ni. Fatigue load regimes	26
4.2	Notched fatigue test specimen [54]. Geometry and loading	26
4.3	Francis turbine runner. Allowable initial crack depth	30
5.1	Basic modes of crack surface displacement	32
5.2	Mode I crack stress field in an infinite plate	33
5.3	Quarter-infinite crack. Notation	35
5.4	Triangle quarter-point element	36
5.5	Superposition principle	37
5.6	Semi-elliptical crack. Notation	40
5.7	Finite plate with semi-elliptical surface crack	41
6.1	General shape optimisation process	50
6.2	Physical spline and mathematical analogue	52
6.3	Stress concentration in T-joint optimisation approaches	55
6.4	Optimised T-joint shape A. FE mesh and max. principal stress	56
6.5	Optimised T-joint shape B. FE mesh and max. principal stress	56
6.6	Optimised T-joint shape C. FE mesh and max. principal stress	56
6.7	Optimised T-joint shape D. FE mesh and max. principal stress	56
6.8	Standard circular T-joint shape. FE mesh and max. principal stress	57

6.9	Standard circular T-joint shape. Stress gradients at largest principal stress . . .	57
6.10	Trailing edge transition shape optimisation strategy	58
6.11	Stress concentration in trailing edge optimisation approaches	59
6.12	Circular trailing edge transition shape. FE mesh and max. principal stress . . .	59
6.13	Optimised trailing edge transition shape. FE mesh and max. principal stress . .	59
7.1	Standard quarter-circular T-joint specimen transition	64
7.2	Shape optimised T-joint specimen transition	64
7.3	T-joint test specimens. Geometry and loading	64
7.4	T-joint test mounted	64
7.5	Beach marks in standard T-joint specimen	66
7.6	Beach marks in optimised T-joint specimen	66
7.7	T-joint specimen weld zone: coarse and inhomogeneous crack surface	66
7.8	T-joint tests SN curve	67
7.9	Circular-shaped trailing edge transition specimen	68
7.10	Shape optimised trailing edge transition specimen	68
7.11	Trailing edge transition test specimen. Geometry and loading	69
7.12	Trailing edge transition test mounted	69
7.13	Strain gauge placement	69
7.14	Failure of trailing edge specimen	69
7.15	3D test $F_{cyl.}-\varepsilon_n$ curves	70
7.16	Cracked surface of cast steel GX5CrNi 13-4 specimen	71
7.17	Cracked surface of rolled steel 34CrNiMo 6 specimen	71
7.18	Three beach marks in rolled steel trailing edge specimen	71
7.19	Central material defect in rolled steel slab	71
7.20	Trailing edge tests SN curve	72
8.1	Neuber analysis. Graphical method	74
8.2	Neuber stress and strain correction and hysteresis loop in 3D test	75
8.3	Modified SN curves from experimental fatigue testing	77
9.1	Regimes in fatigue crack propagation	80
9.2	Plastic superposition for unloading	80
9.3	Requirements of LEFM. Characteristic lengths of the semi-elliptical surface crack .	81
9.4	Geometric notation for semi-elliptical surface crack in T-joint	82
9.5	Growth of semi-elliptical surface cracks in zx -plane of a quarter-circular T-joint .	86
9.6	Growth of semi-elliptical surface cracks in T-joint zx -plane. Standard and shape optimised transitions	86
9.7	Fatigue crack shapes under propagation to failure	87
9.8	Finite plate with semi-elliptical surface crack	88
9.9	SIF- ξ diagrammes for different T-joint stress distributions	90
9.10	Dimensionless SIF along the crack front for different values of ζ and α	91
9.11	Two-parameter fatigue crack growth model	93
9.12	Development of fatigue cracks. Numerical and test results	94
9.13	SIF- ϕ diagrammes for different T-joint stress distributions and $\xi = 0.1$	96
9.14	SIF- ϕ diagrammes for different T-joint stress distributions and $\xi = 0.2$	97
9.15	SIF- ϕ diagrammes for different T-joint stress distributions and $\xi = 0.3$	98
9.16	SIF- ϕ diagrammes for different T-joint stress distributions and $\xi = 0.5$	99

9.17 Fatigue crack growth simulation between beach marks	103
D.1 Static stress–strain curves	130

List of Tables

5.1	Computed values of λ	35
5.2	Comparison of dimensionless SIF values given by the literature	45
6.1	2D shape optimisation strategy	54
6.2	Optimised T-joint shapes and stress concentration	54
7.1	Experimental fatigue test overview	62
7.2	Beach mark data from T-joint fatigue testing	65
9.1	Cycles for an initially semi-elliptical surface crack to become critical	84
9.2	Efficiency of different T-joint shape optimisation cases	87
9.3	T-joint crack stress field coefficients	89
9.4	Dimensionless SIFs for different opening stresses	92
9.5	FCG methodology results for different SIF solutions	100
A.1	Rainier formula	123
C.1	Fatigue test setup and SN data	128
D.1	Setup and results from static tensile testing	131

List of Symbols

A	Location of largest crack depth
a	Crack depth. Semi-axis of elliptic crack along x -axis
a^*	New propagated crack depth
B	Point on crack front where $\zeta/b = 0.10$
b	Width of runner blade
C	Crack front surface point
C	Constant in fatigue crack growth relationship
c	Crack length. Semi-axis of elliptic crack along z -axis
c^*	New propagated crack length
D	Notch depth (chapter 2); Dynamic factor ($\Delta\sigma_{\text{HCF}}/\Delta\sigma_{\text{LCF}}$) (Chapters 3–9); Design node (Chapter 6)
d	Distance
E	Young's modulus
e	Parameter in spline polynomial
F	Force; Geometry factor in stress intensity factor equation
G	Modified geometry factor in stress intensity factor equation
g	Parameter in B-spline polynomial
H	Water head above hydraulic turbine runner
h	Side length of finite element
h_1	Height of runner blade
I_Z	Geometrical moment of inertia about Z -axis
K	Stress intensity factor
K_{I}	Tensile (mode I) stress intensity factor
K_{II}	Sliding crack surface displacement (mode II) stress intensity factor
K^*	Dimensionless stress intensity factor ($= K_{\text{I}}/\sigma_{\text{ref}}(\pi a)^{0.5}$)
\tilde{K}	K at crack front surface point, C
K_{eq}	Equivalent stress intensity factor ($= K_{\text{eq}}(K_{\text{I}}, K_{\text{II}})$)
K_{f}	Fatigue stress concentration factor

K_{op}	Crack opening stress intensity factor
K_t	Elastic stress concentration factor ($= \sigma/\sigma_n$)
K_ε	Inelastic formfactor for strain ($= \varepsilon/\varepsilon_n$)
K_σ	Inelastic formfactor for stress
ΔK	Cyclic range in K_I
ΔK_{th}	Threshold stress intensity factor range
k_n	Polynomial function of stress gradient of order n
L	Load
l	Length
l_{nc}	Length of notch curvature
l_1	Length of runner blade
l_2	Length of band/crown
l_F	Distance between bending force F and location of $M_{\text{b,max}}$
M_b	Bending moment
m	Exponent in fatigue crack growth relationship
N	Fatigue life
n_j	Design node number ($j = 1 \dots p$)
p	Number of spline design nodes
R	Trailing edge transition radius (Chapters 3 and 6); (Local) stress ratio ($= \sigma_{\text{min}}/\sigma_{\text{max}}$)
R_L	Load ratio ($= \text{min. load}/\text{max. load}$)
R_m	Ultimate tensile strength
$R_{\text{p}0.2}$	Yield strength of 0.2 % plastic strain
r	Blade edge radius (Chapters 3 and 6); Crack growth rate (Chapter 4); Polar co-ordinate in crack tip stress field (Chapter 5)
r_0	Semi-size of plastic crack tip zone
S	Polynomial function
t	Time; Plate thickness
t_1	Thickness of runner blade
t_2	Thickness of turbine runner band/crown
u_i	Displacement in i -direction
W_b	Section modulus for bending loading
w	Crack depth co-ordinate
X, Y, Z	Axes of global co-ordinate system
X^*, Y^*	T-joint co-ordinates
x, y, z	Axes of local crack co-ordinate system

Greek Characters

α	Crack aspect ratio ($= a/c$)
β	Crack front intersection angle
γ	z - x plane angle; Exponent in crack closure equation (Walker, Chapter 8)
Δ	Range, difference in
δ	Angle in crack tip stress field (Chapter 5); Factor in stress gradient polynomial, k (Chapter 9)
ε	Local strain
ζ	Co-ordinate with origin at crack surface point, C
η	Dimensionless co-ordinate with origin at deepest crack point, A ($= w/a$)
η_{opt}	Efficiency factor in shape optimisation
θ	Angle in crack tip stress field (Chapter 5); Trailing edge angle (Chapter 6)
ι	Exponent in shape optimisation efficiency equation
κ	Factor in crack tip displacement equation
λ	Exponent in near-surface crack tip stress field equation
ν	Poisson's ratio
ξ	Relative thickness ($= a/t$)
ρ	Notch radius
ρ^*	Characteristic length (Chapter 2)
σ	Local stress
σ_0	Tensile yield stress
σ_1	Largest principal stress
σ_A	Fatigue limit amplitude
σ_a	Stress amplitude
σ_m	Mean stress
σ_n	Nominal stress (net section)
σ_∞	Nominal stress (gross section)
$\Delta\sigma_{\text{HCF}}$	Vibration stress range ($= 2\sigma_{a,\text{HCF}}$)
$\Delta\sigma_{\text{LCF}}$	Start-stop stress range ($= \sigma_m + \sigma_a$)
$\bar{\sigma}$	Effective stress for crack closure (Walker)
τ	Local shear stress
ϕ	Location angle in ellipse
χ	Relative stress field gradient

Subscript

A,B,C Points on crack front

a	Amplitude
b	Bending
BM	Beach mark
c	Critical
circ	Circular
F	Force
f	Fracture, failure, final
i	Initial
L	Arbitrary loading case
m	Middle, mean
max	Maximum
min	Minimum
n	Nominal
n	Numeration
opt	Optimised
tens	Tensile

Superscript

A,B,C,D	Shape optimisation cases
el	Elastic
pl	Plastic

Abbreviations

2D	Two-dimensional
3D	Three-dimensional
BEM	Boundary element method
CAD	Computer aided design
CNC	Computer numerical control
COD	Crack opening displacement
FCG	Fatigue crack growth
FE, FEM, FEA	Finite element (-method, -analysis)
HCF	High cycle fatigue
LCF	Low cycle fatigue
LEFM	Linear elastic fracture mechanics
SCF	Stress concentration factor, K_t
SIF	Stress intensity factor, K
SN	Stress-life

Chapter 1

Introduction

Hydraulic turbines exploiting the energy of water in rivers and reservoirs make a substantial contribution to the generation of electricity worldwide. The advantages of hydroelectric plants over fossil fuel plants are a higher life time, an efficiency rate twice as high and lower costs for maintenance and service. Besides being a renewable and non-polluting source of energy, a hydropower plant can respond instantaneously to changes in the demand for power of the electric grid. Therefore, hydraulic turbines and, in particular, reversible hydraulic pump turbines contribute to the supply of clean and reliable electric power.

The worldwide production of hydropower energy of 2650 TWh/year meets 17 % of the world's entire electricity demand (IEA data for 2001 [1]). The world's total technically feasible hydro potential is estimated at 14 500 TWh/year, of which 56 % is currently considered economically feasible for development. Worldwide 755 GW hydropower is in operation [2]. Within the OECD countries approximately 80 % of the available large hydro resource (stations with an energy output >10 MW) is already used, but only 21 % is exploited worldwide.

Potential technical capacity of the small hydro resource (<10 MW) is estimated at 150–200 GW worldwide. In North America and Europe, a larger share of the technical potential of the small hydro resource has already been developed than in developing countries [3]. Still, small-scale hydropower is generally relatively unexploited, and installed capacity is estimated to grow between 1–6 % per year over the next 20 years.

The nominal output of hydropower installed in Norway sums 27 700 MW and is spread over 581 hydropower stations of more than 1 MW. In 2003, hydro-electric power stations generated 99 % of the country's electric energy production of 119 TWh [4].

1.1 Turbine Design and Classification

Conventional hydropower technologies are technically mature and highly efficient, with conversion efficiencies up to 95 % achievable. Typically, larger turbines have higher efficiencies.

The turbines and electric generators of hydropower stations are installed either in or adjacent to dams and use a tunnel or a pipeline – often referred to as the *penstock* – to carry the water under pressure from the water reservoir to the powerhouse situated below. The penstock may be split into several separate penstocks for individual turbines. In the powerhouse the water is lead to the turbine runner, which transforms the hydraulic energy

into torque and rotation of the shaft and performs useful work by driving the electric generator. A general scheme of hydropower stations is given in Figure 1.1.

There are many types of turbines used for hydropower, and they are chosen based on their particular application and the height of standing water – the so-called *water head* – available to drive them. Water heads between three and several hundred metres are considered to be technically exploitable.

The most common turbine types are:

Francis turbines have a runner with fixed blades, usually between seven and thirteen.

The water enters the turbine in a radial direction with respect to the shaft, and is discharged in an axial direction. Francis turbines are available for 20 to over 900 m of head and can be as large as 800 MW.

Kaplan turbines are *propeller* turbines with all of the three to six blades pivoted for pitch adjustment. The runner design reminds of a boat propeller and may exceed eight metres in diameter. Kaplan turbines are suitable for heads from 10–70 m and may yield more than 250 MW.

Pelton turbines have one or more jets discharging water into an aerated space and impinging on buckets that are placed circumferentially on the runner disk. With runner wheel diameters of over 5 m these turbines are used for 200–1500 m high-head sites and can be as large as 300 MW.

One reason for these three turbines to become today's predominant types is that they supplement each other so that virtually all water heads and volumes are covered. Generally spoken, Pelton turbines are chosen for relatively high water heads and small water discharges, in contrast to Kaplan turbines which suit the lowest heads and largest flow rates. Francis turbines cover the bigger part of the region in between.

One classification of hydraulic turbines is based on the predominant direction of the fluid flow through the runner. In a *radial-flow* machine the path of the fluid is mainly in the plane of rotation. Thus, the fluid enters the rotor at one radius and leaves it at a different radius. Examples of this type of machine are the Francis and the centrifugal turbine. In the case of *axial-flow* machinery like the Kaplan and the propeller turbine the main flow direction is parallel to the axis of rotation. If both axial and radial fluid flow is present, the term *mixed-flow* is used [5].

The categorisation in *impulse* and *reaction* turbines is another way of classification. While the static pressure is constant across the runner of the impulse machine, this pressure decreases as the fluid flows through the reaction machine runner. An example for the impulse machine is the Pelton turbine, whereas the Francis and Kaplan turbines are representative of the reaction type. In both types the fluid transfers energy to the runner in tangential direction.

1.2 Francis Turbines

As noted in Section 1.1, Francis units are reaction turbines of the radial-flow type. The water enters the turbine in a radial direction with respect to the shaft, and is discharged in an axial direction. As the fluid flows through the runner, the static water head pressure decreases gradually. Consequently, the Francis runner has to be completely closed and all

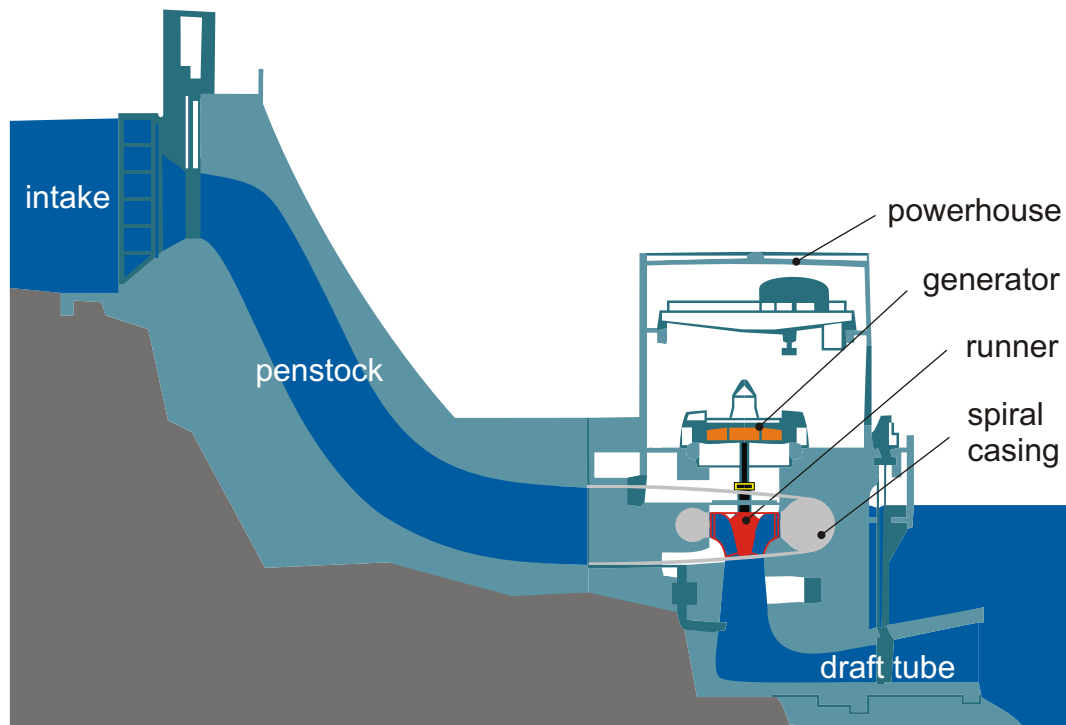


Figure 1.1: Hydroelectric power station. Scheme and Notation.

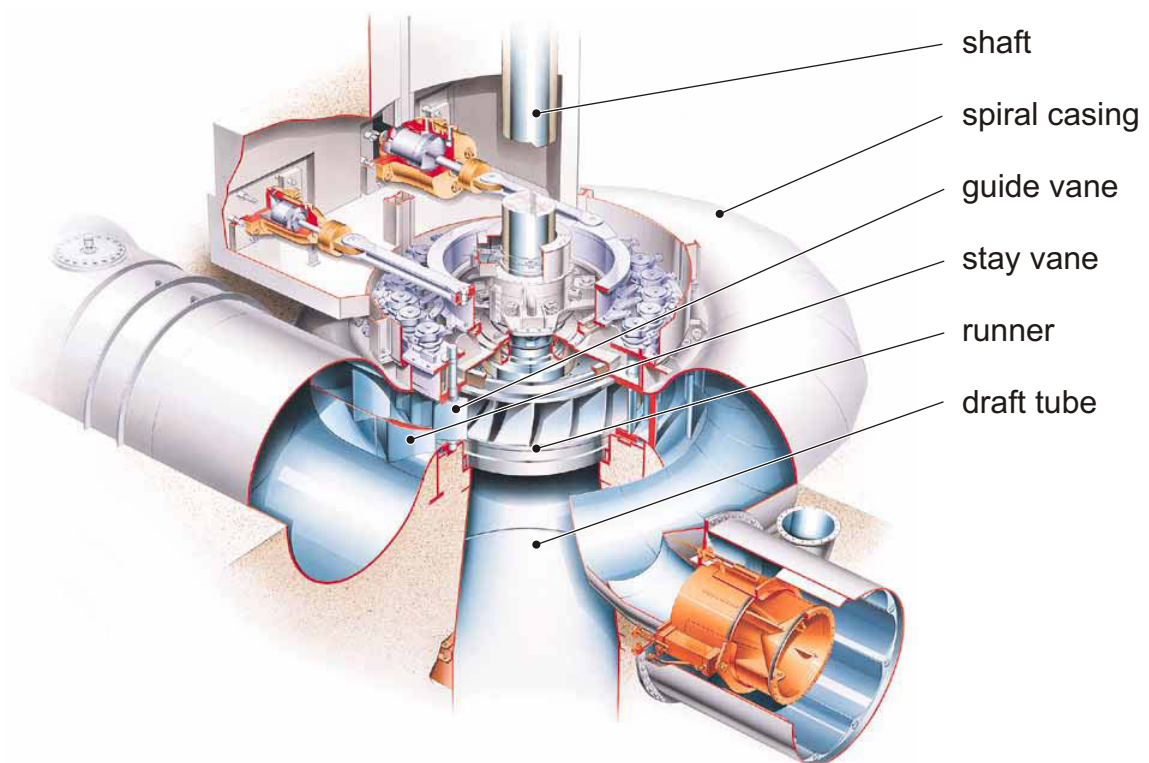


Figure 1.2: Francis turbine. Scheme (printed with friendly permission of General Electric Energy) and Notation.

its passages are entirely filled with working fluid. As this is typical for the reaction turbine runners, these turbines are sometimes denoted as *full* turbines, in opposition to the *partial* impulse turbines [6].

For the Francis turbine, the water flows from the penstock into a *spiral casing* or *scroll case* which distributes the fluid evenly onto the blades of the runner, which is mounted on a common shaft with the generator. The flow of water is hereby first deflected by fixed *stay vanes* and subsequently regulated by means of pivoted *guide vanes* – often called the *wicket gate* – which is opened and closed by an oil-hydraulic servomechanism controlled by a mechanic or electronic *governor*. From the runner outlet the water flow enters the *draft tube*. Here, flow velocity is gradually reduced due to an increase in the draft tube diameter whereby additional energy is gained. Figure 1.2 gives a schematical overview and the notation of a Francis turbine.

1.3 Background and Motivation

In the continuous struggle for reduced costs and increased efficiency, designers approach the limits of the structural integrity of hydropower turbines. Major challenges are fatigue, corrosion, corrosion fatigue, stress corrosion, cavitation and silt erosion damage. Failure in engineering structures due to fatigue loading generally occurs in areas of stress concentration. Decades of operating experience have shown hydraulic turbine runners to develop fatigue cracks in areas where stress concentrations and material defects coincide.

This is the case in the welded areas of high-pressure Francis turbine runners. Here, fatigue cracks tend to occur either very early in life or after ten to twenty years of operation. The failure mechanism is considered to be a combination of low-cycle fatigue from operational start-stop and high-cycle fatigue due to hydraulic load fluctuations. Since the critical area of stress concentration consists of welded material, it has to be assumed that crack propagation from single undetected flaws and inclusions takes place as soon as the runner is taken into service. The following investigations focus on the Francis runner where the interaction of low-cycle and high-cycle fatigue loading in combination with relatively high static loads seemed to be the most interesting and challenging area of research.

To strike a balance between the performance and cost of a turbine runner on one hand and the mechanical integrity of the runner on the other hand, the turbine designer must have tools available for the reliable prediction of fatigue crack growth. A practical application of fatigue crack growth calculation is to investigate how fast a crack is growing from an assumed initial size to catastrophic failure. Representative results may then be helpful to estimate failure-free service life and therewith maximise inspection intervals.

The propagation of semi-elliptical surface cracks can be calculated by means of linear elastic fracture mechanics, provided the stress field and the stress intensity factor are known during the propagation of the crack. Experimental fatigue testing may substantiate calculational results and provide information about the fatigue properties of complex geometries.

The Francis runner areas of stress concentration are manufactured with high accuracy and care. As to date circular transitions prevail, the idea to investigate the benefit of shape optimisation to the fatigue properties of a Francis turbine runner almost suggested itself.

1.4 Outline of the Thesis

The remaining part of the thesis is organised as follows:

Chapter 2 gives an overview of how the fatigue phenomenon has been related to geometrical notches from the early beginnings of fatigue research.

Chapter 3 describes the conditions that influence the mechanical integrity of Francis turbine runners.

Chapter 4 demonstrates a practical fatigue assessment methodology.

Chapter 5 introduces the stress intensity factor with focus on its applicability to notch fatigue problems. The retrieval of a general stress intensity factor solution is explicated.

Chapter 6 presents optimised shape solutions that lower the local stress level in areas of stress concentration and thus increase fatigue properties.

Chapter 7 presents experimental fatigue tests performed on standard and shape optimised transition specimens. The specimen's geometry and the loading applied represent the conditions that prevail at the two most critical areas of the Francis runner with respect to fatigue.

Chapter 8 concentrates on local stresses and transition geometries that are initially uncracked.

Chapter 9 presents fatigue crack growth calculation employing the stress intensity factor solution of Chapter 5 and solutions from the literature. The results are compared to benchmark data from experimental fatigue testing presented in Chapter 7.

Chapter 10 is a summary of the findings in Chapters 4 to 9. Conclusions are drawn and directions for further work are suggested.

Chapter 2

History of Fatigue and the Notch Effect

Efforts and advancements in research on the fatigue phenomenon ever since have been closely connected to failure of technical equipment in service. For more than one and a half centuries, long before the often mentioned de Havilland Comet aircraft crashes took place in 1953 and 1954, failure of vehicles and machinery leading to major accidents and loss of human lives has enforced the interest of engineers and scientists in material fatigue.

The fact that today, with the vast amount of investigation of more than 100 000 works on the field published during the 20th century [7], many questions still remain unanswered, emphasises the need for further research on fatigue.

The following review of the history of fatigue has its focus on the detrimental effect of notches to fatigue life. The review comes with no claim for completeness whatsoever. The aim of it is rather to show the relevance of early works and the contribution of later milestones in fatigue research to the contemporary knowledge of notch fatigue. Historical information found in recent review articles [8, 9, 10, 11] has been notably helpful with this review.

2.1 Early Research on Fatigue

Fatigue is a failure phenomenon that is found in components under fluctuating loads, which are well below the static design loads of the component. With the beginning of the industrial revolution, cast and wrought iron took the place of bricks or wood as construction materials. Thus, components could be designed to withstand tensile forces, which lead to more complex constructions and resulted in an increasing fatigue problem.

It is reported that Poncelet in his lectures at the military school at Metz described metallic structures as being “tired” or “worn out” in 1839 [10]. The first time the term *fatigue* was employed for cracking of metals under repeated loading was in a publication of Braithwaite [12] in 1854.

The first fatigue test results known were published in 1837 by the Royal Hannoverian “Oberbergat” Albert [13] in Clausthal. Struggling with conveyor chain failures in the mines of the Oberharz, he performed fatigue tests of whole components. It seems worth noting that he hereby invented the wire rope.

From the middle of the 19th century, accidents from breaking railway axles regularly topped the news throughout Europe. In 1842, a major train accident near Versailles took the lives of 60 people. The cause of this accident was fatigue failure originating in the locomotive front axle [14]. In the following year the physicist Rankine [15] proposed

ideas on improved fatigue design of railway axles. Morin in his 1853 book “Résistance des Matériaux” [16] reports on cracks in mail coach axles that mainly occurred at geometric discontinuities.

An understanding of the physical fatigue phenomena was hardly present in these early days. Though it was recognised that those cracks often occurred at section changes, the events in the material were still in the dark. Due to the absence of visible plastic deformation, efforts were made to connect fatigue to a mysterious change in the material structure from a fibrous to a brittle crystalline one.

In 1903, a microscopic investigation of Ewing and Humfrey [17] showed short fatigue cracks that grew from cyclic slip bands. The discovery of striations – small ridges on the crack surface that lie perpendicular to the direction of crack propagation – in the late 1950s by Forsyth [18] and Ryder [19] then proved that fatigue crack growth actually is a cycle-by-cycle phenomenon. By that, the theory of an increasing strain-hardening mechanism could be disproved, as it would have led to jumps of the crack front after a couple of cycles instead.

This physical phenomenon of material fatigue was unknown to Wöhler, who was Royal “Obermaschinenmeister” of the “Niederschlesisch-Mährische” Railways in Frankfurt an der Oder, when he began to monitor the service loads of railway axles with self-developed zinc-plate strain gauges [20, 21] in 1858. Wöhler then calculated the largest bending and torsional stresses on the axles, considered how often these largest stresses occurred in service and implicitly suggested design for fatigue life. Due to the lack of fatigue data, Wöhler had to rely on estimations, but from his fatigue tests on notched and unnotched specimens he had recognised that the stress amplitude is the decisive parameter for fatigue life [22]. Besides the realisation of systematic fatigue tests under tensile, bending and torsional loading conditions and the introduction of the “endurance limit” concept, the work of Wöhler includes considerations of the statistical scatter in finite life design as well as (quantified) design suggestions for reduced notch effect.

Wöhler published his fatigue test results in tabular form. The “Wöhler curves” or “SN curves”, as they are known and still used today, were first drawn by Basquin [23] in 1910. For the finite life region, Basquin correlates the stress amplitude, σ_a , and the number of life cycles, N , in the relation

$$\sigma_a^k \cdot N = \text{constant} \quad (2.1)$$

which plots a straight line in the graphs he introduced showing a $\log \sigma_a$ ordinate and a $\log N$ abscissa. Depending on the material and on the notch severity, the exponent k value varies between $k \approx 10$ for smooth steel specimens and $k \approx 3$ for specimens containing a crack or a very sharp notch.

Many results of Wöhler were confirmed by Bauschinger, who was Professor of Mechanics at the Munich Polytechnical School. In 1881 he discovered what in his own words [24, 25] was “the change of the elastic limit by often repeated stress cycles”. This effect, which today is known as the *Bauschinger effect*, is the basis for the hypotheses of Manson [26] from 1953 and Coffin [27] from 1954. Independently from each other they investigated short fatigue lives due to large cyclic (thermal) deformations and related the macroplastic strain amplitude, ε_a , to the number of load cycles to fatigue failure. Fatigue life prediction in the *low-cycle fatigue* regime according to the local concept still bases on this so-called Coffin-Manson relation:

$$\varepsilon_a \cdot N^\beta = \text{constant} \quad (2.2)$$

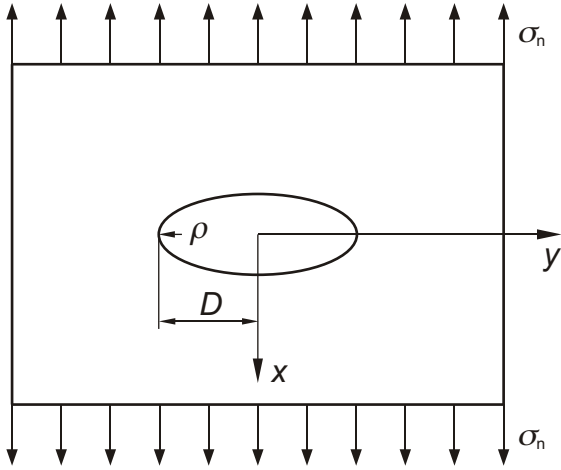


Figure 2.1: Elliptic hole in plate under tension.

2.2 Stress Concentration

As mentioned above, it was soon recognised that geometrical discontinuities generally lead to locally elevated stress levels. The first accurate and analytical determination of the stress concentration factor

$$K_t = \frac{\sigma_{\max}}{\sigma_n} \quad (2.3)$$

was achieved by Kirsch [28] in 1898. Hereby, σ_{\max} is the elastically calculated maximum local stress and σ_n the stress in the nominal section. Kirsch's result for the stress concentration of a cylindrical hole in an infinite plate shows that $K_t = 3$. This was later extended to the case of an elliptical hole by Inglis [29] who in 1913 found the equation for the notch stress concentration to be

$$K_t = 1 + 2\sqrt{\frac{D}{\rho}} \quad (2.4)$$

where $2D$ is the major axis and ρ the notch root radius, as shown in Figure 2.1.

Strain measurement at notches was performed by Preuß [30] at the “Materialprüfungsanstalt” in Darmstadt in 1913. For this purpose, Preuß developed a mechanical-optical extensometer with the distance between the measuring edges of either 0.7 or 3.3 mm. This apparatus allowed strain to be measured at the cross sectional area of flat bars as well as in the groove of the notch itself. Preuß is considered to be the first to employ the ratio between maximum (local) stress in the notch groove and an average stress value (today: *nominal* stress), for tensile loading at least.

In 1937 Neuber, who held the chair for Mechanics in Munich as Bauschinger before him, published his book *Kerbspannungslehre* [31]. The book was translated into English and published in 1946 with the title *Theory of Notch Stresses* [32]. In this work, analytical stress concentration solutions are presented for a large range of notches under different loading conditions: deep and shallow notches, sharp and blunt ones, single and multiple, inner and outer notches in plates and bars were considered under tensile, bending, shear

and torsional loading conditions. At this, Neuber verified Inglis' solution for the elliptic hole.

Later, Neuber [33] proposes the relation between the elastic stress concentration factor, K_t , and inelastic formfactors for stress and strain, K_σ and K_ϵ , to be

$$K_t^2 = K_\sigma \cdot K_\epsilon \quad (2.5)$$

(cf. Chapter 8). Herewith, Neuber already assumed that his original work [34] from 1961 on the notched body under transverse shear stress and large-scale yielding has extended validity. Recent publications [35, 36] could prove this assumption of his to be true.

Diagrams, tables and exact expressions of the classical solutions of K_t as given by Kirsch, Inglis and Neuber are continuously being completed. *Peterson's stress concentration factors* of Pilkey [37] is one of the most extensive modern books for the practical use of stress concentration factors.

2.3 Stress Concentration Factor and Fatigue

However, fatigue tests reveal that the sensitivity of notches to fatigue only approximately follows the notch stress concentration factor. When Gough [38] in 1924 compared fatigue test results with photoelastic measurements, he realised that the stress concentration factor is not fully effective. In 1932 Thum [39] created the fatigue stress concentration factor, K_f , from the relation between the fatigue limit, σ_A , of the unnotched, smooth specimen to the nominal fatigue limit of the notched component, σ_{nA} . Here, N_D which is the fatigue life that corresponds to fatigue strength, was settled to $10^6 \dots 10^7$ load cycles. As a statistically averaged result of fatigue tests performed at zero mean stress (cf. Equation 3.2)

$$K_f = \frac{\sigma_A(K_t = 1)}{\sigma_{nA}(K_t > 1)} \quad , \quad (R = -1) \quad . \quad (2.6)$$

Material and loading conditions as well as the notch and specimen geometry influence K_f [40, 41, 42, 43]. Further parameters that affect K_f are the mean stress level [44] and the surface roughness [38].

Considerable work on the field of stress concentration and fatigue was published by Peterson [45, 42] at Westinghouse from 1930 on. Frost and Dugdale [46] propose an implicit assumption of the K_f - K_t relationships of Neuber and Peterson, suggesting the stress needed to initiate a crack at the notch root would also be sufficient to propagate it to cause failure of the component. This was stated to be valid in most cases of practical importance, where the notches involved are not too severe, K_t being typically below 4.

The "Mikrostützwirkung" concept is one explanation for why $K_f < K_t$, i.e. why the detrimental effect of a notch to fatigue life is less than it may be estimated from the size of the stress concentration factor. The presence of a lower K_f value even in the uncracked infinite life region is explained by plasticity effects. Mikrostützwirkung bases on the fact that only the initial part in the life of a fatigue crack is characterised by the maximum notch stress. The stress concentration decreases with increasing distance from the notch.

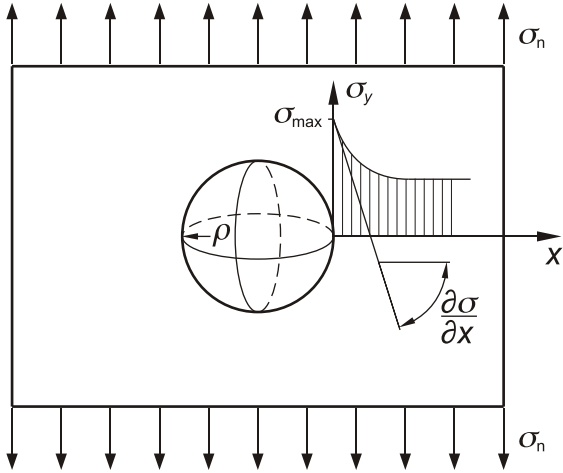


Figure 2.2: Spherical cavity in an infinite body in tension. Stress concentration and stress gradient.

For a propagating crack the relative stress field gradient, χ , is of significant importance:

$$\chi = \frac{1}{\sigma_{\max}} \left| \frac{\partial \sigma_y}{\partial x} \right|_{x=x_0} \quad (2.7)$$

with x_0 the co-ordinate point in the component where maximum stress is achieved (cf. Figure 2.2). According to Klesnil and Lukáš [47], the crack grows perpendicularly to the largest mean stress (for mode I crack surface displacement, cf. Chapter 5) and in the direction of the largest stress gradient.

In order to account for the stress gradient, Neuber averages the crack initiating stress over a small volume at the location of the maximum notch stress. The characteristic length, ρ^* , of this small volume is a material parameter. For steel, $\rho^* = 0.03\text{--}0.5$ mm [33]. Other attempts to correlate K_t and K_f employ the stress gradient [48, 49] or a certain material-dependent critical depth, a^* , below the surface, as introduced by Peterson [42].

The notch sensitivity factor, q , was introduced by Thum [39] in 1932:

$$q = \frac{K_f - 1}{K_t - 1} \quad (2.8)$$

Thum was aware that K_f is not a characteristic material factor and by no means a characteristic factor for the component. He called the factor a “crutch with which one can limp from the unnotched specimen to the notched component” [8]. As a matter of fact, fatigue testing of the actual component is still considered to be most reliable way to ensure sufficient fatigue durability.

2.4 Approaches to Fatigue Design

Parallel to research on the notch stress concentration factor, several guiding principles were developed to handle the (notch-) fatigue problem in engineering. Graf [50] observed in 1931 that the fatigue strength of riveted and welded joints in structural steels does not depend on the static strength of the material. Similarly, the *Gestaltfestigkeit* tenet that Thum and Bautz [51] established in 1935 emphasises the utmost importance of the component shape

for a high fatigue strength. The effect of the material itself is ranged second, as is the magnitude and type of loading.

Like the classical approaches of the cyclic stress (SN curves) and strain range, *Gestaltfestigkeit* presupposes that components initially are uncracked. Thus, fatigue life comprises the number of stress or strain cycles both to initiate a dominant crack (this may represent up to 90 % of the total fatigue life) and to subsequently propagate this dominant flaw until catastrophic failure occurs. These approaches are called *total fatigue life* approaches.

From 1939, Gaßner performed variable-amplitude fatigue tests and developed the doctrine of *Betriebsfestigkeit* [52], what may be translated with “operational fatigue strength”. By dimensioning a component for finite but sufficient fatigue life under variable loads, an “allowable” fatigue life is obtained. At this, the form of the service stress spectrum was measured and extrapolated to the estimated complete in-service spectrum. Here, even the effect of rare high stress cycles was included. Then, the service spectrum was simulated by a variable-amplitude test. Throughout this approach, Gaßner strived for a generalisation and standardisation of the test results in order to obtain generally valid information.

An increasing number of aircraft crashes in the 1950s lead to the *safe-life* approach. This implied that once a component has reached its safe-life, it is scrapped – whether a fatigue damage is present or not. The component’s replacement time was predicted from fatigue tests and conservative safety factors. From the viewpoints of economy and performance, such a conservative approach was obviously not desirable.

In the 1960s, *safe-life* was followed by *fail safe* which implied a design that to some extent is *defect-tolerant*. The idea was that even if an individual member of a large structure fails, sufficient structural integrity prevails. Safe operation is continued until the failure is detected. This structural redundancy is natural to components that feature multiple load paths. One further method of *fail safe* was to decelerate crack growth. This was achieved with the help of crack arresters placed in the path of a crack that is likely to occur. The *fail-safe* approach requires repeated and methodical inspections and adequate crack detection techniques.

The *damage tolerance* method was introduced in the early 1970s and bases on fracture mechanics techniques. Damage tolerance assumes that every engineering component is inherently flawed. The size of an initially present crack is detected or assumed (cf. Chapter 4). Fatigue life is defined to be the number of cycles that are necessary to propagate this initial crack to some critical dimension. The crack propagation life is then calculated by means of empirical crack growth laws based on fracture mechanics.

Chapter 5 of this publication gives a short review on the history of fracture mechanics and addresses the application of linear elastic fracture mechanics to fatigue crack growth from notches. The phenomenon of crack closure, which was discovered in 1968, and its effect on fatigue crack growth is addressed to in Section 8.2.

Chapter 3

Francis Runner

One of the critical parts of a hydraulic turbine is the turbine runner. The runner design varies widely depending on the available pressure and flow. Francis turbines runners typically have between seven and thirteen fixed blades [53]. The construction may either be entirely of cast steel or a welded construction where hot formed blades are welded to the cast ring and crown. Figure 3.1 gives an schematical overview and the notation of a Francis turbine runner.

3.1 Material

In most cases the runners are of stainless steels in 12–17 % Cr martensitic-austenitic or martensitic-ferritic-austenitic grades [54]. While 13Cr-4Ni (DIN GX5CrNi 13-4, standard no. 1.4313) is favoured for cast runners, 16Cr-5Ni material is frequently used for both blade plates (DIN X4CrNiMo 16-5-1, standard no. 1.4418) and ring/crown castings (DIN GX5CrNiMo 16-5, standard no. 1.4405) in welded constructions. The fact that 16Cr-5Ni material may be welded with moderate pre-heating to 50 °C to keep the material well above the dew point eases manufacturing procedures [55, 6]. Moreover, this steel shows a somewhat better cavitation resistance [6] and a slightly higher fatigue limit than lower-alloyed stainless steels [54].

3.2 Manufacturing

The manufacturing process of a high-head Francis turbine runner may proceed as follows:

1. Casting of crown and band. Machining of the weldment areas.
2. Cutting of the blades from rolled steel plates, followed by hot forming, annealing and five-axis profile milling and/or grinding.
3. Blade assembly using positioning templates. Joining of band and blades by double fillet welds. Regular testing of the weld seams for pores and inclusions.
4. Machining of the weld seam to smooth transition geometries.
5. Joining of the crown by double fillet welds. Regular testing of the weld seam for pores and inclusions.

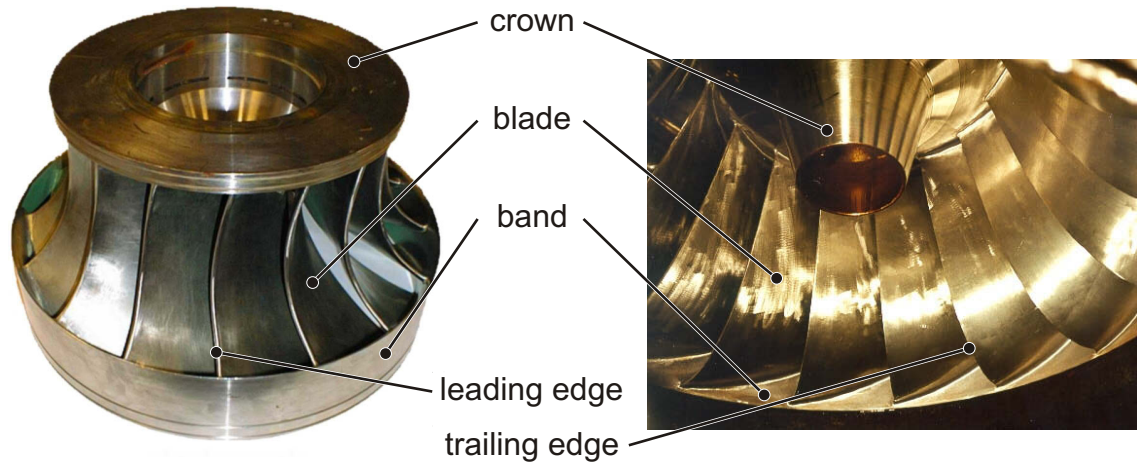


Figure 3.1: Francis turbine runner. Notation. Photography on the right © by Koessler Ges.mbH. Printed with permission.

6. Machining of the weld seams to smooth transition geometries.
7. Annealing in order to relieve the component from residual stresses after welding.
8. Machining of diameters on vertical boring mills.
9. Surface finishing by grinding and polishing.

3.3 Loading

The operation of a hydroelectric power plant is associated with several transient phenomena. Start-up and shut-down operation, modification of operating point, earth fault, out of phase synchronisation during start-up and emergency stop induce unsteady loading conditions [56]. In the case of the Francis turbine interactions between the turbine components are quite common, especially between guide vanes, runner and draft tube [57, 58]. However, the steady and unsteady service loads a Francis turbine runner experiences shall be defined as follows:

- The steady fluid pressure and the centrifugal force make up the steady service loading.
- High-frequency pressure fluctuations due to irregular fluid flow make up the unsteady service loading.

In the following, the start-stop cycle will be referred to as the low-cycle fatigue (LCF) cycle, the high-frequent load cycles from unsteady fluid flow will be referred to as the high-cycle fatigue (HCF) cycles.

After a more general definition of [59], LCF appears at high stress amplitudes with corresponding short fatigue lives up to some 10^4 cycles. If fatigue covers a large number of cycles, about 10^5 cycles and more, it is called HCF. The difference between the two conditions is that LCF is associated with macroplastic deformation in every cycle.

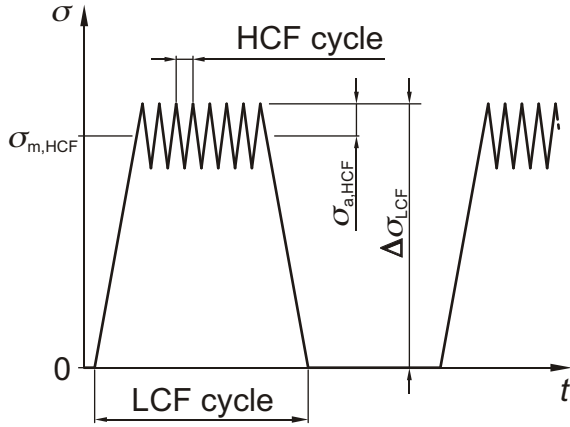


Figure 3.2: Francis turbine runner. Service stress history.

A *dynamic factor*, D , may be introduced to correlate the stress *range* of the LCF and HCF cycles in the form

$$\Delta\sigma_{\text{HCF}} = D \cdot \Delta\sigma_{\text{LCF}} \quad . \quad (3.1)$$

The stress ratio, R , is defined as the ratio between the minimum and the maximum stress, σ_{min} and σ_{max} , respectively:

$$R = \frac{\sigma_{\text{min}}}{\sigma_{\text{max}}} \quad . \quad (3.2)$$

Further, the expressions stress amplitude, $\Delta\sigma$, amplitude stress, σ_a , and the mean stress, σ_m , shall be introduced and defined by the relations

$$\Delta\sigma = 2\sigma_a = \sigma_{\text{max}}(1 - R) \quad , \quad \sigma_{\text{max}} = \sigma_m + \sigma_a \quad . \quad (3.3)$$

3.3.1 LCF Loading

During a complete start-stop cycle, the steady LCF loading goes from zero to a maximum under service conditions and back to zero (cf. Figure 3.2). Most turbines will run for the largest part of service life at the “design point” of highest efficiency, which for the Francis turbine is at 85–95 % of rated power. For safe and gentle turbine operation is reasonable that known regimes of detrimental resonance frequencies are avoided or passed through quickly. System inertia of the Francis wicket gate typically lies between seven and ten seconds. In order to avoid “water hammer” – detrimental pressure impulse from a sudden change in fluid velocity – to occur, start-up and shut-down processes are deliberately prolonged. Published up-loading rates of 50–200 MW per minute [60] yield start-up times of several minutes for large stations. Nevertheless, in multiple turbine sites with several turbines already in service, the start-up of one additional runner may take just 20 seconds [61].

Whereas hydropower stations for pure base-load duty may only see one start-stop cycle per year, other stations in the function of pumped-storage hydropower stations and equipped with reversible pump-turbines see up to ten start-stop cycles per day. In the latter case, the turbine runner would experience more than 50 000 cycles in 20 years of service.

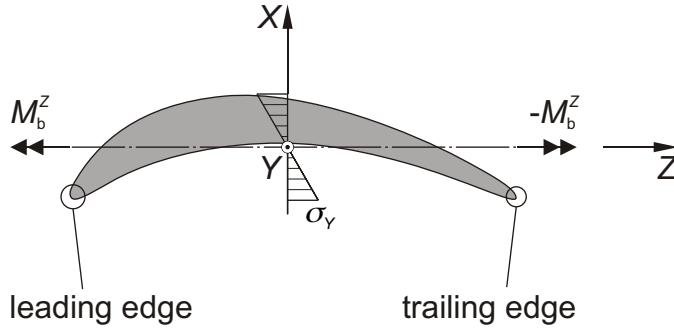


Figure 3.3: Turbine blade subjected to a bending load.

The steady fluid pressure on the runner depends on the water head and on the actual position of the guide vanes. At full load the largest nominal bending stress, σ_b , on the blades may be roughly estimated by the equation

$$\sigma_b = 2b^2 \Delta p t_1^2 \quad (3.4)$$

where b is the blade height, i. e. the distance between ring and crown at the trailing edge, t_1 is the blade thickness and Δp the load range, i. e. the pressure on the blades due to the water head. For Francis runner dimensions typical for moderate water heads, Equation 3.4 results in stress values of 300–400 MPa.

In this rough calculation uniform loading conditions are presumed and the blade is modelled as a straight beam between a ring and crown of infinite stiffness [62]. Considering this simplified geometry it is obvious that the in-service presence of water pressure on one side of the blade and suction on the other side induces bending loading. The largest bending stresses appear where the blade is fixed to the band or crown. At this T-joint geometry, the level of stress and strain is further intensified due to notch effects.

With an outer diameter of up to seven metres and more, centrifugal forces in the Francis runner may be significant already at low rotational speed. Strain gauge measurements on a low-head ($H = 31$ m) Francis turbine with 50 MW in nominal output have shown that the centrifugal load leads to strain values of same order of magnitude as the effect of the (static) pressure load [63]. In this investigation the runner outlet diameter is close to 5 metres, the strain gauges are mounted in the suction and pressure side of two different blades close to the trailing edge and the runner crown.

Further, residual stresses are considered to be present, even though weldments completed at the workshop are generally stress-relieved by annealing.

At the end of the blade where the T-joint merges with the trailing and the leading edge, respectively, the stress gradient due to bending loading on the blade is small (cf. Figure 3.3). Additional (LCF) loading from centrifugal forces on the ring stresses the transition between ring and blade. Thus, for the trailing edge transition, tensile loading is considered to be the predominant loading condition.

3.3.2 HCF Loading

For high-pressure Francis turbine runners, high-cycle fatigue may occur due to transverse blade vibration induced by hydraulic load fluctuations over a spectrum of frequencies. The strength of these fluctuations is a function of the hydraulic pressure, the water velocity and the geometry of the stationary apparatus guiding the water into the runner.

The spiral casing distributes the water flow through the stay- and guide vanes onto the runner equally from all sides. Wakes behind the stay vanes and guide vanes expand to the runner and cause surface pressure pulsations [53]: every time a runner leading edge passes one of the guide vanes, the water flow is getting interrupted what consequently leads to fluctuations of forces and torque. Under one complete rotation of the turbine runner, fluctuations in the water flow as many as there are guide vanes take place in each runner canal. Typically, the number of guide vanes passages is in the range of 18–24.

The unsteady flow from blades passing the guide vanes is normally assumed to induce the predominant HCF vibration stresses. It is however clear that there are also other dynamic forces acting on the runner. For low and medium head Francis runners i. e., the draft tube surges – so-called “Rheingans oscillations” [64] – due to interaction between hydraulic excitation sources (i. e., vortex rope precession) and eigenfrequencies are expected to induce high frequent loading of considerable size [58].

3.4 Notch Stress Analysis

Notch stresses of two areas of the circular-shaped transition between the blade and the band or crown of the Francis turbine runner are subject of investigation. Due to stress concentration, these areas are the runner’s two locations of highest local stress amplitudes and therewith the most critical locations for fatigue.

One location is the wide-stretched *T-joint (2D) transition* itself. This T-joint geometry finally merges with the leading edge and the trailing edge, respectively, where it forms the second location of stress concentration considered: the *trailing edge (3D) transition*.

3.4.1 T-joint

FE model

The welded joint between blade and band or crown (cf. Figure 3.1) can be idealised by a simple T-joint subject to pure bending as shown in Figure 3.4. According to a proposal of [62], the ratio between the blade thickness, t_1 and the ring (or crown) thickness, t_2 , was chosen to $t_1/t_2 = 5/6$. A finite element analysis (FEA) of the T-joint under bending has been carried out in ANSYS using eight-node, second order plane strain elements. Bending loading in the nominal section of the runner blade is hereby introduced by a pressure distribution on the surface elements at ($Y^* = 115$). Due to a (linear) stress gradient, the loading condition is zero for ($X^* = -t_1/2$). Geometry, displacement constraints and loading conditions of the T-joint FE analysis model are shown in Figure 3.5. Poisson’s ratio $\nu = 0.3$.

Transition Modeling

The (static) stress distribution of a Francis turbine runner is usually obtained through a three-dimensional finite element analysis. As a rule, the finite element model is based on the experience of the designer. To keep modelling and computing times within reasonable limits, the designer may decide to use a relatively coarse mesh. This generally yields acceptable results for overall static stresses and deformations as well as for the (lower) natural frequencies of the runner. However, this coarse model neglects geometrical detail

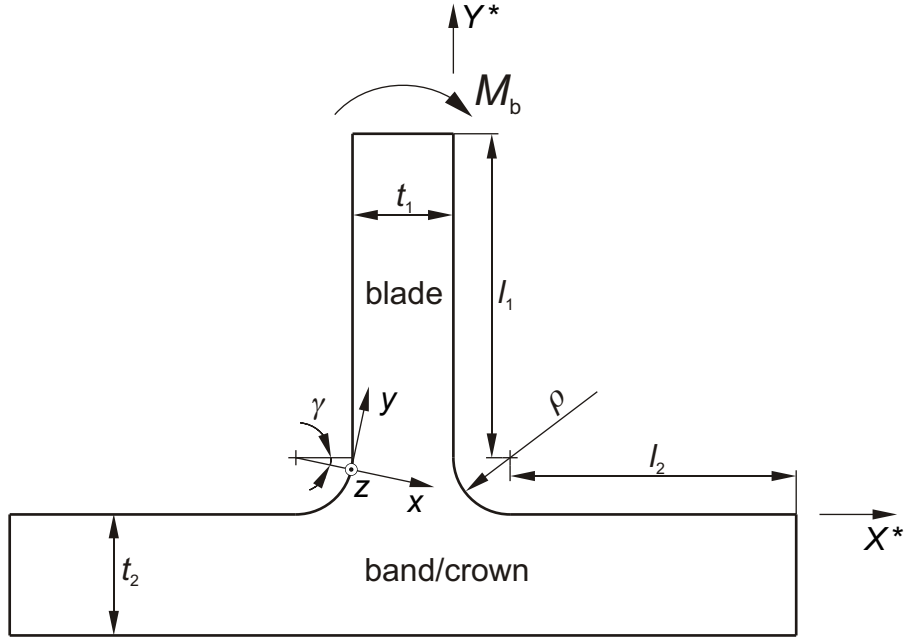


Figure 3.4: Simplified model of T-joint between turbine runner blade and band/crown.

such as the (circular) transition arc between blade and band or crown. Therefore, it will generally underestimate the level of peak stress, which controls the expected fatigue life. The designer can compensate for this deficiency by applying a stress concentration factor to the maximum stress of the sharp-notched coarse-mesh analysis. Should he need information about the detailed stress distribution below the point of maximum stress, a finer model including the transition arc becomes necessary.

The influence of the finite element model on the local maximum stress of the T-joint shall be demonstrated. Two sets of models will be used: one, where the (finite radius) transition arc is explicitly modelled and one, where a sharp right-angle corner has replaced the arc. In both sets of models, the mesh is varied from coarse to fine. Representative meshes are shown in Figures 3.6 and 3.7. The stress distribution below the point of maximum stress will also be calculated and used for the analysis of fatigue crack growth in Chapter 9.

Circular Transition In the first set of models, the ratio between the transition arc radius and the blade thickness is given by $\rho/t_1 = 0.375$. The transition radius has been modelled with mesh densities ranging from two to 38 elements along the quarter-circular transition arc. This corresponds to h_{\min}/t_1 decreasing from 0.287 to 0.016, where h_{\min} denotes the minimum element side length along the surface of the model. The stress concentration factor, K_t , of the T-joint is defined as the ratio between the maximum normal stress, σ_{\max} , and the nominal stress, σ_n , taken as the maximum net section bending stress ($= M_b/W_b$), i. e.,

$$K_t = \frac{\sigma_{\max}}{\sigma_n} . \quad (3.5)$$

Figure 3.8 shows that the stress concentration factor obtained from the finite element analysis converges towards a constant value $K_t = 1.32$ as the mesh is becoming successively

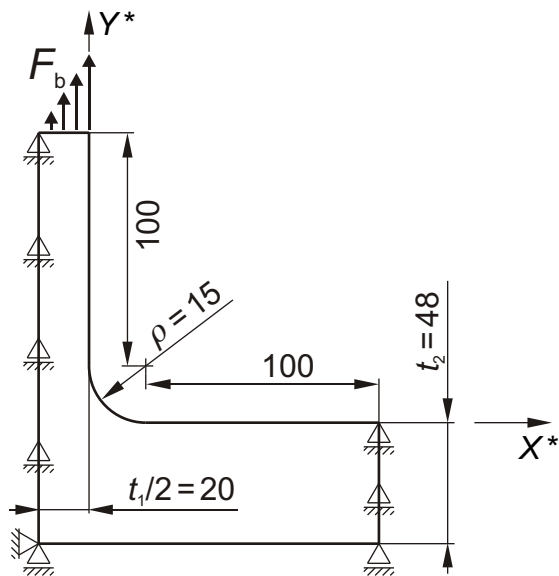


Figure 3.5: FE model of the standard circular T-joint transition under nominal bending load.

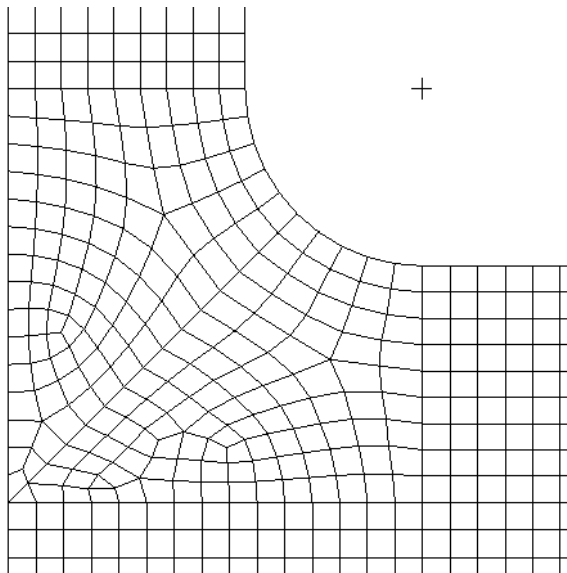


Figure 3.6: Quarter-circular T-joint model FE mesh for $h_{\min}/t_1 = 0.059$.

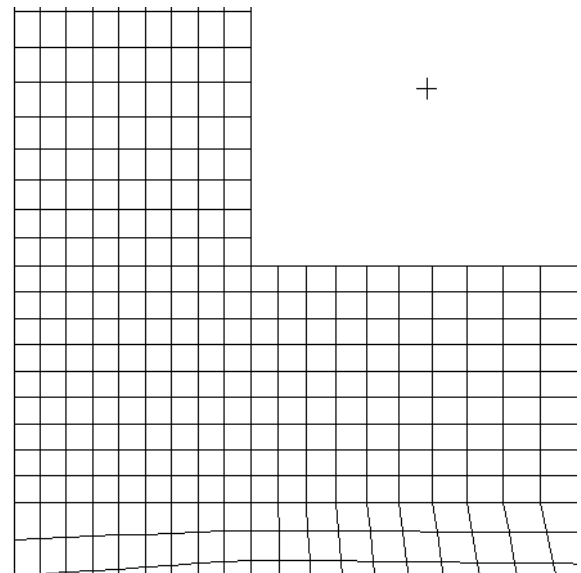


Figure 3.7: Sharp-transition T-joint model FE mesh for $h_{\min}/t_1 = 0.059$.

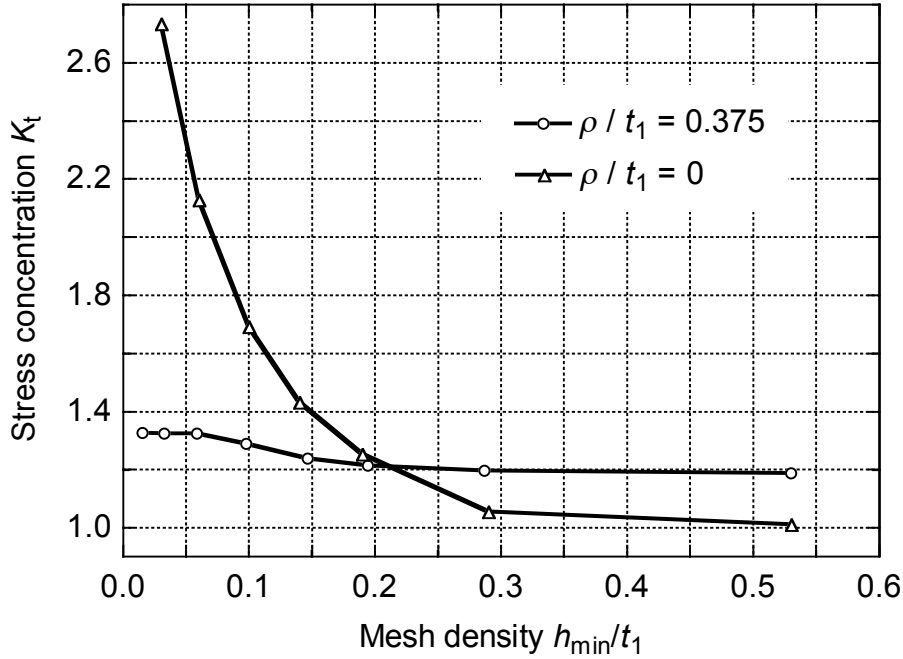


Figure 3.8: T-joint shoulder fillet transition. Influence of FE mesh density and transition radius on stress concentration values.

finer. This value is obtained with sufficient accuracy with ten elements along the quarter-circular transition arc (cf. Figure 3.6). Hereby, the minimum element side length along the surface of the model, h_{\min} , resulted to $h_{\min}/t_1 \approx 0.059$.

Based on finite element analyses of T-joints for transition arcs covering a range of ρ/t_1 ratios, Rainer [65] proposed an analytical expression for K_t . For $\rho/t_1 = 0.375$, this expression reproduces $K_t = 1.32$, as expected. The “Rainer formula” is presented in Section A of the Appendix and can also be found in “Dubbel” [66].

Sharp Transition In a second set of meshes, a sharp corner has replaced the finite radius transition arc. This considerably simplified meshing is frequently used in fluid-dynamic FEA models and so even in structural analyses of Francis turbine runners. Using similar mesh densities as for the smooth transition arc, the stress concentration factor obtained from the finite element analysis is continuously increasing, as the mesh size is decreasing. Figure 3.8 shows that a nominally “correct” value of K_t is obtained for $h_{\min}/t_1 \approx 0.2$. This result is purely accidental, of course. Figure 3.8 also shows that as the mesh becomes coarser, the stress concentration factor approaches $K_t = 1$ and $K_t = 1.19$ for the sharp corner and for the smooth transition, respectively. In practice, a coarse mesh is likely to be used.

3.4.2 Trailing Edge

FE model

For FE stress calculations of the 3D transition, 20-node second order solid elements were used. In the vicinity of the transition, the minimum element side length $h_{\min}/t_1 \approx 0.06$ along the surface of the model gives converging results, yielding $K_t = 1.678$.

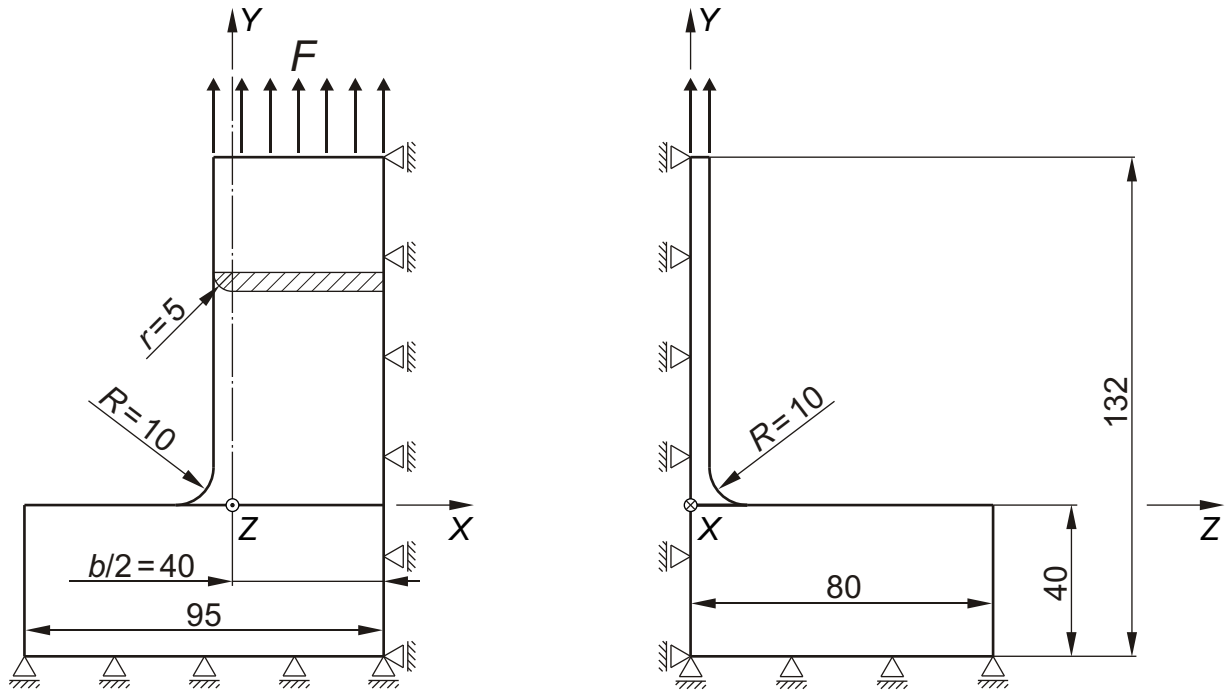


Figure 3.9: FE quarter-model of the standard circular trailing edge transition under nominal tensile load.

Symmetric displacement constraints to the FE eighth-model have been introduced at the complete model's two symmetry planes that point in X and Z direction, respectively. Y -displacement of nodes attached to the model's bottom plane, ($Y = -40$), was set to zero and a uniform (negative) pressure loads plane ($Y = 92$). These boundary conditions differ from the setup in fatigue testing where the test force charges the bottom (clamping) plane, ($Y = -40$), and ($Y = 50$) is a symmetry plane (cf. Figure 7.11). However, the effect of the changed boundary conditions to the SCF should be marginal since the Y -dimension of the bottom (clamping) part of the specimen is large. In FEA the maximum difference in Y -displacement of nodes attached to the plane ($Y = 92$) is 0.55 percent.

Geometry, displacement constraints and loading conditions of the analysis model are shown in Figure 3.9. Poisson's ratio $\nu = 0.3$. FE mesh and stress plot of the largest principal stress, σ_1 , are given in Figure 6.12.

The 3D transition FE model described is limited as it represents the dimensions of the test specimens that will be presented in Chapter 7. In fact, the model dimensions around the transition have a major impact to the resulting stress concentration. This discussion is continued in the following.

Transition Radii and Stress Concentration

The two radii defining the circular transition of the standard 3D specimen were modified systematically in a series of FE stress calculations. The resulting graph of Figure 3.10 reveals the transition radius, R , to be by far the more decisive parameter regarding stress concentration, compared to the influence of blade edge radius, r . Stress concentration values in the present calculation are somewhat higher compared to the results presented

above. The difference lies in the FE model blade dimensions which in the present calculation are larger and thus more representative for the real blade. Blade dimensions in the calculations presented above (cf. Figure 3.9) are representative for the test specimen geometry presented in Chapter 7.

It can be shown that the FE model dimensions around the transition are of eminent influence to the stress concentration. Even for the amply dimensioned blade in this present FEA series, values of stress concentration still rise for larger blade dimensions.

In a further FEA series performed for $R = 10$ mm and $r = 5$ mm, the influence of varying combinations of length and width of the blade, l_1 and b , to stress concentration is investigated. It shall be emphasised that set-up conditions like mesh size, transition geometry, loading and all other geometrical dimensions are left unchanged throughout the investigation. For blade heights $l_1 = 100, 250$ and 500 , stress concentration values approach asymptotical values for $b/h_1 > 3 \dots 3.5$. Up to this point, stress concentration rises for increasing sizes of the blade area, $b \times l_1$ (cf. Figure 3.11).

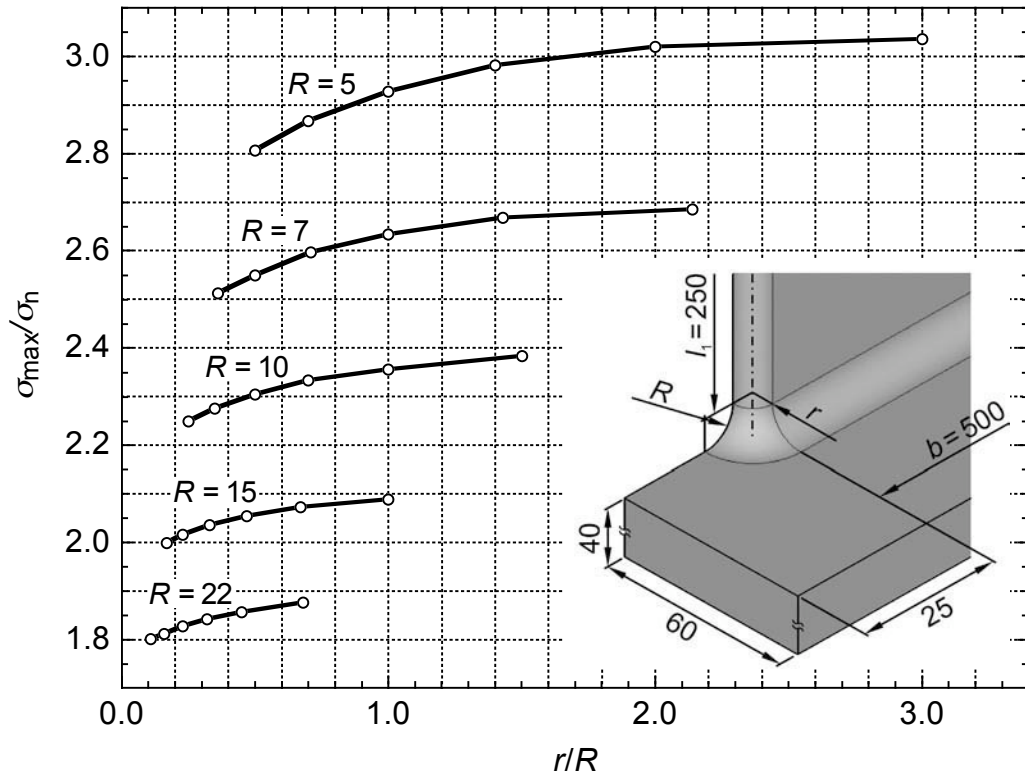


Figure 3.10: Influence of trailing edge transition radii on FE stress analysis.

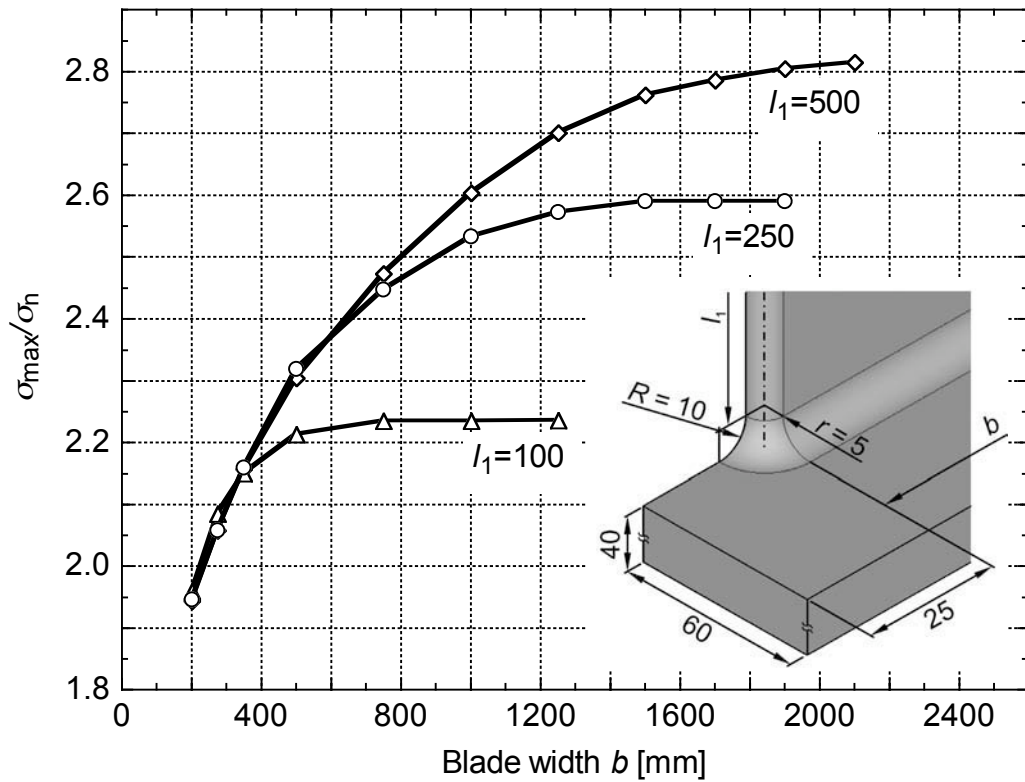


Figure 3.11: Influence of blade size on FE stress analysis of trailing edge transition.

Chapter 4

Fatigue Design Methodology

In Francis turbine runners, fatigue cracks tend to occur either very early in life or after decades of operation. The failure mechanism is considered to be a combination of low-cycle (LCF) and high-cycle (HCF) fatigue (cf. Figure 3.2). Provided that loads are high enough, the start-stop (LCF) cycles may propagate fatigue cracks (cf. Section 9.1.1) from manufacturing defects or even initiate fatigue cracks at areas of stress concentration.

With rotational runner speeds up to a several hundred revolutions per minute, the number of vibrational or high cycle fatigue cycles due to wakes behind the stay- and guide vanes (cf. Section 3.3.2) amounts to several millions per day. Therefore, once a crack has reached the for fatigue crack growth (FCG) critical size with respect to HCF loading, it may grow and cause catastrophic failure in a very short time compared to the design life of the turbine runner.

4.1 Stress-Life Approach

4.1.1 SN Curves

The stress-life (SN) approach to fatigue life assessment considers initially uncracked specimens or components. SN curves or “Wöhler curves” (cf. Chapter 2) represent the fatigue life results of a number of fatigue tests at different stress levels. The curves are sensitive to the specimen material, size and surface roughness, type and frequency of loading, R -ratio, as well as temperature and chemical properties of the environment.

An example of such curves is given in Figure 4.1 which displays the results from [54] for a typical Francis runner material. The specimens were taken from either the core or near the surface of a 500 mm thickness 17 % Cr-4 % Ni martensitic-austenitic-ferritic stainless cast steel member that shows an ultimate tensile strength, $R_m = 910$ MPa and the yield limit of 0.2 % plastic strain, $R_{p0.2} = 661$ MPa. The test specimens (cf. Figure 4.2) show a semi-circular surface notch placed centrally across the thinnest edge. Fatigue testing was performed at a frequency of 20–25 Hz at stress ratio $R = 0$ in sweet water environment. The test rig arrangement provided cyclic mode I crack surface displacement loading (cf. Chapter 5) of the notch root. Here, the nominal stress field is composed of bending and 4 % membrane stress. A stress concentration factor at the circular notch of $K_t = 1.36$ was measured by means of strain gauges.

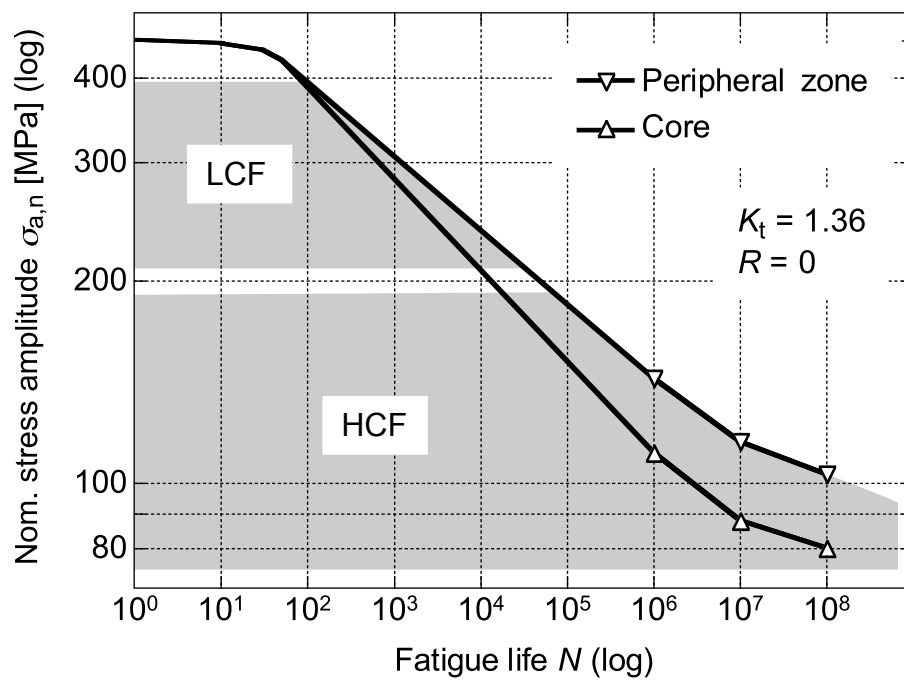


Figure 4.1: Fatigue load regimes in SN curves of 17Cr-4Ni cast material for $R = 0$, $f = 20$ –25 Hz, bending loading of notched specimens with $K_t = 1.36$, cast member thickness 500 mm.

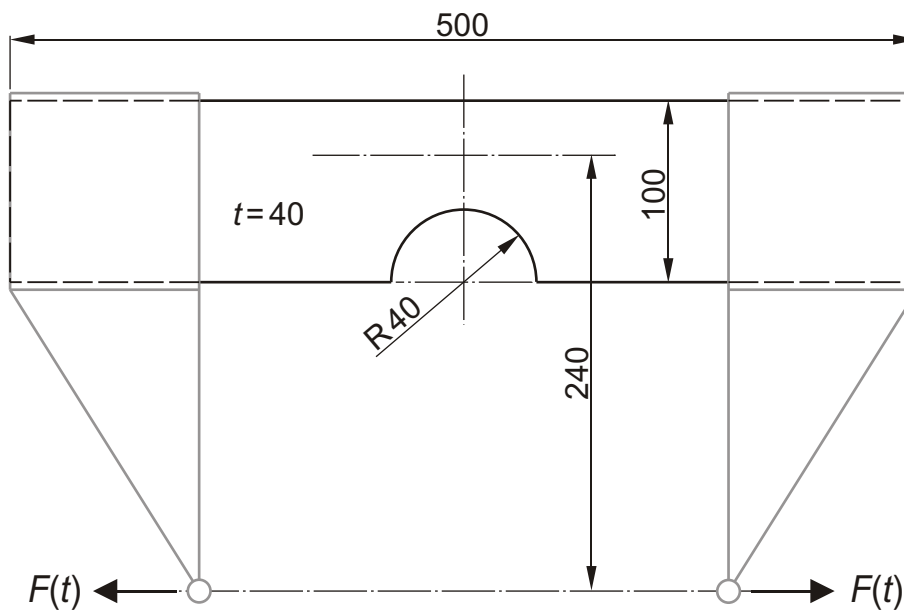


Figure 4.2: Notched test specimen of [54] for a combination of tensile and bending fatigue loading. $K_t = 1.36$. Geometry and loading.

Figure 4.1 demonstrates that the near-surface specimens have a higher fatigue strength than specimens cut out of the cast member core. Specimens that were cut (centrically) out of 150 mm thickness cast members show fatigue test results that are almost identical to the near-surface specimen results of the 500 mm thickness series. This effect can be explained by an increasing number and size of cast defects with increasing distance from the cast member surface. The SN curves displayed base on averaged test results (eleven and eight tests for core and peripheral zone, respectively) for $N = 10^6$, 10^7 and 10^8 and on the ultimate material strength [59].

Both SN curves of Figure 4.1 lack the characteristic fatigue limit, $\sigma_m \pm \sigma_A$, as it is frequently reported from fatigue testing of stainless steel in dry air at $N \approx 10^6$ cycles [54]. Moreover, a further decrease of the endurance limit for increasing N due to the given corrosive environmental conditions has to be assumed. At least for the investigated range up to $N = 10^8$ a fatigue limit is not visible.

Generally, for static or LCF loading the detrimental effect of sweet water to stress corrosion cracking in stainless steel is of little importance. Based on comparative fatigue tests with un-notched round specimens performed both in air and sweet water, [54] reports this detrimental effect to be $\leq 10\%$. The situation changes totally for HCF loading as here the fatigue limit of virtually any material may be affected by any corrosive medium.

From Section 3.3 we recall that LCF appears at high stress amplitudes with correspondingly short fatigue lives up to some 10^4 cycles, whereas HCF covers a large number of cycles, about 10^5 cycles and more. The boundary between LCF and HCF is not exactly defined by a certain number of cycles. The difference is rather that LCF is associated with macroplastic deformation in every cycle, in contrast to HCF which is more related to elastic behaviour on a macro scale of the material [59].

It is a clear disadvantage of the SN approach that true stress-strain behaviour is ignored and all the strains are treated as elastic. Consequently, the SN approach should not be used to estimate fatigue lives below 1000 cycles where the applied strains have a significant plastic component due to high load levels [59]. For rather moderate amounts of plasticity, local strains and stresses may be obtained by means of the Neuber correction for local plasticity according to Equation (2.5), as demonstrated later in Chapter 8.

4.1.2 Fatigue Life Approach

Since all the parameters of the fatigue tests described in this section are representative for the T-joint transition of Chapter 3, the SN curves from [54] presented in the previous section are now applied to a fatigue life approach of the Francis runner:

LCF regime: For $\sigma_{\max} = 400$ MPa and $R = 0$, the LCF stress amplitude, $\sigma_{a,\text{LCF}}$, yields 200 MPa. The corresponding LCF life for thin plates according to Figure 4.1 is $5 \cdot 10^4$ cycles.

HCF regime: For the configuration of 24 guide vanes, five runner rotations per second and an average service time of 6000 hours per year, the number of HCF cycles sums $2.6 \cdot 10^{10}$ in ten years of service. With a representative value of the dynamic factor (3.1), $D = 0.1$ assumed to be constant, $\sigma_{a,\text{HCF}} = 20$ MPa. Thus, even in a low-corrosive medium like sweet water a crackless runner will hardly suffer failure from HCF fatigue only.

In the initially uncracked specimen under cyclic loading, fatigue crack initiation consumes up to 90 % of fatigue life. If fracture-mechanically long cracks are present, the transition from SN curves approach to fatigue crack growth (FCG) simulation by means of LEFM is indicated. FCG simulation investigates the remaining fatigue life as a number of cycles that is necessary to propagate the crack to some critical dimension.

The following section introduces a fracture mechanical damage tolerance criterion which is subsequently applied in fatigue crack growth simulation.

4.2 Damage Tolerance Criterion

The critical area of stress concentration of the Francis runner consists of welded material. It has therefore to be assumed that crack propagation from single undetected flaws and inclusions takes place as soon as the runner is taken into service.

Fatigue life of a component is now calculated as crack propagation life by means of LEFM and an empirical crack growth law. First, the simplified case of a semi-circular surface crack growing by fatigue in a semi-infinite body under homogeneous stress shall be considered. Later, in Chapter 9, finite element stress analysis will be used to predict fatigue crack growth in the critical area of a Francis turbine runner. The growth of a semi-elliptic fatigue crack in the stress field of the T-joint (cf. Section 3.4.1) will then be analysed and results will be compared with those of the simplified calculation of this present section.

The definition of failure described at the beginning of this chapter shall now be reformulated in a fracture-mechanical way: If a crack is propagated by LCF load cycles, the crack size becomes critical when the stress intensity range, ΔK , associated with vibration stresses due to unsteady flow, $\Delta\sigma_{\text{HCF}}$, exceeds the threshold value ΔK_{th} . The stress intensity factor, K , quantifies the crack tip stress field and is treated extensively in Chapter 5. The critical crack size for HCF crack growth, a_c , is given by

$$\Delta K_{\text{HCF}} = G \cdot \Delta\sigma_{\text{HCF}} \sqrt{a_c} = \Delta K_{\text{th}} (R_{\text{HCF}}) \quad . \quad (4.1)$$

For a semi-circular surface crack [67], the geometry factor at the bottom of the crack is $G = 1.17$. In order to simplify the analysis, the variation of the geometry factor along the crack front has been neglected. The threshold stress intensity range, ΔK_{th} , is a function of the stress ratio of the HCF cycle,

$$R_{\text{HCF}} = \frac{\Delta\sigma_{\text{LCF}} - \Delta\sigma_{\text{HCF}}}{\Delta\sigma_{\text{LCF}}} = 1 - D \quad . \quad (4.2)$$

Granted that the crack growth during the LCF cycle obeys Paris' law, Equation (9.2), integration between the initial crack size, a_i , and the critical crack size, a_c , yields, after some rearrangement,

$$a_i = a_c / \left[1 + \left(\frac{m}{2} - 1 \right) \cdot N_{\text{LCF}} \cdot \frac{r_c}{a_c} \right]^{1/\left(\frac{m}{2}-1\right)} \quad . \quad (4.3)$$

N_{LCF} denotes the number of LCF cycles available for the crack to reach its critical size, r_c the LCF crack growth rate for $a = a_c$, i. e.,

$$r_c = \left. \frac{da}{dN} \right|_{a=a_c} = C [G \Delta\sigma_{\text{LCF}} \sqrt{a_c}]^m = r_{\text{th}} / D^m \quad , \quad (4.4)$$

where

$$r_{\text{th}} \equiv C [\Delta K_{\text{th}}(R_{\text{HCF}})]^m \quad . \quad (4.5)$$

Thus, for a given LCF and HCF loading, a_i signifies the allowable initial crack size which just grows to become critical within the number of LCF cycles available.

A conservative upper limit of fatigue crack growth data for martensitic-ferritic (16Cr-5Ni) and austenitic (18Cr-8Ni) stainless turbine runner steels [68, 69] for stress ratios between $R = 0.05$ and 0.7 is given by

$$\frac{da}{dN} = 10^{-11} \Delta K^3 \quad (4.6)$$

with da/dN expressed in m/cycle and ΔK in $\text{MPa}\sqrt{m}$. From the same investigation, the lower bound threshold stress intensity range as a function of the stress ratio [70], R (3.2), was estimated to be

$$\Delta K_{\text{th}} = 6 - 4R \text{ MPa}\sqrt{m} \quad . \quad (4.7)$$

4.3 Simplified Fatigue Crack Growth

Using the data of the previous section, the growth of a semi-circular fatigue crack in a large, homogeneously loaded body was analysed. For design lives of $N = 0, 10\,000$ and $50\,000$ cycles, Figure 4.3 shows the allowable initial crack depth as a function of the LCF stress range. The critical crack size, which corresponds to $N = 0$, has been based on the “full load” loading condition where the dynamic factor, D , of Equation (3.1) is assumed to be $D = 0.1$ and constant. The definitions of stress ranges for LCF and HCF loading, $\Delta\sigma_{\text{LCF}}$ and $\Delta\sigma_{\text{HCF}}$, are such that the respective maximum stress values are identical, as visualised in Figure 3.2.

This simplified design calculation yields a conservative estimate of the allowable crack size if the LCF and HCF stress ranges are set equal to those at the most highly loaded point of the turbine runner. The estimate is expected to be in fair agreement with a more precise analysis as long as stress gradients are small, i. e. for thick sections and generous (notch or transition) radii.

In an attempt to compare the two approaches to fatigue life presented in this chapter, the SN curve LCF life of 50000 cycles (cf. Section 4.1) results in a corresponding initial crack or defect size of 0.12 mm, if the stress concentration of $K_t = 1.36$ is taken into account. It has to be regarded that in the SN approach LCF-HCF interaction is not considered. As discussed above, this interaction shortens the runners fatigue life. This means that the size of a corresponding initial defect in the cast material becomes larger and therewith much the same the typical size of pores in cast steel material.

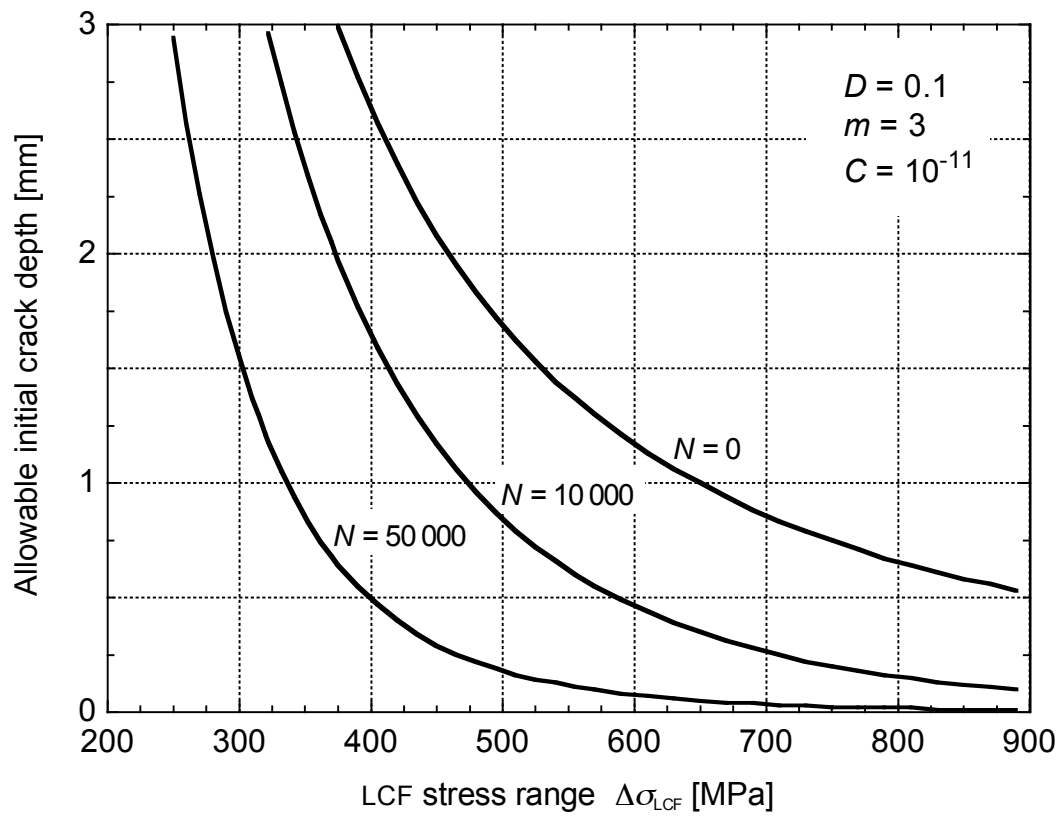


Figure 4.3: Francis turbine runner. Allowable initial crack depth.

Chapter 5

Stress Intensity Factors

5.1 Basics and History

The 1913 publication of Inglis [29] was a pioneering work in fracture mechanics. Inglis extended the work of Kirsch [28] (cf. Section 2.2) and used complex potential functions to describe the stress field in a plate in the vicinity of an elliptical hole. As Inglis' solution allows crack-like geometries to be treated by making the minor axis of the ellipse (and so the notch root radius, ρ , cf. Figure 2.1) small, the work implies a description of the stress field ahead of the crack tip.

Griffith [71] bases his energy concept idea on Inglis' work in 1920. He formulated the concept that a crack in an ideally brittle component will propagate if the total energy of the system is lowered with crack propagation. In 1957, Irwin [72, 73] extended the theory of Griffith to ductile materials by including the energy dissipated by local plastic flow and introduced the concept of the stress intensity factor (SIF), K ,

$$K = F\sigma_\infty\sqrt{\pi a} = G\sigma_\infty\sqrt{a} \quad (5.1)$$

as an expression for static loading of a cracked body. Here, σ_∞ is the nominal stress in the gross section, a denotes the crack length. F and G are dimensionless geometry factors and are influenced by both the crack shape and the specimen geometry around the crack. If K exceeds the material-dependent fracture toughness, K_c , unstable crack growth and instant fracture occurs.

The development of what was meant to be a scale factor to define the magnitude of the crack tip stress field turned out to be the foundation stone of linear elastic fracture mechanics (LEFM).

5.1.1 Different Types of Crack Surface Displacement

Fracture mechanics distinguishes between three basic modes of crack surface displacement: opening, sliding and tearing mode (cf. Figure 5.1), denoted by indices I, II and III, respectively. Any other deformation is a superposition of these basic modes. Since mode I applies for the most cases of practical interest, the subscript on K is often dropped, and K without such a subscript is understood to represent K_I .

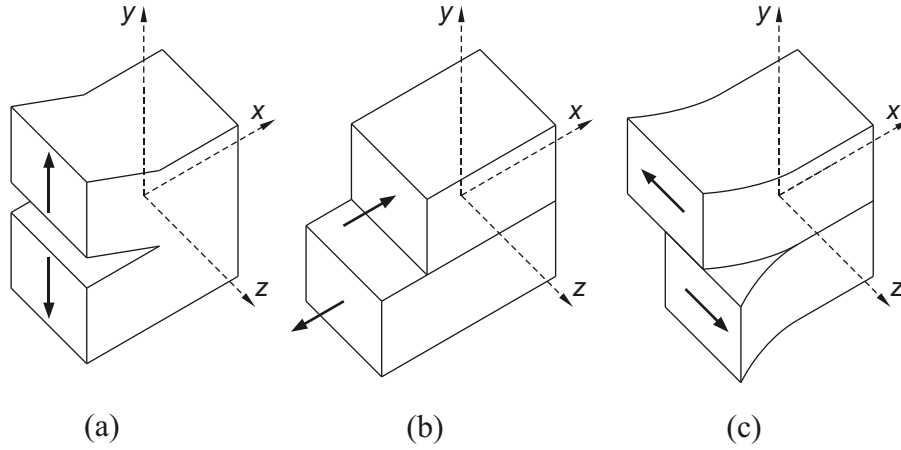


Figure 5.1: The three basic modes of crack surface displacement. (a) Tensile opening (mode I). (b) In-plane sliding (mode II). (c) Antiplane shear (mode III).

5.1.2 SIF Definition

Stress Field

As mentioned above, a crack can be considered to be an elliptical hole of zero height. An exact solution of the crack tip stress field is available for a crack in an infinite plate. However, the concept of the SIF has extended validity and encloses components of finite dimensions [72]. If the attention is restricted to the area around the crack tip, i. e. $r \ll a$ (cf. Figure 5.2), the crack tip stress field can be described with polar co-ordinates as follows:

$$\begin{Bmatrix} \sigma_x \\ \sigma_y \\ \tau_{xy} \end{Bmatrix} = \frac{K_I}{\sqrt{2\pi r}} \cos \frac{\theta}{2} \begin{Bmatrix} 1 - \sin \frac{\theta}{2} \sin \frac{3\theta}{2} \\ 1 + \sin \frac{\theta}{2} \sin \frac{3\theta}{2} \\ \sin \frac{\theta}{2} \cos \frac{3\theta}{2} \end{Bmatrix} \quad (5.2)$$

The stress distribution at the crack tip shows a stress singularity as all stress components go to infinity for $r \rightarrow 0$, for all values of θ .

In fatigue crack growth calculations presented in Chapter 9 the crack tip stress field singularity is of special interest. A more detailed discussion of the stress singularity problem is therefore included in Sections 5.2.1 and 5.2.2.

Considering Equation (5.1), the R relationship (3.2) between minimum and maximum stress, σ_{\min} and σ_{\max} , is consistent with the ratio between the extreme values of the stress intensity factor, K :

$$R = \frac{\sigma_{\min}}{\sigma_{\max}} = \frac{K_{\min}}{K_{\max}} \quad (5.3)$$

Displacements and Crack Opening

A cracked plate under tensile loading as presented in Figure 5.2 will show a crack that is open. The crack edge displacements in y direction, u_y , are of special interest since they

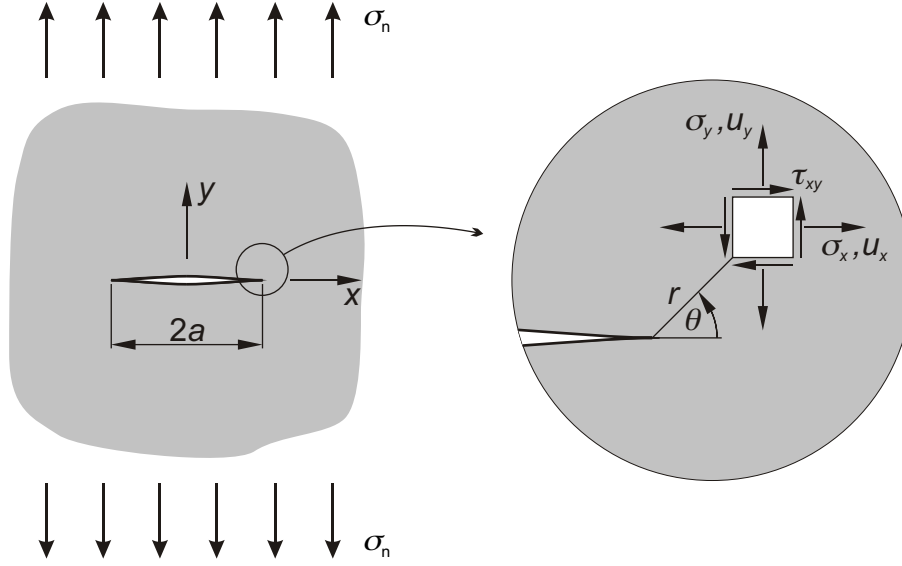


Figure 5.2: Mode I crack in an infinite plate for $r \ll a$. Stress field and displacement co-ordinates.

usually represent the largest deformations of the crack and indicate the crack opening [59]. At the centre of the crack, the crack opening displacement (COD) for plane stress conditions is

$$\text{COD} = 2u_y = 4 \frac{\sigma_n}{E} a = 4a\varepsilon_n \quad (5.4)$$

where $\sigma_n/E = \varepsilon_n$ denotes the nominal strain in the plate.

Considering Equation (5.2), the displacements u_x and u_y in x and y -direction, respectively, become

$$\begin{Bmatrix} u_x \\ u_y \end{Bmatrix} = \frac{K_I}{2E} \sqrt{\frac{r}{2\pi}} \begin{Bmatrix} (1 + \nu) [(2\kappa - 1) \cos \frac{\theta}{2} - \cos \frac{3\theta}{2}] \\ (1 + \nu) [(2\kappa + 1) \sin \frac{\theta}{2} - \sin \frac{3\theta}{2}] \end{Bmatrix} \quad (5.5)$$

where, for plane stress,

$$\kappa = \frac{3 - \nu}{1 + \nu} \quad (5.6)$$

and, for plane strain,

$$\kappa = 3 - 4\nu \quad (5.7)$$

Unlike the character of the stress field, the displacement behaviour is characterised by $r^{+0.5}$, what means the displacements u_i go to zero for $r \rightarrow 0$. According to Equation (5.5) the displacements increase for increasing values of r , but it has to be recalled that $r \ll a$.

For $\theta = \pi$, the displacement in y -direction at the crack tip is obtained. With $\nu = 0.3$, Equation (5.5) gives

$$u_y = \frac{4K}{E} \sqrt{\frac{r}{2\pi}} \quad (\text{plane stress}) \quad (5.8)$$

$$u_y = \frac{4K(1-\nu^2)}{E} \sqrt{\frac{r}{2\pi}} \quad (\text{plane strain}). \quad (5.9)$$

5.2 SIF Retrieval

A large number of methods has been developed for the determination of stress intensity factors [74]: the method of complex stress function by Muskhelishvili [75], the method of conformal mapping by Bowie [76], extrapolation of stress concentration factors of notched components (e.g., of [31]) to vanishing notch radius, the boundary collocation method by Gross et al. [77], the J-integral by Rice [78], the boundary element method (BEM) by Cruse [79], the integral transformation method by Sneddon and Löwengrub [80], the weight function method by Bueckner [81] and Rice [82], the method of asymptotic interpolation by Benthem and Koiter [83], the finite element method (FEM) by Wilson [84], and the element-free Galerkin method by Belytschko et al. [85].

In order to perform most accurate crack growth simulation that takes into account an arbitrary stress field, computational methods seem to become more and more inevitable. A large number of stress intensity factor solutions for semi-elliptical surface cracks under mode I loading, mostly obtained numerically, are published in the frequently updated *Stress Intensity Factors Handbook* [86] edited by Y. Murakami.

5.2.1 Crack Tip Stress Singularity

For mode I crack opening displacement it was shown in Section 5.1.2 that the near crack tip stress field can be expressed by

$$\sigma = \frac{K_I}{\sqrt{r}} G(\theta), \quad r \rightarrow 0 \quad (5.10)$$

with the origin of r on the crack tip and the angle θ according to Figure 5.3. This inverse square root stress singularity at the *interior* border of a sharp crack is an elementary phenomenon in the theory of linear elastic fracture mechanics. For the idealised case of the completely embedded crack in an infinite body, Equation (5.10) remains valid at every point of the crack border. In Section 5.2.2 one common way is explained how this $1/\sqrt{r}$ singularity may be modelled in finite and boundary element calculations.

Singularities that are different from $1/\sqrt{r}$ arise where the crack border meets a free surface, as shown for point C in Figure 5.3. In this case, the near stress field may be written as

$$\sigma = \frac{\widetilde{K}_I}{r^\lambda} G_1(\lambda, \theta, \delta), \quad r \rightarrow 0 \quad (5.11)$$

An absence of the $1/\sqrt{r}$ character at the free surface is described in several publications [87, 88, 89]. For the case of the crack front meeting a free surface perpendicularly, i. e. $\beta = 90^\circ$, Benthem [90] computed λ in the surface layer as a function of Poisson's ratio ν to values

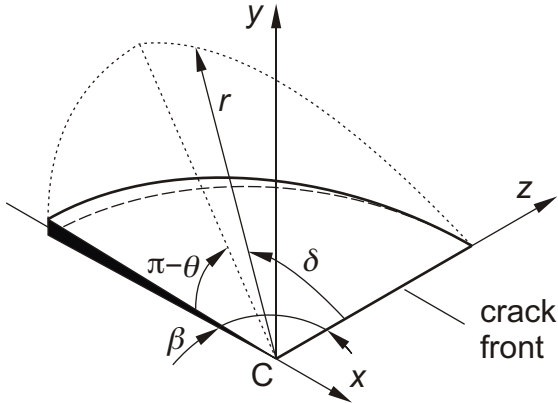


Figure 5.3: Notation of quarter-infinite crack $y = 0$, $x^C > 0$ and $z < 0$ in the half space $x^C > 0$.

Table 5.1: Computed λ values in Equation (5.11) [90]

ν	λ
0.0	0.5
0.15	0.4836
0.3	0.4523
0.4	0.4132
0.5	0.3318

shown in Table 5.1. Here, λ is less than 0.5 except when $\nu = 0$, the theoretical case of a material that is completely incompressible. Thus, for engineering materials the stress intensity factor concept does not hold at the corner or intersection of three free surfaces [91], the classical stress intensity factor vanishes and tends to zero [92].

For steel with $\nu = 0.3$ the dominant near-corner singularity $r^{-0.4523}$ does in practical terms not represent a dramatic deviation from the idealised $1/\sqrt{r}$ -singularity. Pook [93] even comes to the conclusion that

“Corner point singularities do not normally have to be taken into account in the consideration of mode I fatigue crack growth, but may affect the numerical derivation of stress intensity factors for three-dimensional configurations”.

For mixed mode loadings, he suggests the use of a symmetrical part-elliptical crack shape that realises the *critical* intersection angles, which for $\nu < 0.5$ are different from $\beta = 90^\circ$, cf. Figure 5.3. For mode I loading and $\nu = 0.3$, the critical angle is $\beta = 100.4^\circ$ [88].

However, for the practical application of stress intensity factors it should be considered that the zone of non-reliable results is confined to a small region near the intersection point, C, between the crack front and an external free surface [92, 94]. The size of this small region is considered to be a function of geometry, Young’s modulus and the type of loading [95].

Yngvesson and Nilsson [96] account for the free surface by employing constant K_I -values within a distance of approximate 10 % of the crack length from a free surface.

5.2.2 Quarterpoint Finite Elements

To account for the $1/\sqrt{r}$ singularity of the crack tip stress field away from the free outer surface of Section 5.2.1, in both finite and boundary element modeling of discrete cracks the application of quarter-point elements at the crack tip has become a standard procedure. The quarter-point element was developed simultaneously by Henshell and Shaw [97] in 1975 and by Barsoum [98] in 1976. It has significantly improved the accuracy of stress intensity factor calculations, albeit the prediction of stress intensity factors for sliding and twisting mode, K_{II} and K_{III} , is not nearly as accurate as for mode I.

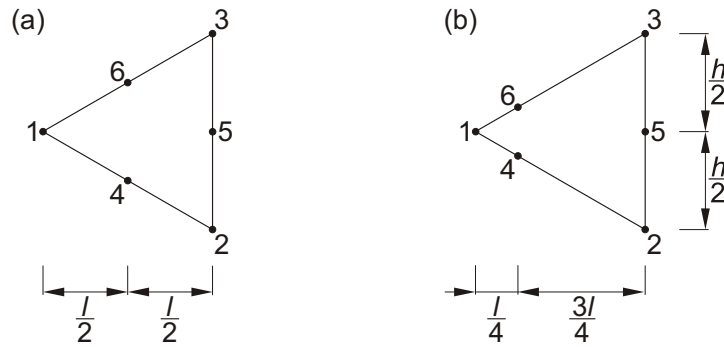


Figure 5.4: Triangle finite element. (a) Common second order element. (b) Natural quarter-point element.

A quarter-point element is created by moving the mid-side node of a standard quadratic or isoparametric finite element to the position one quarter of the way from the crack tip to the far end of the element. By this, a singularity is introduced into the mapping between the element's parametric co-ordinate space and cartesian space.

In Figure 5.4(b) the natural triangle quarter-point element is shown, with node no. 1 situated on the crack tip. The shape of this element is similar to the shape of the collapsed quadrilateral quarter-point element, which places each of the three nodes of the collapsed edge on the crack tip position, "1".

5.2.3 Superposition Principle

For an arbitrarily cracked body, each loading condition has its own characteristic stress intensity solution. Any loading condition may be composed of single load components that act simultaneously on the body. In this case, the resulting overall stress intensity can be obtained as the sum of the contributions to K from the individual load components. According to this principle of superposition, the two load cases of

1. an arbitrary crack-opening loading on the nominal body section and
2. the same geometry showing stresses of the same magnitude that act solely on the crack faces

result in the same stress intensity. This shall be visualised in Figure 5.5 for the case of a central crack in a plate under uniform tension:

The stress intensity factor of the uncracked plate under tension in (a) is zero since no crack is present. Now in (b) the crack is present but its crack faces are loaded by internal stresses of the same magnitude as the nominal stress, S_0 , with signs opposite. As this keeps the crack just closed, a singular stress distribution at the crack tip is not present and the fracture mechanical state of (b) is identical to the one of the uncracked plate in (a). Thus, for (b) $K = 0$.

Due to the principle of superposition, the two load cases the (b) loading condition is composed of may be separated from each other as shown in (c) and (d) for the nominal and the internal load case, respectively. The crack in (c) is now open and shows a stress intensity of value greater than zero. The addition

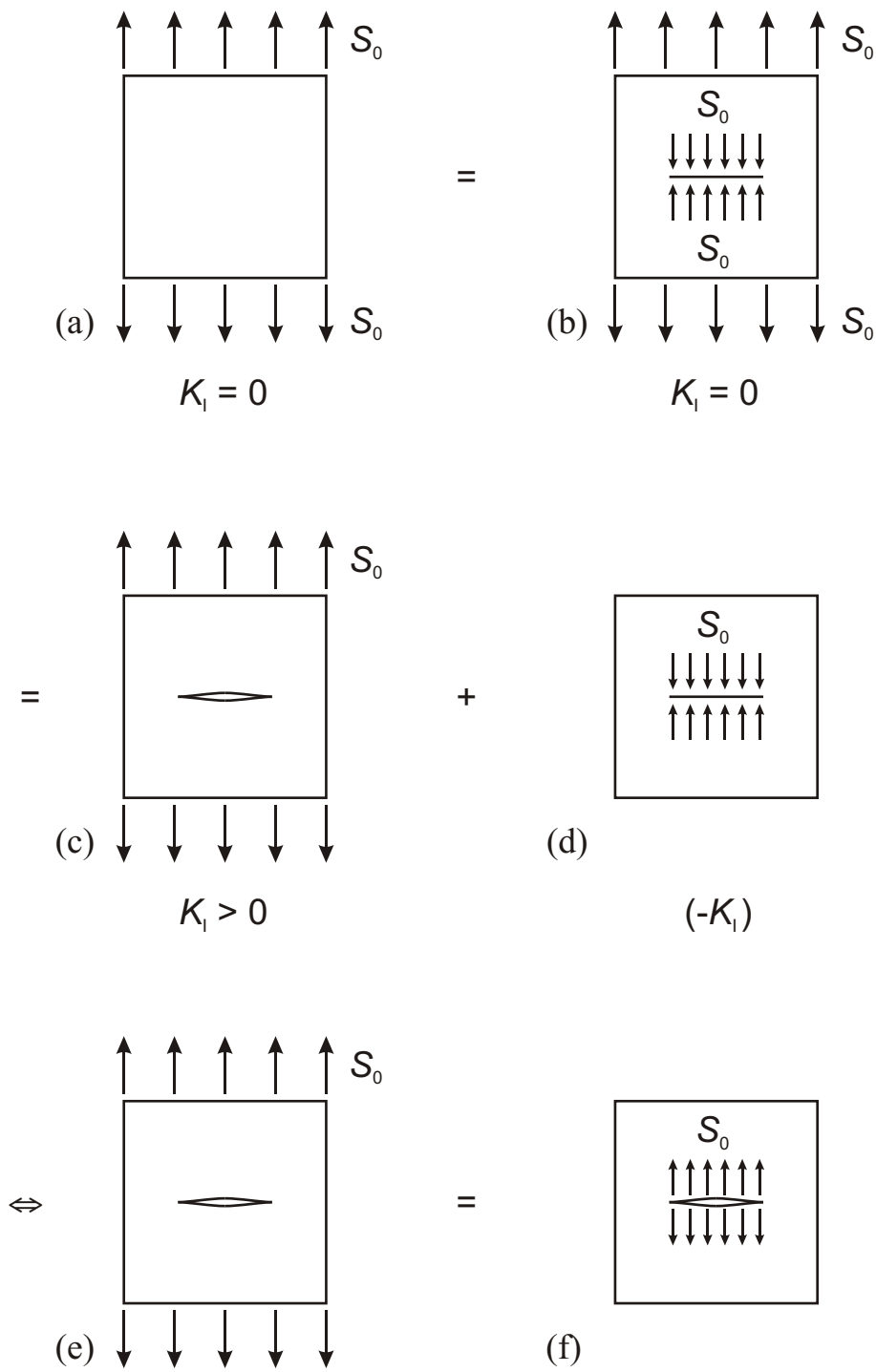


Figure 5.5: The superposition principle.

of the stress intensity factor of cases (c) and (d) results in the solution of (b) which is $K = 0$. Thus, load cases (c) and (d) show identical absolute values of stress intensity. It should be mentioned here that the resulting negative stress intensity factor in (d) is of notional character. Once a crack is closed and $K = 0$, any further closure with $K < 0$ is imaginary.

Inverting the internal stresses on the crack faces of (d), the two load cases are arranged on either side (e) and (f) of the equation.

5.3 Solutions for Fatigue Crack Growth Calculation

Solutions for the stress intensity factor are available for many different crack geometries (cf. Tada et al. [99]), but are often restricted to a few simple stress fields. More complex stress fields are encountered in many engineering structures due to residual stress fields, thermal or contact stresses and at notches.

Notches, as a collective term for holes, shoulders, weld seams, clearance grooves and other geometrical discontinuities, are generally areas of stress concentration. As already mentioned in Chapter 2, fatigue cracks tend to form at stress concentrations due to the here elevated stresses. Along with the stress concentration comes a gradient stress field. In most engineering cases, the stress gradient, χ , of Equation (2.7) is not constant. The largest stress gradient as well as the largest change of the stress gradient is typically found at the notch root.

Stress conditions at the crack front of a propagating crack are influenced by the stress gradient of the nominal stress field. Hence, for accurate calculation of fatigue crack propagation from notches it is required to readjust stress and geometry conditions more often for larger stress gradients, preferably after every single crack propagating load cycle. The determination of both the stress field around the crack and the geometry factor, F , is the main challenge in the fracture mechanical approach to fatigue in notched areas.

Standard stress intensity factor solutions mostly address bodies under tensile loading that contain trivial crack shapes, e. g. the through crack or the circular embedded crack. When applied to crack growth calculation, these standard solutions imply the assumption of a crack shape of the propagating crack that remains unchanged.

Other recommendations assume surface flaws with a constant aspect ratio [100] or drive the crack into a semi-circular shape which then is maintained during subsequent propagation, as it is recommended in the 1991 British Standard PD 6493. This standard was replaced in 1999 by BS 7910 [101] which favours linear substitutes of the real stress distributions. Here, any linearised distribution of stress is considered to be acceptable “provided that it is greater than or equal to the magnitude of the real distribution over the flaw surface”.

The assumption that a growing surface crack under mode I loading conditions forms and keeps the shape of a (plane) semi-ellipse or grows as an elliptical-arc surface flaw has proved to yield reliable results for different geometrical bodies and is frequently made in the literature. Several studies have been carried out on such surface cracks in plates [102, 103, 104, 105], round bars [104, 106, 107, 108, 109, 110, 111, 112, 113], pipes [114, 115, 116, 117, 118, 119, 120], and shells [121, 122] to evaluate the mode I SIF, K_I , and the fatigue crack growth under different loading conditions.

In crack growth calculation even numerical methods are highly time-consuming since a

high frequency in the application of the computational analysis is needed. Solutions that are available in terms of a set of empirical equations or in tabular form offer significant savings of time and resources, provided that such a tool exists for the relevant geometries and loading conditions. A suitable empirical solution covers the entire range of crack sizes and aspect ratios that the crack is likely to show under crack growth calculation. Furthermore, an analytical way to define the stress field with sufficient accuracy should be provided.

The confinement to semi-elliptical crack shapes significantly reduces the computational efforts for two reasons: first, the number of possible crack shapes to be considered in a set of equations is minimised. Secondly, the number of points on the crack shape for which the SIF and the propagation increment has to be calculated is reduced. With a given centre, the ellipse is completely defined by two points on the crack front.

5.3.1 Internal Pore

First, an introduction to the problem of SIF retrieval for FCG calculation purposes shall be given by applying a standard SIF solution to an engineering problem, considering a crack that grows from a material defect. Fatigue cracks often form at inclusions by one of three mechanisms: inclusion cracking, debonding of the interface between the inclusion and the matrix, or cracking at lines of slip in the surrounding matrix. Assuming Poisson's ratio $\nu = 0.3$, the stress concentration factor for an internal spherical pore with radius ρ (cf. Figure 2.2) is 2.05 [31]. For a small crack around the pore, Equation (5.1) for the stress intensity factor forms

$$K = 1.12 \cdot 2.05 \cdot \sigma \sqrt{a\pi} \quad (5.12)$$

as long as $a \ll \rho$, and so the mechanical behaviour of the crack is the one for a plane surface crack in an infinite body. As a increases, K gradually becomes the solution of an embedded circular (penny-shaped) crack:

$$K = \frac{2}{\pi} \cdot \sigma \sqrt{(a + \rho)\pi} \quad (5.13)$$

Thus, for long cracks the pore radius acts as a part of the crack depth.

5.3.2 Newman and Raju

One of the most well-known stress intensity factor solutions for a surface crack in infinite and finite plates under membrane stress or bending has been presented by Newman and Raju [67, 123, 102, 114, 124]. The equations from [102] were derived from FEA for the finite plate under a combination of tensile and bending loading containing a semi-elliptical surface crack. Here, both the thickness and the width of the plate are finite. It is claimed that the ratios of crack length to plate thickness, a/t , and the ratios of crack depth to crack length, a/c , range from 0 to 1.0 in this solution. The set of equations is presented in Section B.1 of the Appendix.

5.3.3 Pommier, Sakae and Murakami

Using the body force method [125], Pommier et al. [113] have derived numerical solutions for the stress intensity factor of a short semi-elliptic mode I surface crack in the z - x plane

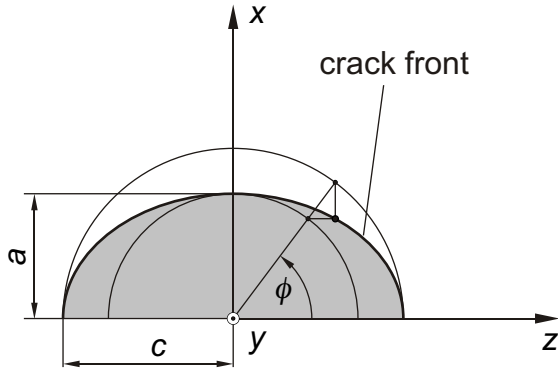


Figure 5.6: Notation of semi-elliptical crack.

of a semi-infinite plate (cf. Figure 5.6). The “undisturbed” normal stress in the y -direction is assumed to vary as

$$\sigma_y(x, z) = \sum_{i=0}^3 \sum_{k=0}^3 \sigma_{ik} (x/a)^i (z/c)^k \quad (5.14)$$

for all y , where the double sum is taken over all ten pairs (i, k) satisfying $i + k \leq 3$. As shown in Figure 5.6, a and c are the lengths of the semi-axes of the crack along the x - and z -axes, respectively. The axis ratio is limited to the interval $0.5 \leq a/c \leq 2$.

By fitting the correction factors $G_{ik}(\phi; a/c)$ to the numerical solutions, Pommier et al. managed to estimate the stress intensity factor along the front of the semi-elliptic crack ($0 \leq \phi \leq \pi$) within 2 % of the numerical results by the equation

$$K(\phi; a/c) = \sum_{i=0}^3 \sum_{k=0}^3 \sigma_{ik} \cdot G_{ik}(\phi; a/c) \sqrt{a} \quad . \quad (5.15)$$

The “engineering” [113] set of equations for the geometry factors are given in Section B.2 of the Appendix.

The advantage of this solution is that it allows the modelling of the (uncracked) stress field by a 3rd order polynomial equation. This should be sufficient for most applications in engineering. In difference to the Newman-Raju formulae, this solution is confined to component dimensions much larger than the crack.

5.3.4 Carpinteri, Brighenti, Huth and Vantadori

This solution has been created during the author’s visit at the Department of Civil Engineering, Environment and Architecture of the University of Parma, and has been published in the International Journal of Fatigue [126]. The work presents tabular values of the stress intensity factor of a finite-thickness plate containing a semi-elliptical surface crack. Thickness ratios of $0.1 \leq a/t \leq 0.7$ and axis ratios of $0.1 \leq a/c \leq 1.2$ are covered, where t denotes the plate thickness.

Finite element analysis with 20-node isoparametric solid elements was employed. The stress singularity was obtained by quarter-point wedge elements arranged in rings around the crack front. Nodal displacement results were employed to obtain the stress intensity

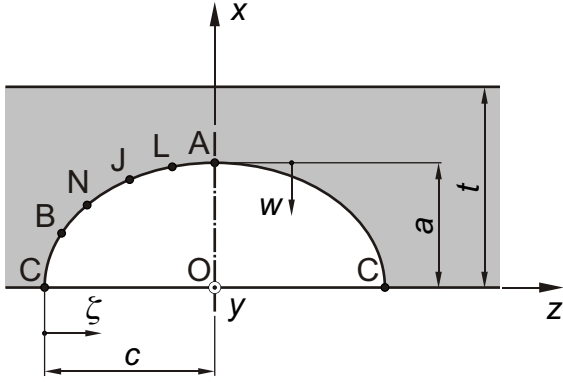


Figure 5.7: Finite plate with semi-elliptical surface crack: geometrical parameters.

factor. Employing Equation (5.9) for plane strain conditions, K was calculated according to

$$K_{\text{I}} = \frac{E\sqrt{2\pi}}{4(1-\nu^2)} \frac{u_y[l/4]}{\sqrt{l/4}} \quad (5.16)$$

where $u_y[l/4]$ denotes the displacement orthogonal to the crack faces, i.e. along the y -direction (cf. Figures 5.1 and 5.6), measured at the quarter-point position, i.e. with a distance equal to $l/4$ from the crack front (cf. Figure 5.4).

As shown in Section 5.2.3, the stress intensity factor for a cracked body subjected to stresses (external or self-equilibrating) can be computed as the stress intensity factor due to stresses acting solely on the defect faces, with the same magnitudes but signs opposite to those of the corresponding stresses in the uncracked body.

In order to obtain the stress intensity factors for arbitrary loading conditions, six different elementary mode I stress distributions on the crack faces are considered: constant, linear, quadratic, cubic, quartic and quintic stress distribution, $\sigma_{\text{I}(n)}$, with $n = (0, \dots, 5)$. Note that the subscript I stands for mode I, whereas n indicates the order of the polynomial which describes the n -th elementary stress field. Each stress distribution $n > 0$ is characterised by a zero value at the deepest point A of the surface crack and a unit value in correspondence to the outer surface of the plate (along the segment $\overline{\text{COC}}$ in Figure 5.7).

For each of these elementary loading conditions the values of K were obtained at five points A, L, J, N and B along the crack front. The elementary loadings can then be combined according to a power series expansion of the actual arbitrary (e.g. T-joint) stress field at the expected crack location. So, by applying the superposition principle of Section 5.2.3, an approximate SIF solution is generated (cf. Section 5.4).

As shown in Figure 5.7 the deepest point A is at $\zeta/c = 1$, with the co-ordinate ζ starting at the the crack front surface points, C. Points L, J, N and B are positioned at $\zeta/c = 0.75, 0.5, 0.25$ and 0.10 , respectively. As symmetrical conditions of geometry and loading are assumed, only one half of the semi-ellipse is regarded.

Due to singularity conditons (cf. Section 5.2.1) that exist for the surface point, C, calculations have been omitted here. One way to cope with the missing surface point value under the crack growth calculation of a semi-elliptical surface crack is presented in Chapter 9.

The elementary stress distributions $\sigma_{\text{I}(n)}$ can be expressed as

$$\sigma_{\text{I}(n)} = (w/a)^n = \eta^n \quad n = (0, \dots, 5) \quad (5.17)$$

where $\eta = w/a$ is a dimensionless co-ordinate and w has its origin at the deepest point, A, on the crack front (cf. Figure 5.7). For the n -th elementary stress distribution, the dimensionless mode I stress intensity factor is defined as

$$K_{I(n)}^* = K_{I(n)} / (\sigma_{\text{ref}(n)} \sqrt{\pi a}) \quad (5.18)$$

where $\sigma_{\text{ref}(n)}$ represents the reference stress, which is assumed to be equal to unity; the stress intensity factor $K_{I(n)}$, related to the n -th load case, is obtained from the displacement field determined through a three-dimensional finite element analysis, by using quarter-point singular elements (cf. Section 5.2.2) to model the crack front.

An arbitrary stress distribution, $\sigma_{I(L)}(w)$ (where the subscript (L) indicates the arbitrary loading condition), acts on the crack faces and can be approximated through a power series expansion as follows:

$$\sigma_{I(L)} \cong \sum_{n=0}^5 \frac{1}{n!} \left[\frac{\partial^{(n)}}{\partial w^{(n)}} (\sigma_{I(L)}) \right] w^n = \sum_{n=0}^5 A_{n(L)} w^n \quad (5.19)$$

By recalling the expression $\eta = w/a$, Equation (5.19) becomes

$$\sigma_{I(L)} \cong \sum_{n=0}^5 A_{n(L)} (a\eta)^n = \sum_{n=0}^5 a^n A_{n(L)} \eta^n = \sum_{n=0}^5 B_{n(L)} \eta^n \quad (5.20)$$

where the n -th coefficient, $B_{n(L)}$, is equal to the following expression:

$$B_{n(L)} = a^n \left[\frac{1}{n!} \frac{\partial^{(n)}}{\partial w^{(n)}} (\sigma_{I(L)}) \right] \quad (5.21)$$

According to the first and last members of Equation (5.20) the arbitrary opening stress distribution $\sigma_{I(L)}$ is approximately equal to a combination of the elementary stresses $\sigma_{I(n)} = \eta^n$ through the coefficients $B_{n(L)}$, with $n = (0, \dots, 5)$ (superposition principle). Therefore, since $K_{I(n)}$ is the stress intensity factor related to η^n , the approximate mode I stress intensity factor for the actual (arbitrary) stress distribution can be obtained as follows:

$$K_{I(L)} \cong \sum_{n=0}^5 B_{n(L)} K_{I(n)} \quad (5.22)$$

Dividing both members of Equation (5.22) by $\sigma_{\text{ref}(L)} \sqrt{\pi a}$ and recalling Equation (5.18), the dimensionless approximate stress intensity factor, defined as $K_{I(L)}^* = K_{I(L)} / \sigma_{\text{ref}(L)} \sqrt{\pi a}$, along the front of a surface crack is given by

$$K_{I(L)}^* \cong \frac{1}{\sigma_{\text{ref}(L)}} \sum_{n=0}^5 B_{n(L)} K_{I(n)}^* \quad (5.23)$$

where $\sigma_{\text{ref}(L)}$ represents the reference stress for the arbitrary stress distribution, L .

Note that when a closed-form expression of the stress field in the vicinity of the crack is not available, the coefficients $A_{n(L)}$ (and therefore $B_{n(L)}$, cf. Equation (5.21)) can numerically be obtained by a polynomial fitting of the considered stress distribution.

5.3.5 Further Solutions

Nilsson

In 1992, Nilsson [127] presented a stress intensity factor solution based on approximated successive crack configurations with a family of curves for which K_I values are known. A fatigue crack growth code [128] prepared in 1998 uses the K values of [129]. The in [128] presented SIF solution for semi-elliptical surface cracks in very wide finite-thickness plates subjected to arbitrary stress states originate in the work of [127].

The stress state on the crack surface can be approximated with a 3rd grade polynomial. Crack aspect ratio a/c values from 0.0625 to 4.0, and values of the relative crack depth, a/t , between 0.1 and 0.8 are covered. For a loading that varies linearly along the crack length, c , a 1999 publication [96] of the work group showed good agreement between (a) fatigue crack growth data derived from [128], (b) results generated by FRANC3D software and (c) experimental fatigue testing.

FRANC3D

The freely distributed FRANC3D [130, 131, 132, 133] software package allows the simulation of non-planar FCG and is not limited to semi-elliptical surface crack shapes. SIF values for plane strain conditions are calculated for arbitrary component geometries, loading conditions and crack shapes by means of the Boundary Element Method (BEM) for several points along the crack front. In order to limit the extensive calculational work, constant SIF values are used over a propagation step that represents several fatigue load cycles. FRANC3D chooses a propagation step size in which the number of cycles is less than 0.5 % of total life. The crack front shape is then automatically adjusted after each increment of crack growth.

Thus, for larger propagation steps computational efforts are reduced at the expense of accuracy. Furthermore, the general assumption of plane strain might not always suit the given stress conditions, e. g. near a free surface (cf. Section 5.2.1).

For larger changes of the crack geometry during propagation simulation it may be necessary to model a new crack element mesh between two propagation steps as the initial meshing remains and is not adjusted by the program automatically. Further, the author encountered difficulties analysing cracks growing from the curved surface of a notch.

BEASY

BEASY [134] is a commercial FCG simulation software. Like FRANC3D the code bases on BEM and shows similar features like multiple crack growth. In addition, BEASY promises automatic remeshing of the crack and component surface what enables the simulation of component surface intersection and extension of the crack to adjacent structures.

5.4 Component Geometry Influence

In the strict sense of fracture mechanics, each cracked structure geometry asks for its very “own” empirical equations set of the stress intensity factor. However, it can be shown that for a relatively small crack the structural component geometry has only minor effect on

the stress intensity factor value, provided that the stress field in the vicinity of the crack is approximately the same.

A review of mode I stress intensity factor solutions related to a semi-elliptical surface crack is presented in Table 5.2 for different structural components under approximately the same uniform opening stress field. In particular, SIF solutions are reported for the relative crack depth, ξ , (defined as the ratio between the crack depth, a , and the characteristic size of the component) equal to 0.1, 0.2, 0.5 and 0.8, whereas the crack aspect ratio, α , (defined as the ratio of crack depth and length, a/c , cf. Figures 5.6 or 5.7) is assumed to be equal to 0.2, 0.5 and 1.0.

The stress intensity factor values shown are related to the deepest point, A ($\zeta/c = 1$), and the surface point, C ($\zeta/c = 0$) or the near-surface point, B ($\zeta/c = 0.1$), on the crack front (cf. Figure 5.7), for a cracked finite-thickness plate under tension [102, 103, 105], a shaft under tension [106], a thin/thick-walled pipe under pressure [120, 122] and a semi-infinite body under remote tension [113].

Analysing the stress intensity factor values related to a given crack configuration and different component geometries (see the K_I^* values on a certain row of Table 5.2), it can be deduced that they are similar to one another when the relative crack depth is not too large. Therefore, the boundary effects seem to be negligible for small cracks embedded in a given stress field, while boundary effects become significant for large values of the relative crack depth.

Pommier et al. [113] apply their set of equations for the semi-infinite body (cf. Section 5.3.3) to “mechanically short” cracks in a cylindrical axle. Härkegård and Huth [135] employ these equations of [113] for cracks emanating from the quarter-circular transition of a T-joint and find experimental data to be consistent with the calculated results (cf. Chapter 9). For “relatively small” cracks Carpinteri et al. [126] apply their solution for the finite thickness plate to the T-joint of [135].

Thus, the application of engineering-code stress intensity factor solutions that consider un-notched geometries to fatigue crack growth calculation from notches may be acceptable, especially for shallow notches and for low relative crack depths, a/t .

Table 5.2: Dimensionless mode I stress intensity factor $K_I^* = K_I/\sigma_0\sqrt{\pi a}$ at deepest point, A, and surface (or near-surface) point, C (or B), of a semi-elliptical surface crack (cf. Figure 5.7) for different structural components under approximately the same uniform opening stress field.

Reference			[102]	[103]	[105]	[106]	[120, 122]	[113]
Geometry			Finite plate	Finite plate	Finite plate	Shaft	Thin/thick pipe	Semi-infinite body
$\xi = 0.1$	$\alpha = 0.2$	A	1.075	1.131	1.095	-	0.873/0.942	-
		B or C	0.531	0.595	0.545	-	0.542/0.564	-
	$\alpha = 0.5$	A	0.902	0.886	0.927	0.908	0.755/0.815	0.877
		B or C	0.704	0.695	0.717	-	0.588/0.633	0.727
	$\alpha = 1.0$	A	0.664	0.666	0.691	0.676	0.554/0.623	0.659
		B or C	0.733	0.706	0.729	-	0.601/0.640	0.753
$\xi = 0.2$	$\alpha = 0.2$	A	1.123	1.097	1.186	-	1.035/1.074	-
		B or C	0.559	0.616	0.561	-	0.607/0.615	-
	$\alpha = 0.5$	A	0.920	0.898	1.019	0.994	0.852/0.889	0.877
		B or C	0.725	0.708	0.732	-	0.670/0.689	0.727
	$\alpha = 1.0$	A	0.668	0.667	0.812	0.723	0.635/0.654	0.659
		B or C	0.744	0.711	0.732	-	0.660/0.680	0.753
$\xi = 0.5$	$\alpha = 0.2$	A	1.431	1.415	1.763	-	1.540/1.603	-
		B or C	0.760	0.751	0.720	-	0.831/0.764	-
	$\alpha = 0.5$	A	1.029	0.989	1.636	-	1.018/1.157	0.877
		B or C	0.864	0.806	0.861	-	0.797/0.857	0.727
	$\alpha = 1.0$	A	0.691	0.688	1.662	-	0.678/0.747	0.659
		B or C	0.820	0.752	0.761	-	0.699/0.782	0.753
$\xi = 0.8$	$\alpha = 0.2$	A	1.885	2.291	2.443	-	2.278/2.481	-
		B or C	1.116	-	1.200	-	1.262/0.929	-
	$\alpha = 0.5$	A	1.161	1.314	2.683	-	1.174/1.560	0.877
		B or C	1.087	-	1.201	-	1.001/1.091	0.727
	$\alpha = 1.0$	A	0.718	0.788	3.178	-	0.717/0.852	0.659
		B or C	0.950	-	0.841	-	0.782/0.919	0.753

Chapter 6

Shape Optimisation

6.1 Introduction

Failure due to fatigue loading in notched engineering structures generally occurs in areas of stress concentration. Fatigue strength is sensitive to the size of amplitude and mean (surface) stresses. Modifications of the component shape at areas of stress concentration may lower the elevated stress level, thus improving the fatigue properties of the mechanical component.

The basic concept of structural optimisation refers to size, topology and shape. Size optimisation determines optimum section properties, such as thickness or diameter. Topology optimisation allows the introduction of holes in structures and is generally applied to problems that focus on savings in weight and improved structural characteristics. In shape optimisation only the boundary shape of a two- or three-dimensional structural component is investigated.

This chapter is addressed to the practical application of shape optimisation to the Francis runner fatigue problem (cf. [136]). Shape optimisation theory and methods that were employed in order to improve the design of notches are presented with no claim for completeness whatsoever.

Two representative areas of the quarter-circular transition between the blade and the band or crown of a Francis turbine runner are subject of investigation. As mentioned before, these areas are the runner's two locations of highest local stress amplitudes due to stress concentration and therewith the most critical locations for fatigue. One area is the wide-stretched *T-joint (2D) transition* itself. This T-joint geometry finally merges with the leading and the trailing edge where it forms the second area considered: the *trailing edge (3D) transition* (cf. Section 3.4).

In general, a decrease in stress concentration is gained by a smoother design of the geometric discontinuity such as increasing the transition radius of a shoulder fillet. Modifications of an insufficient part of the shape may easily generate new, even more severe stress concentrations in direct vicinity to the optimised area. The optimisation target is rather to stress the material equally in the complete area of elevated stresses with the aim of avoiding unnecessary high stresses in one region while material elsewhere lies fallow.

This approach is in analogy with the growth behaviour of biological structures where material is enforced or added to regions of high stress and removed where the stresses are low. Such behaviour has been found e. g. for bone material in contact with implants. Another example for this growth behaviour is the hyperbolic Y-junction shape of tree trunk

forks.

The conclusion is that the most optimal designed structural shape shows a completely constant stress distribution at the lowest possible stress value when loaded. This finding of Baud [137] from 1934 was substantiated by Neuber [138] and comprises the conclusion of Schnack [139] from 1979, that after successful optimisation the constant tangential stress value has to be the largest stress to be found on the optimised shape.

As this ideal shape rarely exists for technical solutions, the application of shape optimisation to engineering problems has the aim to maximise the area of constant tangential stress within given technical and economical limits.

Shape Optimisation and Fatigue in the Literature

In order to find the notch geometry that implies the lowest stress concentration, shape optimisation has been applied in numerous publications of the last decades. Already in 1941, Lehr [44] describes the optimum shape for hollow crankshafts. The 1955 publication of Lansard [140] presents fillets without stress concentration. In 1962, Heywood [141] published his work about designing against fatigue. In tests for Rolls Royce aircraft engines he found out that an optimal fillet in the region of stress concentration significantly increases the life of mechanical engineering structures. He successfully applied this concept to aircraft engines and verified the results by photo-elastic experiments. Around 1970 Neuber, who made major contributions to the research on the stress concentration factor (cf. Chapter 2) proposed analytical solution methods for shape optimisation of notched flat bars [138, 142].

Schmit [143] proposed a general approach to structural optimisation and non-linear mathematical programming in 1960. Francavilla et al. [144] solved a fillet shape optimisation problem to minimise stress concentration by defining the nodal co-ordinates of the discrete finite element model as design variables in 1975. As in the early 1980s computational power was still a limiting factor in three-dimensional analysis, Schnack [145] developed a gradient-free algorithm that controlled shape optimisation calculations and minimised stress concentrations. In 1990, Radaj and Zhang [146] introduced a multiparameter design optimisation with respect to stress concentration. In the same year, Mattheck and Burkhardt [147] state that it is possible to design notches without notch stresses employing a biological growth FE method.

Schnack and Weigl [148] differentiate between the minimisation of maximum stresses, which they call “static shape optimisation” and a “dynamical shape optimisation” which considers a time-dependent behaviour of the shape of structures under fatigue loading. In their two-level loading experiments with photo-elastic specimens, they report non-linear material behaviour at different points along the “statically” optimised shape after 15 000 load cycles. However, they state that

“The differences between the classical static optimization and the dynamical optimization are really very small; the difference can be found in the oscillation of the stress functions, and this is probably due to the local effects (...) on the micro-level.”

Obviously, these local effects strongly depend on loading conditions and material properties. Since this approach has not been followed up by other authors since it was published in

2002, the “static” procedure of minimising the notch stresses still seems to be state-of-the-art in shape optimisation of structures under fatigue loading.

Although it has proved to have large beneficial effect to the fatigue phenomenon, the challenge of employing shape optimisation and to realise the resulting non-trivial geometries is rarely met. Applications reported are most frequently connected to the automotive and aviation industry.

6.2 Basic Theory

In mathematical terms, shape optimisation of continuum structures improves a given topology by minimising an *objective* or *target function* that is subjected to certain constraints on geometry and structural responses such as stress, displacements and natural frequencies. All functions are related to *design variables* that represent co-ordinates of some points in the structure boundary called *design nodes*.

Two kinds of models have to be considered [137]: the *analysis model*, as represented by the finite element model, and the parameterised geometric model of the variable structure which is termed the *design model*. This design model consists of design elements [149] which may be defined by lines or curves of almost any character. So, even complicated boundary shapes can be defined and generated with the help of only a few points on the boundary, the so-called *key points*. Some key points are *design nodes*, which means that their position is re-considered under the optimisation process. Thereby the shape of the design model is modified. Other expressions frequently used for design nodes are “master nodes”, “control nodes”, “control points” and “master points”.

6.2.1 Steps in Shape Optimisation

Shape optimisation is processed in the following steps (cf. Figure 6.1):

1. Prior to the optimisation, the geometry of the structure under investigation has to be defined. Key points are set up to span the structure boundaries. These structure boundaries may be modelled by means of lines, curves or splines. By moving some of the key points at least one structure boundary will be modified under the optimisation process. Some of the co-ordinates of the moving design nodes are chosen to be the design variables. In this manner the design variables directly affect the shape alteration. Dependencies between the design variables may be established.
2. An automatic mesh generator is used to create the finite element model. Then, a finite element analysis is carried out and the displacements and stresses are evaluated.
3. If a gradient-based optimiser is used, the sensitivities of the constraints and the objective function are computed to small changes of the design variables. For this, either the finite difference or the semi-analytical method may be employed.
4. The design variables and therewith the shape of the structure are being optimised. If the convergence criteria for the optimisation algorithm are satisfied, the optimum solution has been found and the process is terminated. Else, a new geometry is defined and the procedure is repeated from step 2.

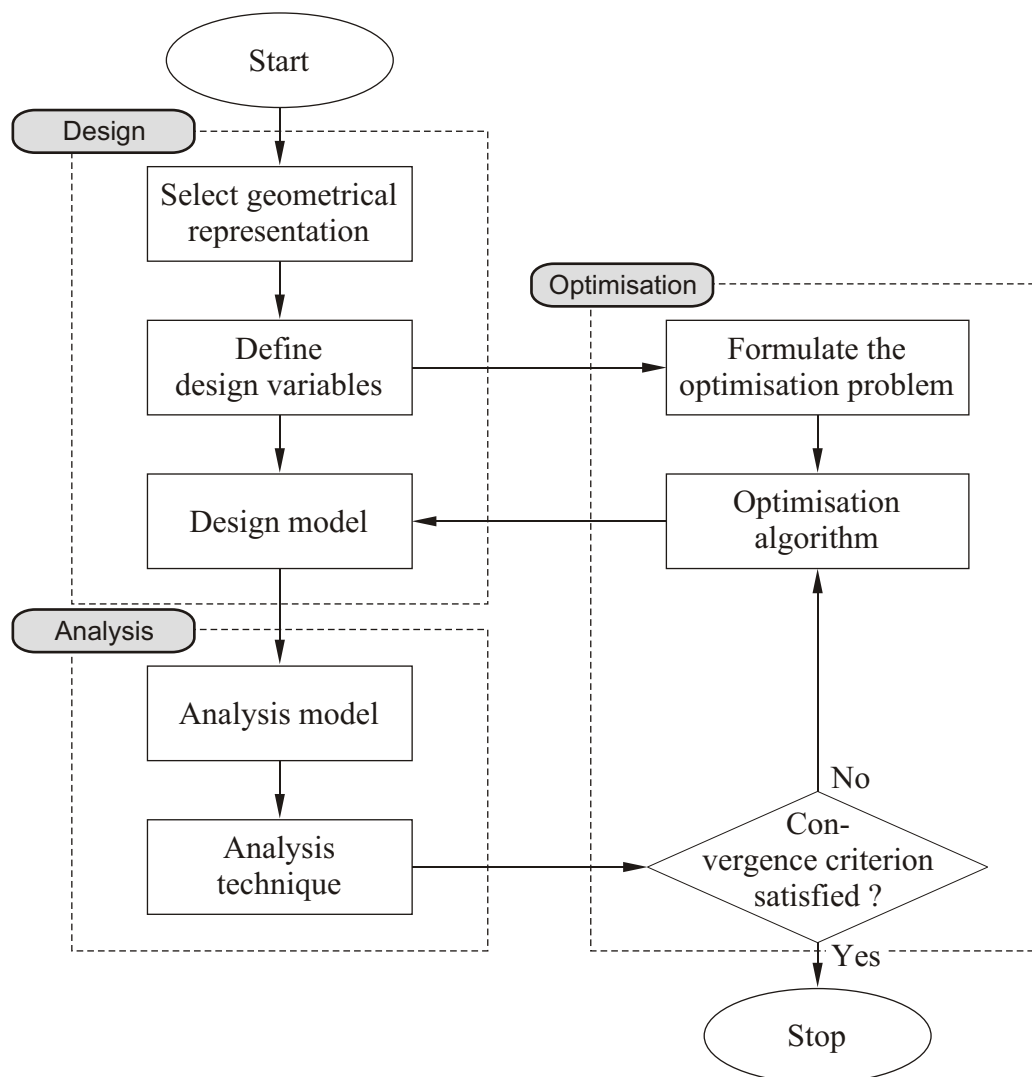


Figure 6.1: The general process of shape optimisation.

6.2.2 Gradient based Optimisation

Gradient based optimisation procedures are computationally expensive due to the sensitivity analysis step. The calculation of the sensitivity coefficients follows the application of a relatively small perturbation to each design variable. Several techniques have been developed. The discrete methods for sensitivity analysis may be classified as follows [150]:

- *Global finite difference method*: A full finite element analysis has to be performed for each design variable, the accuracy of the method depends strongly on the value of the perturbation of the design variables.
- *Semi-analytical method*: The stiffness matrix of the initial finite element solution is retained during the computation of the sensitivities. This provides an improved efficiency over the finite difference method by a relatively small increase in the algorithmic complexity. The accuracy problem involved with the numerical differentiation can be overcome by using the *exact semi-analytical method*.

- *Analytical method*: The finite element equations, the objective and constraint functions are differentiated analytically.

6.2.3 Surface Generation by B-splines

One task in the engineering design of machines, tools and vehicles is the generation of smooth surfaces from a number of nodes or vertices placed through measurement or calculation. In order to connect these vertices by a smooth surface curve, an n -th order polynomial interpolation

$$M_n(x) = a_0 \cdot x^n + a_1 \cdot x^{n-1} + a_2 \cdot x^{n-2} + \dots + a_{n-1} \cdot x + a_n \quad (6.1)$$

may be employed, where the coefficient $a_0 \neq 0$. However, a polynomial order of higher than three easily results in a curve of unacceptable high waviness already when applied to surface curves of only average complexity. On the other hand, polynomials of order less than the number of nodes involved might lack the capability to reach and represent every single node.

It is shown in the literature [149, 151] that in shape optimisation, B-spline curves are well suited to the definition of design elements. Complex geometries can be described in a very compact way by a small set of design variables and a few design elements. Splines represent the shape of an elastic beam in its state of lowest bending energy as it touches points in arbitrary locations in 3D space. Thus, the spline is the continuous connection between chosen points that keeps the minimal bending radius all along the curve at its largest value possible. Since we in general have a decrease in stress concentration for larger notch radii, a spline-modelled design boundary seems to be the most adequate design element for shapes of low stress concentration. The following mathematical definition of splines and B-splines was taken from [152].

Splines

For centuries designers and engineers employed physical splines to draw smooth surface lines [153]. Small weights were attached at the vertices for proper adjustment of the thin wooden or, more recently, plastic beams on the drawing board. In the course of the development of computer aided design (CAD), a mathematical spline definition became necessary. For small deflections, $y' \ll 1$, the bending strain energy

$$W = 0.5 \int \frac{M^2(x)}{EI} y'' dx \quad (6.2)$$

for the spline in Figure 6.2 is at its minimum value. This problem is frequently solved for third-order polynomials that define curve segments of cubic character between the vertices P_j and P_{j+1} , for $j = 0, 1, 2, \dots, n$. The interpolating spline function of order k consists of stepwise mounted k -th order polynomials. The spline function is $(k-1)$ times continuously differentiable and touches all the vertices.

The first derivative is the slope of the curve. If the slope is continuous, the curve has no angles, that is, no sudden changes in direction. The second derivative is related to the radius of curvature.

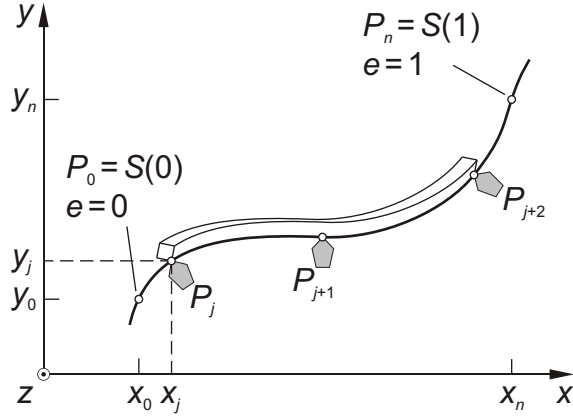


Figure 6.2: Physical spline and mathematical analogue (after Dubbel [152]).

Cubic splines ($k=3$) are preferred as they are the splines of the lowest possible order k featuring an inflection point. In this case, the polynomial takes the form

$$\mathbf{S}(e) = \mathbf{a}_3 \cdot e^3 + \mathbf{a}_2 \cdot e^2 + \mathbf{a}_1 \cdot e + \mathbf{a}_0 = (x(e), y(e), z(e))^T \quad (6.3)$$

The four coefficients $\mathbf{a}_0 \dots \mathbf{a}_3$ are vectors $\mathbf{a}_j = (a_{jx}, a_{jy}, a_{jz})^T$ which can be obtained from the co-ordinates of two points and the respective derivatives. Consequently, any further stepwise adjoined curve part will connect to $\mathbf{S}(e)$ continuously differentiable [154].

With the boundary conditions

$$\begin{aligned} \mathbf{S}(0) &= \mathbf{P}_0 = (x_0, y_0, z_0)^T = && \mathbf{a}_0, \\ \mathbf{S}(1) &= \mathbf{P}_1 = (x_1, y_1, z_1)^T = && \mathbf{a}_3 + \mathbf{a}_2 + \mathbf{a}_1 + \mathbf{a}_0, \\ \mathbf{S}'(0) &= \mathbf{P}'_0 = (x'_0, y'_0, z'_0)^T = && \mathbf{a}_1, \\ \mathbf{S}'(1) &= \mathbf{P}'_1 = (x'_1, y'_1, z'_1)^T = && 3\mathbf{a}_3 + 2\mathbf{a}_2 + \mathbf{a}_1. \end{aligned} \quad (6.4)$$

becomes

$$\mathbf{a}_0 = \mathbf{P}_0, \mathbf{a}_1 = \mathbf{P}'_0, \mathbf{a}_2 = -3\mathbf{P}_0 - 3\mathbf{P}_1 - 2\mathbf{P}'_0 - \mathbf{P}'_1, \mathbf{a}_3 = 2\mathbf{P}_0 - 2\mathbf{P}_1 + \mathbf{P}'_0 + \mathbf{P}'_1$$

and finally

$$\mathbf{S}(e) = \mathbf{P}_0(2t^3 - 3t^2 + 1) + \mathbf{P}_1(-2t^3 + 3t^2) + \mathbf{P}'_0(t^3 - 2t^2 + t) + \mathbf{P}'_1(t^3 - t^2). \quad (6.5)$$

B-splines

For **B**-spline curves only piecewise defined polynomials, the so-called **B**asis-splines (“basis-functions” and “blending-functions” are other common expressions) bridge between the vertices. Such a basis function $N_j^k(g)$ is $(k-2)$ times continuously differentiable and covers the interval $[j; j+k]$. The parameter g interval is now divided into an integer number of segments $g \in [j; j+1] = [g_j; g_{j+1}]$. The expression for the B-spline polynomial becomes

$$\mathbf{S}(g) = \sum_{j=0}^n P_j \cdot S_j^k(g) \quad (6.6)$$

B-spline curves are described by basis-splines in a polygon showing $n + 1$ corners P_j . Higher orders of the polygon result in a more rigid curve behaviour. In difference to the “common” spline described above, B-splines feature a more individual curve design at the polygon corners with less influence of the local design to the overall curve shape (cf. [152]).

B-spline curves form the basis of a popular approximation technique for curves and surfaces and are frequently implemented in modern CAD software and numerical analysis preprocessors. Bèzier curves and surfaces share the mathematical expression, Equation (6.6), of B-spline curves and surfaces but employ so-called “Bernstein-functions” as basis-functions instead.

In the following, the two Francis runner areas that are most critical to fatigue will be re-designed employing B-splines.

6.3 Optimisation of the T-joint Transition

Engineering solutions of shape optimisation are connected to given technical and economical limits. For any of the modifications considered under shape optimisation of the T-joint transition between blade (Y^* -axis) and ring or crown (X^* -axis) of the Francis runner it was an essential requirement to leave the hydromechanical properties of the runner untouched to the greatest possible extent. Turbulent flow is unlikely to be generated as long as the new design was continuously smooth and is applied to the entire T-joint transition, from the leading edge down to the trailing edge.

As explained in Chapter 3, far from the trailing edge the T-joint experiences cyclic nominal bending loading due to hydraulic forces that act on the Francis runner blade. The resulting bending stress concentration will be lowered in the following shape optimisation process.

6.3.1 Optimisation Process

The originally circular shape of the T-joint transition was modelled by a B-spline in the design model. The B-spline was defined by n design nodes D_j with $j \in [1, 2, \dots, n]$. The origin of the D_j co-ordinate system ($X^*; Y^*$) coincides with the virtual sharp fillet corner between the blade and ring or crown surface lines. In order to implement a smooth transition from all B-spline shapes applied, the spline end slopes in D_1 and D_n go parallel with the flanking plane surfaces.

The wide range of possible variations of the spline character and length was minimised in a first optimisation process. Iterative improvements of the shape were carried out manually to approximate what might be an improved design. At this, the effect of random changes of design node positions and inter-nodal dependencies to finite element analysis (FEA) stress results was investigated. Soon it turned out that the expansion of the transition area somehow had to be constrained since large-scale shape changes would be suggested by an automated optimisation routine.

Figure 6.3 shows the four different transition shapes considered. In case A a large-scale change of the shape is allowed. Case B unconventionally extends the transition shape at the expense of the runner ring. Cases C and D represent more realisable approaches as the length of the B-spline is kept small. The corresponding co-ordinates of the design nodes, D , are given in Table 6.1. All D movements are confined to follow straight lines: in case A,

Table 6.1: 2D shape optimisation strategy.

Shape optimisation approach case	Number of design nodes n	Design nodes D_j co-ordinates $X^*; Y^*$	
		$j = 1$	$j = n$
A	4	15;0	0;≤ 39
B	6	15;0	0;15
C	2	≤ 15;0	0;15
D	2	≤ 15;0	0;18
Not optimised	(2)	15;0	0;15

Table 6.2: Shape optimisation approaches. Stress concentration in the final shapes.

Optimisation shape approach case	Stress concentration factor, K_t
A	1.02
B	1.12
C	1.16
D	1.12
Not optimised, circular	1.32

D_n moves on Y^* , whereas in cases C and D, the only movement performed is D_1 sliding in X^* direction. Furthermore, all inner D_j for $1 < j < n$ move in radial direction to the original quarter-circular transition.

Then, for the automated analysis, a gradient-based optimisation procedure implemented in the FE code ANSYS was applied. The procedure implies automated re-meshing of the analysis model. As in the first manual optimisation process, the objective function was to minimise the largest principal stress, σ_1 , on the B-spline design boundary.

6.3.2 Results

The resulting stress concentration factors after the four different optimisation strategies are given in Table 6.2. Figures 6.4–6.7 present plots of the calculated maximum principal stresses, the FE mesh and the final shapes of the optimised design boundaries A–D. Figure 6.8 shows the stress plot of the circular shape for comparison with the standard solution.

Figure 6.9 reveals that the stress slopes of the different design solutions coincide at $x/t_1 = 0.075$. Here, x is the distance from the location of highest stress concentration in negative X^* -direction. To what extent these stress gradient slopes influence fatigue crack growth is a matter of discussion in Chapter 9.

The large-scale shape change of optimisation approach case A shows the most homogenous stress distribution. The remaining stress concentration $K_t = 1.022$ is of only rudimentary character.

The B-spline length of shape approach B is second after the spline in approach A. However, the relatively low stress concentration of $K_t = 1.12$ is the same as in approach D,

which shows a B-spline length that is even less than that of the quarter-circle of the standard transition.

Shape approach cases C with $K_t = 1.16$ and D base on the most simple design boundary definitions regarded. They realise the most effective minimisation of stress concentration if a shorter B-spline length is considered to be advantageous. The fact that in these two cases only external B-spline design nodes were employed is in accordance with the theoretical assumptions on the B-spline shape made above. An expression for the optimisation efficiency as a function of the transition curve length and fatigue life is proposed in Table 9.2 on page 87.

6.4 Optimisation of the Trailing Edge Transition

In the same way as for the T-joint transition, the primary requirement to avert the development of turbulent water flow due to shape optimisation applies now for the trailing edge transition.

As the T-joint geometry meets the trailing edge at the end of the blade, a concave-convex geometry is formed. Tensile fatigue loading is considered to load the resulting convex-concave “trailing edge (3D) transition” (cf. Chapter 3). Due to the symmetry of loading and geometry conditions prevailing, the following simplification shall be established: only one quarter-cylindrical shoulder fillet transition geometry shall be considered from now on.

The standard circular-shaped transition at the trailing edge is defined by two radii (cf. Figures 3.9–3.11). A systematic series of FE stress calculations presented in Section 3.4.2 reveals the transition radius, R , to be clearly the more decisive parameter regarding stress concentration, compared to the influence of the blade edge radius, r .

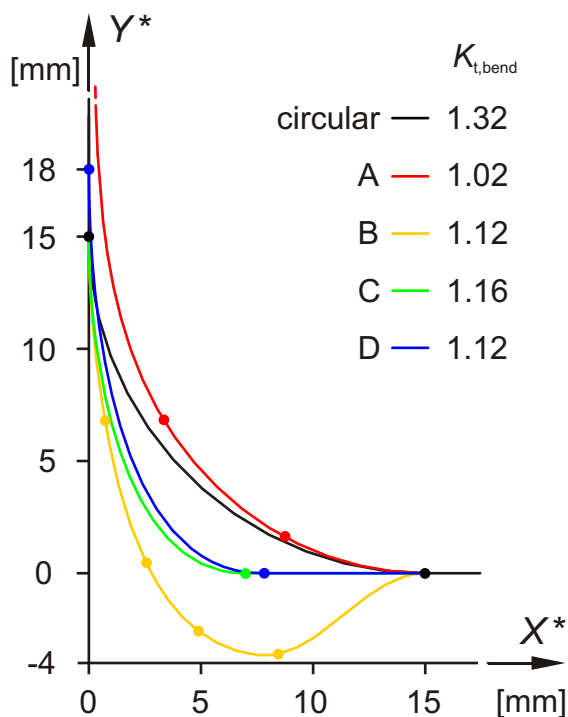


Figure 6.3: Stress concentration in T-joint optimisation approaches.

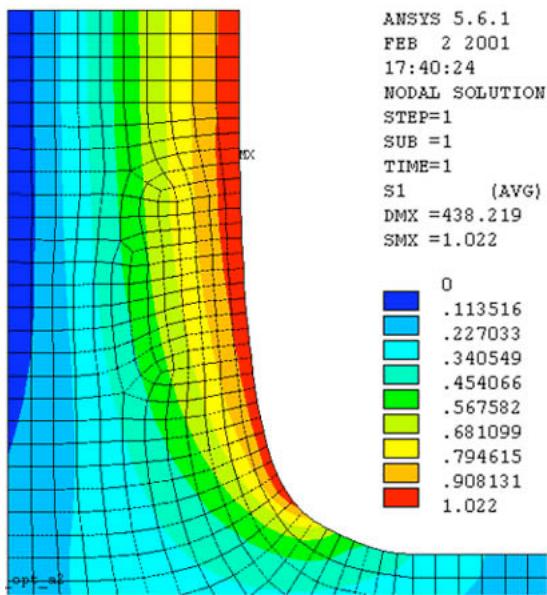


Figure 6.4: Optimised T-joint shape A. FE mesh and maximum principal stress, σ_1 .

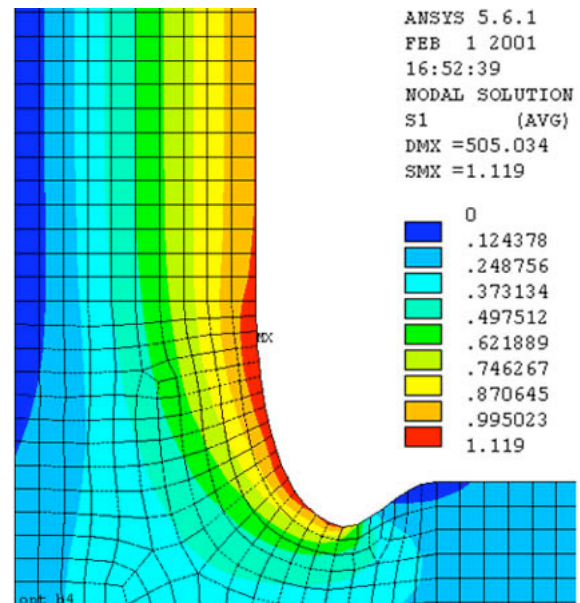


Figure 6.5: Optimised T-joint shape B. FE mesh and maximum principal stress, σ_1 .

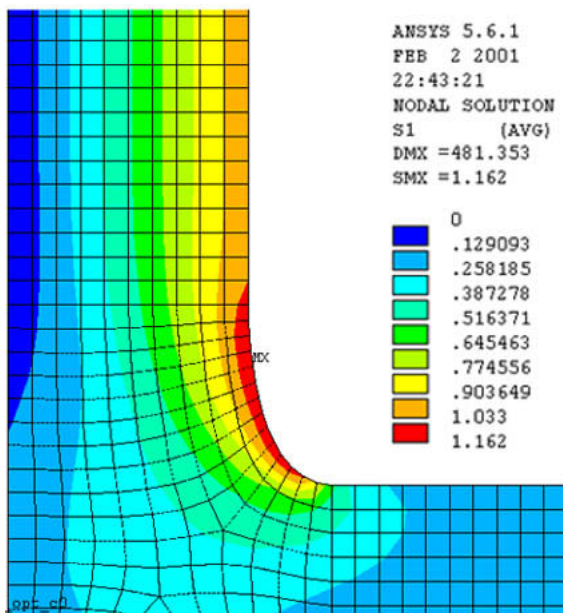


Figure 6.6: Optimised T-joint shape C. FE mesh and maximum principal stress, σ_1 .

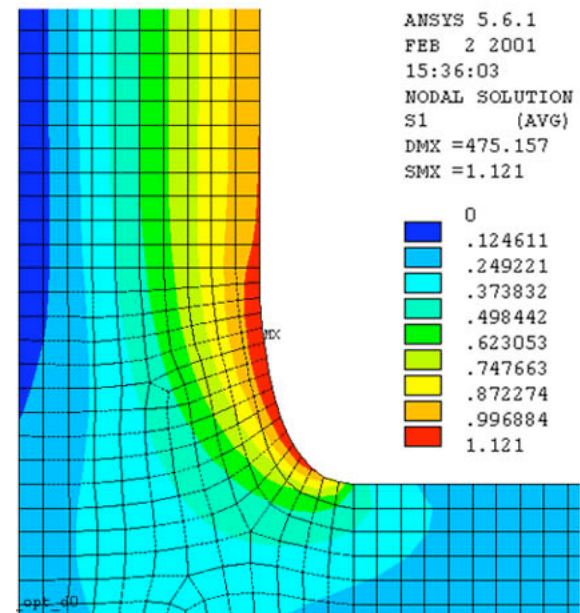


Figure 6.7: Optimised T-joint shape D. FE mesh and maximum principal stress, σ_1 .

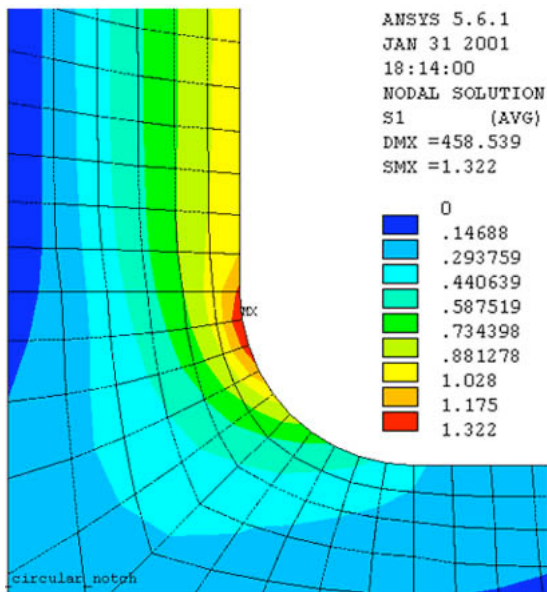


Figure 6.8: Standard circular T-joint shape. FE mesh and maximum principal stress, σ_1 .

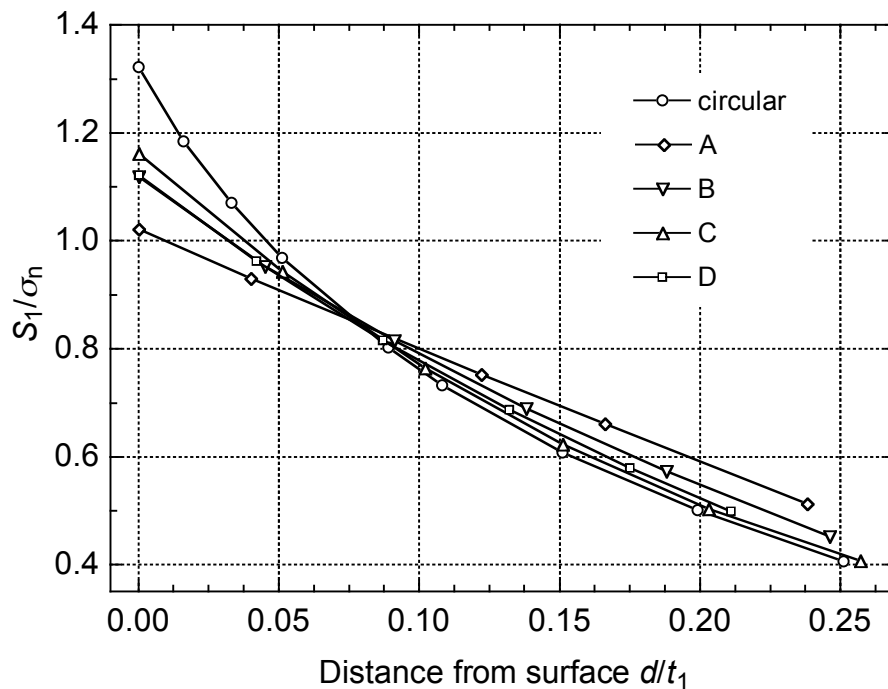


Figure 6.9: Standard circular T-joint shape. Stress gradients at the locations of largest principal stress, σ_1 .

6.4.1 Optimisation Process

In the first step of shape optimisation the trailing edge transition design model was established with the help of B-splines. Five B-splines that follow the shape approach D of Section 6.3 build the longitudinal framework base of the standard quarter-cylindrical shoulder fillet. In approach D the transition geometry is extended by 20 % on the “blade” side of stress concentration. Thus, the upper spline co-ordinates were moved from $(\theta; Y = 10; Z = 15)$ to $(\theta; 12; 15)$ in the cylindrical co-ordinate system shown in Figure 6.10.

The transition surface is then rendered by latitudinal quarter-circles that meet each of the five longitudinal splines perpendicularly. These quarter-circles again are modeled by splines. In their two extreme positions, as they connect the five framework splines end design nodes at the upper and lower surface edge, we shall term them “headspline” and “footspline”, respectively, as denoted in Figure 6.10.

All splines employed show fixed end slopes that guarantee a smooth transition from the curvature to the flanking surfaces, as described above in Section 6.3 for the T-joint transition design model. Since the series of FE calculations presented in Section 3.4.2 revealed that modifications of the blade edge radius, r , have only a minor effect on the stress concentration, the upper design nodes remain untouched on their slightly elevated positions ($Y = 12$) on the blade edge further on. Then, the θ -co-ordinates of the five longitudinal basic framework splines were arranged to $\theta = 0, 21, 50, 76$ and 90 degrees. Now, alternating designs of the 3D transition could be easily controlled by five design variables, which are the footspline design nodes’ radial Z -co-ordinates. Nodal movements are denoted by the arrows in Figure 6.10.

6.4.2 Results

First, the footspline design nodes were allowed to move independently from each other. Design limits individually chosen for each design node provided for reasonable design alterations. The somewhat sturdy shape defined by the red footspline in Figure 6.11 yields a *local* minimum of stress concentration. Here, the stress concentration factor, K_t , is lowered to 1.36 from 1.68 in the standard circular transition. Figure 6.13 presents the plot of the calculated maximum principal stress, the FE mesh and the shape of the optimised “red” design. Figure 6.12 shows the stress plot of the circular shape for comparison with the standard solution.

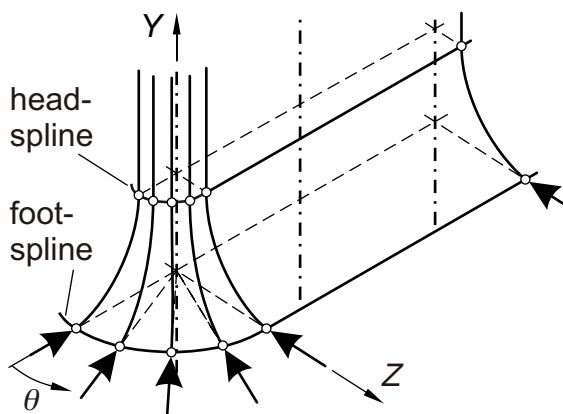


Figure 6.10: Trailing edge transition shape optimisation strategy.

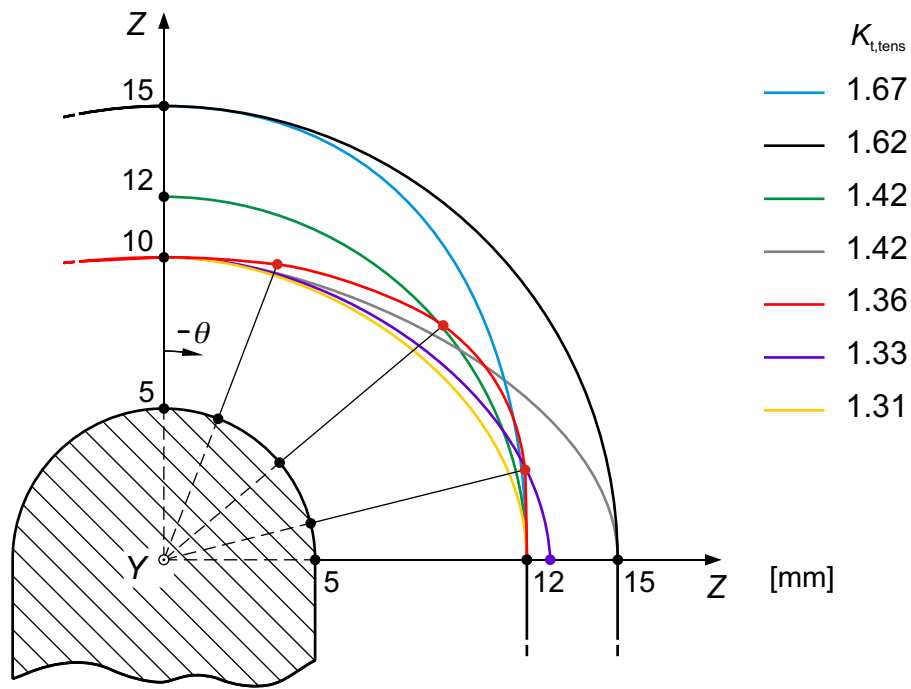


Figure 6.11: Stress concentration in trailing edge optimisation approaches.

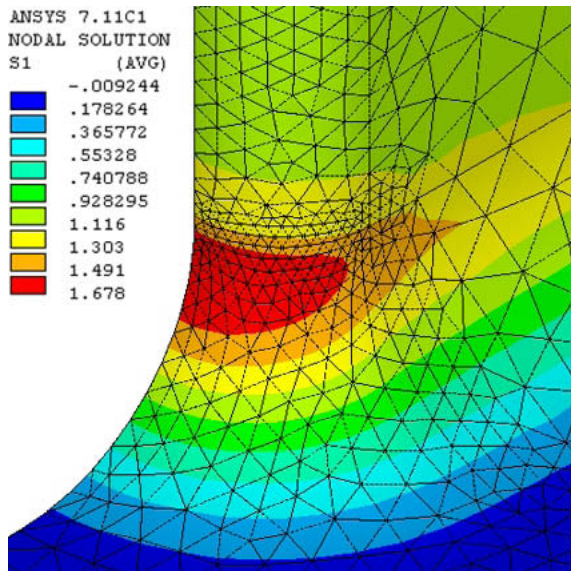


Figure 6.12: Circular trailing edge transition shape. FE mesh and maximum principal stress, σ_1 .

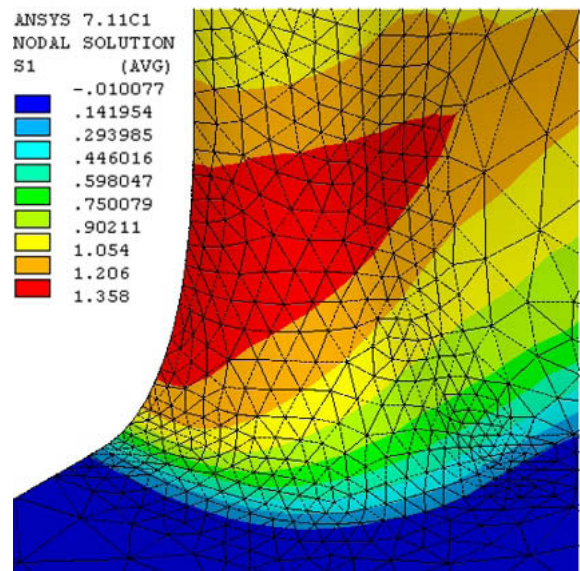


Figure 6.13: Optimised trailing edge transition shape. FE mesh and maximum principal stress, σ_1 .

In Figure 6.11 the shape of the initial 3D transition prior to any shape modifications is represented by the circular black footspline. The respective K_t value of 1.62 is slightly lower than $K_t = 1.68$ which is for the standard transition defined by two radii, R and r . This change in stress concentration is due to the elevated position of the headspline nodes at $Y = 18$ mm according to the implemented shape approach D (cf. Section 6.3).

For the lowest stress concentration found, the foot-spline follows the shape of an ellipse. Here, only two design variables are necessary as the elliptical shape is completely defined by the length of the ellipse's two semi-axes, a and b . The positions of the inner design nodes of the footspline are derived from the equation of the ellipse

$$Z^2(\theta) \left(\frac{\sin^2 \theta}{a^2} + \frac{\cos^2 \theta}{b^2} \right) = 1 \quad . \quad (6.7)$$

The absolute design optimum found in the yellow footspline ellipse lowers K_t from 1.68 in the standard circular transition down to 1.31.

The 2D and 3D transition geometries meet at $\theta = 90^\circ$. A practical solution that smoothly connects the 3D footspline to the 2D transition design optimum found in the previous chapter is represented by the violet footspline. Here, at $(X^* = 7.77 \text{ mm}) \equiv (Z = 12.77 \text{ mm})$, the K_t values are 1.12 and 1.33 for the 2D and 3D transition, respectively. The other way round, in the case of the 2D transition design joining the (yellow) 3D transition design optimum in $(Z = 12 \text{ mm}) \equiv (X^* = 7 \text{ mm})$, the stress concentration factors K_t become 1.19 and 1.31 for the 2D and 3D transition, respectively.

Chapter 7

Fatigue Testing

Two categories of fatigue specimens have been considered. The *2D* bending load specimen describes the T-joint between Francis runner blade and ring or crown, far from the trailing edge. The geometrical shape of the T-joint meeting the trailing edge is represented in the *3D* specimen for tensile fatigue loading.

In addition to the 2D and 3D specimens showing (quarter-)circular shape of the transitions as it is specified in General Electric Energy (GEE) standards, a series of shape optimised specimens for each of the two categories (2D and 3D) has been designed and tested. Test specimen specifications are given in Table 7.1 and in Figures 7.3 and 7.11. Test results are presented in Chapter 8 on the “local approach” to fatigue.

Load levels derived from present fatigue data were chosen to obtain N_f values between 10^4 and $2 \cdot 10^5$. The use of the resulting statistical parameters might be open to question. Nevertheless, this proceeding provides fatigue data of the most interesting N_f range seen from a practical hydropower-engineering point of view (cf. Section 3.3.1). The disregarded range of fatigue life remains to be verified by subsequent experimental testing.

Beach Marking Procedure

In order to visualise the location of the crack front of propagating fatigue cracks for subsequent fatigue crack growth calculation, the so-called “beach marking” technique has been employed. At this, a deliberate reduction of the crack growth rate leads to a different appearance of the crack surface striations that are generated cycle-by-cycle at the crack tip, as described in Chapter 2. After a certain period, which may be defined by voltage fluctuation under monitoring with “potential drop” equipment or simply by a number of load cycles, the intrinsic fatigue loading is resumed. According to Schwarze and Schubert [155], the critical parameters for beach mark visibility are:

- cyclic stress intensity range ΔK ,
- frequency f (for Ni-alloys at elevated temperatures),
- mean stress σ_m ,
- stress ratio R .

Steel at room temperature is considered to be insensitive to fatigue loading frequencies 0–1000 Hz [156]. The influence of the beach mark cycles on the intrinsic load cycles has to be minimised.

Table 7.1: Experimental fatigue testing. Specimen properties and loading conditions.

Specimen		T-joint – 2D	Trailing edge – 3D
Material			
Symbol (DIN 17440)		X4CrNiMo 16-5	34CrNiMo 6
Standard Number		1.4418	1.6582
Product Form		quenched and tempered	quenched and tempered
Heat Treatment		hot rolled plate material	hot rolled bar stock
tensile data			
Yield strength	$R_{p0.2}$	850 MPa	680 MPa
Ultimate tensile strength	R_m	945 MPa	860 MPa
FCG data [K] = MPa \sqrt{m} , $R = 0.1$			
Paris factor	C	$6.67 \cdot 10^{-13}$	
Paris exponent	m	3.22	
Number of test specimens		7 standard, 7 optimised	4 standard, 4 optimised
Stress concentration factor	K_t	1.32 , 1.12	1.68 , 1.36
Fatigue loading			
Min. load / max. load	R_L	0.1	0.1
Nom. elastic stress range	$\Delta\sigma_n$	765 and 820 MPa	500 and 550 MPa
Frequency	f	3 Hz	1.5–2.5 Hz
Temperature	T	23 °C	23 °C
Humidity (rel.)		50 %	50 %

7.1 T-joint Test

The geometry investigated in Section 3.4.1 was scaled 1:2 for fatigue testing (cf. Figure 7.3). The optimised design of the T-joint transition (2D) specimen is given by transition shape D (cf. Section 6.3 and Figure 7.2).

7.1.1 Specimen Manufacturing

The specimens were produced according to the standard manufacturing process for commercial turbine runners at the GEE workshop in Sørumsand, Norway. Moreover, CNC milling was employed in order to realise accurate shaping of the welded transition. No undergrinding was visible at the transition between the curvature and the straight blade.

Manufacturing process:

1. Joining of two plates ($t_1 = 20$ mm, $t_2 = 24$ mm) of X4CrNiMo 16-5-1 rolled steel by a double fillet weld. Testing of the weld seam.
2. Machining of the weld seam: CNC milling to obtain the standard quarter-circular $\rho = 7.5$ mm and shape optimised transition geometries of the two test series.
3. Annealing (stress relieving) of the plates at 580 °C.

4. Cutting of the welded plates into T-joint specimens of width $b = 50$ mm. Surface finishing by grinding and polishing.

7.1.2 Fatigue Testing

The thicker member was fixed to the frame of the fatigue-testing machine, as shown in Figure 7.4. A cyclic bending moment was applied to the thinner, cantilever member by a transverse force. The cylinder force, F , (cf. Figure 7.3) which is necessary to induce the nominal surface stress from bending, σ_b , is given by

$$F = \frac{2 \cdot \sigma_b \cdot I_Z}{t \cdot l_F} \quad (7.1)$$

where the specimen thickness, $t_1 = 20.3$ mm, and the specimen width, b , are considered in the geometrical moment of inertia $I_Z = bt_1^3/12$. The width of the specimens varied between 48 and 56 mm.

It has to be mentioned that the single force in Figure 7.3 does not induce a state of pure bending. However, the shear stress, τ_0 , induced by F is less than 2 % of the largest nominal bending stress, σ_b , and may therefore be disregarded.

The mechanical test rig proved to induce reliable stresses in the nominal blade section in similar tests performed by Hallingstad [157] in 1999. In this work, strain gauges returned erroneous data only when attached to the quarter-circular transition. Stress results from strain measurements in the nominal section of the specimen agreed with stress values obtained from load values measured at the hydraulic test cylinder.

In the investigation by Hallingstad [157], fatigue cracks invariably initiated at grinding defects. The initiating defect was frequently situated outside the quarter-circular transition arc and subsequent crack growth took place in a region of pure bending. Consequently, grinding defects have been removed in the present test specimens in agreement with common practice for commercial high-head Francis turbine runners.

In analogy to [157], failure was defined by an increase of the “blade” deflection at F_{\max} , $\Delta u_{X^*}(F_{\max}) = 2$ mm, measured at the point of force application, $l_F = 200$ mm (cf. Figure 7.3). At this condition, surface cracks showed relative crack depths, a/t_1 , between 0.3 and 0.4.

7.1.3 Beach Marking

The growth of fatigue cracks starting at stress concentrations has been monitored. In order to make the position of the crack front visible, the crack surface was altered by temporarily propagating the crack at a lower growth rate, as described above. More precisely, the load sequence consists of two consecutive blocks. The first one is the effective constant amplitude cyclic bending block containing 4–5000 cycles, characterized by $R = 0.1$, $f = 3$ Hz and sinusoidal shape: this fatigue loading produces crack propagation. The second cyclic loading block is the marker block. Here, R of the nominal stresses has been increased from 0.1 to 0.7. With the maximum stress left unchanged, this setup was maintained over 4–5000 cycles of sinusoidal shape. The flaw size grows just a little during this loading block and, therefore, the crack growth can be neglected. For this reason, the number of cycles of the “marker” block is not taken into account when evaluating fatigue life of the specimen in Chapter 9.



Figure 7.1: T-joint specimen. Standard quarter-circular transition.



Figure 7.2: T-joint specimen. Shape optimised transition (case D).

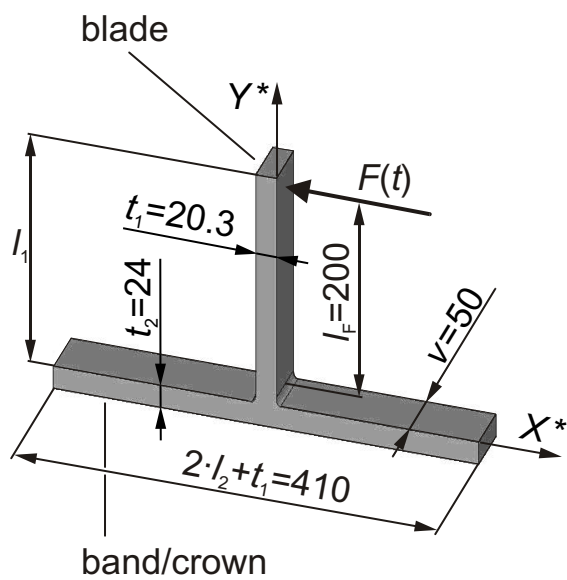


Figure 7.3: T-joint fatigue test specimens. Geometry and loading.



Figure 7.4: T-joint test mounted.

Table 7.2: Data of fatigue crack growth monitored.

Beach mark	Quarter-circular transition specimen 1.7			Shape optimised transition specimen 2.7		
	a	c	N	a	c	N
1	1.57	3.28	23 600	2.45	3.01	90 500
2	2.51	4.24	27 600	3.30	4.20	95 500
3	3.53	6.38	31 600	4.34	5.85	100 500
4	5.13	9.48	35 600	6.00	8.21	105 500

Fatigue cracks were discovered by the application of petroleum spirit to the area of stress concentration. This procedure has proved to track down surface cracks from $2c = 1$ mm in length (cf. Figure 5.6). However, the smallest cracks that were discovered in the 2D test specimens showed a length of 6 mm. It seems possible that some of the monitored surface cracks grew from a sub-surface defect and propagated rapidly as they penetrated the surface (cf. [158]). Another possibility is the coalescence of two or more in-plane cracks.

7.1.4 Results

At the end of experimental tests, beach marks have been identified and measured. The quarter-circular transition of specimen 1.7 (cf. Table C.1) and the shape optimised specimen 2.7 yield the most interesting beach mark results (cf. Figures 7.5 and 7.6) as they show the largest number and smallest dimensions of beach marks created. The respective crack growth data are summarised in Table 7.2: for each of the four beach marks related to specimens 1.7 and 2.7, the crack depth, a , the crack length, c , and the number of load cycles, N , is reported. These data are visualised in Figure 9.12.

As mentioned before, after welding the specimens underwent stress-relieving annealing treatment. Nevertheless, the coarse and inhomogeneous crack surfaces of Figure 7.7 attest to the sustained influence of the welding.

In both the standard quarter-circular and in the shape optimised T-joint specimens tested, all cracks that developed into a dominating fatigue crack initiated at the location of largest stress concentration at the transition. In two of the quarter-circular and in one of the shape optimised specimens, the main fatigue cracks grew as a corner crack from one or both of the specimen edges.

The test results are shown in Figure 7.8. The SN curves are defined by the Basquin Equation (2.1) and are created by means of linear regression curve fit. In this curve fit the sum of the squares of the vertical distances of the result points from the SN curve are minimised.

7.2 Trailing Edge Transition Test

7.2.1 Specimen Manufacturing

The specimens were CNC-milled from 34CrNiMo 6 rolled bar stock and manually polished with emery cloth, all performed by “Ranger Modellbau GmbH” in Neckarsulm, Germany. The specimens show the following specifications:

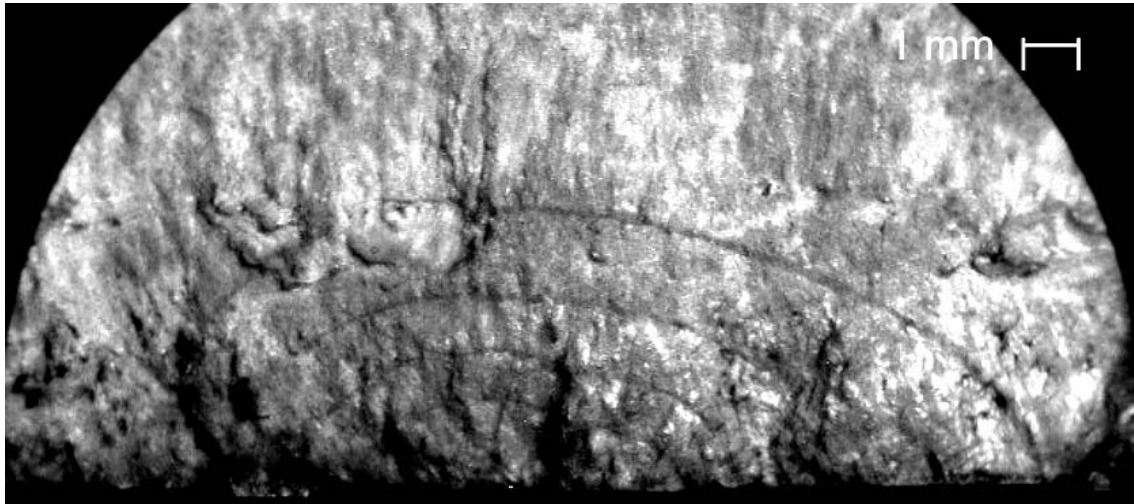


Figure 7.5: Beach marks in standard T-joint specimen 1.7: $\Delta N = 4000$, $N_{\text{BM}} = 4000$.

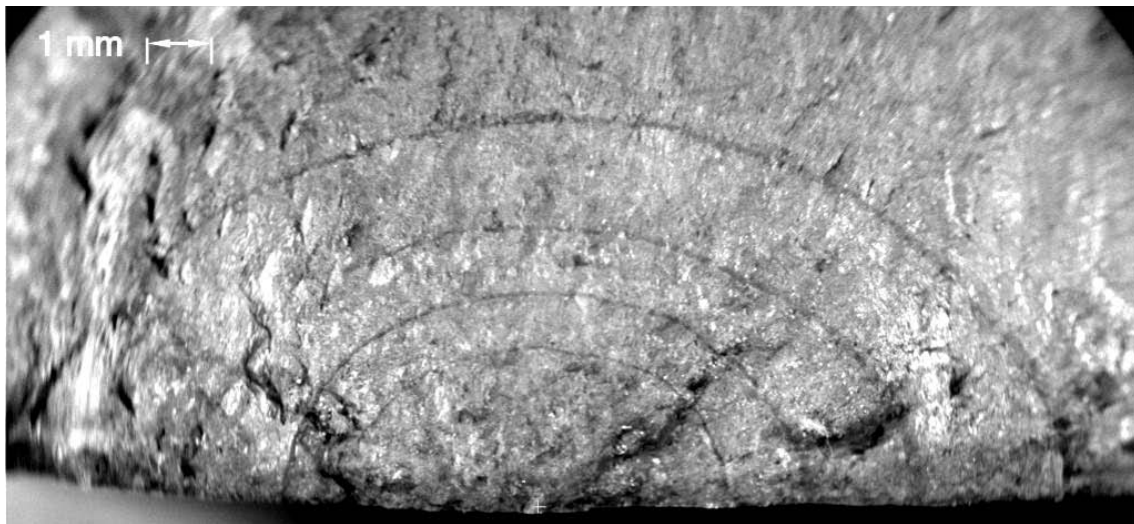


Figure 7.6: Beach marks in optimised T-joint specimen 2.7: $\Delta N = 5000$, $N_{\text{BM}} \geq 5000$.

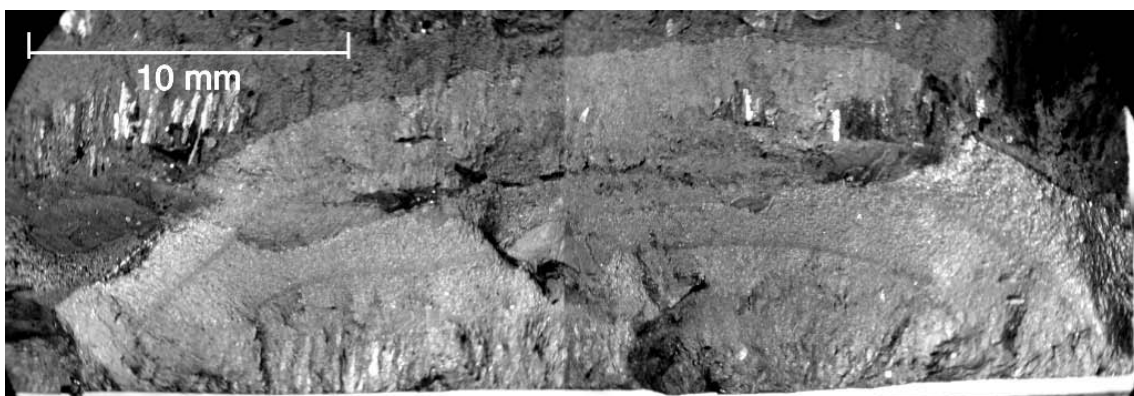


Figure 7.7: T-joint specimen 1.3: coarse and inhomogeneous crack surface in the weld zone (Photograph stitched).

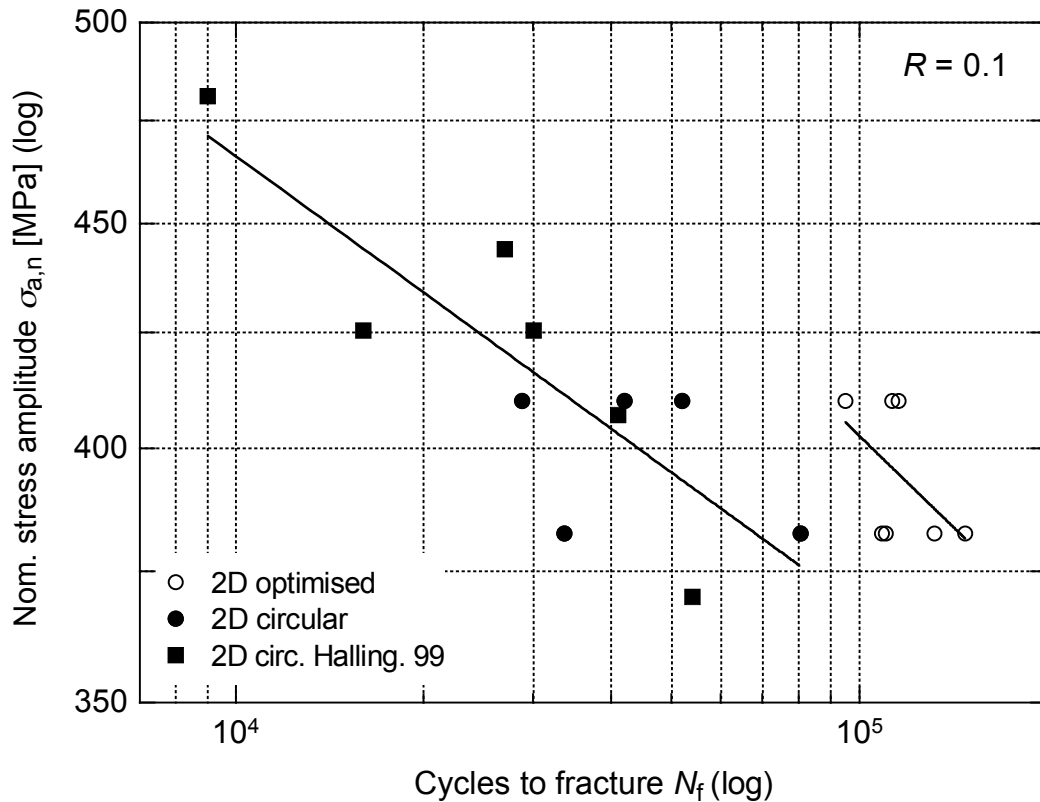


Figure 7.8: SN curve from T-joint specimen fatigue testing.

- Fatigue loading direction and the direction of rolling coincide.
- The design of the specimen showing a circular transition geometry imitates a simplified trailing edge transition of a commercial turbine runner.
- For determination of the size of the test specimens geometry realisation, loading capabilities and manufacturing costs were considered in descending order of priority. Thus, the specimens were scaled as large as possible, limited only by the properties of the test rig available.
- Symmetrical design with respect to membrane loading, cf. Figure 3.9.
- A net section of relatively large height and length to minimise the interaction of notch stress fields.

FE analysis showed that “ring” material absent in the test specimens due to the presence of $\varnothing 33$ mm fastener holes has only a minor effect on the stresses at the transition. In the FE model for the optimised 3D transition specimen showing the respective bore, stress concentration went down from $K_t = 1.364$ to 1.358. The realisation of FEA that is more consistent with the boundary conditions of the fatigue tests would have led to immoderate computing time in shape optimisation calculations.



Figure 7.9: Circular-shaped trailing edge transition specimen.



Figure 7.10: Shape optimised trailing edge transition specimen.

7.2.2 Fatigue Testing

Axial loading of the trailing edge specimen of Figure 7.10 leads to

$$F = \sigma \cdot A \quad (7.2)$$

where the net cross-sectional area $A = 879 \text{ mm}^2$.

Four strain gauges were attached to the net section of each specimen. Figure 7.13 shows the placement of the strain gauges equidistant to the areas of stress concentration, with their vertical centre lines 10 mm away from the trailing edge curvature.

Eight M30 bolts, each of them fastened by 1100 Nm torque, fixed the specimens to the test rig. For the given dimensions of the test specimen and loading conditions, calculation according to [159] and VDI 2230 standard [160] resulted in a safety factor of 1.6 for fatigue failure in the bolts.

With the yield limit $\sigma_{0.2} = 680 \text{ MPa}$ and maximum nominal stresses up to 661 MPa, plasticity appears at the transitions. Even in the nominal section plasticity was monitored. However, after some 1000 load cycles, constant strain amplitude and mean values were established in the nominal section, as visualised in Figure 7.15. In this diagram, a detailed view of the $F-\varepsilon_n$ curves shows increasing values of F_{cyl} in the very first cycles of the fatigue test. The function of these so-called “envelope cycles” is to lower the initial impact on the test rig.

Failure was defined by an increase of the specimen elongation at F_{max} , $\Delta u_Y(F_{\text{max}}) = 1 \text{ mm}$ (cf. Figure 7.11). At this condition, 20–30 % of the specimen “blade” cross section was cracked.

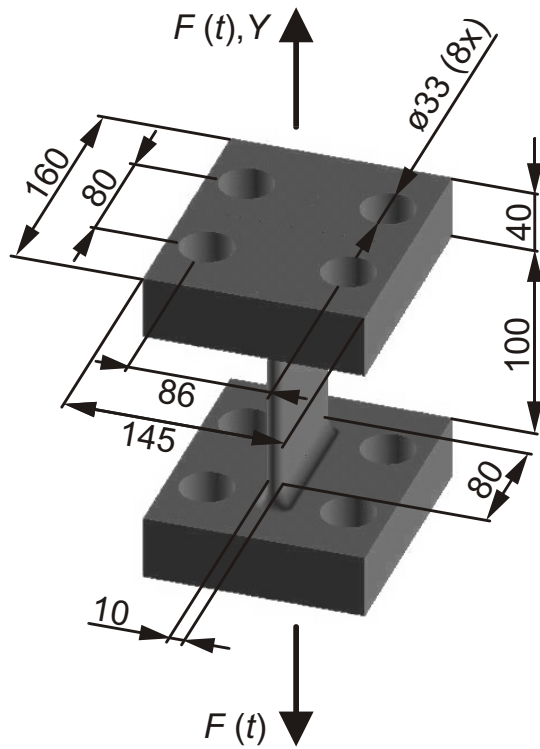


Figure 7.11: Trailing edge transition fatigue test specimens. Geometry and loading.



Figure 7.12: Trailing edge transition test mounted.

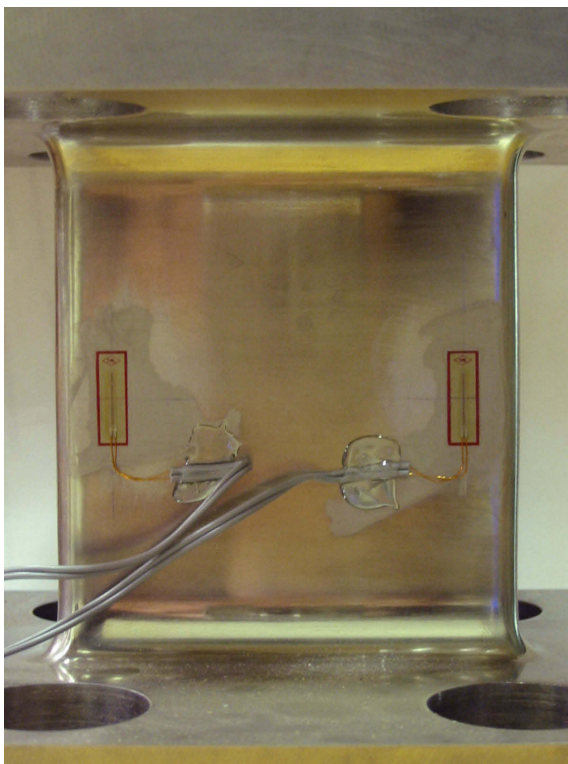


Figure 7.13: Strain gauge placement.



Figure 7.14: Trailing edge test specimen RI. Failure due to crack growing from stress concentration.

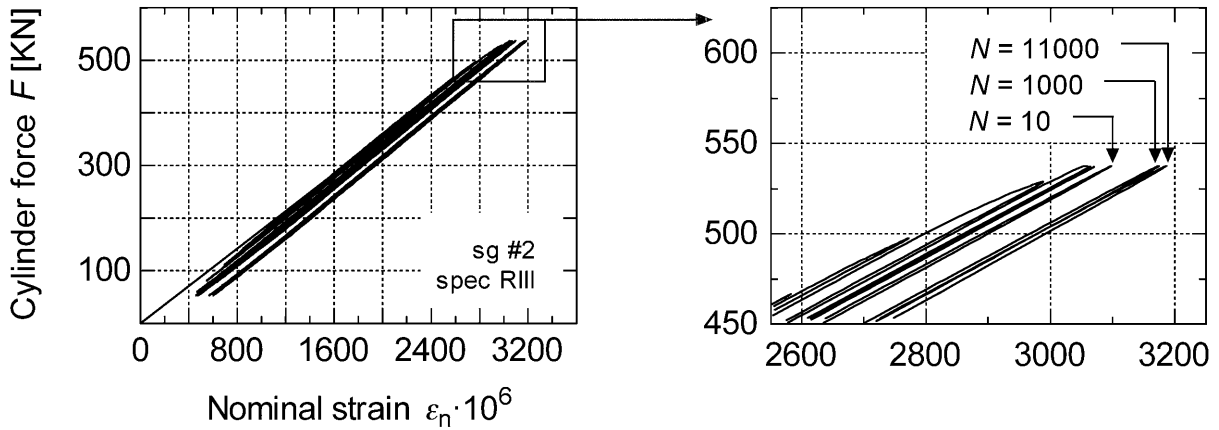


Figure 7.15: $F_{\text{cyl.}}-\varepsilon_n$ curves recorded from 3D specimen RIII, strain gauge 2.

7.2.3 Results

Cast Steel Specimens

Previous fatigue testing of 3D specimens made of a GX4CrNi 13-4 cast steel slab ($200 \times 300 \times 1500$) revealed a low fatigue strength of the cast material. Inclusions and pores of up to 3 mm in size and of all kind of shapes were distributed throughout the volume (cf. Figure 7.16). These defects showed to have a more detrimental effect on fatigue life than the stress concentration of the shape optimised transition. Fatigue cracks leading to failure in the circular shaped specimens grew from the area of stress concentration.

In the shape optimised specimens, multiple fatigue crack growth occurred simultaneously at various locations in the “blade” section.

With 5 of 12 specimens tested, the cast steel series has been abandoned. Hereupon, specimens of rolled steel 34CrNiMo 6 were ordered. Nevertheless, the results of the cast steel specimens with circular transition shape are shown in Figure 7.20.

Rolled Steel Specimens

Crack surfaces of both fatigue crack propagation and of final fracture are smoother and more homogeneous in 34CrNiMo 6 specimens, as shown in Figure 7.17. Both in specimens which show the standard circular and the shape optimised transition, the initiation of fatigue cracks took place at the locations of maximum stress concentration.

The specimens were cut centrally from a rolled steel slab with the longitudinal axis, Y , placed on the axis of symmetry of the cylindrical slab. It turned out that along the axis of symmetry a line of defects are present. These defects lead to fatigue failure in two of the four shape optimised specimens. In the remaining two shape optimised specimens, the dominant cracks initiated at the location of largest stress concentration of the transition.

All of the four specimens with the standard circular transition showed failure from cracks that grew from the location of largest stress concentration. In one case the inner central line defect and a geometrical stress concentration crack propagated simultaneously.

The 3D specimen fatigue test results are shown in Figure 7.20. Again, the SN curves displayed are obtained by linear regression, as described for the 2D specimen test results in Section 7.1.4.

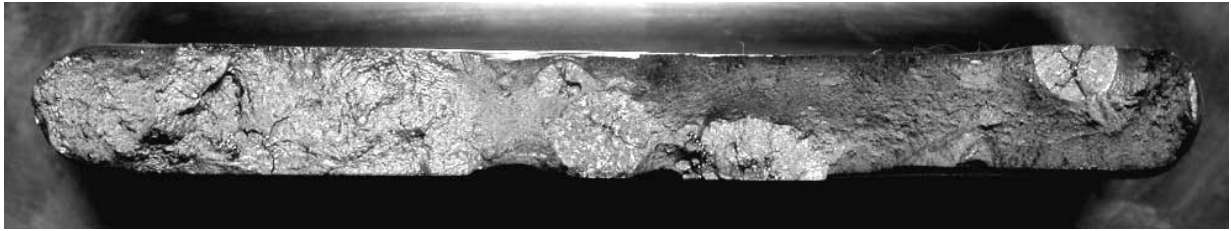


Figure 7.16: Cracked surface of cast steel GX5CrNi 13-4 standard transition shape specimen R5.

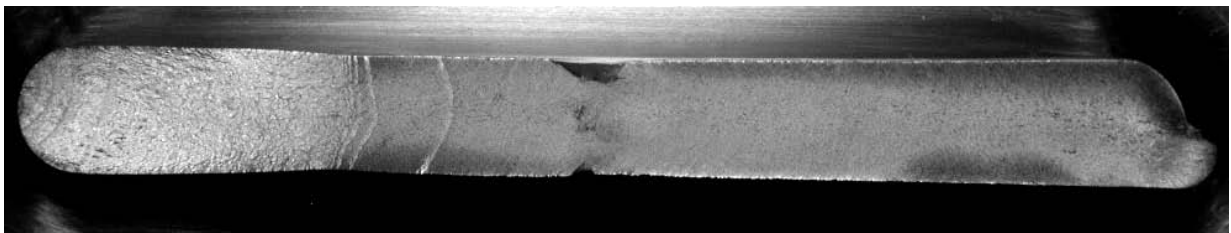


Figure 7.17: Cracked surface of rolled steel 34CrNiMo 6 standard transition shape specimen RII.

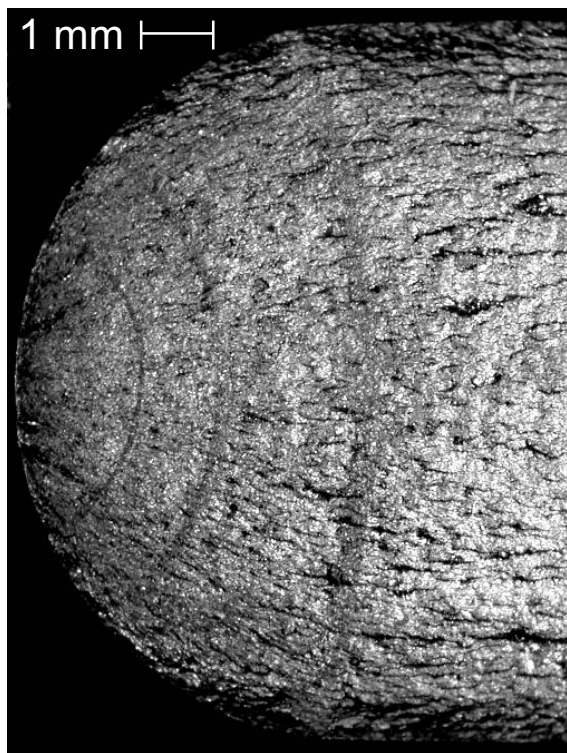


Figure 7.18: Three beach marks of surface crack growing from stress concentration in circular transition shape trailing edge specimen RI.

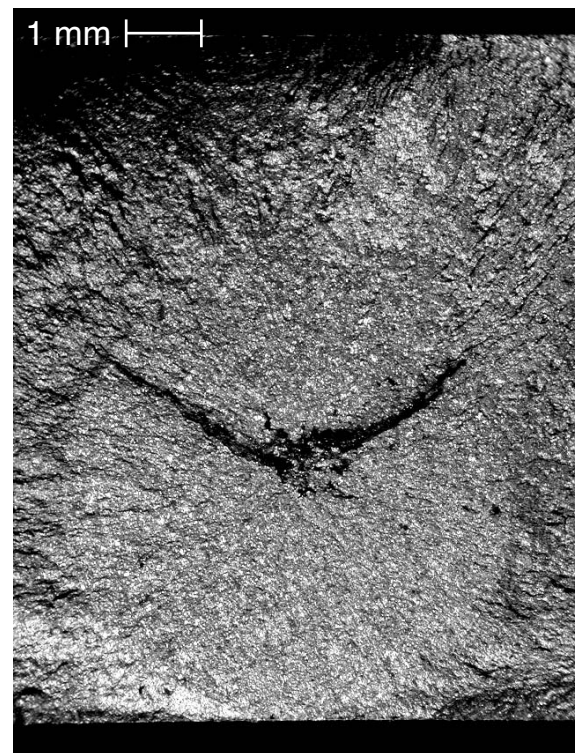


Figure 7.19: Central material defect in specimen RIV.

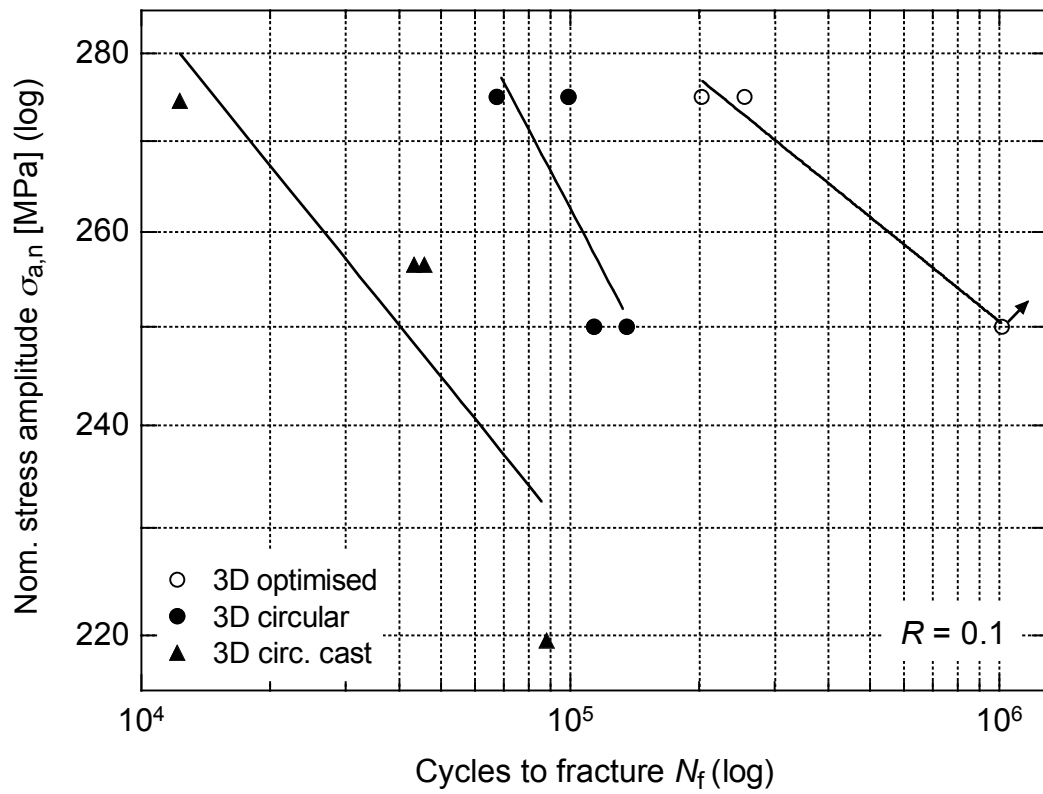


Figure 7.20: SN curve from trailing edge specimen fatigue testing.

Chapter 8

Local Stress Approach

In service life, Francis runners experience low cycle fatigue loading conditions from start-up and shutdown manoeuvres that induce gross-section stresses of the order of the material yield strength. Local plasticity effects have therefore to be taken into account in areas of stress concentration. In fatigue testing, the realisation of these high-level loading conditions kept the number of load cycles to failure, N_f , within practicable limits.

In order to improve the applicability of the results of the T-joint and the trailing edge transition fatigue tests presented Chapter 7, a more general presentation of the SN curves in Figures 7.8 and 7.20 is now provided. Local plasticity effects are accounted for by applying the Neuber rule. In a further step the data are “transformed” to stress ratio $R = 0$. Figure 8.3 presents the adjusted fatigue test data. Each of the three SN curves shown are based on one specimen material respectively, and have been obtained by linear regression.

8.1 Neuber Notch Stress

As already mentioned in Chapter 2, Neuber [34] established the relation between the elastic stress concentration factor, K_t , and the inelastic concentration factors for stress and strain, K_σ and K_ε (the ratio of the maximum local strain to the nominal strain),

$$K_t = \sqrt{K_\sigma K_\varepsilon} \quad . \quad (8.1)$$

For elastic conditions at the notch root, the factors of stress and strain concentration coincide. Once the notch material yields, K_σ and K_ε take different values. Nevertheless, the geometrical mean of both values remains equal to the theoretical elastic stress concentration factor.

The relation is frequently used in a simple analysis method to predict local notch root stress-strain (σ, ε) conditions from nominal stress-strain $(\sigma_n, \varepsilon_n)$. With $\varepsilon_n = \sigma_n/E$, Equation (8.1) yields

$$\sigma\varepsilon = (K_t\sigma_n)^2/E = \text{constant}, \quad (8.2)$$

for constant values of σ_n , the so-called “Neuber-hyperbola”.

The values of local stress, σ , and local strain, ε , at the notch root are obtained by the intersection of the two following curves in the σ - ε diagram (cf. Figure 8.1):

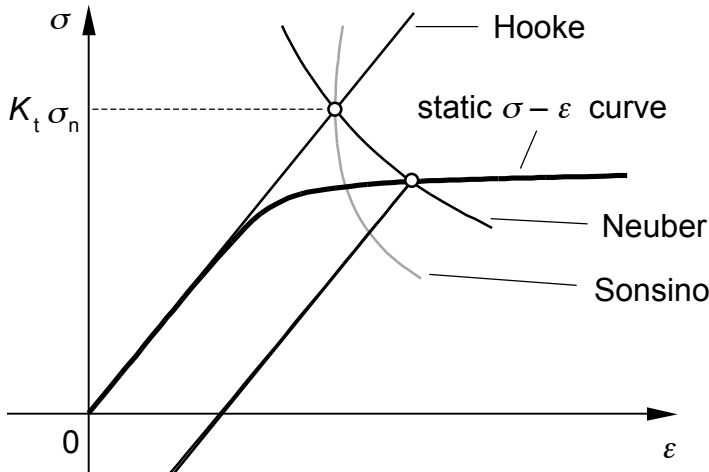


Figure 8.1: Neuber analysis of local stress and strain. Graphical method.

1. the Neuber hyperbola that contains point $K_t \cdot \sigma_n$ on Hooke's straight line of linear elasticity,
2. the cyclic stress-strain curve.

Neuber's rule may be extended to account for load reversals. Equation 8.2 then forms:

$$\Delta\sigma\Delta\varepsilon = (K_t\Delta\sigma_n)^2/E = \text{constant}. \quad (8.3)$$

In the present experimental fatigue tests the amount of cyclic plastic strain, $\Delta\varepsilon_{pl}$, is either marginal or non-existent. This can be stated from the Neuber correction procedure for the 3D test specimen that shows the largest values of stress concentration and load amplitude. This graphical procedure is displayed in Figure 8.2. Thus, the application of the *static* (tensile) $\sigma-\varepsilon$ curve of the specimens material (cf. Appendix D) seemed to be feasible in plasticity correction procedures of the fatigue test results displayed in Figure 8.3.

For "mild" notches that show a plastic strain below 5 percent, a modification proposed by Sonsino [161] cuts the amount of plastic strain by half (cf. Figure 8.1). However, given the excellent accordance of Neuber's rule and recent investigations on sharp and shallow notches with K_t in a range from 12 down to 1.35 [36], the Sonsino suggestion will not be considered here. As shown in Figure 8.2, local stress is quite insensitive to the amount of local plastic strain in the present investigation anyway.

The experimental fatigue tests described in Chapter 7 have been carried out at a load ratio $R_L = 0.1$. Corrected for plasticity effects, the eight test configurations (combinations of specimen shape and loading) show local stress ratios, R , between 0.41 and 0.02 (cf. Table C.1).

In fatigue crack growth calculation later in Chapter 9, the plasticity adjusted values will present the notch root surface stresses, whereas the stress conditions in the depth are considered to be unchanged from the nominal conditions with $R = R_L = 0.1$.

8.2 Effect of Stress Ratio

In 1968, Elber [162, 163, 164] discovered that a crack is closed for a considerable portion of the tensile load cycle. Since a fatigue crack only propagates as long as it is open, the

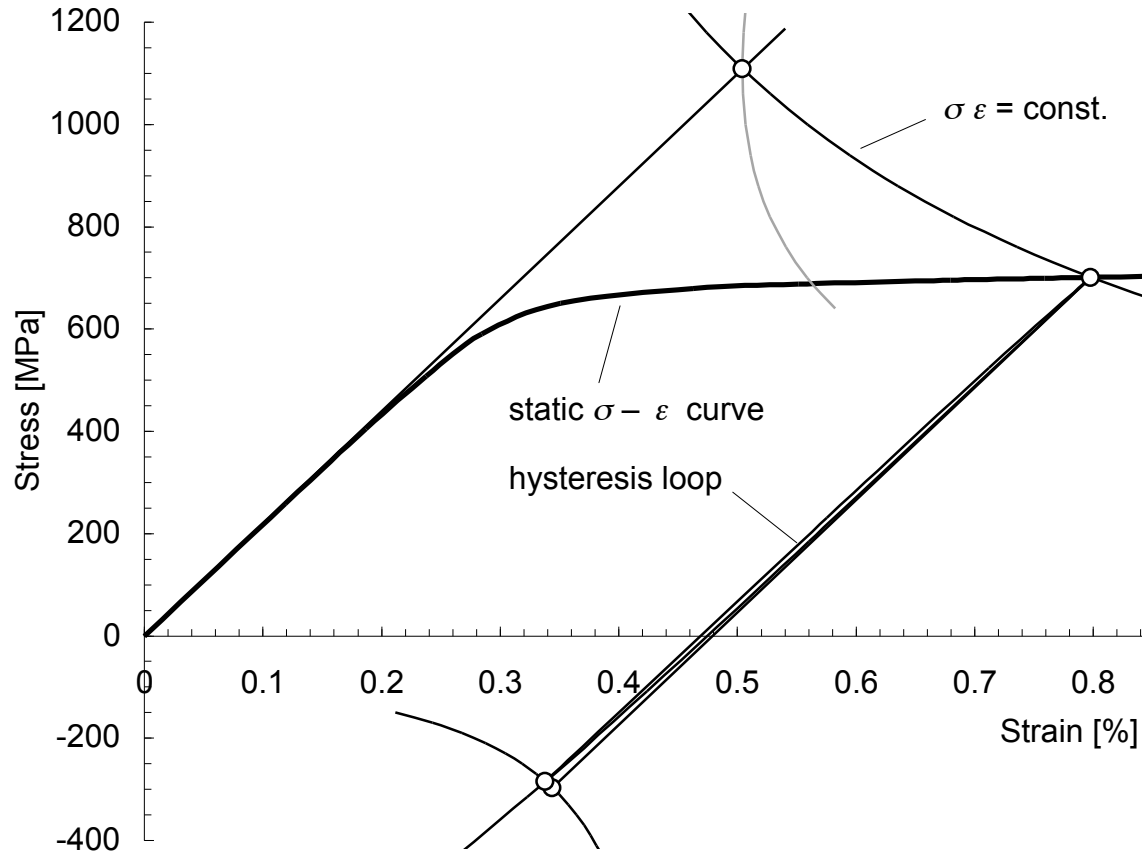


Figure 8.2: Trailing edge specimen fatigue test. Neuber stress and strain correction and hysteresis loop. $K_t = 1.678$, $R_L = 0.1$, $\sigma_{an} = 410$ MPa. $R = -0.41$, $\sigma_a = 493$ MPa.

crack closure phenomenon is a primary parameter to fatigue crack growth. For constant-amplitude loading, Elber introduced an effective stress intensity factor, ΔK_{eff} , as the difference between the maximum stress intensity factor at σ_{max} , K_{max} , and the crack opening stress intensity factor, K_{op} :

$$\Delta K_{\text{eff}} = K_{\text{max}} - K_{\text{op}} \quad . \quad (8.4)$$

Several experimental techniques to determine K_{op} have been developed. By an optical measurement method which is in use since 1976, the crack opening load is obtained from the load vs. differential displacement curve. The so-called linear fitting and offset compliance technique uses microgauge crack opening values. It is recommended by the American Society for Testing and Materials [165] due to its experimental simplicity.

In 1997, Donald [166, 167] showed that crack tip activity affects growth rates already below the opening load, most significantly near the threshold value ΔK_{th} . Paris et al. [168] suggest correction factors for the “apparently overstated” crack opening stress intensity factor. At this, they assume partial crack closure to be present due to crack surface roughness at a small distance behind the crack tip.

As experimental methods require vast amounts of time and resources, empirical methods are always welcome. The Walker Equation (8.5) estimates the effect of the stress ratio, R , on the crack growth rate with an empirical fit [169]. For constant amplitude loading it

is reasonable to assume that the compressive portion of the load cycle does not contribute to fatigue crack growth. Walker introduces an effective stress, $\bar{\sigma}$, that “predicts the effect of the stress ratio [169]”, thus results in the same crack growth rate as any actual combination of σ_{\max} and R :

$$\bar{\sigma} = \sigma_{\max}(1 - R)^\gamma \quad (8.5)$$

where γ is a material dependent correction factor. For AISI 4340 (DIN 40NiCrMo 6 - 1.6565) annealed steel, γ takes the values 0.42 and 0 for $R \geq 0$ and $R < 0$, respectively [170]. With $K_{\max} = \Delta K(1 - R)^{-1}$ derived from equations (3.3) and (5.3), the Paris Equation (9.2) becomes

$$\frac{da}{dN} = C_0 \left(\frac{\Delta K}{(1 - R)^{1-\gamma}} \right)^{m_0} \quad (8.6)$$

where C_0 and m_0 denote the material constants for $R = 0$.

It can be shown that the resulting da/dN vs. ΔK curves on a log-log plot are parallel straight lines of slope m_0 [171]. After some rearrangement becomes (8.6)

$$\frac{da}{dN} = \frac{C_0}{(1 - R)^{m_1(1-\gamma)}} (\Delta K)^{m_0} \quad (8.7)$$

Thus, constants C and m of the Paris equation (9.2) become

$$C = \frac{C_1}{(1 - R)^{m_1(1-\gamma)}}, \quad m = m_0. \quad (8.8)$$

This means that the slope m is unaffected by the stress ratio, R .

The solution of Smith, Watson and Topper [172] proposes $\gamma = 0.5$ for metallic materials, independently of R .

The SN data of the present investigation displayed in Figure 8.3 have been transformed to $R = 0$ by applying the Walker Equation (8.5). The γ values of [170] introduced above apply to fatigue crack growth only. In the present fatigue tests, the most part of fatigue life may be considered to be governed by fatigue crack growth. Adjustment of stresses due to these γ values is therefore of tentative character.

Chapter 9

Fatigue Crack Growth Analysis

9.1 Introduction

9.1.1 Regimes of Fatigue Crack Growth

The application of linear elastic fracture mechanics (LEFM) methods to structural fatigue life prediction problems has gained widespread acceptance since the pioneering work of Paris and co-workers [173, 174, 175] starting in 1961. They were the first to relate the increment of fatigue crack propagation per stress cycle to the *range* of Irwin's stress intensity factor, K (5.1),

$$\Delta K = K_{\max} - K_{\min} = \Delta\sigma_{\infty} F \sqrt{\pi a} \quad (9.1)$$

in the power law function

$$\frac{da}{dN} = C(\Delta K)^m \quad (9.2)$$

where the constants C and m are dependent on the material microstructure, environment, temperature and the stress ratio, R (3.2).

Paris' law (9.2) describes fatigue crack growth with a linear variation of $\log da/dN$ vs. $\log \Delta K$. This stable crack growth behaviour characterises regime B of the fatigue resistance curve in Figure 9.1. At extreme values of ΔK , crack growth rates change and the fatigue resistance curve becomes sigmoidal for most engineering alloys.

Below the threshold value for fatigue crack growth, ΔK_{th} , the behaviour of *short* cracks may be different from the fatigue resistance curve of Figure 9.1. One of the outstanding characteristics of a short crack is that it stays open [176],[177],[178],[179]. Thus, the plastic zone of the small crack lacks the protective effect crack closure gives to long cracks. This is valid even if $R_{\min} < 0$. The transition from closure-free short-crack behaviour to the closure-influenced long-crack behaviour was studied and documented by Blom and co-workers [180]. Journet et al. [178] and Nicholls et al. [179] have observed that in the large majority of cases, small-crack propagation rates exceed those of long cracks based on the development of crack closure with increasing crack length.

The *average* growth increment of long cracks however becomes smaller as the fatigue resistance curve approaches ΔK_{th} in regime A for decreasing crack growth rates.

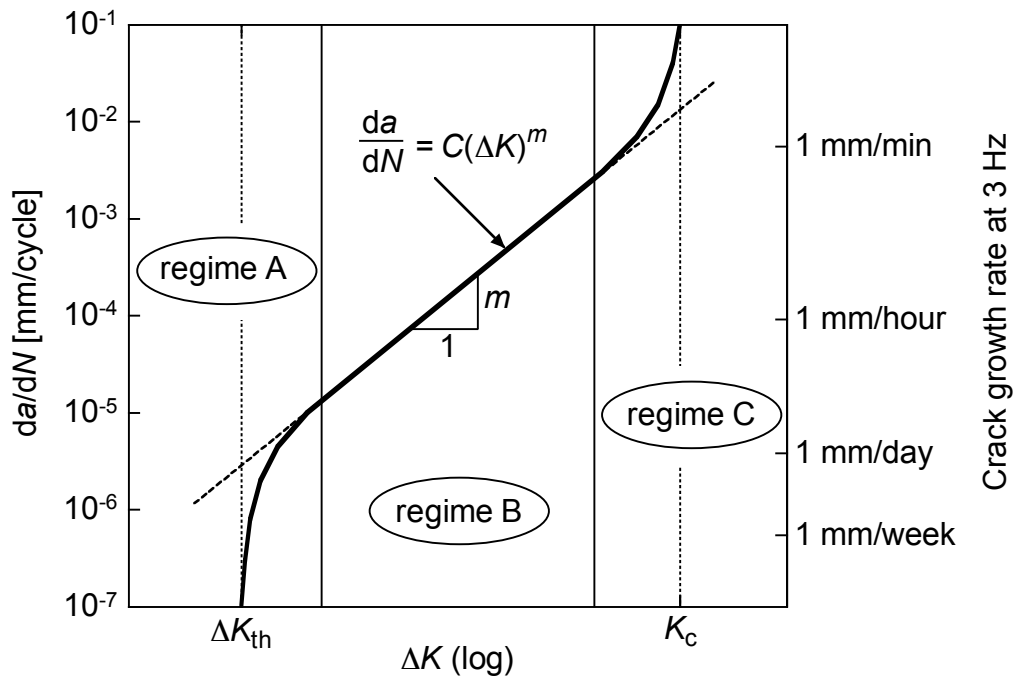


Figure 9.1: Different regimes in fatigue crack propagation. Near-threshold regime A, Paris regime B, high growth rate regime C.

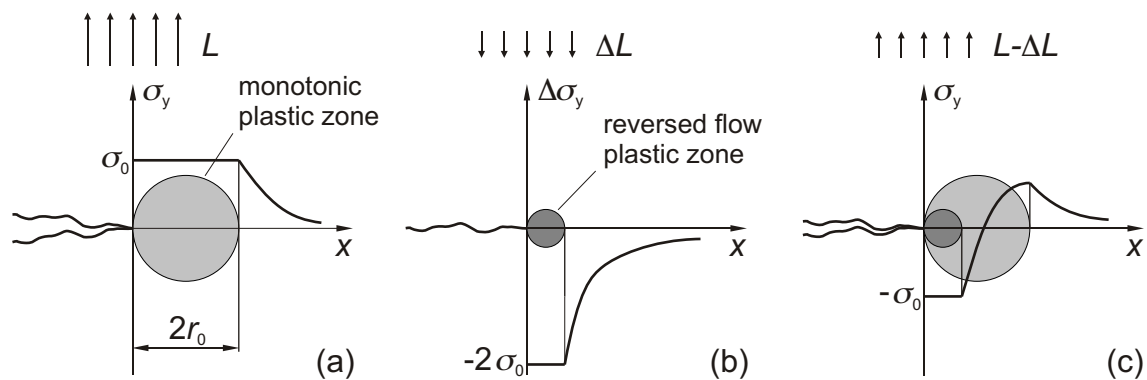


Figure 9.2: Plastic superposition for unloading. Adding (b) for load $-\Delta L$ with a doubled yield stress to (a) gives solution (c) that results after unloading from L to $L - \Delta L$. Reloading, $L - \Delta L$ to L restores (a). Adapted from Rice [181].

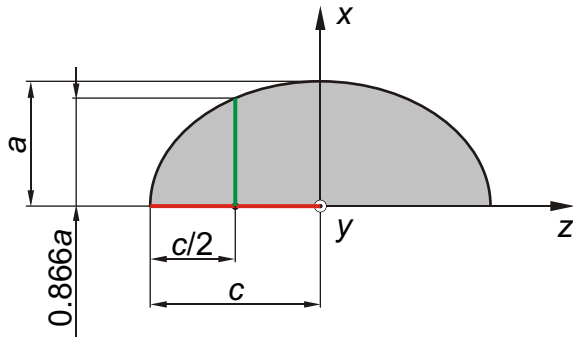


Figure 9.3: Plastic zone size and LEFM requirements. Characteristic lengths of the semi-elliptic surface crack due to Irwin [72].

9.1.2 Size of plastic Zone

The application of LEFM to fatigue crack growth calculation presumes that the size of the plastic zone at the crack tip, $2r_0$, is much smaller than characteristic lengths of the crack. For static loading, Irwin [72] estimates

$$2r_0 = \frac{1}{3\pi} \left(\frac{K_I}{\sigma_0} \right)^2 \quad (9.3)$$

for plane strain conditions. σ_0 is the tensile yield stress of the material. For plane stress this is noted to be three times as large.

According to Rice [181], K_I and σ_0 may be substituted by ΔK_I and $2\sigma_0$, respectively, for *cyclic* loading, ΔL . This is due to the occurrence of reverse plastic flow in the plastic crack tip region with the first increment of load reduction, $L - \Delta L$. As shown in Figure 9.2, plastic superposition for unloading adds twice the negative yield stress to the monotonic plastic zone which is restored under reloading, $L - \Delta L$ to L . The resulting stress range becomes $\Delta\sigma = 2\sigma_0$ for cyclic loading, ΔL .

For a semi-elliptical surface crack, Irwin suggests the characteristic lengths to be (a) the depth at the quarter points of the crack surface length, which is $0.866a$ and, (b) the semi-axis c of the ellipse, which is the crack length (cf. Figure 9.3). In the cases investigated and presented in this publication, the described characteristic lengths exceed the cyclic plastic zone size for plane stress conditions (derived according to Rice [181]) by a factor > 12 . Thus, the required condition $2r_0 \leq c/10$ proposed by Irwin [182] for LEFM is fulfilled.

Another criterion for the application of LEFM to fatigue crack growth is defined in ASTM E 647 [165]. Here it is required that any significant dimension, d , satisfies the relation

$$d \geq \frac{4}{\pi} (K_I/\sigma_0)^2 \quad . \quad (9.4)$$

For a semi-elliptical surface crack e.g., d would be the in-plane size of the specimen's uncracked ligament. In other words, plasticity limitations on LEFM are satisfied if the distance of the crack tip to any of the specimen's surfaces ahead of the crack tip is four times the size of the plastic zone, $2r_0$.

9.1.3 Application of SIF Solutions

As already mentioned in Chapter 5, for accurate calculation of fatigue crack propagation at notches it is required to consider variations in stress and geometry conditions as the

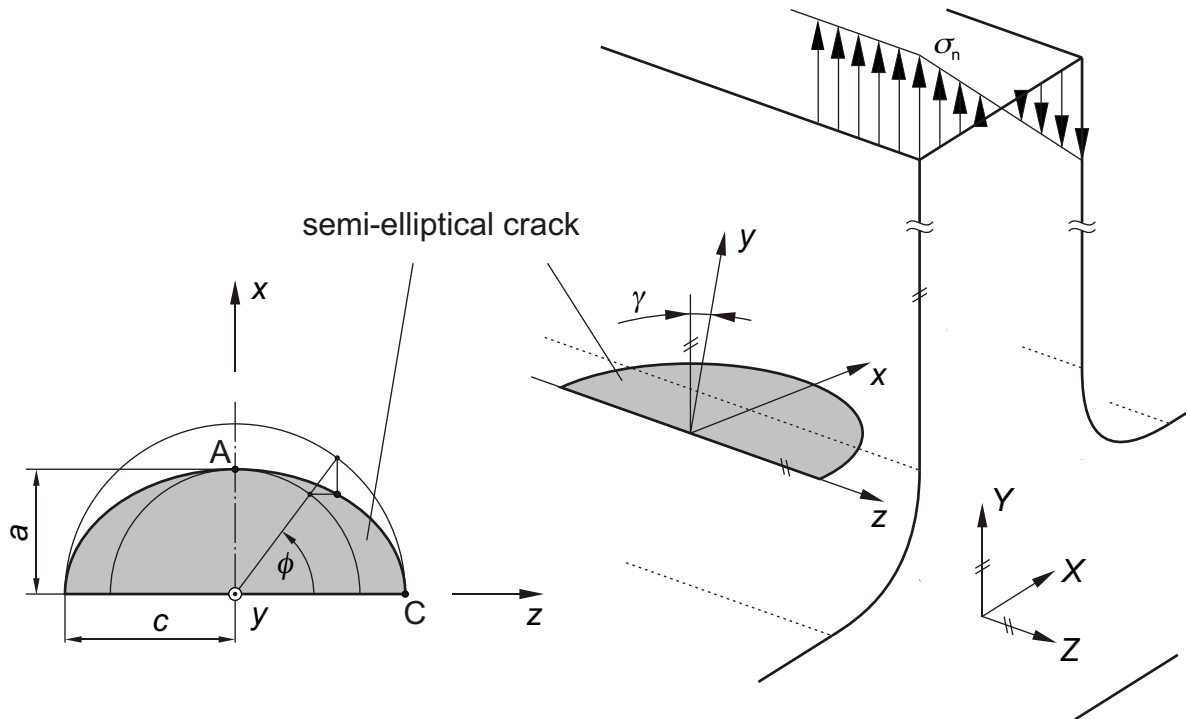


Figure 9.4: Geometric notation for semi-elliptical surface crack at location of highest stress concentration in T-joint under nominal bending loading.

crack grows. Thus, for crack growth calculation it is necessary to adjust the stress intensity factor range, ΔK (9.1), for every single crack propagating load cycle.

However, in some cases blocks of constant stress cycles (fixed increments of crack growth) or constant crack growth rate (finite crack growth increments) for approximate but conservative approaches seem to be reasonable ([101] chapter S.2). The crack growth simulation code FRANC3D (cf. Section 5.3.5) propagates cracks in increment blocks with constant values of ΔK . Here, cycle-by-cycle calculation of the SIF by means of BEM would be too time-consuming.

Solutions for the cycle-by-cycle determination of both the stress field around the crack and the geometrical factor, F , of the stress intensity factor for semi-elliptical surface cracks in plates and semi-finite bodies are presented in Chapter 5. It could be shown that the application of such solutions to notched areas seems to be feasible.

In the following, some of the SIF solutions presented in Chapter 5 shall be implemented and their application to Paris-type FCG simulation shall be demonstrated.

9.2 Pommier et al. SIF Code Implementation

In Chapter 4, the growth of a semi-circular fatigue crack in a homogeneous stress field was studied. Now, the more general case of the growth of a semi-elliptic fatigue crack in a (spatially) variable stress field will be analysed, employing stress intensity factors of the Pommier et al. [113] engineering code presented in Section 5.3.3.

In particular, the stress field below the surface of the T-joint transition arc shall be considered. It is assumed that the fatigue crack will initiate somewhere along the line of

maximum principal stress and propagate on a plane defined by this line (z -axis) and the direction of the steepest stress descent (x -axis). In the standard quarter-circular shaped T-joint transition of Figures 3.4 (page 18) and 9.4, the zx -plane is at an angle $\gamma \approx 10^\circ$ to the horizontal ZX -plane.

In the present case, the largest principal stress, σ_1 , varies with the x -co-ordinate only and can be written as

$$\sigma_1(x) = k(x/t_1) \cdot \sigma_n \quad , \quad (9.5)$$

where, by definition,

$$k(0) \equiv K_t \quad . \quad (9.6)$$

If $x/t_1 \ll 1$, the dimensionless function $k(x/t_1)$ is well approximated by the polynomial

$$k_n(x/t_1) = \sum_{i=0}^n \delta_i \cdot (x/t_1)^i \quad . \quad (9.7)$$

If k_n were an exact representation of k , then $\delta_0 \equiv K_t$.

In order to determine the relevant stress distribution of the current T-joint with sufficient accuracy, a particularly fine mesh was used which is not necessarily representative of a standard design calculation. The circles in Figure 6.9 on page 57 show the normalised nodal stresses along the x -axis, $k(x/t_1) \equiv \sigma_1/\sigma_n$ for the standard quarter-circular shaped T-joint transition. For $0 \leq x/t_1 \leq 0.25$, the nodal stresses are well fitted by the 3rd order polynomial (the respective full line in Figure 6.9)

$$k_3(x/t_1) = 1.3133 - 8.0947 \cdot (x/t_1) + 30.021 \cdot (x/t_1)^2 - 48.898 \cdot (x/t_1)^3 \quad . \quad (9.8)$$

In the problem of the T-joint, stresses do not vary in z -direction. Thus, Equation (5.14) from page 40 becomes

$$\sigma_1(x) = \sum_{i=0}^3 \sigma_{i0} (x/a)^i \quad . \quad (9.9)$$

By comparing Equation (9.9) with Equations (9.5) and (9.7), we obtain

$$\sigma_{i0} \equiv \delta_i \cdot (a/t_1)^i \cdot \sigma_n \quad , \quad i = 0 \dots 3 \quad . \quad (9.10)$$

Combining Equations (5.15) and (9.10) yields the following equations for the stress intensity factors at points A($a;0$) and C($0;c$) (cf. Figure 9.4)

$$K_A = G_A(a/c) \cdot \sigma_n \cdot \sqrt{a} \quad (9.11)$$

$$K_C = G_C(a/c) \cdot \sigma_n \cdot \sqrt{a} \quad (9.12)$$

where the geometry factors

$$G_A = \sum_{i=0}^3 \delta_i \cdot (a/t_1)^i \cdot G_{i0} (\phi = \pi/2; a/c) \quad (9.13)$$

Table 9.1: Number of LCF cycles ($\Delta\sigma_1(x=0) = 500$ MPa, $m = 3$, $C = 10^{-11}$) required for an initially semi-circular surface crack to become critical with respect to vibrational loading ($D = 0.1$).

Stress field and type of crack growth analysis	$a_i = c_i$ [mm]	a_c [mm]	c_c [mm]	N
Membrane stress field (simplified analysis)	0.5	1.44	1.44	14 550
Membrane stress field (Pommier analysis)	0.5	1.45	1.69	15 900
T-joint stress field (Pommier analysis)	0.5	2.81	4.67	35 700
Membrane stress field (simplified analysis)	1.0	1.44	1.44	4 180
Membrane stress field (Pommier analysis)	1.0	1.51	1.69	5 370
T-joint stress field (Pommier analysis)	1.0	2.85	4.72	22 150

$$G_C = \sum_{i=0}^3 \delta_i \cdot (a/t_1)^i \cdot G_{i0}(\phi = 0; a/c) \quad (9.14)$$

As mentioned before in Section 5.3.3, it has been assumed that the influence of the finite blade thickness, t_1 , can be neglected for low relative crack depths, a/t_1 .

9.2.1 FCG in the Stress Field of the quarter-circular T-joint Transition

Now the equations of Pommier et al. [113] are applied to the growth of a semi-elliptic fatigue crack in the zx -plane below the surface of the T-joint. Based on Equation (9.2), the growth of the semi-axes of the crack is determined by

$$\frac{da}{dN} = C \cdot (\Delta K_A)^m \quad (9.15)$$

$$\frac{da}{dN} = C \cdot (\Delta K_C)^m \quad (9.16)$$

where the stress intensity ranges are given by Equations (9.11) and (9.12) with the nominal stress range, $\Delta\sigma_n$, substituted for σ_n .

In particular, the growth of an initially semi-circular surface crack shall be considered, i. e.

$$a(N=0) = c(N=0) = a_i \quad . \quad (9.17)$$

This case was investigated in Chapter 4 for a homogeneous stress distribution with the stress range equal to that at the most highly loaded location of the T-joint. The semi-circular crack was then assumed to retain its shape ($G_C = G_A$) as it grew under the start-stop LCF cycle. The initial crack size was determined such that the stress intensity range along the crack front under the vibrational HCF cycle remained below the threshold value for a given number of LCF cycles.

For the sake of completeness, the growth of similar initial cracks in a homogeneous stress field has also been analysed taking Equations (5.14), (5.15) and (9.11)–(9.16) into account. For $\Delta\sigma_1(x=0) = 500$ MPa, $D = 0.1$ and $t_1 = 20$ mm, the crack growth equations (9.15) and (9.16), with C and m taken from Equation (4.6), have been integrated by means of a 5th order Runge-Kutta-Fehlberg scheme [183]. The step-wise integration is continued until $\Delta K_{\text{HCF}} \geq \Delta K_{\text{th}}(R_{\text{HCF}})$ is satisfied everywhere along the crack front, which is the definition of failure introduced in Chapter 4.

The history of crack development, $a(N)$ and $c(N)$, is shown in Figure 9.5. The number of cycles required for the initially semi-circular crack to become critical (with respect to the vibrational loading) is somewhat higher than that obtained by the preceding, simplified analysis (cf. Table 9.1).

Using the same assumptions, crack growth in the spatially variable stress field of the T-joint was also analysed. As can be seen from Table 9.1, the number of cycles required for the crack to become critical is larger than that predicted for the membrane stress field. Since the crack is growing into an area of reduced stress, the in-depth growth rate, da/dN , becomes lower than that at the surface, dc/dN , i. e. $c > a$ as shown in Figure 9.5. Since the model's range of validity ($0.5 \leq a/c \leq 2$) is only violated in the final phase of crack propagation, this is considered to have only a minor influence on the number of cycles predicted.

9.2.2 Shape Optimisation and FCG Methodology

A number of shape optimised T-joint transitions have been presented in Chapter 6. For different shapes of the transition, the maximum stress concentration is found at different locations on the transition surface (cf. Figures 6.4–6.8, 6.12 and 6.13). Consequently, fatigue cracks in the optimised T-joint specimen are likely to initiate and propagate from a location different from the $\gamma \approx 10^\circ$ location which is for the standard quarter-circular shaped T-joint transition (cf. Figure 9.4).

In analogy to the procedure described above in the beginning of Section 9.2 for the quarter-circular shaped T-joint transition, the crack propagation path 3rd-order stress field polynomials of the optimised T-joint shape solutions A–D, $k_3^{\text{opt}}(x/t_1)$, have been found to be

$$k_3^{\text{opt(A)}}(x/t_1) = 1.0212 - 2.2894 \cdot (x/t_1) + 0.7415 \cdot (x/t_1)^2 - 0.4529 \cdot (x/t_1)^3 \quad (9.18)$$

$$k_3^{\text{opt(B)}}(x/t_1) = 1.1159 - 3.7001 \cdot (x/t_1) + 4.8760 \cdot (x/t_1)^2 - 3.4065 \cdot (x/t_1)^3 \quad (9.19)$$

$$k_3^{\text{opt(C)}}(x/t_1) = 1.1618 - 4.6886 \cdot (x/t_1) + 8.5251 \cdot (x/t_1)^2 - 6.7884 \cdot (x/t_1)^3 \quad (9.20)$$

$$k_3^{\text{opt(D)}}(x/t_1) = 1.1215 - 3.9855 \cdot (x/t_1) + 5.6386 \cdot (x/t_1)^2 - 3.2532 \cdot (x/t_1)^3 \quad (9.21)$$

for $0 \leq x/t_1 \leq 0.35$.

For conditions similar to the calculations of Section 9.2.1, FCG of initially semi-circular cracks in the stress fields described by Equations (9.18)–(9.21) produce Figure 9.6. As shown in Table 9.2, the crack that propagates from shape A allows the largest number of LCF fatigue cycles before HCF occurs and therewith N_f is reached. The development of the crack front in the case the quarter-circular and the shape D optimised transition is shown in Figure 9.7(a) and (b), respectively, in fixed increments of $\Delta N = 5000$.

Fatigue life of the standard quarter-circular shape is exceeded by a factor up to 1.8. With an increase by factor 1.5, shapes B and D still show a significant increase in life cycles.

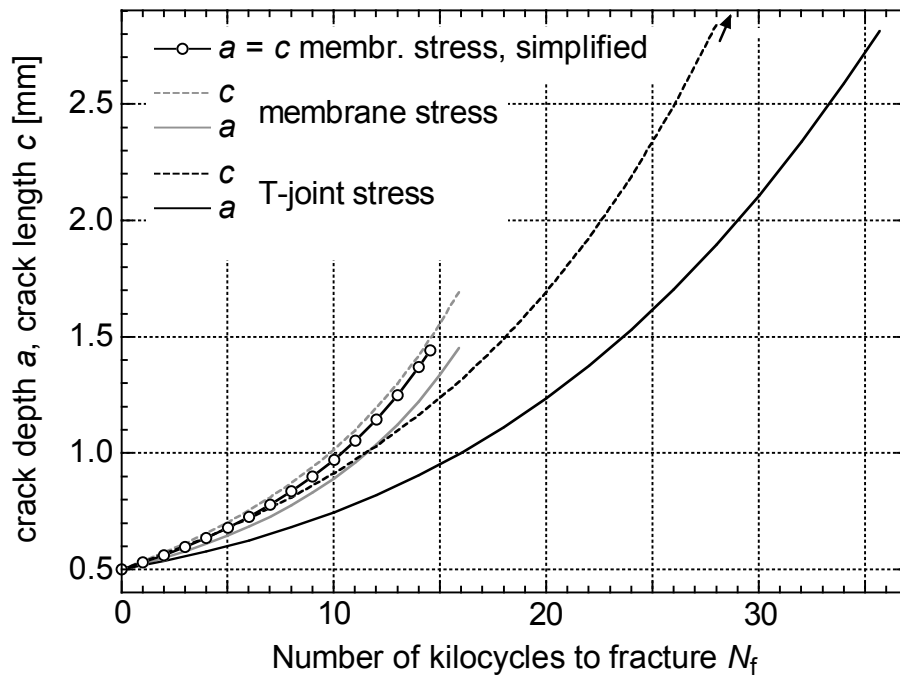


Figure 9.5: Growth of semi-elliptical surface cracks in zx -plane of the T-joint shown in Figure 9.4 for $t_1 = 20$ mm, $\Delta\sigma_1(x = 0) = 500$ MPa, $m = 3$, $C = 10^{-11}$.

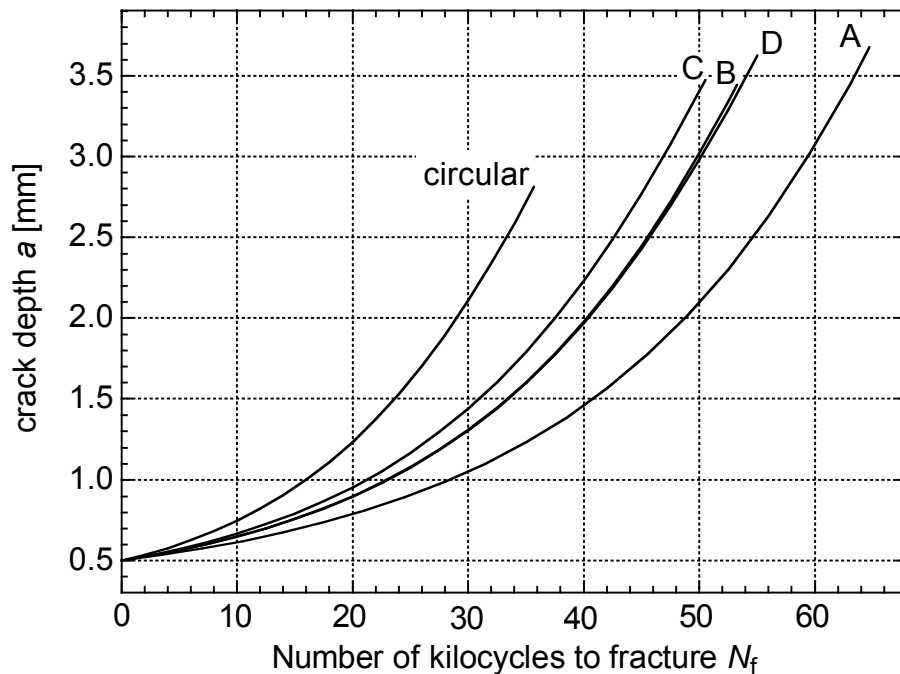


Figure 9.6: Growth of semi-elliptical surface cracks in T-joint zx -plane. Standard quarter-circular and shape optimised transition geometries, $t_1 = 20$ mm, $\Delta\sigma_1(x = 0) = 500$ MPa, $m = 3$, $C = 10^{-11}$.

Table 9.2: Optimisation efficiency, η_{opt} (9.22), for $\iota = 0.3$. The influence of different optimised shapes on stress concentration and fatigue life.

Optimisation shape approach case	K_t	N_f	$\frac{N_{\text{opt}}}{N_{\text{circ}}}$	$\frac{L_{\text{opt}}}{L_{\text{circ}}}$	η_{opt}
A	1.022	64 730	1.813	1.99	1.47
B	1.119	53 240	1.491	1.28	1.38
C	1.162	50 500	1.415	0.76	1.54
D	1.121	55 000	1.541	0.91	1.58
Not optimised	1.322	35 700	(1)	(1)	(1)

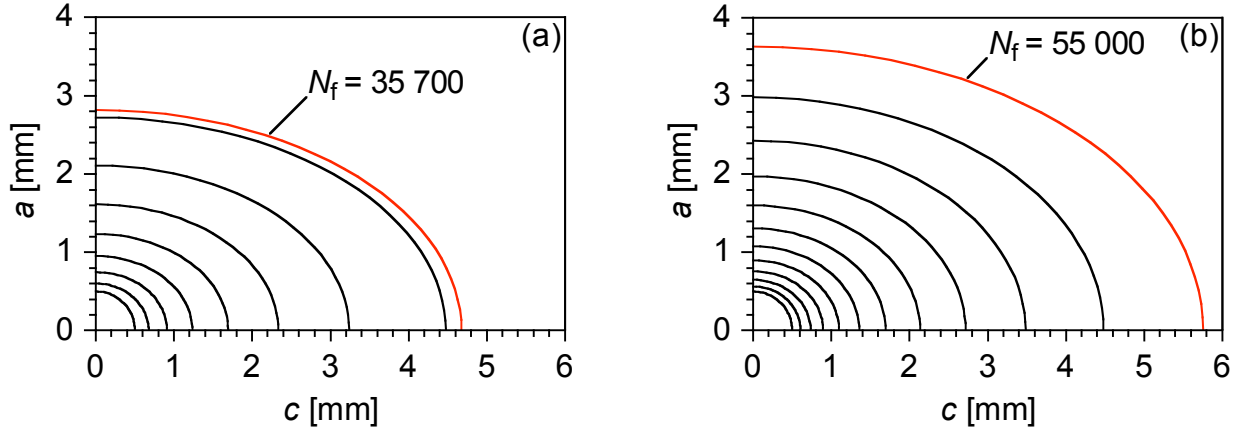


Figure 9.7: Shapes of semi-elliptical fatigue cracks. Propagation in steps of $\Delta N = 5000$ to failure (red shape) in stress field of (a) quarter-circular, (b) shape optimised (case D) T-joint transition for $t_1 = 20$ mm, $\Delta\sigma_n = 500/1.322$ MPa, $m = 3$, $C = 10^{-11}$.

Fatigue life in Shape C is still enhanced by a factor 1.4, and it seems to be noteworthy that this increase in life was achieved with a transition curvature length, L_{nc} , which is shorter than the respective dimension in the standard quarter-circular transition.

In an attempt to assess the optimised shapes with respect to the favoured effects of (i) life increase and (ii) lower manufacturing costs due to a shorter length of the transition curvature (i. e. reduced welding and machining), an optimisation efficiency factor, η_{opt} , shall be introduced with

$$\eta_{\text{opt}} = \frac{N_{\text{opt}}}{N_{\text{circ}}} \cdot \left(\frac{L_{\text{nc,circ}}}{L_{\text{nc,opt}}} \right)^\iota \quad (9.22)$$

where the cost influence may be reduced by choosing $0 \leq \iota < 1$. With $\iota = 0.3$, Table 9.2 reveals that shape D is the most efficient shape solution with regard to increased life at low manufacturing costs.

9.3 Carpinteri et al. SIF Code Implementation

Now, the SIF solution of Carpinteri et al. [126] will be employed. Similar to the work of Pommier et al., the procedure presented in Section 9.3.1 solves general 3D fatigue crack

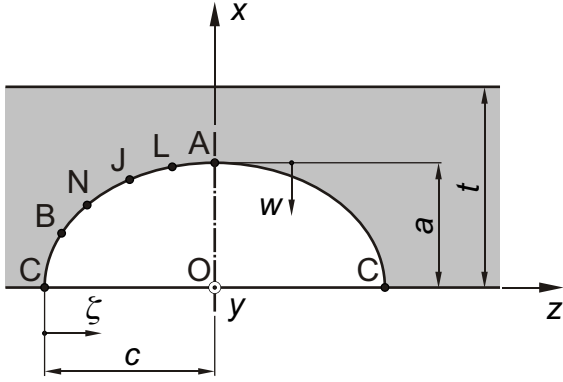


Figure 9.8: Finite plate with semi-elliptical surface crack. Geometrical parameters.

growth problems with crack sizes small with respect to the structural component. The procedure consists of the following steps:

1. Calculation of the SIFs by means of FEA for a finite thickness plate under elementary stress distributions applied to the crack faces.
2. Evaluation of the uncracked stress field in the structural component.
3. Approximate SIF evaluation for the real cracked structural component by employing the results deduced in step 1, and by applying the superposition principle and the power series expansion of the actual stress field determined in the previous step 2.
4. Fatigue crack growth analysis by applying Paris' crack propagation law [175].

9.3.1 SIFs for T-joints

Again, growth of a semi-elliptic fatigue crack in the zx -plane below the surface of the T-joint (cf. Figure 9.4) shall be considered. As mentioned in Section 7.1.2, the loading condition of the experimental tests performed consists of a transversal force, F . In addition to a bending moment that causes mode I crack surface displacement, F induces a shear stress into the blade which results in (sliding) mode II crack surface displacement of the surface crack in Figure 9.4.

The work of Carpinteri et al. [126] employs an equivalent SIF, $K_{\text{eq}} = K_{\text{eq}}(K_{\text{I}}, K_{\text{II}})$, where K_{II} is computed according to a solution of [184].

In the experimental fatigue tests performed, the shear stress, τ_0 , is less than 2 % of the largest nominal bending stress, σ_{bn} . As mentioned above in Section 7.1.2, τ_0 shall therefore not be subject of further considerations. Moreover, ignoring τ_0 maintains comparability between the Pommier et al. [113] and Carpinteri et al. [126] SIF values and FCG results.

For the T-joint transition, the distribution of the largest principal stress in the x -direction beneath the location of the highest stress concentration of the uncracked specimen, $\sigma_1(x)$, (cf. Figure 9.4 and Section 9.2) can be described by the 5th-order polynomial

$$k_5(x/t_1) = 1.3077 - 7.8008 \cdot (x/t_1) + 28.836 \cdot (x/t_1)^2 - 63.878 \cdot (x/t_1)^3 + 70.766 \cdot (x/t_1)^4 - 30.092 \cdot (x/t_1)^5 \quad (9.23)$$

Table 9.3: Coefficients $B_{n(b)}$ obtained from a numerical interpolation of the actual stress distribution at the location of largest principal stress in the T-joint under bending load, for relative crack depths, $\xi = a/t_1$, in the range $0 \leq \xi \leq 0.7$. (a) Quarter-circular transition. (b) Shape optimised (case D) transition. (c) Nominal section (pure bending).

(a)	Coefficient $B_{n(b,circ)}$, $n = 0, \dots, 5$
	$B_{0(L)} = 1.3077 - 7.8008 \cdot \xi + 28.836 \cdot \xi^2 - 63.878 \cdot \xi^3 + 70.766 \cdot \xi^4 - 30.092 \cdot \xi^5$
	$B_{1(L)} = 7.8008 \cdot \xi - 57.672 \cdot \xi^2 + 191.634 \cdot \xi^3 - 283.064 \cdot \xi^4 + 150.46 \cdot \xi^5$
	$B_{2(L)} = 28.836 \cdot \xi^2 - 191.634 \cdot \xi^3 + 424.596 \cdot \xi^4 - 300.92 \cdot \xi^5$
	$B_{3(L)} = 63.878 \cdot \xi^3 - 283.064 \cdot \xi^4 + 300.092 \cdot \xi^5$
	$B_{4(L)} = 70.766 \cdot \xi^4 - 150.46 \cdot \xi^5$
	$B_{5(L)} = 30.092 \cdot \xi^5$
(b)	Coefficient $B_{n(b,opt)}$, $n = 0, \dots, 5$
	$B_{0(L)} = 1.1215 - 3.9659 \cdot \xi + 5.1553 \cdot \xi^2 - 0.004 \cdot \xi^3 - 8.149 \cdot \xi^4 + 6.3835 \cdot \xi^5$
	$B_{1(L)} = 3.9659 \cdot \xi - 10.3106 \cdot \xi^2 + 0.012 \cdot \xi^3 + 32.596 \cdot \xi^4 - 31.9175 \cdot \xi^5$
	$B_{2(L)} = 5.1553 \cdot \xi^2 - 0.012 \cdot \xi^3 - 48.894 \cdot \xi^4 + 63.835 \cdot \xi^5$
	$B_{3(L)} = 0.004 \cdot \xi^3 + 32.596 \cdot \xi^4 - 63.835 \cdot \xi^5$
	$B_{4(L)} = -8.149 \cdot \xi^4 + 31.9175 \cdot \xi^5$
	$B_{5(L)} = -6.3835 \cdot \xi^5$
(c)	Coefficient $B_{n(bn)}$, $n = 0, 1$
	$B_{0(L)} = 1 - 2\xi$
	$B_{1(L)} = 2\xi$

for the quarter-circular T-joint transition. In the case of the case D shape optimised transition, $\sigma_1(x)$ yields

$$k_5^{\text{opt(D)}}(x/t_1) = 1.1215 - 3.9659 \cdot (x/t_1) + 5.1553 \cdot (x/t_1)^2 - 0.004 \cdot (x/t_1)^3 - 8.149 \cdot (x/t_1)^4 + 6.3835 \cdot (x/t_1)^5 \quad (9.24)$$

for $0 \leq x/t_1 \leq 0.7$.

The coefficients $B_{n(L)}$ (cf. Table 9.3) are then determined by applying Equation (5.21), where the terms $d^{(n)}\sigma_b(w)/dw^{(n)}$ can be approximated by a polynomial fitting of the stress distribution $\sigma_1(w)$. The in-crack-plane co-ordinate, w , has its origin at the deepest point on the crack front, A, and is directed in the opposite direction of x (cf. Figure 9.8). The approximate dimensionless SIF (5.18), $K_{I(b)}^*$, is obtained from Equation (5.23).

K_I^* vs. Crack Depth

The dimensionless stress intensity factor $K_{I(b,circ)}^*$ for a cracked plate with the crack loaded by the stress distribution $\sigma_1(x) = \sigma_{b,circ}(x)$ of the quarter-circular transition is plotted in Figure 9.9(a) against the relative crack depth, $\xi = a/t$. $\sigma_{b,opt}(x)$ represents the stress field in the case D type shape optimised T-joint transition. The related SIF $K_{I(b,opt)}^*$ is given in Figure 9.9(b). $K_{I(bn)}^*$ for a cracked plate subjected to stresses $\sigma_{bn}(X)$ (cf. Figure 9.4),

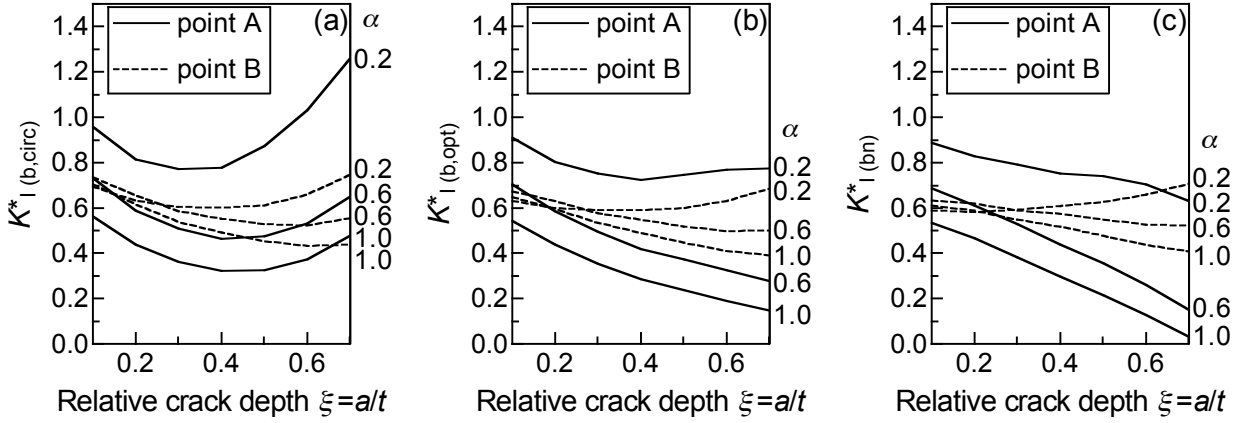


Figure 9.9: Dimensionless SIF against ξ for different values of the crack aspect ratio, $\alpha = a/c$, and stress distributions from nominal bending load at three T-joint locations. (a) Quarter-circular transition, $\sigma_{b,circ}$. (b) Shape optimised transition, $\sigma_{b,opt}$. (c) Nominal section, σ_{bn} .

where the subscripts b and n stand for “bending” and “nominal”, respectively, is displayed in Figure 9.9(c). The nominal case corresponds to that of the T-joint under bending loading, with the surface crack located in the nominal section, far from the geometrical transition.

For the lowest relative crack depths, stress intensity factors for the surface-cracked quarter-circular T-joint geometry show decreasing values at both the near-surface point, B, and the deepest point, A (cf. Figure 9.9(a)). For higher values of ξ , K^* values at point B increase again but recover entirely only for $\alpha = a/c = 0.2$. All K^* values at point A show an increase for $\xi \geq 0.4$. For higher ξ values, the high- α curves almost recover up to values which they show for the lowest values of ξ . The $\alpha = 0.2$ curve exceeds the initial, low- ξ K^* values for $\xi > 0.6$.

For the case of the shape optimised transition (cf. Figure 9.9(b)), K^* values are generally lower than for the crack in the quarter-circular transition. The dimensionless SIF $K_{I(b,opt)}^*$ at points A and B monotonically decreases for increasing ξ values. Only for $\alpha = 0.2$, K^* values at both points show an increase for higher relative crack depths.

In the nominal bending stress field (cf. Figure 9.9(c)) the trend is similar to that discussed for the crack in the shape optimised transition, with K^* values generally lower. For all the considered values of the crack aspect ratio, α , the dimensionless SIF $K_{I(bn)}^*$ at the deepest point, A, monotonically decreases by increasing the relative crack depth. At the near-surface point, B, the behaviour is different only for low values of the crack aspect ratio: for $\alpha = 0.2$, it can be observed a monotonic increase of K^* for increasing values of the relative crack depth, ξ .

Variation of K_I^* along the Crack Front

The stress concentration effect on the SIF is analysed for different points along the crack front. For different values of $\xi = a/t$ and $\alpha = a/c$, results are plotted in Figure 9.10 for a cracked plate under the stress distribution $\sigma_{b,circ}(w)$ (cases (a)–(c), $K_t = 1.32$), the stress distribution $\sigma_{b,opt}(w)$ (cases (d)–(f), $K_t = 1.12$) and the stress distribution $\sigma_{bn}(w)$ (cases (g)–(i), $K_t = 1.00$).

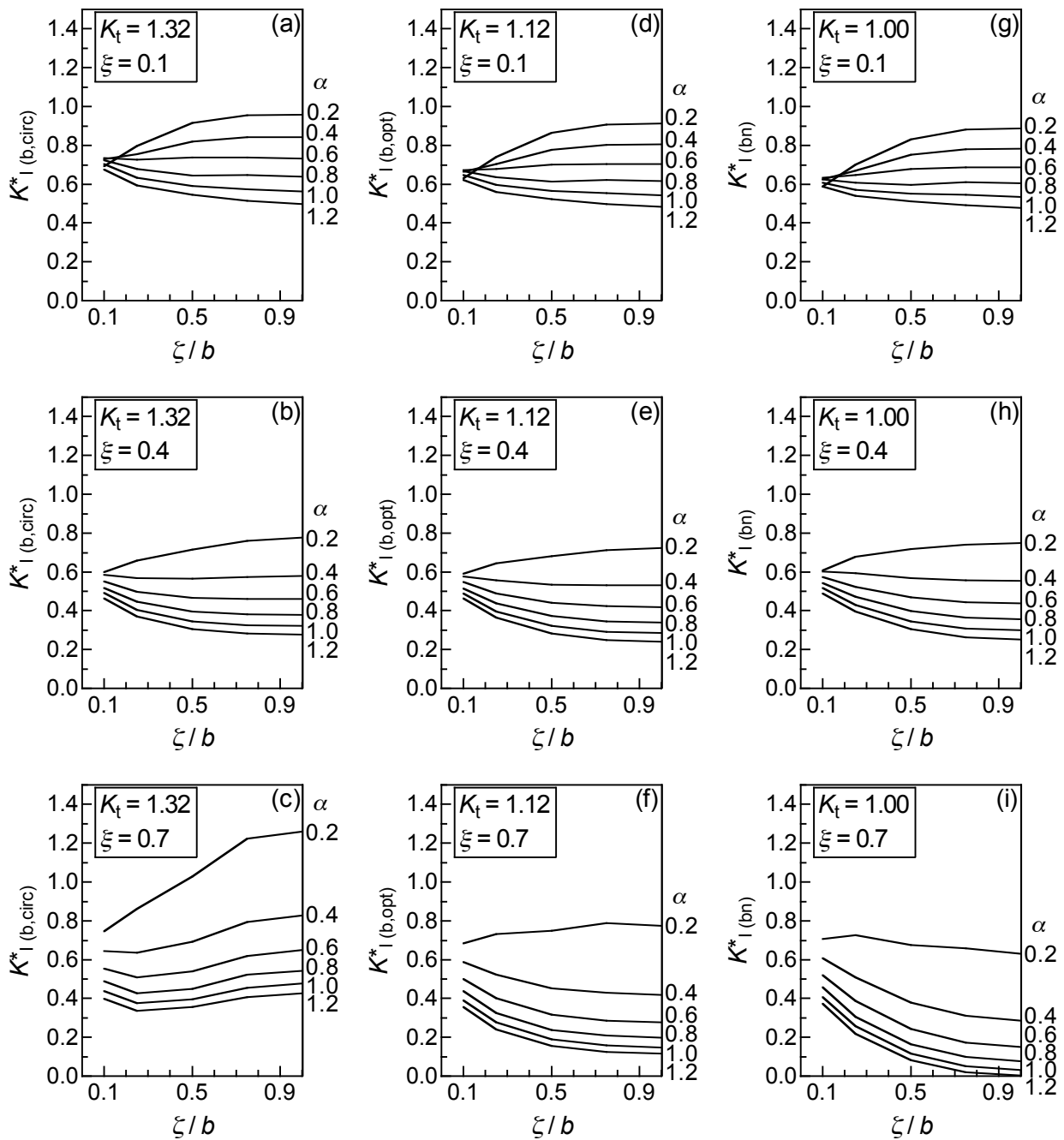


Figure 9.10: Dimensionless SIF along the crack front for different values of ζ and α , in different T-joint stress fields. (a)–(c) Quarter-circular transition. (d)–(f) Shape optimised transition. (g)–(i) Nominal section far from the transition.

Table 9.4: Dimensionless stress intensity factors for different opening stresses: Constant ($K_{I(0)}^*$) elementary stresses; $\sigma_{bn}(w)$ bending stresses ($K_{I(bn)}^*$), $\sigma_{b,circ}(w)$ local stresses at quarter-circular transition ($K_{I(b,circ)}^*$) and $\sigma_{b,opt}(w)$ local stresses at shape optimised transition ($K_{I(b,opt)}^*$).

α	ξ	$K_{I(b,circ)}^*$			$K_{I(b,opt)}^*$			$K_{I(bn)}^*$			$K_{I(0)}^*$		
		0.1	0.4	0.7	0.1	0.4	0.7	0.1	0.4	0.7	0.1	0.4	0.7
0.2	A	0.958	0.777	1.260	0.911	0.722	0.775	0.886	0.750	0.630	1.009	1.333	1.920
	B	0.693	0.599	0.745	0.630	0.590	0.684	0.588	0.608	0.706	0.625	0.804	1.232
0.6	A	0.733	0.462	0.649	0.702	0.418	0.276	0.687	0.437	0.149	0.790	0.871	0.928
	B	0.734	0.552	0.554	0.673	0.547	0.501	0.632	0.573	0.520	0.679	0.790	0.983
1.0	A	0.561	0.322	0.476	0.542	0.285	0.148	0.535	0.298	0.032	0.622	0.661	0.647
	B	0.702	0.491	0.437	0.646	0.489	0.391	0.609	0.516	0.408	0.657	0.727	0.816

For $\xi = 0.4$, the dimensionless stress intensity factor K^* values are quite similar for all stress fields considered (e. g., see (b), (e) and (h)), while the values are significantly lower for the shape optimised transition and yet lower for the nominal section, compared to the values for the quarter-circular stress field if high values of ξ are examined (for example, see (c), (f) and (i)). The same tendency is shown for $\xi = 0.1$, with differences in values just marginal.

Furthermore, for low values of ξ (cf. Figures 9.10(a), (d) and (g)), the dimensionless stress intensity factors increase for low values of α and decrease for high α values. On the other hand, for high values of ξ , $K_{I(bn)}^*$ decreases for all the considered values of α (cf. Figure 9.10(i)). The behaviour of the stress intensity factor $K_{I(b,opt)}^*$ is similar to that of $K_{I(bn)}^*$, except that $K_{I(b,opt)}^*$ increases for high values of ξ and low values of α (cf. $\alpha = 0.2$ in Figure 9.10(f)).

It may be remarked that an increasing stress concentration factor, K_t , leads to an increase of the dimensionless stress intensity factor, K^* , especially in the deepest point on the crack front (point A, $\zeta/b = 1.00$).

Some values of the dimensionless SIFs at point A and point B of a surface crack in a plate under $\sigma_{b,circ}$, $\sigma_{b,opt}$ and σ_{bn} opening stresses are reported in Table 9.4 for several values of ξ and α . SIFs under constant elementary stress are reported in the last column.

9.3.2 FCG Simulation

Employing the SIF results found in the previous section, the growth of a semi-elliptical surface crack in a plate due to mode I fatigue loading calculated using the Paris law (9.2). Propagation rates are calculated for the deepest point on the crack front, A, and for the near-surface point, B, which is situated at $\zeta/c = 0.1$ (cf. Figures 9.8, 5.7 and Section 5.3.4). Values of $K_{I(n)}^*$ at the surface point, C, have not been computed (cf. Section 5.3.4).

Points A and B propagate in the zx -plane perpendicular to the crack front (cf. Figure 9.11). It is assumed that the crack front hereby keeps its semi-elliptical shape. Thus, under one cyclic loading the crack front with semi-axes a and c grows to a new configuration

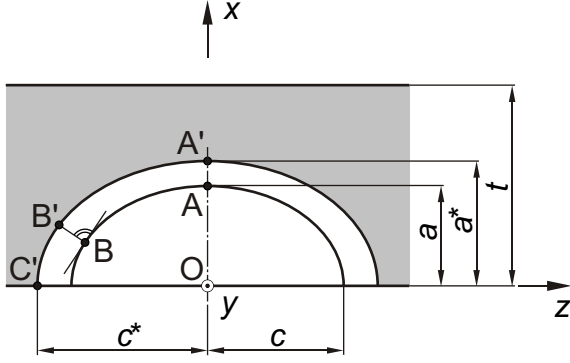


Figure 9.11: Two-parameter model of fatigue crack growth.

that is defined by the expression

$$\frac{x^2}{(a^*)^2} + \frac{z^2}{(c^*)^2} = 1 \quad (9.25)$$

where a^* and c^* are the semi-axes of the surface crack after one load cycle (Figure 9.11).

Fatigue crack growth paths are generated numerically for different initial surface cracks and for three cyclic stress fields, $\sigma_{b,circ}$, $\sigma_{b,opt}$ and σ_{bn} (cf. Figures 9.12(a)(d), (b)(e) and (c)(f), respectively). Loading conditions and initial ξ values of the numerical simulations are chosen according to the experimentally observed surface cracks.

Beach mark data for cracks that propagated in the stress field of quarter-circular and shape optimised T-joint specimen transitiones were created in experimental fatigue tests presented in Chapter 7 (cf. Table 7.2). Here, the nominal loading conditions are characterised by the stress range $\Delta\sigma_{bn} = 820$ MPa and the load ratio $R_L = 0.1$. Material constants in the Paris Equation (9.2) for $R = 0.1$ were employed and were assumed to be $m = 3.26$ and $C = 3.85 \cdot 10^{-13}$ (with da/dN expressed in m/cycle and ΔK in $\text{MPa}\sqrt{\text{m}}$).

Beach mark data of the crack in the nominal T-joint section are taken from [157]. The respective load data are $\Delta\sigma_{bn} = 616$ MPa and $R_L = 0.3$. Here, Paris data for $R = 0.5$ were employed, giving $m = 3.1$ and $C = 2 \cdot 10^{-12}$.

Fatigue crack propagation paths in the diagram of $\alpha = a/c$ against $\xi = a/t$ are shown in Figures 9.12(a)–(c) for $\sigma_{b,circ}(w)$, $\sigma_{b,opt}(w)$ and $\sigma_{bn}(w)$, respectively. Seven different initial cracks are considered (No.s from 1 to 7), with an initial shape defined by two parameters (ξ_i, α_i) : the relative crack depth, ξ_i , is equal for all the six cracks of each stress field considered, whereas the initial flaw aspect ratio, α_i , ranges from 0.2 to 1.2.

As can be observed in Figure 9.12, fatigue crack growth paths tend to converge to a common asymptote. For the cracked nominal section and the cracks that grow in the stress field of the shape optimised T-joint transition, the crack configurations approach decreasing values of α for increasing values of ξ . The slope of the nominal section asymptote in Figure 9.12(c) is steeper than the one in Figure 9.12(b) for the shape optimised transition. In the case of the quarter-circular transition stress field, fatigue crack growth paths converge to a common α value that increases for higher ξ values (cf. Figure (9.12(a))).

Experimental results are reported in Figure 9.12(d)–(f), where the solid symbols indicate the values of ξ and α for the semi-ellipses that best fit the “beach marked” crack fronts during the fatigue tests performed (cf. Section 7.1.3). As can be observed, the numerical fatigue crack growth paths are in satisfactory agreement with the experimental results.

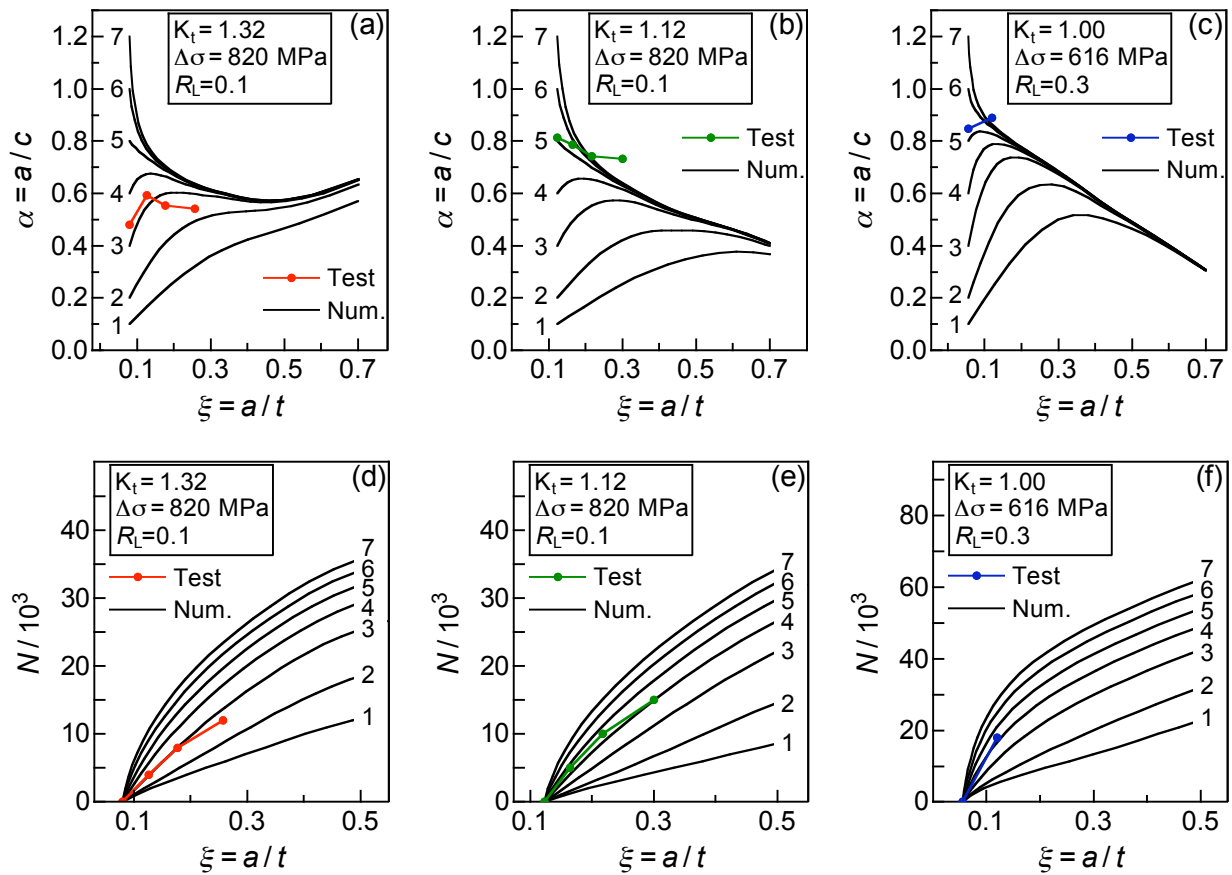


Figure 9.12: Development of fatigue cracks in different T-joint stress fields for different initial values of α . (a)(d) Quarter-circular transition. (b)(e) Shape optimised transition. (c)(f) Unnotched nominal section. Numerical Simulation (curves 1–7) and beach mark results from experimental fatigue testing (circular symbols).

In Figures 9.12(d)–(f) the number of loading cycles, N , against the relative crack depth, ξ , is displayed for the stress distributions $\sigma_{b,circ}(w)$, $\sigma_{b,opt}(w)$ and $\sigma_{bn}(w)$, respectively. The seven initial flaws (No.s 1–7) considered in Figures 9.12(a)–(c) are examined. Again, beach mark data from experimental tests are displayed. It can be observed that the depth of the surface crack grows more rapidly for initial low values of α (for instance, crack No. 1) compared to cases characterised by high values of α (for instance, crack No. 7).

A more detailed presentation of these comparative results is provided in Section 9.4.3.

9.4 Methods Comparison

So far, different stress intensity factor solutions for linear and non-linear stress gradients in surface-cracked plates have been presented. A fatigue crack growth methodology for Francis runner surface cracks has been established and applied to cracks in standard and shape optimised transitions, employing SIFs of Pommier et al. [113]. Applying the work of Carpinteri et al. [126], beach marks from experimental fatigue testing have been investigated by fatigue crack growth simulation.

Comparative investigations of the different SIF solutions and the individual FCG methods associated are carried out in the following.

9.4.1 SIF Values

Figures 9.13 to 9.16 show the dimensionless stress intensity factors, K^* , of the Pommier et al. [113] and the Carpinteri et al. [126] solutions for relative crack depths $\xi = 0.1, 0.2, 0.3$ and 0.5 . Since Pommier et al. consider the semi-infinite body, SIF values displayed for a certain relative thickness, ξ , are here calculated for a crack depth, a , obtained for the finite thickness solutions [102, 126]. The stress fields considered are again T-joint stress distributions from nominal bending loading in the quarter-circular transition, $\sigma_{b,circ}$, in the shape optimised transition, $\sigma_{b,opt}$, and in the nominal section, σ_{bn} . Additionally, the stress field in the nominal section under nominal tensile loading, $\sigma_{tens,n}$, is displayed. The solution of Newman and Raju [102] provides SIF values for the two latter stress fields and is reproduced in the respective diagrams. All K^* values presented are drawn vs. the crack front location angle, ϕ , as it is defined in Figure 5.6 on page 40.

For $\xi = 0.1$ (cf. Figures 9.13(a)–(d)), K^* values generated by the Pommier et al. solution for the deepest point, A, exceed the Carpinteri et al. values by 0.025–0.035. This is observed for all stress distributions and for all considered crack aspect ratios, α . For the near-surface point, B, Pommier and Carpinteri SIFs are approximately the same for $\alpha = 1.0$ and 1.2 . For lower α values, Pommier values exceed those of Carpinteri by 0.04–0.06.

For high values of α , Newman-Raju values follow the Pommier solution for all points along the crack front. For lower α , Newman-Raju SIF values exceed Pommier values between points A and B. For $\alpha = 0.5$, the difference is between 0.025 and 0.1. However, in points B and C this difference is reduced to 0–0.02.

For $\xi = 0.2$ (cf. Figures 9.14(a)–(d)) the Carpinteri and Pommier solutions are in good agreement. In point A the difference in SIF values ranges between 0 and 0.02. At point B the set of curves is more spread for Pommier than for Carpinteri and shows lower SIF values for high values of α and higher SIF values for low α values, for all stress distributions.

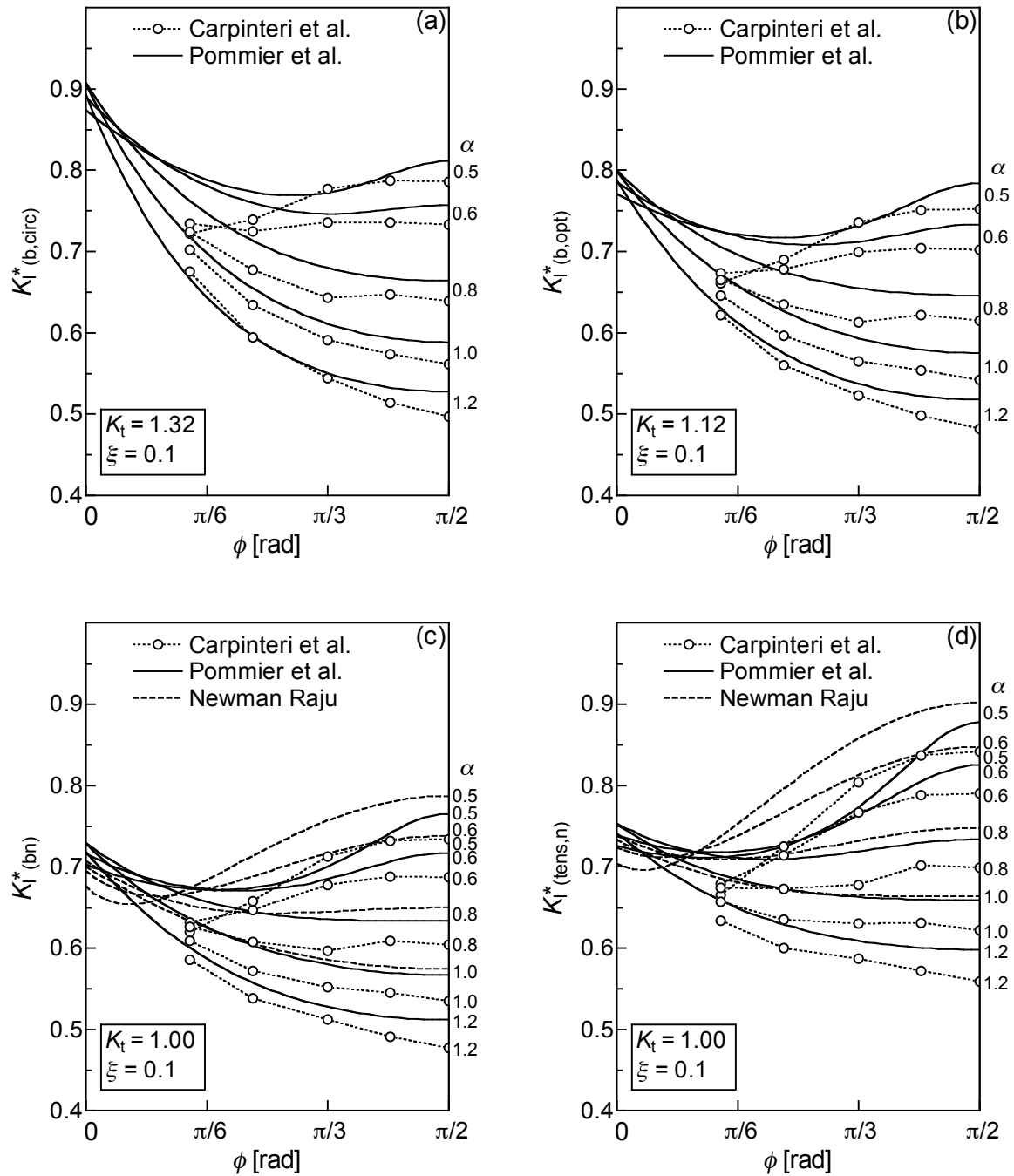


Figure 9.13: Dimensionless SIF along the crack front for $\xi = a/t = 0.1$ after solutions of [102, 113, 126], with ϕ defined as shown in Fig. 5.6. T-joint stress distributions from nominal bending (a)–(c) and nominal tensile load (d). (a) Quarter-circular transition, $\sigma_{b,circ}$. (b) Shape optimised transition, $\sigma_{b,opt}$. (c) Nominal section, σ_{bn} . (d) Nominal section, $\sigma_{tens,n}$.

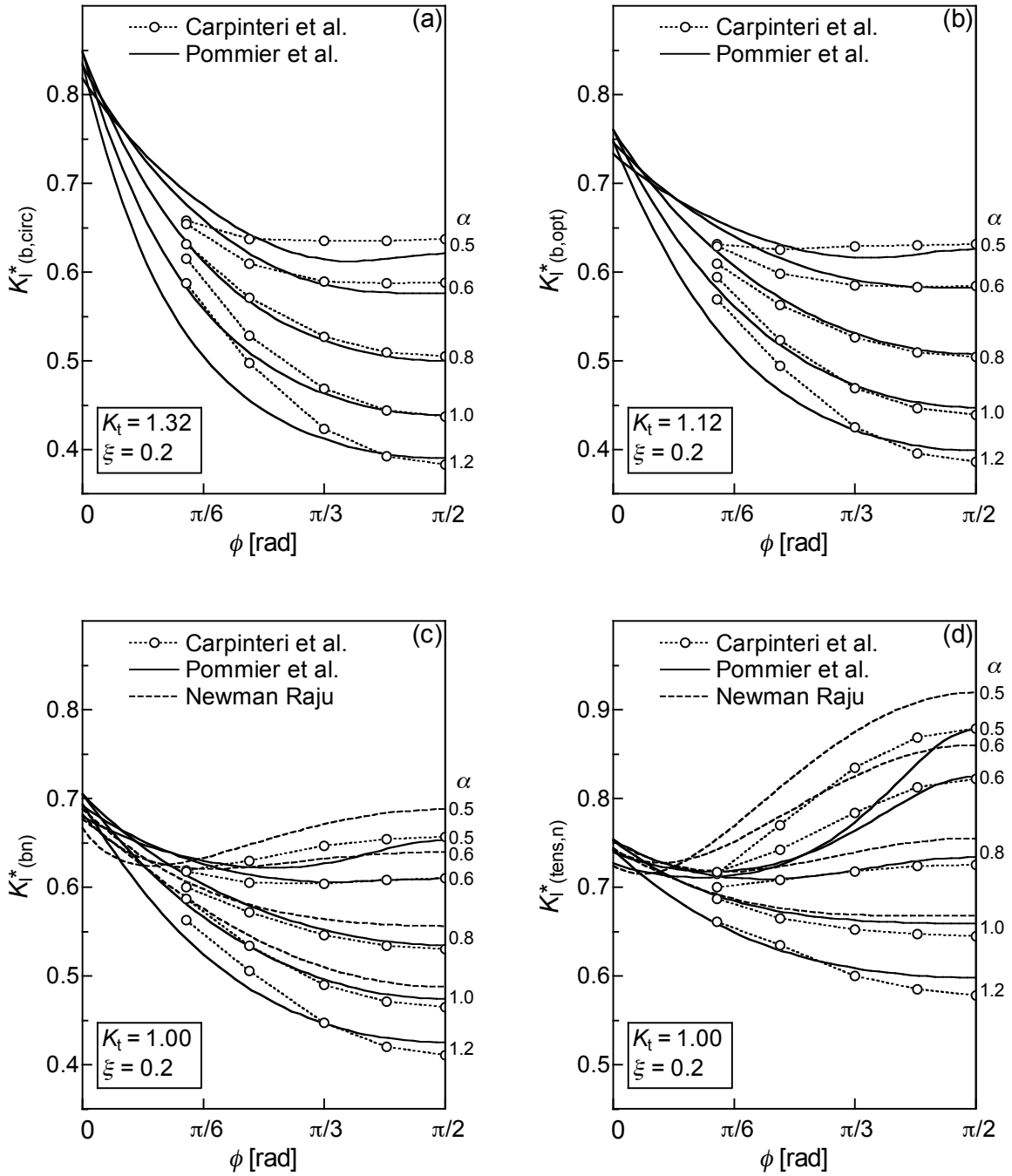


Figure 9.14: Dimensionless SIF along the crack front for $\xi = a/t = 0.2$ after solutions of [102, 113, 126], with ϕ defined as shown in Fig. 5.6. T-joint stress distributions from nominal bending (a)–(c) and nominal tensile load (d). (a) Quarter-circular transition, $\sigma_{b,circ}$. (b) Shape optimised transition, $\sigma_{b,opt}$. (c) Nominal section, σ_{bn} . (d) Nominal section, $\sigma_{tens,n}$.

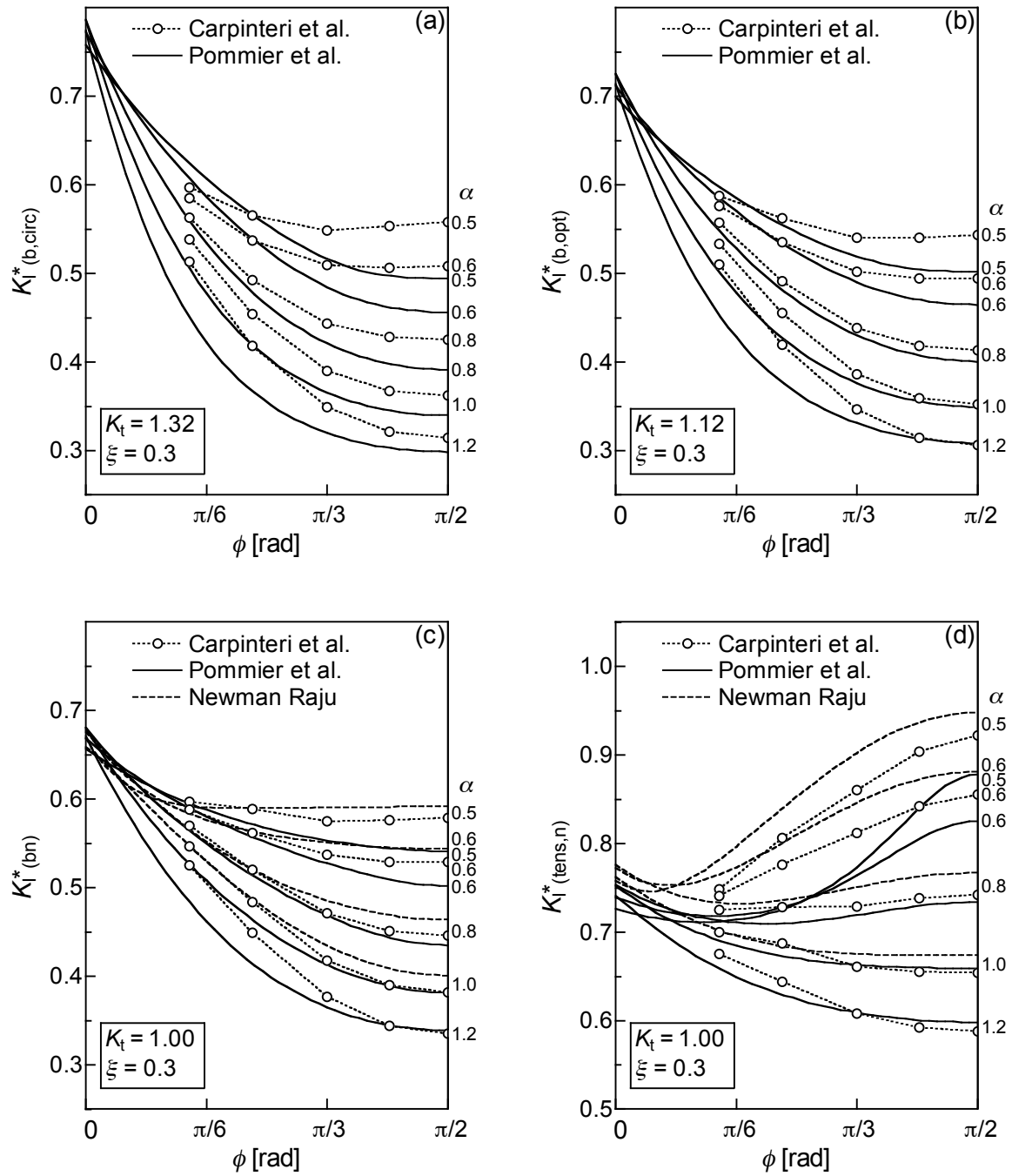


Figure 9.15: Dimensionless SIF along the crack front for $\xi = a/t = 0.3$ after solutions of [102, 113, 126], with ϕ defined as shown in Fig. 5.6. T-joint stress distributions from nominal bending (a)–(c) and nominal tensile load (d). (a) Quarter-circular transition, $\sigma_{b,circ}$. (b) Shape optimised transition, $\sigma_{b,opt}$. (c) Nominal section, σ_{bn} . (d) Nominal section, $\sigma_{tens,n}$.

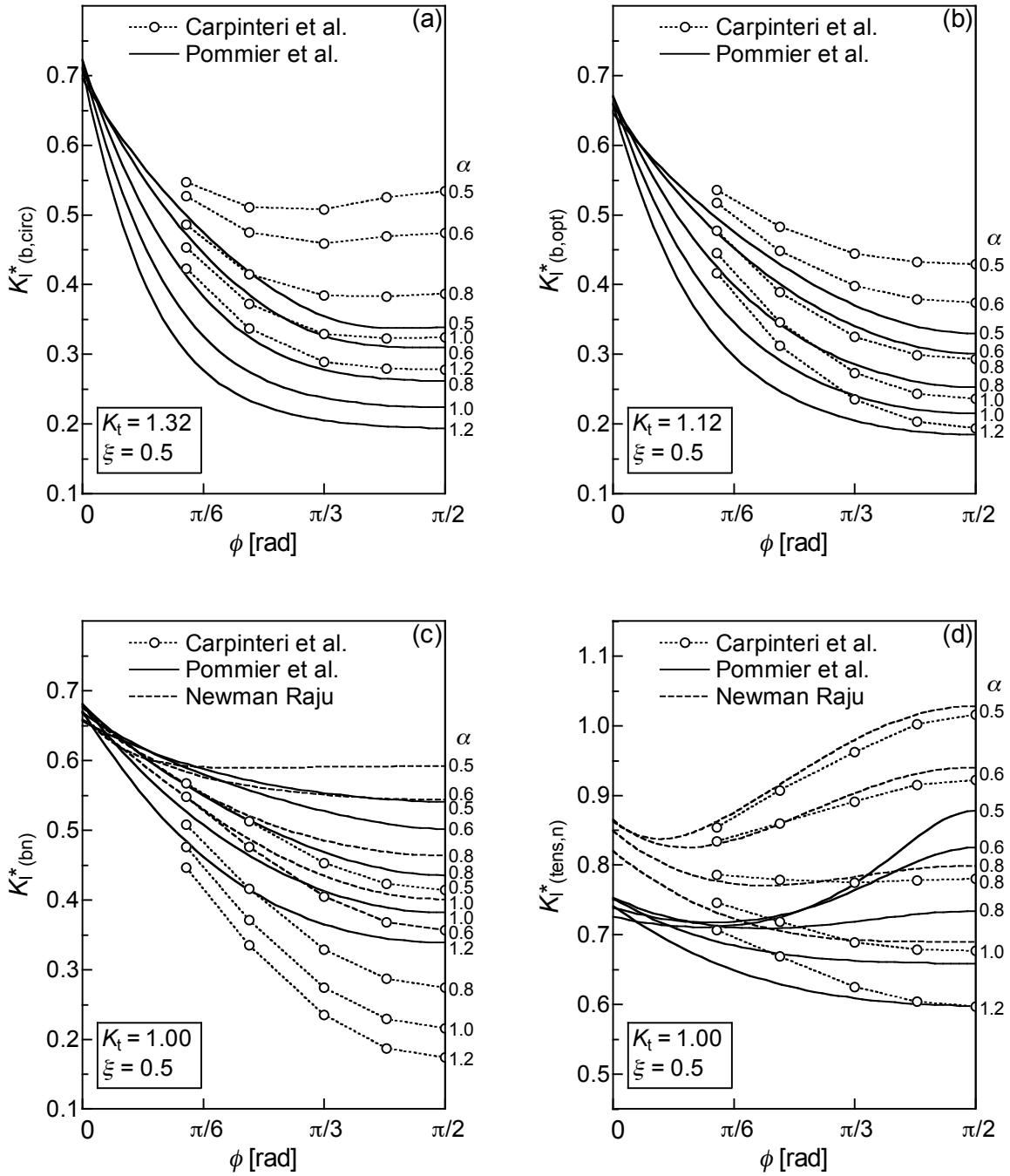


Figure 9.16: Dimensionless SIF along the crack front for $\xi = a/t = 0.5$ after solutions of [102, 113, 126], with ϕ defined as shown in Fig. 5.6. T-joint stress distributions from nominal bending (a)–(c) and nominal tensile load (d). (a) Quarter-circular transition, $\sigma_{b,circ}$. (b) Shape optimised transition, $\sigma_{b,opt}$. (c) Nominal section, σ_{bn} . (d) Nominal section, $\sigma_{tens,n}$.

Table 9.5: FCG methodology results for different SIF solutions. Number of LCF cycles ($\Delta\sigma_1(x=0) = 500$ MPa, $m = 3$, $C = 10^{-11}$) required for initially semi-circular surface crack to become critical with respect to vibration loading ($D = 0.1$).

Stress field	Type of crack growth analysis	$a_i = c_i$ [mm]	a_c [mm]	c_c [mm]	N [cycles]
Membrane	simplified	0.5	1.44	1.44	14 550
	Newman-Raju [102]	0.5	1.48	1.65	16 340
	Pommier et al. [113]	0.5	1.45	1.69	15 890
	Carpinteri et al. [126]	0.5	1.78	1.89	24 310
Bending	Newman-Raju	0.5	1.75	2.10	20 780
	Pommier et al.	0.5	1.72	2.18	20 250
	Carpinteri et al.	0.5	2.22	2.59	32 270
T-joint	Pommier et al.	0.5	2.81	4.67	35 700
circular	Carpinteri et al.	0.5	4.26	6.35	61 580

Newman-Raju fits well for high α but generates SIF values that exceed the Pommier and Carpinteri values for low α values by more than 0.1.

For $\xi = 0.3$ (cf. Figures 9.15(a)–(d)), methods that consider a finite body thickness give similar values while Pommier values for low α values fall behind. This effect is most significant for SIF values in the deepest point, A, and especially in the case of the non-linear stress distributions (cf. Figures 9.15(a)(b)).

For $\xi = 0.5$ (cf. Figures 9.16(a)–(d)) the trends described above for $\xi = 0.3$ are intensified, with exception of the nominal bending stress field (cf. Figure 9.15(c)) as here Carpinteri values are much lower than those derived from Newman-Raju [102] (finite plate width) and Pommier [113] (infinite width).

9.4.2 FCG Methodology Calculation

In Sections 9.2.1 and 9.2.2, Fatigue crack growth simulation according to the FCG methodology presented in Chapter 4 was calculated for standard and shape-optimised T-joint geometries. The investigation is now completed by the nominal bending load case and the Carpinteri et al. FCG method based on SIF values presented above. FCG results derived from Newman-Raju equations (cf. Section 5.3.2) are displayed where applicable.

Values of the relative crack depths covered by the Carpinteri et al. [126] solution ($0.1 \leq \xi \leq 0.7$) are higher than the ξ values of the chosen initial crack configuration. SIF values for the respective crack depths ($\xi < 0.1$) were therefore generated by linear extrapolation of the $\xi = 0.1$ and $\xi = 0.2$ SIF values.

The values displayed in Table 9.5 show excellent agreement between crack depths, crack lengths and fatigue life results from Newman-Raju and Pommier et al. Further, it becomes clear that the SIF values of Carpinteri et al. [126] that were extrapolated to relative crack depths below $\xi = 0.1$ are lower than for other solutions employed.

9.4.3 FCG Calculation and Beach Marks

It is of interest to find out how well predictions that base on the fatigue crack growth models presented agree with experimental observations. Results from different crack growth simulation tools are now compared with beach mark data from experimental fatigue testing (cf. Section 7.1.4).

Stress Correction for Plasticity

In order to account for plasticity effects at the T-joint transition that occur due to high loading rates under fatigue testing (cf. Chapter 7), the effect of a local, effective stress range at the transition surface on the FCG simulation has been investigated. For the Pommier et al. FCG simulation method, the local stress range at the surface point, C, was reduced to the local stress amplitude value derived from Neuber plasticity correction (8.3). Further modification to an equivalent stress amplitude, $\bar{\sigma}_a$, was performed according to Walker's equation for crack closure (8.5). At the deepest point, A, stress conditions were assumed to show the elastic behaviour as defined in Equations (9.8) and (9.21).

Carpinteri et al. propagate the crack front at the deepest point, A, and at the near-surface point, B. By definition, the location of B is at $x = 0.436a$ for all crack aspect ratios, $\alpha = a/c$. Thus, the point B x -co-ordinate of a crack that propagates in plate thickness direction changes continuously. As amplitudes of the local stress field for a certain configuration and for fixed values of x are constant, point B is not as well suited for modifications of the surface stress field as is point C where stress ranges are constant.

For the relative crack depths and loading conditions considered it is therefore assumed that stresses at point B are unaffected from plasticity effects that appear in the surface zone at the transition. Stress field modifications that account for surface layer effects in the Carpinteri et al. FCG method may preferably be realised by the definition of a completely new stress field and by new coefficients $B_{n(L)}$ (5.21) instead.

Stress correction for plasticity effects was performed for the Pommier et al. method only (cf. "Pommier corr." curves in Figures 9.17(a) and (b)). The equivalent values of stress range, $\overline{\Delta\sigma}_C$, employed at the surface point, C, are 892 MPa and 875 MPa in the stress field of the quarter-circular and the shape optimised T-joint transition, respectively. Material constants in the Paris crack growth equation (9.2) for both FCG methods and all points along the crack front are set to the values for $R = 0.1$, which are $m = 3.26$ and $C = 6.15 \cdot 10^{-13}$. Thus, crack lengths calculated for the "Pommier corr." curves employing $\overline{\Delta\sigma}_C$ are slightly overestimated.

For the specimens showing the quarter-circular and the shape-optimised transition, $\sigma_n = 820$ MPa and $R = 0.1$. The number of load cycles that significantly propagate the crack front between beach marks is $\Delta N = 4000$ and $\Delta N = 5000$, respectively (cf. Figures 9.17(a) and (b)). In the case of the crack that propagates in the nominal section under pure bending loading, $\sigma_n = 616$ MPa, $R = 0.3$ and $\Delta N = 18\,000$. Here, $m = 3.1$ and $C = 2 \cdot 10^{-12}$ (for $R = 0.5$)(cf. Figure 9.17(c)).

Results

Already in Section 9.4.2 it was observed that SIF values derived from Carpinteri et al., which are extrapolated to relative crack depths $\xi < 0.1$, are relatively low. This is obvious for the beach marks and calculated crack fronts in the nominal bending stress field in

Figure 9.17(c), with $a_i = 1.1$ mm and $c_i = 1.3$ mm. The same applies to the stress field of the quarter-circular T-joint transition (cf. Figure 9.17(a)) where the initial crack shows $\xi < 0.08$. In the case of the stress field of the shape optimised T-joint transition, Carpinteri et al. FCG slightly underestimates beachmarks, especially if further retardation of FCG at the surface points due to the effect of notch surface plasticity is taken into consideration.

It can generally be stated that the Carpinteri et al. FCG simulation method satisfactorily reproduces the crack shape aspect ratio of beach marks from experimental fatigue testing. Extrapolation of SIF values to relative crack depths that are below the covered range of $0.1 \leq \xi \leq 0.7$ underestimates beach marks. As the effect of the finite plate thickness for small relative crack depths should be marginal, the Carpinteri et al. SIF values are apparently low for $\xi = 0.1$. This assumption is substantiated by SIF data presented in Figures 9.13–9.15.

Applying the Pommier et al. SIF solution, FCG results are in good agreement with beach mark results. Overestimation of crack lengths, c , can be attributed to surface plasticity effects.

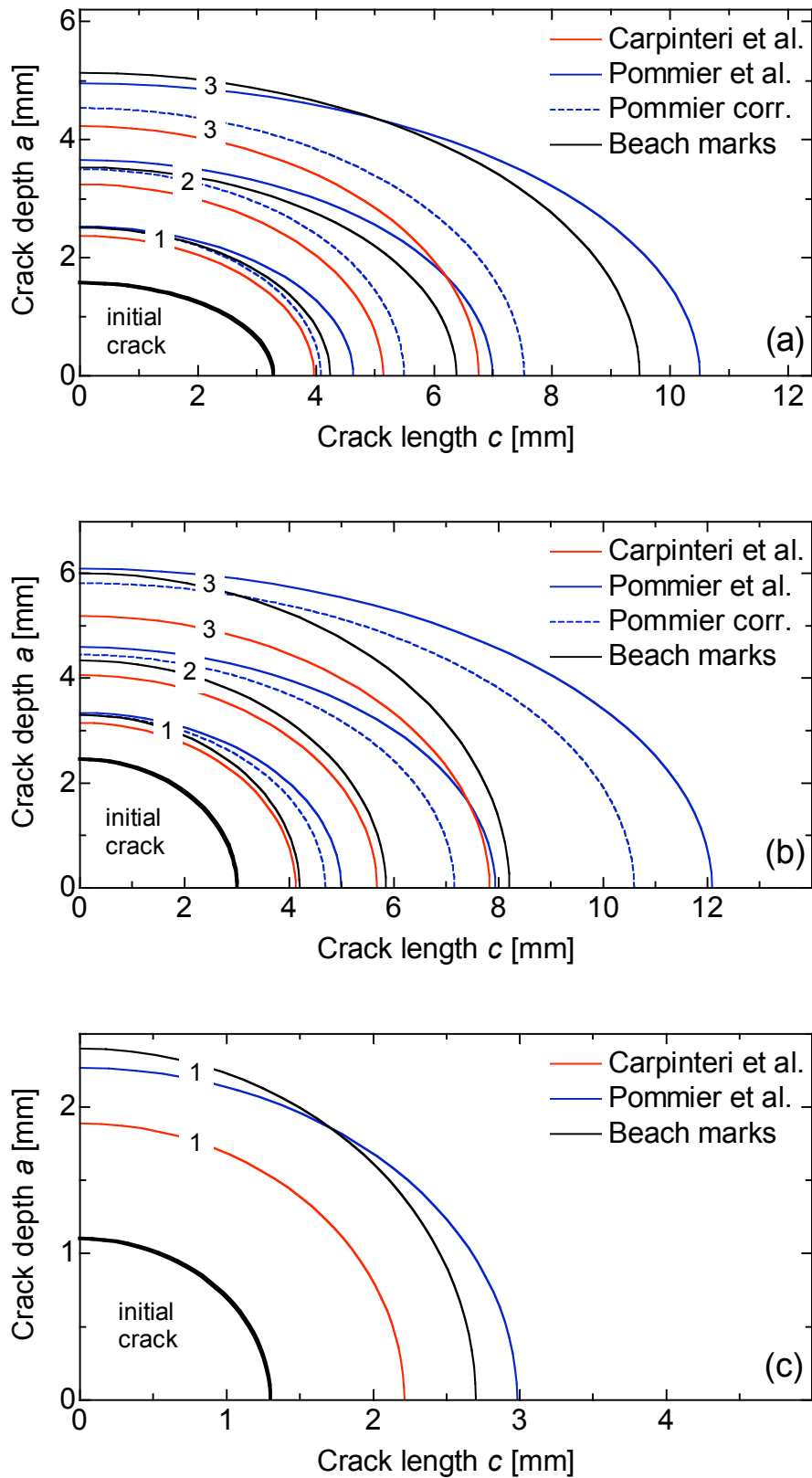


Figure 9.17: Fatigue crack growth simulation between beach marks from T-joint specimen tests under nominal bending fatigue loading. (a) Quarter-circular transition (specimen 1.7), $\Delta N = 4000$. (b) Shape optimised transition (specimen 2.7), $\Delta N = 5000$. (c) Nominal section (beach marks from [157]), $\Delta N = 18\,000$.

Chapter 10

Summary

10.1 Discussion and Conclusions

A design procedure for turbine runners has been suggested, which considers the growth of a crack under start-stop cycles until the crack becomes large enough to grow under vibrational loading. In particular, fatigue crack growth in the transition between the blade and the band or crown of a Francis turbine runner has been analysed. The transition has been idealised by simple models where the transition between the two members is characterised by constant curvatures.

Finite Element Analysis

The stress concentration factor of the T-joint transition is acceptably predicted by an FE model, when there are at least 5-6 second-order quadrilateral elements along the quarter-circular transition arc. A simplified, coarse FE model, neglecting the finite transition curvature, can be used to compute the undisturbed (nominal) stress field.

Three-dimensional (3D) FEA of the trailing edge transition showed that the transition radius, R , is more decisive for stress concentration than the blade edge radius, r . Moreover, the blade dimensions of the model proved to have a significant influence on the stress concentration factor.

Stress Intensity Factors

Comparing various results found in the literature, the detailed component geometry showed to have only minor impact to the stress intensity factor (SIF) values, especially for relatively small cracks. Therefore, in order to simplify the problem, the stress intensity factors of semi-elliptic surface cracks in plates under non-linear stress fields are computed by means of solutions of Pommier et al. [113] and of Carpinteri et al. [126].

The solution of Pommier et al. [113] provides approximate equations derived from body force analysis. The solution considers a large plate subjected to a 3rd grade polynomial distribution of the stress field in direction of the crack depth, a , and covers crack aspect ratios a/c between 0.5 and 2.

In the work of Carpinteri et al. [126], a finite-thickness plate with a semi-elliptical surface crack has been analysed. Relative crack depths, a/t , between 0.1 and 0.7, and crack aspect ratios, a/c , between 0.1 and 1.2 are covered. 3D FE analysis has been carried

out to determine the SIF values for different elementary loading conditions applied to the cracked plate. These loading conditions have been used to model the actual stress field at the expected crack location in the T-joint specimen and, by applying the superposition principle and the power series expansion of an arbitrary stress field, an approximate SIF for the cracked T-joint has been obtained.

Shape Optimisation

In order to increase fatigue properties in the critical locations of the Francis runner, the (2D) T-joint and (3D) trailing edge transitions have been shape optimised. For this, the standard circular shapes have been modelled employing B-splines. Manual and ANSYS-automated iterative modifications of the B-splines then resulted in lower stress concentration. The following statements can be given:

- The higher the stress concentration, the steeper is the slope of the notch stress gradient. In the T-joint, the stress slopes of the design solutions considered coincide at $a/t_1 = 0.075$ (cf. Figure 6.9).
- Stress concentration in the T-joint due to bending load could virtually be eliminated. The required geometrical changes reduce stress concentration to a minimum but create a shape that is considered to be more sensitive to manufacturing tolerances.
- In T-joint shape optimisation, a B-spline, defined by end slopes and end point coordinates only, proved to be the most effective design boundary solution for a reasonable grade of optimisation, i. e. for a transition zone that is slightly enlarged. This most effective B-spline boundary solution was also employed in shape optimisation of the trailing edge transition and resulted in a similar reduction of the stress concentration.
- The shape optimisation strategy presented for the trailing edge transition employs five design variables and yields a number of different shape optimisation solutions. These *local* optimum solutions show a level of stress concentration which is only slightly elevated, compared to the *absolute* optimisation solution found. The absolute optimum solution shows the lowest stress concentration at the trailing edge transition and reduces the problem to only two design variables. Design requirements beyond mechanical integrity, e. g. hydromechanical design criteria, may be met by a shape solution that follows a local optimum shape solution. A local optimum solution has been realised in the optimised 3D fatigue test specimens.
- Reasonable shape optimisation reduces the stress concentration factor, K_t , from 1.32 to 1.12 in the T-joint transition. For the trailing edge specimen, the stress concentration of $K_t = 1.68$ was reduced to 1.31 in the absolute optimum solution of the moderately optimised geometry.

Fatigue Testing

Standard circular-shaped and moderately optimised transitions were subjected to experimental fatigue testing. The T-joint specimens underwent stress-relieving annealing treatment after welding. Nevertheless, coarse and inhomogeneous surfaces of cracks in the welded transition zone attest to the sustained influence of the welding.

The trailing edge tests revealed a low fatigue strength of cast steel material. Inclusions and pores of up to 3 mm in size and of various shapes were distributed evenly in the cast steel material. These defects proved to have a more detrimental effect to fatigue strength than the stress concentration of the optimised transition.

Further, it can be stated that high-quality hot-rolled steel may show material defects that are sensitive to fatigue loading: the centre line of the trailing edge specimens coincided with that of the cylindrically rolled bar stock from which they were machined. All along this longitudinal axis a material discontinuity was observed. In two of the eight hot-rolled steel specimens tested, fatigue cracks grew from this material defect, before fatigue cracks propagated from the (shape optimised) transitions.

Both the shape optimised T-joint and trailing edge specimens showed an increase in fatigue life by a factor 2–2.5, compared to the quarter-circular shaped specimens.

Fatigue Crack Growth Calculation

Using the SIF solutions described above in combination with Paris' law, the growth of surface cracks in a variable T-joint stress field can be predicted. Predictions compare well with beach marks observed in T-joint specimens with quarter-circular and shape optimised transitions.

Beach mark shapes are reproduced well by the Carpinteri et al. [126] solution. Fatigue crack growth (FCG) of small cracks at a relative crack depth $a/t < 0.2$ is somewhat underpredicted due to low SIF values compared to the solutions of Pommier et al. [113] and Newman and Raju [102].

Failure in FCG calculation has been defined by the condition $\Delta K_{\text{HCF}} \geq \Delta K_{\text{th}}(R_{\text{HCF}})$ all along the crack front. This condition may be reconsidered and failure may be defined earlier for a state with HCF crack growth present at a few points on the crack front.

Exemplary fatigue crack growth calculations of a crack which grows from the location of highest stress concentration on different T-joint transitions have been performed. For the moderately optimised T-joint shape D, Pommier-code FCG simulation yields an increase in FCG life of 54 percent, compared to the standard quarter-circular transition. The T-joint transition solution that shows the lowest stress concentration factor, $K_t = 1.02$, increases fatigue life by 81 percent in the exemplary calculation of FCG in pre-cracked T-joints. Considering further the results from experimental fatigue testing, the conclusion can be drawn that shape optimisation is recommendable for Francis turbine runner design.

10.2 Suggestions for further Work

In the course of this work, more SN data of 16Cr-5Ni material derived from notched and smooth specimens would have been helpful, especially for lives $N = 10^4$ – 10^6 .

In shape optimisation, it should be possible to eliminate the stress concentration at the trailing edge transition by a further extension of the transition zone.

For low relative crack depths, $a/t \leq 0.2$, SIF values of the Carpinteri et al. solution should be revised.

The propagation of fatigue cracks from the Francis runner trailing edge transition might be investigated by means of FRANC3D or similar FCG simulation codes. Beach mark results have been generated in experimental fatigue testing of the trailing edge specimen, and the comparison with FCG calculations would be interesting.

In the present work, constant (LCF) amplitude loading has been considered. The fatigue methodology presented can easily be adjusted for an arbitrary load history. Recording of representative in-service fatigue load history data and the subsequent application of the rain-flow method in combination with the Miner rule might be an appropriate method to adjust loading conditions and thus enhance the accuracy of fatigue life predictions in specific components.

Bibliography

- [1] Key world energy statistics. Technical report, International Energy Agency, Paris, 2003.
- [2] *The International Journal on Hydropower & Dams World Atlas and Industry Guide*. Aqua Media International, Sutton, Surrey, England, 2000.
- [3] Renewables for power generation – Status and prospects. Technical report, International Energy Agency, Paris, France, 2003. ISBN 92-64-0191-89.
- [4] Håkon Opsund. The energy sector and water resources in Norway 2004. Technical report, Norwegian Ministry of Petroleum and Energy, 2004. ISSN 1501-6390.
- [5] B. S. Massey. *Mechanics of Fluids*. Chapman & Hall, London, sixth edition, 1989. ISBN 0-412-34280-4.
- [6] A. Kjølle. Hydropower in Norway – Mechanical Equipment. Survey, NTNU, Department of Energy and Process Engineering, Trondheim, 2001.
- [7] J. Y. Mann. *Bibliography on the fatigue of materials, components and structures*, volume 1–4, covering 1838–1969. Pergamon Press, Oxford, 1970–1990.
- [8] W. Schütz. Zur Geschichte der Schwingfestigkeit. *Materialwissenschaft und Werkstofftechnik*, 24:203–232, 1993. ISSN 0933-5137. English version: A history of fatigue. *Engineering Fracture Mechanics*, 54(2):263–300, 1996. ISSN 0013-7944.
- [9] K. H. Kloos. 100 Jahre Materialforschung und -prüfung als Grundlage innovativer Produktentwicklungen. *Materialwissenschaft und Werkstofftechnik*, 28:305–339, 1997. ISSN 0933-5137.
- [10] S. Suresh. *Fatigue of Materials*. Cambridge University Press, Cambridge, 2nd edition, 1998. ISBN 0-521-57046-8.
- [11] J. Schijve. Fatigue of structures and materials in the 20th century and the state of the art. *International Journal of Fatigue*, 25:679–702, 2003. ISSN 0142-1123.
- [12] F. Braithwaite. On the fatigue and consequent fracture of metals. *Minutes of Proceedings of the Institution of Civil Engineers*, 13:463–474, 1854.
- [13] W. A. J. Albert. Über Tragseile am Harz. *Archive für Mineralogie, Geognosie, Bergbau und Hüttenkunde*, 10:215–234, 1837.

- [14] R. A. Smith. The Versailles railway accident of 1842 and the first research into metal fatigue. In H. Kitagawa and T. Tanaka, editors, *Fatigue 90. Proceedings of the 4th International Conference on Fatigue and Fatigue Thresholds, 15-20 July, 1990 in Honolulu*, volume 4, pages 2033–2041, Birmingham. Materials and Component Engineering Publications Ltd. ISBN 1-8721-3608-7.
- [15] W. J. M. Rankine. On the causes of the unexpected breakage of the journals of railway axles; and on the means of preventing such accidents by observing the Law of Continuity in their construction. *Minutes of Proceedings of the Institution of Civil Engineers*, 2:105–108, 1843.
- [16] A. Morin. *Leçons de Mécanique pratique — Résistance des Matériaux*. Paris, Librairie de L. Hachette et Cie, 1853.
- [17] J. A. Ewing and J. C. W. Humfrey. The fracture of metals under repeated alternations of stresses. *Philosophical Transactions of the Royal Society of London. A, Mathematical and Physical Sciences*, 200:241–250, 1903. ISSN 0080-4614.
- [18] P. J. E. Forsyth. The application of “fractography” to fatigue failure investigations. Technical Report 257, Royal Aircraft Establishment, Farnborough, 1957.
- [19] D. A. Ryder. Some quantitative information obtained from the examination of fatigue fracture surfaces. Technical Report 288, Royal Aircraft Establishment, Farnborough, 1958.
- [20] A. Wöhler. Bericht über die Versuche, welche auf der königl. Niederschlesisch-Märkischen Eisenbahn mit Apparaten zum Messen der Biegung und Verdrehung von Eisenbahnwagenachsen während der Fahrt angestellt wurden. *Zeitschrift für Bauwesen*, 8:641–652, 1858.
- [21] A. Wöhler. Versuche zur Ermittlung der auf die Eisenbahnwagen-Achsen einwirkenden Kräfte und die Widerstandsfähigkeit der Wagen-Achsen. *Zeitschrift für Bauwesen*, 10:583–616, 1860.
- [22] A. Wöhler. Über die Festigkeits-Versuche mit Eisen und Stahl. *Zeitschrift für Bauwesen*, 20:73–106, 1870.
- [23] O. H. Basquin. The exponential law on endurance tests. In *Proceedings of the annual meeting – American Society for Testing and Materials*, volume 10, pages 625–630, 1910. ISSN 1047-9376.
- [24] J. Bauschinger. Über die Veränderung der Elastizitätsgrenze und des Elastizitätsmoduls verschiedener Metalle. *Der Civilingenieur – Organ des Sächsischen Ingenieur- und Architekten-Vereins*, 27:289–348, 1881.
- [25] J. Bauschinger. Über die Veränderung der Elastizitätsgrenze und der Festigkeit des Eisens und Stahls durch Strecken und Quetschen, durch Erwärmen und Abkühlen und durch oftmals wiederholte Beanspruchung. *Mittheilungen aus dem Mechanisch-technischen Laboratorium München*, 13:1–115, 1886.

- [26] S. S. Manson. Behaviour of materials under conditions of thermal stress. In *Heat Transfer Symposium*, pages 9–75. University of Michigan, Engineering Research Institute, 1953.
- [27] L. F. Coffin. A study of the effects of cyclic thermal stresses on a ductile metal. *Transactions of the American Society of Mechanical Engineers*, 76(6):931–950, 1954.
- [28] G. Kirsch. Die Theorie der Elastizität und die Bedürfnisse der Festigkeitslehre. *Zeitschrift des Vereines Deutscher Ingenieure*, 42:797–807, 1898.
- [29] C. E. Inglis. Stresses in a plate due to the presence of cracks and sharp corners. *Transactions of the Institution of Naval Architects*, 55:219–241, 1913. ISSN 0035-8967.
- [30] E. Preuß. Versuche über die Spannungsverteilung in gekerbten Zugstäben. *Zeitschrift des Vereines Deutscher Ingenieure*, 57:664–667, 1913.
- [31] H. Neuber. *Kerbspannungslehre. Grundlagen für eine genaue Spannungsrechnung*. Springer-Verlag, Berlin, 1937, 1958 and 1985.
- [32] H. Neuber. *Theory of Notch Stresses*. Ann. Arbor, Michigan, 1946.
- [33] H. Neuber. Über die Berücksichtigung der Spannungskonzentration bei Festigkeitsberechnungen. *Konstruktion im Maschinen-, Apparate- und Gerätebau*, 20(7):245–251, 1968. ISSN 0720-5953.
- [34] H. Neuber. Theory of stress concentration for shear strained prismatical bodies with arbitrary non-linear stress–strain law. *Transactions of the ASME, Journal of Applied Mechanics*, 28:544–550, 1961. ISSN 0021-8936.
- [35] G. Härkegård and H.-J. Huth. Approximate viscoplastic notch analysis. In S. Murakami and N. Ohno, editors, *Creep in Structures, Proceedings of the 5th IUTAM Symposium on Creep in Structures, April 2000 in Nagoya, Japan*, pages 287–296. Dordrecht, 2001. Kluwer Academic Publishers. ISBN 0-7923-6737-5.
- [36] G. Härkegård and T. Mann. Neuber prediction of elastic-plastic strain concentration in notched tensile specimens under large-scale yielding. *Journal of Strain Analysis for Engineering Design*, 38(1):79–94, 2003. ISSN 0309-3247.
- [37] W. D. Pilkey. *Peterson's stress concentration factors*. John Wiley and Sons, New York, 2nd edition, 1997. ISBN 0-471-53849-3.
- [38] H. J. Gough. *The Fatigue of Metals*. Scott, Greenwood, London, 1924.
- [39] A. Thum and W. Buchmann. *Dauerfestigkeit und Konstruktion*. VDI-Verlag, Berlin, 1932.
- [40] A. Thum and W. Bautz. Zur Frage der Formziffer. *Zeitschrift des Vereines Deutscher Ingenieure*, 79:1303–1306, 1935.
- [41] R. B. Heywood. The relationship between fatigue and stress concentration. *Aircraft Engineering*, 19:81–84, 1947.

- [42] R. E. Peterson. *Stress Concentration Design Factors*. John Wiley, New York, 1953.
- [43] R. E. Peterson. *Metal Fatigue*, chapter Notch Sensitivity, pages 293–306. McGraw-Hill, New York, 1959.
- [44] E. Lehr. Formgebung und Werkstoffausnutzung. *Stahl und Eisen, Zeitschrift für das deutsche Eisenüttenwesen, Zeitschr. der Nordwestlichen Gruppe des Vereins Deutscher Eisen- und Stahlindustrieller und des Vereins Deutscher Eisenhüttenleute*, 61(43), 1941. ISSN 0340-4951.
- [45] R. E. Peterson. Stress concentration and fatigue strength. *Proceedings (American Society for Testing and Materials)*, 30 (part 1):298–310, 1930. ISSN 0066-0515.
- [46] N. E. Frost and D. S. Dugdale. Fatigue tests on notched mild steel plates with measurement of fatigue cracks. *Journal of the Mechanics and Physics of Solids*, 5:182–192, 1957. ISSN 0022-5096.
- [47] M. Klesnil and P. Lukáš. *Fatigue of Metallic Materials*, volume 7 of *Materials Science Monographs*. Elsevier, Amsterdam, 1980. ISBN 0-444-99762-8.
- [48] E. Siebel and H. Meuth. Die Wirkung von Kerben bei schwingender Beanspruchung. *VDI-Zeitschrift*, 91(13):319–323, 1949. ISSN 0042-1766.
- [49] E. Siebel and M. Stieler. Ungleichförmige Spannungsverteilung bei schwingender Beanspruchung. *VDI-Zeitschrift*, 97(5):121–126, 1955. ISSN 0042-1766.
- [50] O. Graf. *Dauerfestigkeit von Stählen mit Walzhaut ohne und mit Bohrung, von Niet- und Schweißverbindungen*. VDI, Berlin, 1931.
- [51] A. Thum and W. Bautz. Die Gestaltfestigkeit. *Stahl und Eisen, Zeitschrift für das deutsche Eisenhüttenwesen*, 55:1025–1029, 1935. ISSN 0340-4803.
- [52] E. Gaßner. Festigkeitsversuche mit wiederholter Beanspruchung im Flugzeugbau. *Deutsche Luftwacht, Ausg. Luftwissen*, 6:61–64, 1939.
- [53] A. Ruprecht, M. Maihöfer, M. Heitele, and T. Helmrich. Massively parallel computation of the flow in hydro turbines. 2002. 21st IAHR Symposium on Hydraulic Machinery and Systems, September 9–12, 2002 in Lausanne, CH.
- [54] O. Buxbaum and H. Ostermann. Ausfallsichere Bemessung von Laufrädern für Wasserkraftmaschinen aus rostfreiem Stahlguss unter Berücksichtigung von Korrosion und Gefügestand. Technical report, Fraunhofer Institute for Structural Durability, Darmstadt, Germany, 1983.
- [55] H. Brekke. Choice of materials for water turbines and the influence this has on design manufacture, testing and operation. Lecture at Kværner Brug A/S, NTNU, Trondheim, 1984.
- [56] C. Nicolet, F. Avellan, P. Allenbach, A. Sapin, J.-J. Simond, S. Kvicinsky, and M. Crahan. Simulation of transient phenomena in Francis turbine power plants: hydroelectric interaction. pages 1–12. 13th Conference on Waterpower, July 29–31, 2003 in Buffalo, New York, USA.

- [57] M. Heitele, T. Helmrich, M. Maihöfer, and A. Ruprecht. New insight into an old product by high performance computing – Simulation of the flow through an entire Francis turbine. 5th European SGI/CRAY MPP Workshop, 1999 in Bologna, Italy.
- [58] H. Bjørndal, T. Moltubakk, and H. Aunemo. Flow induced stresses in a medium head Francis runner - Strain gauge measurements in an operating plant and comparison with Finite Element Analysis. 10th International Meeting of the IAHR Work Group on the Behaviour of Hydraulic Machinery Under Steady Oscillatory Conditions, June 26–28, 2001 in Trondheim, Norway.
- [59] J. Schijve. *Fatigue of Structures and Materials*. Kluwer Academic Publications, Dordrecht, 2001. ISBN 0-7923-7013-9.
- [60] T. K. Nielsen. Limitations of the load regulating ability of water power plants. 10th International Meeting of the IAHR Work Group on the Behaviour of Hydraulic Machinery Under Steady Oscillatory Conditions, June 26–28, 2001 in Trondheim, Norway.
- [61] S. P. Mansoor, D. I. Jones, D. A. Bradley, F. C. Aris, and G. R. Jones. Reproducing oscillatory behaviour of a hydroelectric power station by computer simulation. *Control Engineering Practice*, 8:1261–1272, 2000.
- [62] H. Brekke. Design of pumps and turbines (in Norwegian). Lecture note at NTNU, Department of Energy and Process Engineering, Trondheim, Norway, 1998.
- [63] M. Farhat, S. Natal, F. Avellan, F. Paquet, P. Y. Lowys, and M. Couston. Onboard measurements of pressure and strain fluctuations in a model of low head Francis turbine. Part I: Instrumentation. 21st IAHR Symposium on Hydraulic Machinery and Systems, September 9–12, 2002 in Lausanne, CH.
- [64] W. J. Rheingans. Power swings in hydroelectric power plants. *Transactions. American Society of Mechanical Engineers*, 62:171–184, 1940.
- [65] G. Rainer. Parameterstudien mit Finiten Elementen – Berechnung der Bauteilfestigkeit von Schweißverbindungen unter äußeren Beanspruchungen. *Konstruktion*, 37(2):45–52, 1985. ISSN 0720-5953.
- [66] W. Beitz and K.-H. Grothe, editors. *Dubbel – Taschenbuch für den Maschinenbau*, chapter E, page 103. Springer-Verlag, Berlin, 20th edition, 2001. ISBN 3-540-67777-1.
- [67] J. C. Newman Jr. and I. S. Raju. Analysis of surface cracks in finite plates under tension or bending loads. Technical Report TP-1578, NASA, 1979.
- [68] J. R. Griffiths and G. Oates. Fatigue problems in power engineering. *Metal Science: a Publication of the Metals Society*, 11(8–9):285–292, 1977. ISSN 0306-3453.
- [69] C. E. Richards and T. C. Lindley. The influence of stress intensity and microstructure on fatigue crack propagation in ferritic materials. *Engineering Fracture Mechanics*, 4:951–978, 1972. ISSN 0013-7944.

- [70] J. M. Barsom and S. T. Rolfe. *Fracture and Fatigue Control in Structures: Applications of Fracture Mechanics*. Prentice-Hall, New Jersey, 2nd edition, 1987. ISBN 0-13-329863-9.
- [71] A. A. Griffith. The phenomenon of rupture and flow in solids. *Philosophical Transactions of the Royal Society of London. A, Mathematical and Physical Sciences*, 221:163–198, 1920. ISSN 0080-4614.
- [72] G. R. Irwin. Analysis of stresses and strains near the end of a crack traversing a plate. *Transactions of the ASME, Journal of Applied Mechanics*, 24:361–364, 1957. ISSN 0021-8936.
- [73] G. R. Irwin. Fracture. In S. Flugge, editor, *Handbuch der Physik*, volume IV, pages 551–590. Springer-Verlag, Berlin, 1958. ISBN 3-540-02412-3.
- [74] T. Fett and D. Munz. *Stress intensity factors and weight functions*. Computational Mechanics Publications, Southampton UK and Boston USA, 1997.
- [75] N. I. Muskhelishvili. *Some Basic Problems of Mathematical Theory of Elasticity*. Noordhoff, Holland, 1953.
- [76] O. L. Bowie. Analysis of an infinite plate containing radial cracks, originating at the boundaries of an internal circular hole. *Journal of Mathematical Physics*, 35(1):60–71, 1956. ISSN 0022-2488.
- [77] B. Gross, J. E. Strawley, and W. F. Brown. Stress intensity factors for a single-edge-notched tension specimen by boundary collocation of a stress function. Technical Note D-2603, NASA, 1965.
- [78] J. R. Rice. A path independent integral and the approximate analysis of strain concentration by notches and cracks. *Journal of Applied Mechanics*, 16:1–12, 1968. ISSN 0021-8936.
- [79] T. A. Cruse. Numerical solutions in three-dimensional elastostatics. *International Journal of Solids and Structures*, 5:1259–1274, 1969. ISSN 0020-7683.
- [80] I. N. Sneddon and M. Löwengrub. *Crack Problems in the Classical Theory of Elasticity*. Wiley, New York, 1969.
- [81] H. F. Bueckner. A novel principle for the computation of stress intensity factors. *Zeitschrift für Angewandte Mathematik und Mechanik*, 50:529–546, 1970. ISSN 0044-2267.
- [82] J. R. Rice. Some remarks on elastic-tip stress fields. *International Journal of Solids and Structures*, 8:751–758, 1972. ISSN 0020-7683.
- [83] J. P. Benthem and W. T. Koiter. Asymptotic approximations to crack problems. In G. C. Sih, editor, *Mechanics of Fracture I. Proceedings of an International Conference on Dynamic Crack Propagation*. Noordhoff International Publ., Leyden, 1973. ISBN 90-01-79861-6.

- [84] W. K. Wilson. Finite element methods for elastic bodies containing cracks. In G. C. Sih, editor, *Mechanics of Fracture I*, chapter Methods of Analysis and Solution of Crack Problems, pages 484–515. Noordhoff International Publ., Leyden, 1973.
- [85] T. Belytschko, Y.Y. Lu, and L. Gu. Element-free Galerkin methods. *International Journal for Numerical Methods in Engineering*, 37:229–256, 1994. ISSN 0029-5981.
- [86] Y. Murakami, editor. *Stress Intensity Factors Handbook*, volume 4 and 5. Elsevier Science, Oxford, 2001. ISBN 0-08-034809-2.
- [87] R. J. Hartranft and G. C. Sih. Alternating method applied to edge and surface crack problems. In G. C. Sih, editor, *Methods of Analysis and Solutions to Crack Problems*, volume 1, pages 179–238. Noordhoff International Publishing, Dordrecht, 1973. ISBN 90-0179-860-8.
- [88] Z. P. Bažant and L. F. Estenssoro. Surface singularity and crack propagation. *International Journal of Solids and Structures*, 15(5):405–426, 1979. ISSN 0020-7683.
- [89] C. W. Smith and J. S. Epstein. Measurement of near tip field near the right angle intersection of straight front cracks. In J. T. Pindera and B. Krasnowski, editors, *Modelling Problems in Crack Tip Mechanics, Proceedings of the 10th Canadian Fracture Conference, August 24-26, 1983, University of Waterloo, Waterloo, Ontario, Canada*, pages 325–333, Dordrecht, 1984. Martinus Nijhoff Publishers. ISBN 90-247-3067-8.
- [90] J. P. Benthem. State of stress at the vertex of a quarter-infinite crack in a half-space. *International Journal of Solids and Structures*, 13:479–492, 1977. ISSN 0020-7683.
- [91] G. C. Sih and Y. D. Lee. Review of triaxial crack border stress and energy behavior. *Theoretical and Applied Fracture Mechanics*, 12:1–17, 1989. ISSN 0167-8442.
- [92] G. Shen and G. Glinka. Weight functions for a surface semi-elliptical crack in a finite thickness plate. *Theoretical and Applied Fracture Mechanics*, 15:247–255, 1991. ISSN 0167-8442.
- [93] L. P. Pook. Some implications of corner point singularities. *Engineering Fracture Mechanics*, 48(3):367–378, 1994. ISSN 0013-7944.
- [94] G. C. Sih and C. T. Li. Initiation and growth characterization of corner cracks near circular hole. *Theoretical and Applied Fracture Mechanics*, 13:69–80, 1990. ISSN 0167-8442.
- [95] L. P. Pook. A note on corner point singularities. *International Journal of Fracture*, 53:R3–R8, 1992. ISSN 0376-9429.
- [96] M. Yngvevsson and F. Nilsson. Fatigue crack growth of surface cracks under non-symmetric loading. *Engineering Fracture Mechanics*, 63:375–393, 1999. ISSN 0013-7944.
- [97] R. D. Henshell and K. G. Shaw. Crack tip finite elements are unnecessary. *International Journal for Numerical Methods in Engineering*, 9:495–507, 1975. ISSN 0029-5981.

- [98] R. S. Barsoum. On the use of isoparametric finite elements in linear fracture mechanics. *International Journal for Numerical Methods in Engineering*, 10:25–37, 1976. ISSN 0029-5981.
- [99] H. Tada, P. C. Paris, and G. R. Irwin. *The Stress Analysis of Cracks Handbook*. Paris Productions, St. Louis, USA, 2nd edition, 1985.
- [100] ASME. Rules for inservice inspection of nuclear power plant components. In *ASME Boiler and Pressure Vessel Code*, volume 11. American Society of Mechanical Engineers, Fairfield, New York, 1981.
- [101] *Guide on methods for assessing the acceptability of flaws in metallic structures. BS 7910*, volume 3. British Standards Institution, London, 1999. ISBN 0-580-33081-8.
- [102] J. C. Newman Jr. and I. S. Raju. An empirical stress intensity factor equation for the surface crack. *Engineering Fracture Mechanics*, 15(1–2):185–192, 1981. ISSN 0013-7944.
- [103] M. Isida, H. Noguchi, and T. Yoshida. Tension and bending of finite thickness plates with semi-elliptical surface crack. *International Journal of Fracture*, 26:157–188, 1984. ISSN 0376-9429.
- [104] A. Carpinteri. Propagation of surface cracks under cyclic loading. In A. Carpinteri, editor, *Handbook of Fatigue Crack Propagation in Metallic Structures*, pages 653–705. Elsevier Science B.V., Amsterdam, 1994. ISBN 0-444-81645-3.
- [105] X. Wang and S. B. Lambert. Local weight functions for semi-elliptical surface cracks in finite thickness plates. *Theoretical and Applied Fracture Mechanics*, 23:199–208, 1995. ISSN 0167-8442.
- [106] N. Nisitani and D. H. Chen. Stress intensity factor for a semi-elliptical surface crack in a shaft under tension. *Transactions of the Japan Society of Mechanical Engineers*, 50:1077–1082, 1984. ISSN 0387-5008.
- [107] T. Lorentzen, N. E. Kjær, and T. Henriksen. The application of fracture mechanics to surface cracks in shafts. *Engineering Fracture Mechanics*, 23:1005–1014, 1986. ISSN 0013-7944.
- [108] R. G. Forman and V. Shivakumar. Growth behaviour of surface cracks in the circumferential plane of solid and hollow cylinders. In *Fracture Mechanics, ASTM STP 905*, volume 17, pages 59–74. American Society for Testing and Materials, Philadelphia, 1986.
- [109] A. Carpinteri. Shape change of surface cracks in round bars under cyclic axial loading. *International Journal of Fatigue*, 15:21–26, 1993. ISSN 0142-1123.
- [110] A. Carpinteri and R. Brighenti. Fatigue propagation of surface flaws in round bars: a three-parameter theoretical model. *Fatigue & Fracture of Engineering Materials & Structures*, 19:1471–1480, 1996. ISSN 1460-2695.

- [111] X. B. Lin and R. A. Smith. Shape growth simulation of surface cracks in tension fatigued round bars. *International Journal of Fatigue*, 19:461–469, 1997. ISSN 0142-1123.
- [112] N. Couroneau and J. Royer. Simplified model for the fatigue growth analysis of surface cracks in round bars under mode i. *International Journal of Fatigue*, 20:711–718, 1998. ISSN 0142-1123.
- [113] S. Pommier, C. Sakae, and Y. Murakami. An empirical stress intensity factor set of equations for a semi-elliptical crack in a semi-infinite body subjected to a polynomial stress distribution. *International Journal of Fatigue*, 21(3):243–251, 1999. ISSN 0142-1123.
- [114] I. S. Raju and J. C. Newman Jr. Stress intensity factors for internal and external surface cracks in cylindrical vessels. *Journal of Pressure Vessel Technology*, 104:293–298, 1982. ISSN 0094-9930.
- [115] T. Nishioka and S. N. Atluri. Analysis of surface flaw in pressure vessel by new 3-dimensional alternating method. *Journal of Pressure Vessel Technology*, 104:299–307, 1982. ISSN 0094-9930.
- [116] D. W. A. Rees. Fatigue crack growth in thick walled cylinders under pulsating internal pressure. *Engineering Fracture Mechanics*, 33:927–940, 1989. ISSN 0013-7944.
- [117] M. Bergman. Stress intensity factors for circumferential surface cracks in pipes. *Fatigue & Fracture of Engineering Materials & Structures*, 18:1155–1172, 1995. ISSN 1460-2695.
- [118] X. B. Lin and R. A. Smith. Numerical analysis of fatigue growth of external surface cracks in pressurised cylinders. *International Journal of Pressure Vessels and Piping*, 71(293–300), 1997. ISSN 0308-0161.
- [119] A. Carpinteri and R. Brighenti. Circumferential surface flaws in pipes under cyclic axial loading. *Engineering Fracture Mechanics*, 60:383–396, 1998. ISSN 0013-7944.
- [120] R. Brighenti. Axially-cracked pipes under pulsating internal pressure. *International Journal of Fatigue*, 22(7):559–567, 2000. ISSN 0142-1123.
- [121] P. F. Joseph, R. D. Cordes, and F. Erdogan. Surface cracks in toroidal shells. *Nuclear Engineering Design*, 158:263–276, 1995. ISSN 0029-5493.
- [122] A. Carpinteri, R. Brighenti, and A. Spagnoli. External surface cracks in shells under cyclic internal pressure. *Fatigue & Fracture of Engineering Materials & Structures*, 23:467–476, 2000. ISSN 1460-2695.
- [123] I. S. Raju and J. C. Newman Jr. Stress-intensity factors for a wide range of semi-elliptical surface cracks in finite-thickness plates. *Engineering Fracture Mechanics*, 11:817–829, 1979. ISSN 0013-7944.

- [124] J. C. Newman, Jr. and I. S. Raju. Stress-intensity factor equations for cracks in three-dimensional finite bodies subjected to tension and bending loads. In S. N. Atluri, editor, *Computational Methods in the Mechanics of Fracture*, volume 2 of *Computational methods in mechanics*, chapter 9, pages 311–334. Elsevier Science B.V., Amsterdam, 1986. ISBN 0-444-87955-2.
- [125] Y. Murakami. Analysis of stress intensity factors of mode I, II and III for inclined surface cracks of arbitrary shape. *Engineering Fracture Mechanics*, 22(1):101–104, 1985. ISSN 0013-7944.
- [126] A. Carpinteri, R. Brighenti, H.-J. Huth, and S. Vantadori. Fatigue growth of a surface crack in a welded T-joint. *International Journal of Fatigue*, 27(1):59–69, 2005. ISSN 0142-1123.
- [127] F. Nilsson. A consistent few parameter crack growth description procedure. *International Journal of Fracture*, 54:35–44, 1992. ISSN 0376-9429.
- [128] L. Nilsson. Estimation of crack growth in surface cracked plates subjected to a complex stress field. SAQ/FoU-report, 1998.
- [129] L. Nilsson. Stress-intensity factors for semi-elliptical surface cracks in plates subjected to a complex stress field. SAQ/FoU-report, 1998.
- [130] B. J. Carter, C.-S. Chen, A. R. Ingraffea, and P. A. Wawrzynek. A topology based system for simulating 3D crack growth in solid and shell structures. In B. L. Karihaloo, Y.-W. Mai, M. I. Ripley, and R. O. Ritchie, editors, *Advances in fracture research*, volume 4, pages 1923–1934. ICF 9, 1997.
- [131] B. J. Carter, P. A. Wawrzynek, and A. R. Ingraffea. Automated 3-D crack growth simulation. *International Journal for Numerical Methods in Engineering*, 47:229–253, 2000. ISSN 0029-5981.
- [132] Cornell Fracture Group. *FRANC3D 2.6. Concepts and user guide*. Cornell University, Ithaca, New York, 2003.
- [133] Cornell Fracture Group. *FRANC3D 2.6. Menu and dialog reference*. Cornell University, Ithaca, New York, 2003.
- [134] Computational Mechanics BEASY Ltd. *BEASY User Guide*. Ashurst, Southampton, UK, 2003.
- [135] G. Härkegård, H.-J. Huth, and S. Faanes. FEA-based fatigue assessment methodology for hydraulic turbine runners. In A. Strang et al., editors, *Proceedings of the 5th International Charles Parsons Turbine Conference*, pages 1105–1118, London, 2000. IOM Communications Ltd. ISBN 1-86125-113-0.
- [136] H.-J. Huth. Fatigue crack growth from shape-optimised notches in hydraulic turbine runners. In A. F. Blom, editor, *Proceedings of the Eighth International Fatigue Congress*, volume 5, pages 3007–3014, Stockholm, Sweden, 2002. ISBN 1-901537-33-1.
- [137] R. V. Baud. Fillet profiles for constant stress. *Product Engineering*, 5:133–134, April 1934. ISSN 0032-9754.

- [138] H. Neuber. Zur Optimierung der Spannungskonzentration. In *Continuum Mechanics and related Problems of Analysis*, pages 375–380. Nauka Publishing House, Moscow, 1972.
- [139] E. Schnack. An optimization procedure for stress concentrations by the finite element technique. *International Journal for Numerical Methods in Engineering*, 14:115–124, 1979. ISSN 0029-5981.
- [140] R. Lansard. Fillets without stress concentration. *Proceedings of the Society for Experimental Stress Analysis*, 13(1):97–104, 1955.
- [141] R. B. Heywood. *Designing against Fatigue*. Chapman and Hall, London, 1962.
- [142] H. Neuber. Der zugbeanspruchte Flachstab mit optimalem Querschnittsübergang. *Forschung im Ingenieurwesen*, 35(1):29–30, 1969. ISSN 0015-7899.
- [143] L. A. Schmit. Structural design by systematic synthesis. In *Proceedings of the 2nd Conference on Electronic Computation*, New York, 1960. American Society of Civil Engineers.
- [144] A. Francavilla, C. V. Ramakrishnan, and O. C. Zienkiewicz. Optimization of shape to minimize stress concentration. *Journal of Strain Analysis*, 10(2):63–70, 1975. ISSN 0309-3247.
- [145] E. Schnack and G. Iancu. Shape design of elastostatic structures based on local perturbation analysis. *Structural Optimization*, 1:117–125, 1989. ISSN 1436-2503.
- [146] D. Radaj and S. Zhang. Multiparameter design optimization in respect of stress concentration. In H. A. Eschenauer, C. Mattheck, and N. Ohlhoff, editors, *Engineering Optimization in Design Processes: Proceedings of the International Conference Karlsruhe Nuclear Research Center, Germany, September 3-4, 1990*, pages 181–189. Springer Verlag, Berlin, 1991. ISBN 0-3875-35896.
- [147] C. Mattheck and S. Burkhardt. A new method of structural shape optimisation based on biological growth. *International Journal of Fatigue*, 12(3):185–190, 1990. ISSN 0142-1123.
- [148] E. Schnack and W. Weigl. Shape optimization under fatigue using continuum damage mechanics. *Computer-Aided Design*, 34:929–938, 2002. ISSN 0010-4485.
- [149] V. Braibant and C. Fleury. Shape optimal design using B-splines. *Computer Methods in Applied Mechanics and Engineering*, 44(3):247–267, 1984. ISSN 0045-7825.
- [150] Y. Tsompanakis, N. D. Lagaros, and M. Papadrakakis. Innovative computational methods for shape optimization. 5th GRACM Congress on Computational Mechanics, July 7-12, 2002 in Vienna, Austria.
- [151] W. Waldmann, M. Heller, and G. X. Chen. Optimal free-form shapes for shoulder fillets in flat plates under tension and bending. *International Journal of Fatigue*, 23:509–523, 2001. ISSN 0142-1123.

- [152] W. Beitz and K.-H. Küttner, editors. *Dubbel – Taschenbuch für den Maschinenbau*, chapter A. Springer-Verlag, Berlin, 18th edition, 1995. ISBN 3-540-57650-9.
- [153] B. N. Veelo. *Variations of Shape in Industrial Geometric Models*. PhD thesis, Norwegian University of Science and Technology, Trondheim, 2004. ISBN 82-471-6431-0.
- [154] J. Ferguson. Multivariable curve interpolation. *Journal of the Association for Computing Machinery*, 11(2):221–228, 1964. ISSN 0004-5411.
- [155] D. Schwarze* and F. Schubert. Applicability of a “marker-technique” to support the examination of crack growth behaviour in brittle and ductile Ni-alloys at 500 and 750 °C (in German). In *Berichte des Forschungszentrums Jülich*. Institut für Werkstoffe und Verfahren der Energietechnik, 1999. ISSN 0944-2952, Jül 3728. *Ph.D thesis D 82 (Dissertation RWTH Aachen, 1999).
- [156] D. Radaaj. *Ermüdungsfestigkeit – Grundlagen für Leichtbau, Maschinen- und Stahlbau*. Springer-Verlag, Berlin, 1995. ISBN 3-540-58348-3.
- [157] A. Hallingstad. Fatigue properties of Francis runner weldment. Master’s thesis, NTNU, Trondheim, 1999.
- [158] D. N. Dai, D. A. Hills, G. Härkegård, and J. Pross. Simulation of the growth of near-surface defects. *Engineering Fracture Mechanics*, 59(4):415–424, 1998. ISSN 0013-7944.
- [159] G. Niemann. *Maschinenelemente*, volume 1 – Konstruktion und Berechnung von Verbindungen. Springer-Verlag, Berlin, 2nd edition, 1981. ISBN 3-540-06809-0.
- [160] VDI 2230 – Systematische Berechnung hochbeanspruchter Schraubenverbindungen – Zylindrische Einschraubenverbindungen. In *VDI-Handbuch Konstruktion*. VDI-Verlag, Düsseldorf, 1986.
- [161] C. M. Sonsino. Einfluß von Kaltverformungen bis 5 % auf das Kurzzeitschwingfestigkeitsverhalten metallischer Werkstoffe. Technical Report LBF-Report FB-161, Fraunhofer-Institut für Betriebsfestigkeit, Darmstadt, 1982.
- [162] W. Elber. *Fatigue crack propagation: some effects of crack closure on the mechanisms of fatigue crack propagation and cyclic tensile loading*. PhD thesis, University of New South Wales, Australia, 1968.
- [163] W. Elber. Fatigue crack closure under cyclic tension. *Engineering Fracture Mechanics*, 2(1):37–45, 1970. ISSN 0013-7944.
- [164] W. Elber. The significance of fatigue crack closure. In *ASTM STP 486*, pages 230–242. American Society for Testing and Materials, Philadelphia, 1971.
- [165] ASTM. E 647 – Standard Test Method for Measurements of Fatigue Crack Growth Rates. In *Annual Book of ASTM Standards*, volume 03.01. American Society for Testing and Materials, West Conshohocken, 1997.

- [166] J. K. Donald. Introducing the compliance ratio concept for determining effective stress intensity. *International Journal of Fatigue*, 19(93):191–195, 1997. ISSN 0142-1123.
- [167] J. K. Donald and P. C. Paris. An evaluation of ΔK_{eff} estimation procedure on 6061-T6 and 2024-T3 aluminum alloys. *International Journal of Fatigue*, 21:S47–S57, 1999. ISSN 0142-1123.
- [168] P. C. Paris, H. Tada, and J. K. Donald. Service load fatigue damage — a historical perspective. *International Journal of Fatigue*, 21:S35–S46, 1999. ISSN 0142-1123.
- [169] E. K. Walker. The effect of stress ratio during crack propagation and fatigue for 2024-T3 and 7075-T6 aluminum. In *Effects of Environment and Complex Load History on Fatigue Life, ASTM STP 462*, pages 1–14. American Society for Testing and Materials, Philadelphia, 1970. ISBN 8-031-0050-7.
- [170] K. R. Dennis. Fatigue crack growth of gun tube steel under spectrum loading. Master's thesis, Virginia Polytechnic Institute and State University, Engineering Science and Mechanics Department, Blacksburg, Va, USA, May 1986.
- [171] N. E. Dowling. *Mechanical Behaviour of Materials*. Prentice Hall, London, 1999. ISBN 0-13-026956-5.
- [172] K. N. Smith, P. Watson, and T. H. Topper. A stress-strain function for the fatigue of metals. *Journal of Materials, JMLSA*, 5(4):767–778, 1970. ISSN 0022-2453.
- [173] P. C. Paris, M. P. Gomez, and W. E. Anderson. A rational analytic theory of fatigue. *The Trend in Engineering at the University of Washington*, 13:9–14, 1961. ISSN 0362-0018.
- [174] P. C. Paris. *The growth of cracks due to variations in load*. PhD thesis, Lehigh University, 1962.
- [175] P. C. Paris and F. Erdogan. A critical analysis of crack propagation laws. *Transactions of the ASME. Series D, Journal of Basic Engineering*, 85D(4):528–534, 1963. ISSN 0021-9223.
- [176] O. R. Ritchie and J. Lankford. *Materials Science and Engineering*, 84:11–16, 1986. ISSN 0025-5416.
- [177] J. F. Knott. Near-threshold growth of defects in engineering materials. In R. O. Ritchie and E. A. Starke, editors, *Fatigue '87 : papers presented at the Third International Conference on Fatigue and Fatigue Thresholds, held at the University of Virginia, Charlottesville, Virginia, June 28-July 3, 1987*, volume 1, page 497. EMAS, Warley. ISBN 0-947817-23-9.
- [178] B. G. Journet, A. Lefrancois, and A. Pineau. *Fatigue & Fracture of Engineering Materials & Structures*, 12:237, 1989. ISSN 1460-2695.
- [179] D. J. Nicholls and J. W. Martin. *Materials Science and Engineering*, A128:141, 1990. ISSN 0025-5416.

- [180] A. F. Blom, A. Hedlund, W. Zhao, A. Fathulla, B. Weiss, and R. Stickler. Short fatigue crack growth in Al 2024 and Al 7475. In K. J. Miller and E. R. de los Rios, editors, *The Behaviour of Short Fatigue Cracks*, pages 37–66. Mechanical Engineering Publications, London, 1986. ISBN 0-85298-615-7.
- [181] J. R. Rice. Mechanics of crack tip deformation and extension by fatigue. In *Fatigue crack propagation, ASTM STP 415*, pages 247–309. American Society for Testing and Materials, Philadelphia, 1967.
- [182] G. R. Irwin. Characterization of part-through cracks in tension. In J. L. Swedlow, editor, *The Surface Crack: Physical Problems and Computational Solutions*, pages 1–10. ASME, New York, 1972.
- [183] N. C. Shamma. *Mathematical Algorithms in Visual Basic for Scientists and Engineers*. McGraw-Hill, New York, 1996. ISBN 0-07-912003-2.
- [184] M. Ichikawa and T. Takamatsu. Fracture toughness test for the thin plate under mode II loading. *Transactions of the Japan Society of Mechanical Engineers*, 51:1115–1121, 1985. ISSN 0387-5008.
- [185] A. Thum, C. Petersen, and O. Svenson. *Verformung, Spannung und Kerbwirkung*. VDI-Verlag, Düsseldorf, 1960.

Appendix A

Stress Concentration Factor Formula due to Rainer

In the following table A.1, the stress concentration factor formula published by Rainer [65] in 1985 is presented. Figures and layout after Dubbel [66].

Rainer's investigation comprises 100 different round and flat bar geometries showing grooves and shoulder fillets. On the basis of the stress concentration factor results derived by means of FEA, equations of [185] were modified and integrated in the formula below.

Table A.1: Equation for calculation of concentration factors at notched symmetric bars.

	flat bar		round bar		round bar		round bar	
	notch	shoulder fillet	notch	shoulder fillet	notch	shoulder fillet	notch	shoulder fillet
	z b	z b	z b t					
<i>A</i>	0.10 0.08	0.55 0.40	0.10 0.12 0.40	0.10 0.12 0.40	0.10 0.12 0.40	0.44 0.40 0.40	0.44 0.40 0.40	
<i>B</i>	0.7 2.2	1.1 3.8	1.6 4.0 15.0	1.6 4.0 15.0	1.6 4.0 15.0	2.0 6.0 25.0	2.0 6.0 25.0	
<i>C</i>	0.13 0.20	0.20 0.20	0.11 0.10 0.10	0.11 0.10 0.10	0.11 0.10 0.10	0.30 0.80 0.20	0.30 0.80 0.20	
<i>k</i>	1.00 0.66	0.80 0.66	0.55 0.45 0.35	0.55 0.45 0.35	0.55 0.45 0.35	0.60 0.40 0.45	0.60 0.40 0.45	
<i>l</i>	2.00 2.25	2.20 2.25	2.50 2.66 2.75	2.50 2.66 2.75	2.50 2.66 2.75	2.20 2.75 2.25	2.20 2.75 2.25	
<i>m</i>	1.25 1.33	1.33 1.33	1.50 1.20 1.50	1.50 1.20 1.50	1.50 1.20 1.50	1.60 1.50 2.00	1.60 1.50 2.00	
	$z = \text{tension}$	$b = \text{bending}$	$t = \text{torsion}$	$t = \text{torsion}$	$t = \text{torsion}$			

$$K_t = 1 + \left(\frac{A}{\left(\frac{t}{\rho}\right)^k} + B \left(\frac{1 + \frac{a}{\rho}}{\frac{a}{\rho} \sqrt{\frac{a}{\rho}}} \right)^l + C \frac{\frac{a}{\rho}}{\left(\frac{a}{\rho} + \frac{t}{\rho}\right) \left(\frac{t}{\rho}\right)^m} \right)^{-\frac{1}{2}}$$

Appendix B

Stress Intensity Factor Solutions

B.1 SIF Formulae due to Newman and Raju

These are the Newman and Raju [102] engineering set formulae for the finite plate containing a semi-elliptical surface crack. For $0 < a/c \leq 1$, $0 \leq a/t < 1$, $c/b < 0.5$ and $0 \leq \phi \leq \pi$, the stress intensity factor for combined tension and bending loads, S_t and S_b , respectively, is

$$K_I = (S_t + HS_b) \sqrt{\pi \frac{a}{Q}} F\left(\frac{a}{t}, \frac{a}{c}, \frac{c}{b}, \phi\right) \quad (\text{B.1})$$

$$F = (M1 + M2\xi^2 + M3\xi^4) f_\phi g_\phi f_w \quad (\text{B.2})$$

$$M1 = 1.13 - 0.09\alpha \quad (\text{B.3})$$

$$M2 = -0.54 + \frac{0.89}{0.2 + \alpha} \quad (\text{B.4})$$

$$M3 = 0.5 - (1/(0.65 + \alpha)) + 14(1 - \alpha)^{24} \quad (\text{B.5})$$

$$g_\phi = 1 + (0.1 + 0.35\xi^2)(1 - \sin^2 \phi) \quad (\text{B.6})$$

$$f_\phi = (\alpha^2 \cos^2 \phi + \sin^2 \phi)^{0.25} \quad (\text{B.7})$$

$$f_w = \left(\sec\left(\frac{\pi c}{2b} \sqrt{\xi}\right)\right)^{0.5} \quad (\text{B.8})$$

$$p = 0.2 + \alpha + 0.6\xi \quad (\text{B.9})$$

$$G1 = -1.22 - 0.12\alpha \quad (\text{B.10})$$

$$G2 = 0.55 - 1.05\alpha^{0.75} + 0.47\alpha^{1.5} \quad (\text{B.11})$$

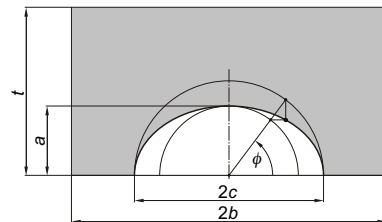
$$H1 = 1 - 0.34\xi - 0.11\alpha\xi \quad (\text{B.12})$$

$$H2 = 1 + G1\xi + G2\xi^2 \quad (\text{B.13})$$

$$H = H1 + (H2 - H1) \sin^p \phi \quad (\text{B.14})$$

$$Q = 1 + 1.464\alpha^{1.65} \quad (\text{B.15})$$

with $\alpha = \frac{a}{c}$ and $\xi = \frac{a}{t}$.



B.2 SIF Formulae due to Pommier et al.

The engineering code solution for the stress intensity factor of a semi-elliptic mode I surface crack in a large body of Pommier et al. [113] assumes the normal stress to vary as

$$\sigma_y[x, z] = \sum_{i=0}^3 \sum_{k=0}^3 \sigma_{ik} (x/a)^i (z/c)^k \quad . \quad (\text{B.16})$$

Here, $i + k \leq 3$. The crack axis ratio $a/c = (\frac{a}{c})$ is limited to the interval $0.5 \leq \alpha \leq 2$. $K_{\text{I}}[\phi = 0] = \sigma_0 F_{\text{I}}[\phi] \sqrt{\pi a}$ and $K_{\text{I}}[\phi = \pi/2] = \sigma_0 F_{\text{I}}[\phi] \sqrt{\pi c}$.

For the formfactor, F_{I} , the following solution is presented:

$$F_{\text{I}}[\phi, i, k, \alpha] = F_0 \{1 + (-1 + H) \cdot T[i + k]\} \quad (\text{B.17})$$

$$H[\phi, i, k, \alpha] = G_i T[i] + G_k T[k] + (G_{ik} - G_i - G_k) \cdot T[i \cdot k] \quad (\text{B.18})$$

$$T[i] = \{2 \arctan [1000 \cdot i]\} / \pi \quad (\text{B.19})$$

$$F_0[\phi, \alpha] = C_0 + C_2(\phi^2) + C_4(\phi^4) \quad (\text{B.20})$$

$$C_0[\alpha] = 1.225 - 0.8512\alpha + 0.3414\alpha^2 - 0.0561\alpha^3 \quad (\text{B.21})$$

$$C_2[\alpha] = -0.54781 + 0.97969\alpha - 0.52601\alpha^2 + 0.10557\alpha^3 \quad (\text{B.22})$$

$$C_4[\alpha] = 0.11569 - 0.18205\alpha + 0.09851\alpha^2 - 0.02134\alpha^3 \quad (\text{B.23})$$

$$G_k[\phi, \alpha, k] = N_k + P_k \cdot \cos^k \phi \quad (\text{B.24})$$

$$P_k[k, \alpha] = \{0.493 - 0.096k + 0.009k^2\} + \\ + \alpha \{0.105 + 0.0645k - 0.0105k^2\} - \\ - \alpha^2 \{0.0204 + 0.0039k - 0.00069k^2\} \quad (\text{B.25})$$

$$N_k[k] = 0.3 - 0.165k + 0.025k^2 \quad (\text{B.26})$$

$$G_i[\phi, \alpha, i] = N_i + P_i \cdot \sin^i \phi \quad (\text{B.27})$$

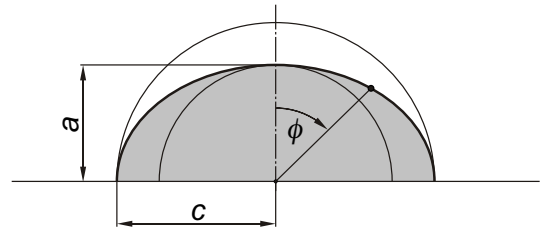
$$P_i[i, \alpha] = \{1.2728 - 0.439i + 0.09i^2\} - \\ - \alpha \{0.5643 - 0.24675i + 0.0693i^2\} + \\ + \alpha^2 \{0.1478 - 0.07781i + 0.02489i^2\} \quad (\text{B.28})$$

$$N_i[i] = 0.0375(1 + (-1)^i) \quad (\text{B.29})$$

$$G_{ik}[\phi, \alpha, i, k] = N_{ik} + P_{ik} \cdot \sin^i \phi \cdot \cos^k \phi \quad (\text{B.30})$$

$$P_{ik}[i, \alpha] = \{0.575 - 0.0313(k - i) - 0.11863(k - i)^2\} + \\ + \alpha \{-0.0866 + 0.06706(k - i) + 0.05393(k - i)^2\} + \\ + \alpha^2 \{0.021 - 0.0157(k - i) - 0.01193(k - i)^2\} \quad (\text{B.31})$$

$$N_{ik}[i] = 0.015(1 + (-1)^i) \quad (\text{B.32})$$



Appendix C

Experimental Fatigue Test Data

C.1 Fatigue Test SN Data

In the following table C.1 the setup and SN results from experimental fatigue testing are presented. A load ratio $R_L = 0.1$ applies to all fatigue tests performed. Stress values indicated for $\sigma_{a, \text{Walker}}$ are corrected for local plasticity after Neuber [34] (8.2) and transformed to the state of equivalent zero-to-maximum ($R = 0$) local stresses according to Walker [169] (8.5).

Table C.1: Setup and SN data from experimental fatigue testing.

Specimen type	Material	Transition	Specimen no.	σ_{an}	N_f	$\sigma_a^{el} = K_t \cdot \sigma_{an}$	σ_{max}	R	$\sigma_{a,Walker}$	γ
T-joint	X 4 CrNiMo 16-5	Circular	1.1	383	–	506	888	-0.13	444	0
			1.2	383	–	506	888	-0.13	444	0
			1.3	383	80 500	506	888	-0.13	444	0
			1.4	383	33 600	506	888	-0.13	444	0
			1.5	410	28 800	542	892	-0.20	446	0
			1.6	410	52 000	542	892	-0.20	446	0
			1.7	410	42 000	542	892	-0.20	446	0
Trailing edge	34 CrNiMo 6	Circular	2.1	383	148 000	429	856	0.02	424	0.42
			2.2	383	132 000	429	856	0.02	424	0.42
			2.3	383	108 800	429	856	0.02	424	0.42
			2.4	383	110 300	429	856	0.02	424	0.42
			2.5	410	95 000	460	875	-0.04	438	0
			2.6	410	113 000	460	875	-0.04	438	0
			2.7	410	115 600	460	875	-0.04	438	0
GX 5 CrNi 13-4	GX 5 CrNi 13-4	Circular	R I	250	113 500	420	689	-0.21	345	0
			R II	250	135 300	420	689	-0.21	345	0
			R III	275	99 100	461	701	-0.41	351	0
			R IV	275	67 300	461	701	-0.41	351	0
			S II	250	–	341	665	-0.02	333	0
			S III ₁)	250	1 012 000 ^a	341	665	-0.02	333	0
			S I	275	202 600	375	687	-0.17	343	0
S III ₂)	275	255 000	375	687	-0.17	343	0			
S IV	275	–	375	687	-0.17	343	0			
Optimised	Optimised	Optimised	R 1	257	43 251	430	655	-0.20	327	0
			R 2	257	45 800	430	655	-0.20	327	0
			R 5	220	88 200	368	608	-0.13	304	0
			R 6	275	12 300	461	673	-0.24	336	0
			S 1	220	–	300	538	-0.06	269	0
			S 1	220	–	300	538	-0.06	269	0

^aRun-out, no fatigue crack visible.

Appendix D

Material Stress–Strain Data

Static stress–strain curves from static tensile testing are presented in Figures D.1(a)–(f) for the different materials used in the experimental fatigue tests of Chapter 7. These materials are

1. X4CrNiMo 16-5 hot rolled plate material, quenched and tempered;
2. 34CrNiMo 6 hot rolled bar stock material, quenched and tempered;
3. GX5CrNi 13-4 cast material, quenched and tempered.

For the specimens of materials (1) and (2) the direction of applied force under testing and the forge direction of the material coincide. The specimens of material (2.) were taken from a rod of 200 mm in diameter, 30 mm from the rod cross section centre. Material (3) specimens are taken from a cast steel slab ($200 \times 300 \times 1500$), 70 mm below the slab surface. All tensile tests were performed and analysed by SINTEF Materials Technology, Trondheim.

In Figures D.1(b), (d) and (f) the lines of 0, 0.01 and 0.2 % plastic strain are shown. Young’s modulus, E , is estimated to 220 GPa in D.1(a) and (b). For (c), $E = 180$ GPa.

An overview over setup and result data is given in Table D.1.

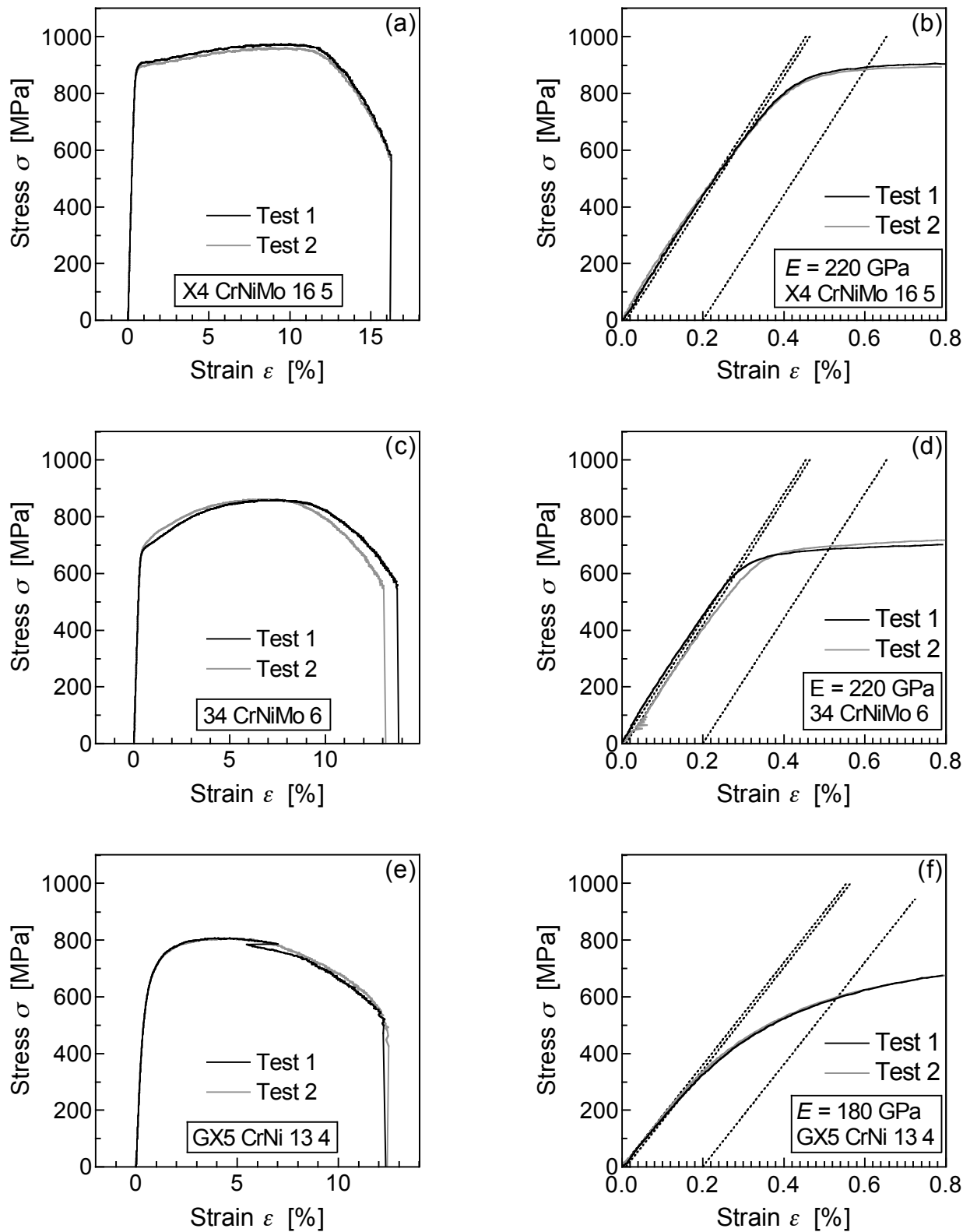


Figure D.1: Static stress-strain curves of the materials used in experimental fatigue testing. (a)(b) X4CrNiMo 16-5. (c)(d) 34CrNiMo 6. (e)(f) GX5CrNi 13-4.

Table D.1: Static tensile material testing. Setup and results.

Material	Specimen no.	Diameter [mm]	Gauge length		Young's modulus E [GPa]	Ultimate load L_{\max} [kN]	Yield strength		Ultimate strength R_m [MPa]	Strain at L_{\max} [%]
			l_i [mm]	l_f [mm]			$R_{p0.01}$ [MPa]	$R_{p0.2}$ [MPa]		
X4CrNiMo 16-5-1	1	7.03	25	-	220	37.59	636	896	974	9.94
	2	7.09	25	-	220	37.72	623	884	961	9.73
34CrNiMo 6	1	7.05	25	41.9	220	33.54	507	685	859	7.41
	2	7.07	25	42.7	220	33.81	455	696	862	7.03
GX5CrNi 13-4	1	7.94	27.5	-	180	39.95	311	606	807	4.06
	2	7.93	27.5	-	180	39.83	246	602	806	4.36

Appendix E

Visual Basic Codes

E.1 Newman-Raju FCG Subroutine

```
' K_NR81 Macro
,
' Copyright 2004 by Hans-Jörg Huth. This code may not be used for purposes that are
' not related to the PhD research of Hans-Jörg Huth without his prior written consent.
' Hans.Jorg.Huth@ntnu.no
,
' Macro imported from K_NR79, K_PSM99.
,
' Growth of semi-elliptic surface crack in finite plate under bending
' according to Newman & Raju "An empirical stress-intensity factor equation
' for the surface crack", 1981
,
' To be fixed in code on new calculation: - plate length b
,                                           - membrane and/or bending load
,
' Length unit is [mm]
,
,
Sub K_NR81()

    Dim a As Double, ai As Double, anew As Double, af As Double, afinal As Double
    Dim c As Double, ci As Double, cnew As Double, ac As Double, cfinal As Double
    Dim t As Double, tF As Double
    Dim sigmin As Double, sigmax As Double, dsigc As Double
    Dim dsig As Double, dsigtens As Double, dsigbend As Double, dsiga As Double
    Dim dK As Double, dKnm As Double, ParisC As Double, Parism As Double
    Dim N As Double, Nf As Double, Nmax As Double, Noutput As Double
    Dim m As Double, Fnm As Double
    Dim alfa As Double, beta As Double, gamma As Double
    Dim ellx As Double, elly As Double
    Dim pi As Double

    Dim M1 As Double, M2 As Double, M3 As Double, gphi As Double, fphi As Double
    Dim Fa As Double, Fc As Double, Fadim As Double, Fcdim As Double, fw As Double
    Dim G1 As Double, G2 As Double, H1 As Double, H2 As Double, HH As Double, Q As Double

    Dim PHI As Variant
    Dim i As Integer, j As Integer, g As Integer, R As Integer, v As Integer
    Dim d As Integer, o As Integer, Kill As Integer

    Dim ICoeff As Double, IExp As Double, H As Double
    Dim k1 As Double, k2 As Double, k3 As Double, k4 As Double, k5 As Double
    Dim l1 As Double, l2 As Double, l3 As Double, l4 As Double, l5 As Double
    Dim DeltaKa As Double, DeltaKc As Double, DeltaKathHCF As Double, DD As Double

    pi = (4 * (Atn(1)))

    ai = Cells(7, 6).Value           'initial crack depth
    ci = Cells(8, 6).Value           'initial crack semi-length    all in [mm]
```

```

af = Cells(9, 6).Value           'max crack length           /
t = Cells(10, 6).Value          'plate thickness           _/
b = 2000                        'plate length in [mm]
PHI = Array(0, (pi / 2))        ' PHI = 0 -> "c", PHI = pi/2 -> "a"

sigmax = Cells(12, 6).Value      'max stress
sigmin = Cells(13, 6).Value      'min stress
DD = Cells(16, 6).Value          'HCF stress ratio sig_a / sig_m

Parism = Cells(18, 6).Value      'crack growth exponent
ParisC = Cells(19, 6).Value      'crack growth coefficient
rarb = Cells(20, 6).Value        'initial da/dN
DeltaKathHCF = Cells(21, 6).Value 'threshold value for DKa_HCF and DKc_HCF

H = Cells(24, 6).Value           'Increment value at x0
ICoeff = Cells(25, 6).Value      'Increment Increase Coefficient
IExp = Cells(26, 6).Value        'Increment Increase Exponent

Noutput = Cells(29, 6).Value     'Integer, number of outputs
Nmax = Cells(30, 6).Value

pi = (4 * (Atn(1)))

dsig = sigmax - sigmin
dsigtens = (sigmax - sigmin) * 1# 'Adjust amount of membrane
dsigbend = (sigmax - sigmin) * 0# 'and bending stress in dsig

If af > 10 Then
    MsgBox " max. crackdepth exceeds the bending stress trendline array 0 < a < 10 mm "
    GoTo 100
End If

anew = ai
cnew = ci
i = 0

If af < ai Then
    MsgBox " The chosen value " & af & " m for maximal crack depth is too low"
    Exit Sub
End If

'_____Begin output loop_____

d = 0
Do

'_____Begin calculation loop_____

Do
    a = anew
    c = cnew
    alfa = a / c
    beta = a / t
    gamma = c / b

    i = i + 1                'procedure counter for calculation loops
    H = H * (((i + ICoeff) / i) ^ IExp) 'Integration step increasement
    N = N + H                'Next step

    If gamma >= 0.5 Then
        Beep
        MsgBox " ratio cracklength c / platelength b is less/equal than 0.5 "
        Kill = 1
        GoTo 80

    ElseIf alfa > 1# Then
        Beep
        MsgBox " ratio crackdepth a / cracklength c exceeds 1.0 "
        Kill = 1
        GoTo 80

```

```

ElseIf beta > 0.8 Then
  Beep
  MsgBox " ratio crackdepth a / plate thickness t exceeds 0.8 "
  Kill = 1
  GoTo 80

End If

'----- Newman-Raju 81 , crack depth a -----
M1 = 1.13 - (0.09 * alfa)
M2 = -0.54 + (0.89 / (0.2 + alfa))
M3 = 0.5 - (1# / (0.65 + alfa)) + (14 * ((1# - alfa) ^ 24))
gphi = 1 + ((0.1 + (0.35 * ((beta) ^ 2))) * ((1 - Sin(PHI(1))) ^ 2))
fphi = (((alfa ^ 2) * ((Cos(PHI(1))) ^ 2) + ((Sin(PHI(1))) ^ 2)) ^ 0.25
fw = (Cos((gamma * pi / 2) * (beta ^ 0.5))) ^ (-0.5)
Fa = (M1 + (M2 * (beta ^ 2)) + (M3 * (beta ^ 4))) * fphi * gphi * fw 'Formfactor
p = 0.2 + alfa + (0.6 * beta)
G1 = -1.22 - (0.12 * alfa)
G2 = 0.55 - (1.05 * (alfa ^ 0.75)) + (0.47 * (alfa ^ 1.5))
H1 = 1 - (0.34 * beta) - (0.11 * alfa * beta)
H2 = 1 + (G1 * beta) + (G2 * (beta ^ 2))
HH = H1 + ((H2 - H1) * ((Sin(PHI(1))) ^ p))
Q = 1 + (1.464 * (alfa ^ 1.65))

'-----
dsiga = dsigtens + (HH * dsigbend)

a = a / 1000 '*****[m]*****
DeltaKa = Fa * dsiga * Sqr(pi * a / (Q)) 'SIF a [MPa*m^0.5]
DeltaKaHCF = DeltaKa * (DD) 'SIF a (HCF) [MPa*m^0.5]
Fadim = DeltaKa / (dsig * Sqr(pi * a)) 'Dimensionless K

'----- Integration Runge-Kutta-Fehlberg , crack depth a -----
k1 = H * E(N, a, DeltaKa, ParisC, Parism, alfa)
k2 = H * E(N + H / 4, a + k1 / 4, DeltaKa, ParisC, Parism, alfa)
k3 = H * E(N + 3# / 8 * H, a + 3# / 32 * (k1 + 3 * k2), DeltaKa, ParisC, Parism, alfa)
k4 = H * E(N + 12# / 13 * H, a + 1932# / 2197 * k1 - 7200# / 2197 * k2 + 7296# / _
2197 * k3, DeltaKa, ParisC, Parism, alfa)
k5 = H * E(N + H, a + 439# / 216 * k1 - 8 * k2 + 3680# / 513 * k3 - 845# / _
4104 * k4, DeltaKa, ParisC, Parism, alfa)

anew = a + (25# / 216 * k1) + (1408# / 2565 * k3) + (2197# / 4104 * k4) - (k5 / 5)
anew = anew * 1000 '*****[mm]*****

'----- Newman-Raju 81 , crack length c -----
M1 = 1.13 - (0.09 * alfa)
M2 = -0.54 + (0.89 / (0.2 + alfa))
M3 = 0.5 - (1# / (0.65 + alfa)) + (14 * ((1# - alfa) ^ 24))
gphi = 1 + ((0.1 + (0.35 * ((beta) ^ 2))) * ((1 - Sin(PHI(0))) ^ 2))
fphi = (((alfa ^ 2) * ((Cos(PHI(0))) ^ 2) + ((Sin(PHI(0))) ^ 2)) ^ 0.25
fw = (Cos((gamma * pi / 2) * (beta ^ 0.5))) ^ (-0.5)
Fc = (M1 + (M2 * (beta ^ 2)) + (M3 * (beta ^ 4))) * fphi * gphi * fw 'Formfactor
p = 0.2 + alfa + (0.6 * beta)
G1 = -1.22 - (0.12 * alfa)
G2 = 0.55 - (1.05 * (alfa ^ 0.75)) + (0.47 * (alfa ^ 1.5))
H1 = 1 - (0.34 * beta) - (0.11 * alfa * beta)
H2 = 1 + (G1 * beta) + (G2 * (beta ^ 2))
HH = H1 + ((H2 - H1) * ((Sin(PHI(0))) ^ p))
Q = 1 + (1.464 * (alfa ^ 1.65))

'-----
dsigc = dsigtens + (HH * dsigbend)

c = c / 1000 '*****[m]*****
DeltaKc = Fc * dsigc * Sqr(pi * a / (Q)) 'SIF c [MPa*m^0.5]
DeltaKcHCF = DeltaKc * (DD) 'SIF c (HCF) [MPa*m^0.5]
Fcdim = DeltaKc / (dsig * Sqr(pi * a)) 'Dimensionless K

'----- Integration Runge-Kutta-Fehlberg , crack length c -----
l1 = H * U(N, c, DeltaKc, ParisC, Parism, alfa)
l2 = H * U(N + H / 4, c + l1 / 4, DeltaKc, ParisC, Parism, alfa)
l3 = H * U(N + 3# / 8 * H, c + 3# / 32 * (l1 + 3 * l2), DeltaKc, ParisC, Parism, alfa)
l4 = H * U(N + 12# / 13 * H, c + 1932# / 2197 * l1 - 7200# / 2197 * l2 + 7296# / _
2197 * l3, DeltaKc, ParisC, Parism, alfa)

```

```

15 = H * U(N + H, c + 439# / 216 * 11 - 8 * 12 + 3680# / 513 * 13 - 845# / _
    4104 * 14, DeltaKc, ParisC, Parism, alfa)

cnew = c + (25# / 216 * 11) + (1408# / 2565 * 13) + (2197# / 4104 * 14) - (15 / 5)
cnew = cnew * 1000      '*****[mm]*****
a = a * 1000            '*****[mm]*****
c = c * 1000            '*****[mm]*****
,-----

If d = 0 Then GoTo 80                                     'output of initial values

If DeltaKaHCF > DeltaKathHCF Then                         'definition of failure (HCF)
  If DeltaKcHCF > DeltaKathHCF Then
    Beep
    MsgBox " The SIF threshold for HCF has been reached all along the crack front "
    Kill = 1
    GoTo 80
  Else
    Beep
    MsgBox " The SIF threshold for HCF has been reached at point A "
    Kill = 1
    GoTo 80
  End If
End If

If a > af Then                                           'definition of failure (af)
  Beep
  MsgBox " The fracture crack depth af = " & af & " mm has been reached "
  Kill = 1
  GoTo 80
End If

If i > 100000 Then                                       'End dead loop
  Beep
  MsgBox " The calculation has been terminated after 100000 calculation steps "
  Kill = 1
  GoTo 80
End If

Loop Until N >= (Noutput * d)

'____begin output to Pivot table_____
80 Cells(74 + d, 1).Value = N                            'Output to pivot (A , 74+d)
   Cells(74 + d, 2).Value = a                            'Output to pivot (B , 74+d)
   Cells(74 + d, 3).Value = c                            'Output to pivot (C , 74+d)
   Cells(74 + d, 4).Value = DeltaKa                      'Output to pivot (D , 74+d)
   Cells(74 + d, 5).Value = DeltaKc                      'Output to pivot (E , 74+d)
   Cells(74 + d, 6).Value = a / c                       'Output to pivot (F , 74+d) alpha
   Cells(74 + d, 7).Value = a / t                       'Output to pivot (G , 74+d) xi
   Cells(74 + d, 8).Value = Fadim ' / Sqr(Q)             'Output to pivot (H , 74+d)
   Cells(74 + d, 9).Value = Fcdim ' / Sqr(Q)            'Output to pivot (I , 74+d)

'____begin drawing ellipse from a_d and c_d_____

For g = 0 To 30
  ellx = c * (1 - (g ^ 2 / 900))
  elly = Sqr(((a ^ 2) * (1 - ((ellx ^ 2) / ((c ^ 2))))))
  Cells(74 + g, 10 + (2 * d)).Value = ellx              'Output to pivot (J+2d , 74+g)
  Cells(74 + g, 11 + (2 * d)).Value = elly              'Output to pivot (K+2d, 74+g)
Next g

If Kill = 1 Then GoTo 100                                'this was the final output, terminate

d = d + 1
If d > 25 Then
  Beep
  MsgBox " The max number of 25 outputs has been exceeded. Please increase Noutput. "
  GoTo 100
End If

```

```

Loop
'-----end output loop-----
100    Cells(31, 6).Value = N                'Output to pivot (F , 31)
        Cells(32, 6).Value = anew           'Output to pivot (F , 31)
        Cells(33, 6).Value = cnew         'Output to pivot (F , 31)

        MsgBox " Simulation K_NR81 done! "
        ActiveWindow.SmallScroll Down:=60
End Sub

Function E(N As Double, a As Double, DeltaKa As Double, ParisC As Double, Parism As Double, _
    alfa As Double) As Double

    E = ParisC * (DeltaKa ^ Parism) 'E = da/dN

End Function

Function U(N As Double, c As Double, DeltaKc As Double, ParisC As Double, Parism As Double, _
    alfa As Double) As Double

    U = ParisC * (DeltaKc ^ Parism) 'U = dc/dN

End Function

```

E.2 Pommier et al. FCG Subroutine

```

,
' K_PSM99 Macro
,
' Copyright 2004 by Hans-Joerg Huth. This code may not be used for purposes that are
' not related to the PhD research of Hans-Jörg Huth without his prior written consent.
' Hans.Jorg.Huth@ntnu.no
,
' Growth of semi-elliptic surface crack in semi-infinite body
' subjected to a max. 3rd grade polynomial stress distribution
' -> Stress intensity factor solution of Pommier et al. is calculated
' -> Numerical integration of Paris' law
' -> Graphical output
,
' Units are [mm/cycle] , [MPa*m^0.5]
,
Sub K_Pommier99()

    Dim a As Double, ai As Double, anew As Double, af As Double, afinal As Double
    Dim c As Double, ci As Double, cnew As Double, ac As Double, cfinal As Double
    Dim t As Double, tF As Double
    Dim sigmin As Double, sigmax As Double, dsiga As Double, dsigc As Double
    Dim dK As Double
    Dim Parism As Double, ParisC As Double
    Dim N As Double, Nf As Double, Nmax As Double, Noutput As Double
    Dim alfa As Double, ellx As Double, elly As Double
    Dim pi As Double

    Dim Trendline As Variant, PHI As Variant
    Dim i As Integer, g As Integer, R As Integer, v As Integer, d As Integer

    Dim ICoeff As Double, IExp As Double, H As Double
    Dim k1 As Double, k2 As Double, k3 As Double, k4 As Double, k5 As Double
    Dim l1 As Double, l2 As Double, l3 As Double, l4 As Double, l5 As Double

    Dim nn As Integer, nnmax As Integer, mm As Integer, mmmmax As Integer, Kill As Integer

    Dim Tm As Double, Tn As Double, Tnm As Double, Tnnmm As Double
    Dim CO As Double, C2 As Double, C4 As Double
    Dim FOa As Double, FOc As Double, HH As Double
    Dim Pm As Double, Pn As Double, Pnm As Double
    Dim Nm As Double, Nnm As Double, Gm As Double, Gn As Double, Gnm As Double

```

```

Dim Fnma As Double, Fnmc As Double
Dim Fa As Double, Fastress As Double, Fc As Double, Fcstress As Double
Dim DeltaKa As Double, DeltaKc As Double, DeltaKaHCF As Double, DeltaKcHCF As Double
Dim DeltaKathHCF As Double, DD As Double
Dim sigsuma As Double, sigsumc As Double

pi = (4 * (Atn(1)))

ai = Cells(7, 6).Value           'initial crack depth           \
ci = Cells(8, 6).Value           'initial crack semi-length     all in [mm]
af = Cells(9, 6).Value           'max crack length               /
t = Cells(10, 6).Value           'thickness of loaded beam (->stress distribution in semi-inf. plate)

sigmax = Cells(12, 6).Value      'max stress
sigmin = Cells(13, 6).Value      'min stress
DD = Cells(16, 6).Value          'HCF stress ratio Dsig_HCF / Dsig_LCF

Parism = Cells(18, 6).Value      'crack growth exponent
ParisC = Cells(19, 6).Value      'crack growth coefficient
DeltaKathHCF = Cells(21, 6).Value 'threshold value for DKa_HCF and DKc_HCF

H = Cells(24, 6).Value           'Increment value at x0
ICoeff = Cells(25, 6).Value      'Increment Increase Coefficient
IExp = Cells(26, 6).Value        'Increment Increase Exponent

Noutput = Cells(29, 6).Value     'Integer, number of outputs written from N = 0 to Nmax
Nmax = Cells(30, 6).Value        'Max value of load cycles after which calculation is terminated

nnmax = Cells(35, 6).Value       'Pommier-stress exponent tension
mmmmax = Cells(36, 6).Value      'Pommier-stress exponent bending

tF = 40 / t                       'trendline scaling factor (t1. based on t1 = 40mm)

anew = ai                         'initial values
cnew = ci
i = 0                             'procedure counter for calculation loops
N = 0                             'number of load cycles

PHI = Array(0, (pi / 2)) ' PHI = 0 -> "a", PHI = pi/2 -> "c" , in contrary to NR_81

If af > 10 Then
    MsgBox " max. crackdepth exceeds the bending stress trendline array 0 < a < 10 mm "
    GoTo 100
End If

If af < ai Then
    MsgBox " The chosen value " & af & " mm for maximal crack depth is too low"
    Exit Sub
End If

If (nnmax + mmmmax) > 3 Then
    MsgBox " The sum of the Pommier stress field exponents n and m exceeds 3"
    Exit Sub
End If

'_____Begin output loop_____
d = 0
Do
'For d = 0 To Noutput
'_____Begin calculation loop_____
Do
    a = anew
    c = cnew
    alfa = a / c

    i = i + 1           'procedure counter for calculation loops
    H = H * (((i + ICoeff) / i) ^ IExp) 'Integration step increasement
    N = N + H          'Next step

```

```

If alfa < 0.1 Then                                     'Pommier: alfa < 0.5
  Beep
  MsgBox " ratio crackdepth a / cracklength c is beyond 0.1 "
  GoTo 100

ElseIf alfa > 2 Then                                   'Pommier: alfa < 2
  Beep
  MsgBox " ratio crackdepth a / cracklength c i above 2 "
  GoTo 100

End If

'____begin trendline defining the bending force slope _____
' ### trendlines are based on FE-calculations with t = 40mm ###
' ### activate/disable trendline by deleting/adding < ' > ###
'
'____quarter-circular transition trendlines follow_____
'
Trendline = Array(1.2521, (-0.1383 * a * tF), (0.0062 * ((a * tF) ^ 2)), (-0.0001 * ((a * tF) ^ 3)))
'is Trendline for ultra fine meshed quarter-circular transition (R0) -> circ. test specimen -> nn = 0, mm = 3, x/t1=0.5
'
Trendline = Array(1.3133, (-0.2024 * a * tF), (0.0188 * ((a * tF) ^ 2)), (-0.0008 * ((a * tF) ^ 3)))
'is Trendline for ultra fine meshed quarter-circular transition (R0) -> circ. test specimen -> nn = 0, mm = 3, x/t1=0.25
'
'
Trendline = Array(1.4315, (-0.08265 * a * tF))
'is Trendline for sharp transition (S4)                                     -> nn = 0, mm = 1
'
'____constant gradient trendlines follow_____
'
Trendline = Array(1, (-a * tF / 10))
'is Trendline for dsiga/dx = sigmax/5 in semi-infinite plate             -> nn = 0, mm = 1

Trendline = Array(1, (-a * tF / 15))
'is Trendline for dsiga/dx = sigmax/7.5 in semi-infinite plate          -> nn = 0, mm = 1

Trendline = Array(1, (-a * tF / 20))
'is Trendline for pure bending stress in semi-infinite plate            -> nn = 0, mm = 1
'
'      (dsiga/dx = sigmax/10)

Trendline = Array(0.9995, (-0.0503 * a * tF), (8e-05 * ((a * tF) ^ 2)), (-3e-06 * ((a * tF) ^ 3)))
'is Trendline for almost pure bending stress in 3rd grade stress field -> nn = 0, mm = 3
'
'      (dsiga/dx = sigmax/10)

Trendline = Array(1, (-a * tF / 40))
'is Trendline for dsiga/dx = sigmax/20 in semi-infinite plate          -> nn = 0, mm = 1

Trendline = Array(1, (-a * tF / 80))
'is Trendline for dsiga/dx = sigmax/40 in semi-infinite plate          -> nn = 0, mm = 1

Trendline = Array(1, (-a * tF / 160))
'is Trendline for dsiga/dx = sigmax/80 in semi-infinite plate          -> nn = 0, mm = 1

Trendline = Array(1)
'is Trendline for pure membrane stress in semi-infinite plate          -> nn = 0, mm = 0
'
'      '____ Pommier-paper example trendline follows_____
'
Trendline = Array(1, (-0.075 * a * tF), (0.0019 * ((a * tF) ^ 2)), (-2e-05 * ((a * tF) ^ 3)))
'is Trendline for cubic stress (max. = 1 at surface)                     -> nn = 0, mm = 3

'
'      '____ Parma-paper example trendline follows_____
'
Trendline = Array(1, (-0.075 * a * tF), (0.0019 * ((a * tF) ^ 2)), (-2e-05 * ((a * tF) ^ 3)))
'is Trendline of the "Oř"-crack stress field                             -> nn = 0, mm = 3

```

```

'____optimised transition trendlines follow_____
,
'Trendline = Array(1.1636, (-0.1151 * a * tF), (0.0051 * ((a * tF) ^ 2)), (-0.0001 * ((a * tF) ^ 3)))
'is Trendline for bend_spline_49_fine          -> nn = 0, mm = 3

'Trendline = Array(1.0212, (-0.0572 * a * tF), (0.0005 * ((a * tF) ^ 2)), (-7e-07 * ((a * tF) ^ 3)))
'is Trendline for bend_opt_a2                  -> nn = 0, mm = 3

'Trendline = Array(1.1159, (-0.0925 * a * tF), (0.003 * ((a * tF) ^ 2)), (-5e-05 * ((a * tF) ^ 3)))
'is Trendline for bend_opt_b4                  -> nn = 0, mm = 3

'Trendline = Array(1.1618, (-0.1172 * a * tF), (0.0053 * ((a * tF) ^ 2)), (-0.0001 * ((a * tF) ^ 3)))
'is Trendline for bend_opt_c0                  -> nn = 0, mm = 3

'Trendline = Array(1.1215, (-0.0996 * a * tF), (0.0035 * ((a * tF) ^ 2)), ((-5e-05) * ((a * tF) ^ 3)))
'is Trendline for bend_opt_d0 -> opt. test specimen -> nn = 0, mm = 3, x/t1=0.35

'Trendline = Array(1.1221, (-0.1004 * a * tF), (0.0037 * ((a * tF) ^ 2)), ((-6e-05) * ((a * tF) ^ 3)))
'is Trendline for bend_opt_d0 -> opt. test specimen -> nn = 0, mm = 3, x/t1=0.5

'____definition and modification of stress range_____

dsiga = sigmax - sigmin                                'delta stress at point a
dsigc = (sigmax - sigmin)                              'delta stress at point c

'_____begin calc. of stress slope after Pommier, Sakae, Murakami in a-direction_____
Fnma = 0
Fa = 0
Fastress = 0
sigsuma = 0

For nn = 0 To nnmax                                'nn = element of {0 ; 1}
For mm = 0 To mmmax                                'mm = element of {0 ; 1 ; 2 ; 3}

If d = 0 Then GoTo 10
If N >= (Noutput * d) Then
'If N >= (Nmax * d / Noutput) Then
10 Cells(73 + d, 53 + mm).Value = Trendline(mm + nn) 'Output for linear/quadratic/cubic stress
End If

'_____begin calc. of SIF after Pommier, Sakae, Murakami for a_____

Tm = ((2 * (Atn(1000 * mm))) / (pi))
Tn = ((2 * (Atn(1000 * nn))) / (pi))
Tnm = ((2 * (Atn(1000 * nn * mm))) / (pi))
Tnmnm = ((2 * (Atn(1000 * (nn + mm)))) / (pi))

C0 = (1.225 - (0.8512 * alfa) + (0.3414 * (alfa ^ 2)) - (0.0561 * (alfa ^ 3)))
C2 = (-0.54781 + (0.97969 * alfa) - (0.52601 * (alfa ^ 2)) + (0.10557 * (alfa ^ 3)))
C4 = (0.11569 - (0.18205 * alfa) + (0.09851 * (alfa ^ 2)) - (0.02134 * (alfa ^ 3)))

FOa = (C0 + (C2 * ((PHI(0)) ^ 2)) + (C4 * ((PHI(0)) ^ 4)))

Pm = ((0.493 - (0.096 * mm) + (0.009 * (mm ^ 2))) + (alfa * (0.105 + (0.0645 * mm) - _
(0.0105 * (mm ^ 2)))) - ((alfa ^ 2) * (0.0204 + (0.0039 * mm) - (0.00069 * (mm ^ 2))))))
Nm = (0.3 - (0.165 * mm) + (0.025 * (mm ^ 2)))
Gm = (Nm + (Pm * ((Cos(PHI(0))) ^ mm)))

Pn = ((1.2728 - (0.439 * nn) + (0.09 * (nn ^ 2))) - (alfa * (0.5643 - (0.24675 * nn) + _
(0.0693 * (nn ^ 2)))) + ((alfa ^ 2) * (0.1478 - (0.07781 * nn) + (0.02489 * (nn ^ 2))))))
nn = (0.0375 * (1 + ((-1) ^ nn)))
Gn = (nn + (Pn * ((Sin(PHI(0))) ^ nn)))

Pnm = ((0.575 - (0.0313 * (mm - nn)) - (0.11863 * ((mm - nn) ^ 2))) + (alfa * _
(-0.0866 + (0.06706 * (mm - nn)) + (0.05393 * ((mm - nn) ^ 2)))) + _
((alfa ^ 2) * (0.021 - (0.0157 * (mm - nn)) - (0.01193 * ((mm - nn) ^ 2))))))

```

```

      Nnm = (0.015 * (1 + ((-1) ^ nn)))
      Gnm = (Nnm + (Pnm * ((Sin(PHI(0))) ^ nn) * ((Cos(PHI(0))) ^ mm)))

      HH = ((Gm * Tm) + (Gn * Tn) + ((Gnm - Gn - Gm) * Tnm))

      Fnma = (FOa * (1 + ((-1 + HH) * Tnnmm)))
      Fastress = Fastress + (Fnma * Trendline(mm + nn))
      'actual F_I at a
      'accumulated F_I * stress concentration

      sigsuma = sigsuma + Trendline(mm + nn)
      'accumulated stress concentration

      Next mm
      Next nn

      a = a / 1000
      '*****[m]*****
      Fa = Fastress
      'Fa = DeltaKa / (dsiga * Sqr(pi * a))
      DeltaKa = Fastress * dsiga * Sqr(pi * a)
      'SIF A [MPa*m^0.5]
      DeltaKaHCF = DeltaKa * (DD)
      'SIF A (HCF) [MPa*m^0.5]

      '_____begin numeric integration Runge-Kutta-Fehlberg of Paris eq. for a_____

      k1 = H * E(N, a, DeltaKa, ParisC, Parism)
      k2 = H * E(N + H / 4, a + k1 / 4, DeltaKa, ParisC, Parism)
      k3 = H * E(N + 3# / 8 * H, a + 3# / 32 * (k1 + 3 * k2), DeltaKa, ParisC, Parism)
      k4 = H * E(N + 12# / 13 * H, a + 1932# / 2197 * k1 - 7200# / 2197 * k2 + 7296# / -
          2197 * k3, DeltaKa, ParisC, Parism)
      k5 = H * E(N + H, a + 439# / 216 * k1 - 8 * k2 + 3680# / 513 * k3 - 845# / -
          4104 * k4, DeltaKa, ParisC, Parism)

      anew = a + (25# / 216 * k1) + (1408# / 2565 * k3) + (2197# / 4104 * k4) - (k5 / 5)
      anew = anew * 1000
      '*****[mm]*****

      '_____begin calc. of SIF after Pommier, Sakae, Murakami for c_____

      Fnmc = 0
      Fc = 0
      Fcstress = 0
      sigsumc = 0

      For nn = 0 To nnmax
      For mm = 0 To mmmax

          Tm = ((2 * (Atn(1000 * mm))) / (pi))
          Tn = ((2 * (Atn(1000 * nn))) / (pi))
          Tnm = ((2 * (Atn(1000 * nn * mm))) / (pi))
          Tnnmm = ((2 * (Atn(1000 * (nn + mm)))) / (pi))

          C0 = (1.225 - (0.8512 * alfa) + (0.3414 * (alfa ^ 2)) - (0.0561 * (alfa ^ 3)))
          C2 = (-0.54781 + (0.97969 * alfa) - (0.52601 * (alfa ^ 2)) + (0.10557 * (alfa ^ 3)))
          C4 = (0.11569 - (0.18205 * alfa) + (0.09851 * (alfa ^ 2)) - (0.02134 * (alfa ^ 3)))

          F0c = (C0 + (C2 * ((PHI(1)) ^ 2)) + (C4 * ((PHI(1)) ^ 4)))

          Pm = ((0.493 - (0.096 * mm) + (0.009 * (mm ^ 2))) + (alfa * (0.105 + (0.0645 * mm) - _
              (0.0105 * (mm ^ 2)))) - ((alfa ^ 2) * (0.0204 + (0.0039 * mm) - (0.00069 * (mm ^ 2))))))
          Nm = (0.3 - (0.165 * mm) + (0.025 * (mm ^ 2)))
          Gm = (Nm + (Pm * ((Cos(PHI(1))) ^ mm)))

          Pn = ((1.2728 - (0.439 * nn) + (0.09 * (nn ^ 2))) - (alfa * (0.5643 - (0.24675 * nn) + _
              (0.0693 * (nn ^ 2)))) + ((alfa ^ 2) * (0.1478 - (0.07781 * nn) + (0.02489 * (nn ^ 2)))))
          nn = (0.0375 * (1 + ((-1) ^ nn)))
          Gn = (nn + (Pn * ((Sin(PHI(1))) ^ nn)))

          Pnm = ((0.575 - (0.0313 * (mm - nn)) - (0.11863 * ((mm - nn) ^ 2))) + (alfa * _
              (-0.0866 + (0.06706 * (mm - nn)) + (0.05393 * ((mm - nn) ^ 2)))) + _
              ((alfa ^ 2) * (0.021 - (0.0157 * (mm - nn)) - (0.01193 * ((mm - nn) ^ 2)))))
          Nnm = (0.015 * (1 + ((-1) ^ nn)))
          Gnm = (Nnm + (Pnm * ((Sin(PHI(1))) ^ nn) * ((Cos(PHI(1))) ^ mm)))

          HH = ((Gm * Tm) + (Gn * Tn) + ((Gnm - Gn - Gm) * Tnm))

          Fnmc = (F0c * (1 + ((-1 + HH) * Tnnmm)))
          'actual F_I at c

```

```

    Fcstress = Fcstress + (Fnmc * Trendline(mm + nn))          'accumulated F_I * stress concentration

    Next mm
    Next nn

    c = c / 1000          '*****[m]*****
    Fc = Fcstress          'accumulated F_I
    DeltaKc = Fcstress * dsigc * Sqr(pi * a)          'SIF C [MPa*m^0.5]
    DeltaKcHCF = DeltaKc * (DD)          'SIF C (HCF) [MPa*m^0.5]

'-----begin numeric integration Runge-Kutta-Fehlberg of Paris eq. for c-----

    l1 = H * U(N, c, DeltaKc, ParisC, Parism)
    l2 = H * U(N + H / 4, c + l1 / 4, DeltaKc, ParisC, Parism)
    l3 = H * U(N + 3# / 8 * H, c + 3# / 32 * (l1 + 3 * l2), DeltaKc, ParisC, Parism)
    l4 = H * U(N + 12# / 13 * H, c + 1932# / 2197 * l1 - 7200# / 2197 * l2 + 7296# / 2197 * l3, _
        DeltaKc, ParisC, Parism)
    l5 = H * U(N + H, c + 439# / 216 * l1 - 8 * l2 + 3680# / 513 * l3 - 845# / 4104 * l4, DeltaKc, _
        ParisC, Parism)

    cnew = c + (25# / 216 * l1) + (1408# / 2565 * l3) + (2197# / 4104 * l4) - (15 / 5)
    cnew = cnew * 1000          '*****[mm]*****
    a = a * 1000          '*****[mm]*****
    c = c * 1000          '*****[mm]*****
,-----

    If d = 0 Then GoTo 80          'output of initial values

    If DeltaKaHCF > DeltaKathHCF Then          'definition of failure (HCF)
        If DeltaKcHCF > DeltaKathHCF Then
            Beep
            MsgBox " The SIF threshold for HCF has been reached all along the crack front "
            Kill = 1
            GoTo 80
        Else
            Beep
            MsgBox " The SIF threshold for HCF has been reached at point A "
            Kill = 1
            GoTo 80
        End If
    End If

    If anew > af Then          'definition of failure (af)
        Beep
        MsgBox " The fracture crack depth af = " & af & " mm has been reached "
        Kill = 1
        GoTo 80
    End If

    If N > Nmax Then
        Beep
        MsgBox " The number of load cycles Nmax = " & Nmax & " has been reached "
        Kill = 1
        GoTo 80
    End If

    If i > 100000 Then          'End dead loop
        Beep
        MsgBox " The calculation has been terminated after 100000 calculation steps "
        Kill = 1
        GoTo 80
    End If

    Loop Until N >= (Noutput * d)          'outputs every Noutput cycles
'Loop Until N >= ((Nmax * d) / Noutput)          'outputs d times until Nmax

'-----end calculation loop, begin output to Pivot table-----

80    Cells(74 + d, 1).Value = N          'Output to pivot (A , 74+d)
    Cells(74 + d, 2).Value = a          'Output to pivot (B , 74+d)
    Cells(74 + d, 3).Value = c          'Output to pivot (C , 74+d)

```

```

Cells(74 + d, 4).Value = DeltaKa           'Output to pivot (D , 74+d)
Cells(74 + d, 5).Value = DeltaKc         'Output to pivot (E , 74+d)
Cells(74 + d, 6).Value = a / c           'Output to pivot (F , 74+d) alpha
Cells(74 + d, 7).Value = a / t           'Output to pivot (G , 74+d) xi
Cells(74 + d, 8).Value = Fa               'Output to pivot (H , 74+d)
Cells(74 + d, 9).Value = Fc               'Output to pivot (I , 74+d)

'_____begin drawing ellipse from a_d and c_d_____

For g = 0 To 30
  ellx = cnew * (1 - (g ^ 2 / 900))
  elly = Sqr(((anew) ^ 2) * (1 - ((ellx ^ 2) / ((cnew) ^ 2))))
  Cells(74 + g, 10 + (2 * d)).Value = ellx      'Output to pivot (T+2d , 74+g)
  Cells(74 + g, 11 + (2 * d)).Value = elly      'Output to pivot (U+2d, 74+g)
Next g

If Kill = 1 Then GoTo 100                    'this was the final output, terminate

d = d + 1
If d > 25 Then
  Beep
  MsgBox " The max number of 25 outputs has been exceeded. Increase Noutput. "
  GoTo 100
End If

Loop

'_____end output loop_____

100 Cells(31, 6).Value = N                   'Output to pivot (F , 31)
Cells(32, 6).Value = anew                    'Output to pivot (F , 31)
Cells(33, 6).Value = cnew                    'Output to pivot (F , 31)

MsgBox " Simulation K_PSM99 done! "
ActiveWindow.SmallScroll Down:=60

End Sub

Function E(N As Double, a As Double, DeltaKa As Double, ParisC As Double, Parism As Double) As Double
  pi = (4 * (Atn(1)))
  E = ParisC * (DeltaKa ^ Parism) 'E = da/dN
End Function

Function U(N As Double, c As Double, DeltaKc As Double, ParisC As Double, Parism As Double) As Double
  pi = (4 * (Atn(1)))
  U = ParisC * (DeltaKc ^ Parism) 'U = dc/dN
End Function

```

E.3 Carpinteri et al. FCG Subroutine

```

' K_Parma04 Macro
,
' Copyright 2004 by Hans-Joerg Huth. This code may not be used for purposes that are
' not related to the PhD research of Hans-Jörg Huth without his prior written consent.
' Hans.Jorg.Huth@ntnu.no
,
' Growth of semi-elliptic surface crack in finite plate
' subjected to a max. 5th grade polynomial stress distribution in crackdepth dir. x
' -> Stress Intensity Factor solution tables of Carpinteri, Brighenti, Huth and Vantadori are interpolated
' -> Numerical integration of Paris' law
' -> Graphical output
,
' Units are [mm , mm/cycle] , [MPa*mm^0.5]
,
Sub K_Parma04()

    Dim a As Double, ai As Double, anew As Double, af As Double, afinal As Double, da As Double
    Dim c As Double, ci As Double, cnew As Double, ac As Double, cfinal As Double
    Dim b As Double, xb As Double, zb As Double, deltab As Double, db As Double
    Dim xbnew As Double, zbnew As Double, deltaxb As Double, deltazb As Double
    Dim t As Double, tF As Double
    Dim sigmin As Double, sigmax As Double, dsiga As Double, dsigb As Double
    Dim F0 As Double, F1 As Double
    Dim F00 As Double, F01 As Double, F10 As Double, F11 As Double
    Dim alfa As Double, alfaten As Double, ksi As Double, ksiten As Double
    Dim alfa0 As Double, alfa1 As Double, ksi0 As Double, ksi1 As Double
    Dim Parism As Double, ParisC As Double
    Dim N As Double, Nf As Double, Nmax As Double, Noutput As Double
    Dim m As Double, Fnm As Double
    Dim ellx As Double, elly As Double
    Dim pi As Double, Sinphi As Double

    Dim Bcoeff As Variant

    Dim alfacount As Integer, ksicount As Integer, Kill As Integer
    Dim i As Integer, g As Integer, v As Integer, d As Integer

    Dim ICoeff As Double, IExp As Double, H As Double
    Dim k1 As Double, k2 As Double, k3 As Double, k4 As Double, k5 As Double
    Dim l1 As Double, l2 As Double, l3 As Double, l4 As Double, l5 As Double

    Dim B0 As Double, B1 As Double, B2 As Double, B3 As Double, B4 As Double, B5 As Double

    Dim mm As Integer, mmmax As Integer, mmmmin As Integer

    'begin Variables for functions E, U:

    Dim Fa As Double, Fb As Double
    Dim Famm As Double, Fastress As Double, Fbmm As Double, Fbstress As Double
    Dim DeltaKa As Double, DeltaKb As Double, DeltaKaHCF As Double, DeltaKbHCF As Double
    Dim DeltaKathHCF As Double, DD As Double
    Dim sigsuma As Double, sigsumb As Double

    pi = (4 * (Atn(1)))

    ai = Cells(7, 6).Value           'initial crack depth           \
    ci = Cells(8, 6).Value           'initial crack semi-length     all in [mm]
    af = Cells(9, 6).Value           'max crack length              /
    t = Cells(10, 6).Value           'thickness of loaded beam (->stress distribution in
    ,                                 semi-inf. plate)

    sigmax = Cells(12, 6).Value       'max stress
    sigmin = Cells(13, 6).Value       'min stress
    DD = Cells(16, 6).Value           'HCF stress ratio sig_a / sig_m

    Parism = Cells(18, 6).Value       'crack growth exponent
    ParisC = Cells(19, 6).Value       'crack growth coefficient
    DeltaKathHCF = Cells(21, 6).Value 'threshold value for DKa_HCF and DKc_HCF

```

```

H = Cells(24, 6).Value           'Increment value at x0
ICoeff = Cells(25, 6).Value      'Increment Increase Coefficient
IExp = Cells(26, 6).Value        'Increment Increase Exponent

Noutput = Cells(29, 6).Value     'Integer, number of outputs written from N = 0 to Nmax
                                 '(default 20)
Nmax = Cells(30, 6).Value       'Max value of load cycles after which calculation is
                                 'terminated

mmmax = 5                        'grade of stress field polynomial
mmmin = 0

'tF = 40 / t                      'Bcoeff scaling factor (t1. based on t1 = 40mm),
                                 'yet to be implemented

anew = ai                         'initial values
cnew = ci
i = 0                             'procedure counter for calculation loops
N = 0                             'number of load cycles

If t <> 20 Then
  MsgBox " t = 20 mm is the only plate thickness allowed by now "
  Exit Sub
End If

If af < ai Then
  MsgBox " The chosen value " & af & " mm for maximal crack depth is lower than the initial crack depth "
  Exit Sub
End If

'_____Begin output loop_____
d = 0
Do
'For d = 0 To Noutput              'number of outputs "Noutput", e.g. 20
'_____Begin calculation loop_____
Do
  a = anew
  c = cnew
  alfa = a / c
  ksi = a / t
  zb = c * 0.9                    'z-coordinate of point B on crack front
  xb = (Sqr(0.19)) * a            'x-coordinate of point B on crack front
  b = Sqr((xb ^ 2) + (zb ^ 2))

  i = i + 1                       'procedure counter for calculation loops
  H = H * (((i + ICoeff) / i) ^ IExp) 'Integration step increasement
  N = N + H                       'Next step

  If alfa < 0.1 Then
    Beep
    MsgBox " ratio crackdepth a / cracklength c is less than 0.1 "
    Kill = 1
    GoTo 80

  ElseIf alfa > 1.2 Then
    Beep
    MsgBox " ratio crackdepth a / cracklength c is greater than 1.2 "
    Kill = 1
    GoTo 80

  ElseIf ksi < 0.025 Then
    Beep
    MsgBox " ratio crackdepth a / plate thickness t is less than 0.025 "
    Kill = 1
    GoTo 80

  ElseIf ksi > 0.7 Then

```

```

Beep
MsgBox " ratio crackdepth a / plate thickness t is greater than 0.7 "
Kill = 1
GoTo 80

End If

'-----begin Bcoeff defining the stress gradient -----
'### B-coefficients are based on stress field trendlines with plate thickness t = 20mm ###
'### activate/disable set of coefficients B0 ... B5 by deleting/adding < ' > ###
,
,
'-----quarter-circular transition R0-----
B0 = 1.31 - (0.3844 * a) + (0.0686 * (a ^ 2)) - (0.0072 * (a ^ 3)) + (0.0004 * (a ^ 4)) - _
      (7e-06 * (a ^ 5))
B1 = (0.3844 * a) - (0.1372 * (a ^ 2)) + (0.0216 * (a ^ 3)) - (0.0016 * (a ^ 4)) + _
      (3.5e-05 * (a ^ 5))
B2 = (0.0686 * (a ^ 2)) - (0.0216 * (a ^ 3)) + (0.0024 * (a ^ 4)) - (7e-05 * (a ^ 5))
B3 = (0.0072 * (a ^ 3)) - (0.0016 * (a ^ 4)) + (7e-05 * (a ^ 5))
B4 = (0.0004 * (a ^ 4)) - (3.5e-05 * (a ^ 5))
B5 = (7e-06 * (a ^ 5))
'are B-coefficients for ultra fine meshed quarter-circular transition (R0) -> circ. 2D test specimen, t=20mm
'-----
'-----optimised transition d0-----
'B0 = 1.121 - (0.1983 * a) + (0.0129 * (a ^ 2)) - (5e-07 * (a ^ 3)) - (5e-05 * (a ^ 4)) + _
      (2e-06 * (a ^ 5))
'B1 = (0.1983 * a) - (0.0258 * (a ^ 2)) + (1.5e-06 * (a ^ 3)) + (0.0002 * (a ^ 4)) - _
      (1e-05 * (a ^ 5))
'B2 = (0.0129 * (a ^ 2)) - (1.5e-06 * (a ^ 3)) - (0.0003 * (a ^ 4)) + (2e-05 * (a ^ 5))
'B3 = (5e-07 * (a ^ 3)) + (0.0002 * (a ^ 4)) - (2e-05 * (a ^ 5))
'B4 = -(5e-05 * (a ^ 4)) + (1e-05 * (a ^ 5))
'B5 = -(2e-06 * (a ^ 5))
'are B-coefficients for optimised transition (d0) -> opt. 2D test specimen, t=20mm
'-----
'-----Parma-paper "0ř-crack -----
'B0 = 1.21 - (0.28 * a) + (0.0424 * (a ^ 2)) - (0.00481 * (a ^ 3)) + (0.000277 * (a ^ 4)) - _
      (6.25e-06 * (a ^ 5))
'B1 = (0.28 * a) - (0.0847 * (a ^ 2)) + (0.0144 * (a ^ 3)) - (0.0011 * (a ^ 4)) + _
      (3.12e-05 * (a ^ 5))
'B2 = (0.0424 * (a ^ 2)) - (0.0144 * (a ^ 3)) + (0.00166 * (a ^ 4)) - (6.25e-05 * (a ^ 5))
'B3 = (0.00481 * (a ^ 3)) - (0.0011 * (a ^ 4)) + (6.25e-05 * (a ^ 5))
'B4 = (0.000277 * (a ^ 4)) - (3.12e-05 * (a ^ 5))
'B5 = (6.25e-06 * (a ^ 5))
'are B-coefficients for quarter-circular transition -> Parma-paper examples, t=20mm
'-----
'-----pure tension -----
'B0 = 1
'B1 = 0
'B2 = 0
'B3 = 0
'B4 = 0
'B5 = 0
'are B-coefficients for membrane stress
'-----
'-----pure bending -----
'B0 = 1 - (a / 10)
'B1 = a / 10
'B2 = 0
'B3 = 0
'B4 = 0
'B5 = 0
'are B-coefficients for bending stress field, nominal section, t=20mm
'-----
Bcoeff = Array(B0, B1, B2, B3, B4, B5)

'-----definition and modification of nominal stress range-----

dsiga = sigmax - sigmin
dsigb = sigmax - sigmin
'nominal delta stress for FCG in A
'nominal delta stress for FCG in B

```

```

'_____find closest alfa and ksi neighbours of Fa in table: alfa0,alfa1,ksi0,ksi1_____

    alfacount = 1
    ksicount = 1
    alfaten = alfa * 10
    ksiten = ksi * 10
    Do
        alfa1 = alfacount
        If alfaten = alfa1 Then
            alfa0 = alfa1
            Exit Do
        ElseIf alfaten < alfa1 Then
            alfa0 = alfa1 - 1
            Exit Do
        Else: alfacount = alfacount + 1
        End If
    Loop While alfaten > alfa1

    Do
        ksi1 = ksicount
        If ksiten = ksi1 Then
            ksi0 = ksi1
            Exit Do
        ElseIf ksiten < ksi1 And ksicount = 1 Then
            ksi0 = 0
            If ksiten = 0.25 Then
                ksi1 = ksi0
            End If
            Exit Do
        ElseIf ksiten < ksi1 And ksicount > 1 Then
            ksi0 = ksi1 - 1
            Exit Do
        Else: ksicount = ksicount + 1
        End If
    Loop While ksiten > ksi1

'_____begin calc. of SIF and stress in A_____

    Famm = 0
    Fa = 0
    Fastress = 0
    sigsuma = 0

    For mm = mmin To mmax

        If d = 0 Then GoTo 10
        If N >= (Noutput * d) Then
            Cells(73 + d, 53 + mm).Value = Bcoeff(0)
            End If
        'Output for stress concentration at A
        'once every Noutput cycles

'_____Fa interpolation_____

    F00 = Worksheets("Parma_KI").Cells(5 + alfa0 - 1 + (mm * 29), 2 + ksi0).Value
    F01 = Worksheets("Parma_KI").Cells(5 + alfa0 - 1 + (mm * 29), 2 + ksi1).Value
    F10 = Worksheets("Parma_KI").Cells(5 + alfa1 - 1 + (mm * 29), 2 + ksi0).Value
    F11 = Worksheets("Parma_KI").Cells(5 + alfa1 - 1 + (mm * 29), 2 + ksi1).Value

    If alfa0 = alfa1 Then
        F0 = F00
        F1 = F01
    Else
        If F10 > F00 Then
            F0 = F00 + ((F10 - F00) * (alfaten - alfa0) / (alfa1 - alfa0)) 'linear interpolation
        Else
            F0 = F00 - ((F00 - F10) * (alfaten - alfa0) / (alfa1 - alfa0))
        End If
        If F11 > F01 Then
            F1 = F01 + ((F11 - F01) * (alfaten - alfa0) / (alfa1 - alfa0)) 'linear interpolation
        Else
            F1 = F01 - ((F01 - F11) * (alfaten - alfa0) / (alfa1 - alfa0))
        End If
    End If

```

```

End If

If ksi0 = ksi1 Then
    Famm = FO
Else
    If F1 > FO Then
        Famm = FO + ((F1 - FO) * (ksiten - ksi0) / (ksi1 - ksi0)) 'linear interpolation
    Else
        Famm = FO - ((FO - F1) * (ksiten - ksi0) / (ksi1 - ksi0))
    End If
End If

Fastress = Fastress + (Famm * Bcoeff(mm)) 'accumulated K_I(L) = F_I *Kt(a)
sigsuma = sigsuma + Bcoeff(mm) 'accumulated stress concentration

Next mm

a = a / 1000 '*****[m]*****
Fa = Fastress 'Fa = DeltaKa / (dsiga * Sqr(pi * a))
DeltaKa = Fastress * dsiga * Sqr(pi * a) 'SIF a [MPa*m^0.5]
DeltaKaHCF = DeltaKa * (DD) 'SIF a (HCF)

'_____begin numeric integration Runge-Kutta-Fehlberg of Paris eq. for a_____

k1 = H * E(N, a, DeltaKa, ParisC, Parism)
k2 = H * E(N + H / 4, a + k1 / 4, DeltaKa, ParisC, Parism)
k3 = H * E(N + 3# / 8 * H, a + 3# / 32 * (k1 + 3 * k2), DeltaKa, ParisC, Parism)
k4 = H * E(N + 12# / 13 * H, a + 1932# / 2197 * k1 - 7200# / 2197 * k2 + 7296# / 2197 * k3, _
    DeltaKa, ParisC, Parism)
k5 = H * E(N + H, a + 439# / 216 * k1 - 8 * k2 + 3680# / 513 * k3 - 845# / 4104 * k4, DeltaKa, _
    ParisC, Parism)

anew = a + ((25# / 216 * k1) + (1408# / 2565 * k3) + (2197# / 4104 * k4) - (k5 / 5))
anew = anew * 1000 '*****[mm]*****

'_____begin calc. of SIF and stress in B_____

Fnmb = 0
Fb = 0
Fbstress = 0
sigsumb = 0

For mm = mmin To mmax

'_____Fb interpolation_____

F00 = Worksheets("Parma_KI").Cells(19 + alfa0 - 1 + (mm * 29), 2 + ksi0).Value
F01 = Worksheets("Parma_KI").Cells(19 + alfa0 - 1 + (mm * 29), 2 + ksi1).Value
F10 = Worksheets("Parma_KI").Cells(19 + alfa1 - 1 + (mm * 29), 2 + ksi0).Value
F11 = Worksheets("Parma_KI").Cells(19 + alfa1 - 1 + (mm * 29), 2 + ksi1).Value

If alfa0 = alfa1 Then
    FO = F00
    F1 = F01
Else
    If F10 > F00 Then
        FO = F00 + ((F10 - F00) * (alfaten - alfa0) / (alfa1 - alfa0)) 'linear interpolation
    Else
        FO = F00 - ((F00 - F10) * (alfaten - alfa0) / (alfa1 - alfa0))
    End If
    If F11 > F01 Then
        F1 = F01 + ((F11 - F01) * (alfaten - alfa0) / (alfa1 - alfa0)) 'linear interpolation
    Else
        F1 = F01 - ((F01 - F11) * (alfaten - alfa0) / (alfa1 - alfa0))
    End If
End If

If ksi0 = ksi1 Then
    Fbmm = FO
Else
    If F1 > FO Then

```

```

        Fbmm = F0 + ((F1 - F0) * (ksiten - ksi0) / (ksi1 - ksi0))      'linear interpolation
    Else
        Fbmm = F0 - ((F0 - F1) * (ksiten - ksi0) / (ksi1 - ksi0))
    End If
End If

Fbstress = Fbstress + (Fbmm * Bcoeff(mm))      'accumulated F_I *Kt(b)
sigsumb = sigsumb + Bcoeff(mm)                'accumulated stress concentration

Next mm

b = b / 1000      '*****[m]*****
Fb = Fbstress      'accumulated F_I
DeltaKb = Fbstress * dsigb * Sqr(pi * a)      'SIF b [MPa*m^0.5]
DeltaKbHCF = DeltaKb * (DD)      'SIF b (HCF)

'-----begin numeric integration Runge-Kutta-Fehlberg of Paris eq. for b-----

l1 = H * U(N, b, DeltaKb, ParisC, Parism)
l2 = H * U(N + H / 4, b + l1 / 4, DeltaKb, ParisC, Parism)
l3 = H * U(N + 3# / 8 * H, b + 3# / 32 * (l1 + 3 * l2), DeltaKb, ParisC, Parism)
l4 = H * U(N + 12# / 13 * H, b + 1932# / 2197 * l1 - 7200# / 2197 * l2 + 7296# / 2197 * l3, _
    DeltaKb, ParisC, Parism)
l5 = H * U(N + H, b + 439# / 216 * l1 - 8 * l2 + 3680# / 513 * l3 - 845# / 4104 * l4, DeltaKb, _
    ParisC, Parism)

deltab = (25# / 216 * l1) + (1408# / 2565 * l3) + (2197# / 4104 * l4) - (15 / 5)
deltab = deltab * 1000      '*****[mm]*****
a = a * 1000      '*****[mm]*****
b = b * 1000      '*****[mm]*****

'----calculate cnew : growth perpendicular to crackfront-----

deltaxb = (deltab) / (Sqr(1 + ((zb ^ 2) * (a ^ 4) / ((xb ^ 2) * (c ^ 4))))))
deltazb = Sqr((deltab ^ 2) - (deltaxb ^ 2))
xbnew = xb + deltaxb
zbnew = zb + deltaxb
cnew = zbnew / (Sqr(1 - ((xbnew / anew) ^ 2)))

'-----

If d = 0 Then GoTo 80      'output of initial values

If DeltaKaHCF > DeltaKathHCF Then      'definition of failure (HCF)
    If DeltaKbHCF > DeltaKathHCF Then
        Beep
        MsgBox " The SIF threshold for HCF has been reached all along the crack front "
        Kill = 1
        GoTo 80
    Else
        Beep
        MsgBox " The SIF threshold for HCF has been reached at point A "
        Kill = 1
        GoTo 80
    End If
End If

If a > af Then      'definition of failure (af)
    Beep
    MsgBox " The fracture crack depth af = " & af & " mm has been reached "
    Kill = 1
    GoTo 80
End If

    If N > Nmax Then
        Beep
        MsgBox " The number of load cycles Nmax = " & Nmax & " has been reached "
        Kill = 1
        GoTo 80
    End If

If i > 1000000 Then      'End dead loop

```

```

    Beep
    MsgBox " The calculation has been terminated after 1000000 calculation steps "
    Kill = 1
    GoTo 80
End If

Loop Until N >= (Noutput * d)                'outputs every Noutput cycles

'_____end calculation loop, begin output to Pivot table_____

80    Cells(74 + d, 1).Value = N                'Output to pivot (A , 74+d)
    Cells(74 + d, 2).Value = a                'Output to pivot (B , 74+d)
    Cells(74 + d, 3).Value = c                'Output to pivot (C , 74+d)
    Cells(74 + d, 4).Value = DeltaKa         'Output to pivot (D , 74+d)
    Cells(74 + d, 5).Value = DeltaKb         'Output to pivot (E , 74+d)
    Cells(74 + d, 6).Value = alfa            'Output to pivot (F , 74+d) alpha
    Cells(74 + d, 7).Value = ksi             'Output to pivot (G , 74+d) xi
    Cells(74 + d, 8).Value = Fa              'Output to pivot (H , 74+d)
    Cells(74 + d, 9).Value = Fb              'Output to pivot (I , 74+d)

'_____begin drawing ellipse from a_d and c_d_____

    For g = 0 To 30
        ellx = cnew * (1 - (g ^ 2 / 900))
        elly = Sqr(((anew) ^ 2) * (1 - ((ellx ^ 2) / ((cnew) ^ 2))))
        Cells(74 + g, 10 + (2 * d)).Value = ellx        'Output to pivot (J+2d , 74+g)
        Cells(74 + g, 11 + (2 * d)).Value = elly        'Output to pivot (K+2d, 74+g)
    Next g

If Kill = 1 Then GoTo 100                'this was the final output, terminate

d = d + 1
If d > 25 Then
    Beep
    MsgBox " The max. number of 25 outputs has been exceeded. Increase Noutput. "
    GoTo 100
End If

Loop

'_____end output loop_____

100    Cells(31, 6).Value = N                'Output to pivot (F , 31)
    Cells(32, 6).Value = anew                'Output to pivot (F , 31)
    Cells(33, 6).Value = cnew                'Output to pivot (F , 31)

    MsgBox " Simulation K_Parma04 done! "
    ActiveWindow.SmallScroll Down:=60

End Sub

Function E(N As Double, a As Double, DeltaKa As Double, ParisC As Double, Parism As Double) As Double

    E = ParisC * (DeltaKa ^ Parism) 'E = da/dN

End Function

Function U(N As Double, b As Double, DeltaKb As Double, ParisC As Double, Parism As Double) As Double

    U = ParisC * (DeltaKb ^ Parism) 'U = db/dN

End Function

```